

Structural Engineering Report No. ST-99-1

**BEHAVIOR OF SHEAR CONNECTORS IN
STEEL FRAMES WITH REINFORCED
CONCRETE INFILL WALLS**

**William K. Saari, Arturo E. Schultz,
Jerome F. Hajjar, and Carol K. Shield**

February 1999

**Department of Civil Engineering
Institute of Technology
University of Minnesota
Minneapolis, Minnesota 55455**

Abstract

This report investigates the behavior of headed shear studs for use in steel frames with composite reinforced concrete infill walls (S-RCW infill systems) for seismic applications. Shear studs in infill walls behave differently from studs in composite beams, for which the majority of past research has been conducted. The reason for this lies in the orientation of the studs with respect to the concrete. In infill walls, the studs lie in the plane of the concrete panel, whereas in composite beams, the studs are aligned perpendicular to the concrete slab. This results in the line of shear studs in infill walls being close to the parallel edges of the faces of the infill wall. Furthermore, in addition to cyclic shear forces, shear studs in infill walls are also subjected to axial tension/compression forces due to sidesway and overturning of the lateral resistance system.

An experimental program was developed to quantify the strength and deformation capacities of shear studs for use in S-RCW infill systems addressing the above issues, and to verify existing design equations, namely AISC LRFD, PCI, and Japanese design equations. A modification of the classic push-out test setup was made to accommodate the application of cyclic shear loading and axial tensile loading. Two different steel reinforcement configurations were used, one providing little confining reinforcement around the shear studs, and the other utilizing a steel reinforcement cage to provide ample confinement to the shear stud. This was done to examine the impact of the parallel edges present in infill walls.

Results from the testing program show that the presence of axial tension greatly reduced the stud shear strength and deformation capacity when no steel confining reinforcement was provided, indicating the absence of concrete confinement due to the close proximity of the parallel edges. When confining reinforcement was provided, test results generally correlated well with existing design equations, although several recommendations are made for improving existing strength predictions for shear connectors in infill walls. When cyclic shear loading was applied, the governing failure

mode was low cycle fatigue of the shear stud, resulting in a significant loss in deformation capacity of the studs.

Acknowledgements

This research was sponsored by the National Science Foundation (Grant No. CMS-9632506) under Dr. Shih-Chi Liu, and by the University of Minnesota. Additional financial support was provided by a GAANN Fellowship sponsored by the U.S. Department of Education, and by the University of Minnesota. In-kind funding and materials were provided by LeJeune Steel Company, Minneapolis, Minnesota; Cemstone, Minneapolis, Minnesota; and Ambassador Steel Company, Minneapolis, Minnesota. The authors would like to thank Paul M. Bergson, Lawrence A. Kloiber, Xiangdong Tong, Katsuyoshi Nozaka, and Daniel Enz for their contributions to this research. Any opinions, findings, conclusions, or recommendations presented by the author are those of the author, and are not necessarily the views of the sponsors.

Table of Contents

ABSTRACT	III
ACKNOWLEDGEMENTS	V
TABLE OF CONTENTS	VIII
LIST OF TABLES	XI
LIST OF FIGURES	XIII
1. INTRODUCTION	1
1.1 STEEL FRAME WITH REINFORCED CONCRETE INFILL WALLS SYSTEM.....	2
1.2 BEHAVIORAL ISSUES CONCERNING SHEAR STUD CONNECTIONS	3
1.2.1 Forces on Shear Studs	3
1.2.2 Shear Stud Orientation	4
1.2.3 Infill Wall Reinforcement.....	4
1.3 OBJECTIVES	4
1.4 ORGANIZATION OF REPORT.....	5
2. REVIEW OF PAST LITERATURE	6
2.1 MONOTONIC SHEAR TESTS	6
2.2 FATIGUE SHEAR STUD TESTS.....	8
2.3 SEISMIC SHEAR STUD TESTS.....	9
2.4 COMBINED LOADING SHEAR STUD TESTS.....	11
2.5 INFILL PANEL TESTS	11
2.6 SHEAR STUD STRENGTH EQUATIONS FOR DESIGN	13
2.6.1 American Institute of Steel Construction (AISC).....	13
2.6.2 Prestressed Concrete Institute (PCI).....	13
2.6.3 National Earthquake Hazards Reduction Program (NEHRP).....	15
2.6.4 Concrete Capacity Method (CC Method).....	15

3. EXPERIMENTAL PROGRAM.....	18
3.1 EXPERIMENTAL TEST SETUP	18
3.1.1 <i>General Test Setup Characteristics</i>	18
3.1.2 <i>Reinforcement Configurations</i>	21
3.2 FABRICATION OF TEST SPECIMENS	27
3.2.1 <i>Specimen Construction</i>	28
3.3 LOADING PROCEDURE.....	30
3.3.1 <i>Load Combinations</i>	30
3.3.2 <i>Instrumentation and Data Collection</i>	32
3.3.3 <i>Test Control and Loading Procedure</i>	33
4. EXPERIMENTAL OBSERVATIONS	36
4.1 SPECIMEN 1 (1-PB-MS-0)	36
4.1.1 <i>Observed Response to Load History</i>	37
4.1.2 <i>Condition after Testing</i>	37
4.1.3 <i>Measured Response</i>	38
4.2 SPECIMEN 2 (1-PB-NS-1)	39
4.2.1 <i>Observed Response to Load History</i>	39
4.2.2 <i>Condition after Testing</i>	40
4.2.3 <i>Measured Response</i>	41
4.3 SPECIMEN 3 (1-PB-MS-1)	41
4.3.1 <i>Observed Response to Load History</i>	41
4.3.2 <i>Condition after Testing</i>	43
4.3.3 <i>Measured Response</i>	43
4.4 SPECIMEN 4 (1-PB-CS-0)	44
4.4.1 <i>Observed Response to Load History</i>	44
4.4.2 <i>Condition after Testing</i>	45
4.4.3 <i>Measured Response</i>	46
4.5 SPECIMEN 5 (2-CG-MS-0).....	46

4.5.1	<i>Observed Response to Load History</i>	47
4.5.2	<i>Condition after Testing</i>	47
4.5.3	<i>Measured Response</i>	47
4.6	SPECIMEN 6 (2-CG-NS-1)	48
4.6.1	<i>Observed Response to Load History</i>	48
4.6.2	<i>Condition after Testing</i>	49
4.6.3	<i>Measured Response</i>	49
4.7	SPECIMEN 7 (2-CG-MS-1).....	50
4.7.1	<i>Observed Response to Load History</i>	50
4.7.2	<i>Condition after Testing</i>	50
4.7.3	<i>Measured Response</i>	51
4.8	SPECIMEN 8 (2-CG-CS-1).....	51
4.8.1	<i>Observed Response to Load History</i>	52
4.8.2	<i>Condition after Testing</i>	52
4.8.3	<i>Measured Response</i>	53
5.	ASSESSMENT OF LOAD-DISPLACEMENT BEHAVIOR	54
5.1	SPECIMEN 1 (1-PB-MS-0)	54
5.2	SPECIMEN 2 (1-PB-NS-1)	56
5.3	SPECIMEN 3 (1-PB-MS-1)	57
5.4	SPECIMEN 4 (1-PB-CS-0)	58
5.5	SPECIMEN 5 (2-CG-MS-0).....	60
5.6	SPECIMEN 6 (2-CG-NS-1)	62
5.7	SPECIMEN 7 (2-CG-MS-1).....	63
5.8	SPECIMEN 8 (2-CG-CS-1).....	64
6.	DATA ANALYSIS	66
6.1	COMPARISON TO CURRENT DESIGN EQUATIONS.....	66
6.1.1	<i>Shear Strength of Headed Shear Studs in Wall Panels</i>	67
6.1.2	<i>Tensile Strength of Headed Shear Studs in Wall Panels</i>	70

6.1.3	<i>Combined Shear and Tension Strength of Shear Studs in Wall Panels</i>	71
6.2	EFFECTIVE SECANT STIFFNESS	73
6.3	DEFORMATION CAPACITY	76
6.4	ENERGY DISSIPATION CAPACITY	77
7.	SUMMARY AND CONCLUSIONS	79
7.1	EXPERIMENTAL PROCEDURE.....	79
7.1.1	<i>Test Setup</i>	80
7.1.2	<i>Instrumentation and Loading</i>	81
7.2	TEST RESULTS	82
7.2.1	<i>Monotonic Shear Behavior</i>	82
7.2.2	<i>Monotonic Axial Tension Behavior</i>	83
7.2.3	<i>Cyclic Loading</i>	83
7.3	DESIGN RECOMMENDATIONS.....	84
7.4	FURTHER RESEARCH.....	90
A.	TEST VERIFICATION	167
A.1	TRANSLATION IN THE Y DIRECTION (Δ_y).....	167
A.2	ROTATION ABOUT THE Z-AXIS (θ_z).....	168
A.3	TRANSLATION IN THE X DIRECTION (Δ_x)	168
A.4	ROTATION ABOUT THE Y-AXIS (θ_y)	169
A.5	TRANSLATION IN THE Z-DIRECTION (Δ_z)	170
A.6	ROTATION ABOUT THE X-AXIS (θ_x).....	170
A.7	VERIFICATION OF SLIP MEASUREMENTS.....	170

List of Tables

Table 3.1 Steel reinforcement properties.....	95
Table 3.2 Mix design for concrete mix.....	95
Table 3.3 Concrete material properties for Series 1	96
Table 3.4 Concrete material properties for Series 2	96
Table 3.5 Specimen labeling system.....	97
Table 3.6 Schedule of tests	98
Table 3.7 South face instrumentation	99
Table 3.8 North face instrumentation	100
Table 3.9 Acoustic emission instrumentation.....	100
Table 3.10 Data collection rates for Specimen 4.....	101
Table 3.11 Loading rates for Specimen 4	102
Table 3.12 Loading rates for Specimen 8.....	102
Table 4.1 Ultimate values for load and displacement.....	102
Table 6.1 Load and displacement values for the first trilinear break point	103
Table 6.2 Load and displacement values for the second trilinear break point	103
Table 6.3 Comparison of Peak Strengths from Measured and Predicted Results	104
Table 6.4 Deformation capacities	104

List of Figures

Figure 1.1	Prototype infill wall-steel frame system.....	105
Figure 3.1	Elevation of the experimental test setup.....	105
Figure 3.2	Plan view of the experimental test setup	106
Figure 3.3	Photograph of the experimental test setup	106
Figure 3.4	Possible failure modes in infill wall systems	107
Figure 3.5	“Perimeter Bar” steel reinforcement configuration.....	107
Figure 3.6	Photograph of the “Perimeter Bar” steel reinforcement configuration	108
Figure 3.7	“Cage” steel reinforcement configuration.....	108
Figure 3.8	Photograph of the “Cage” steel reinforcement configuration	109
Figure 3.9	South face instrumentation.....	110
Figure 3.10	North face instrumentation.....	111
Figure 3.11	Acoustic emission instrumentation	112
Figure 3.12	Other LVDT’s and dial gages	113
Figure 3.13	Cyclic slip history for Specimen 4	113
Figure 3.14	Cyclic slip history for Specimen 8	113
Figure 4.1	Crack Pattern for Specimen 1, north face.....	114
Figure 4.2	Photograph of Specimen 1, south face, after testing	115
Figure 4.3	Deformed stud for Specimen 1	116
Figure 4.4	Load versus slip for Specimen 1	116
Figure 4.5	Load versus separation for Specimen 1.....	117
Figure 4.6	Load versus column displacement for Specimen 1	117
Figure 4.7	Crack pattern for Specimen 2, south face.....	118
Figure 4.8	Photo of Specimen 2, north face, after testing	119
Figure 4.9	Load versus column displacement for Specimen 2	120
Figure 4.10	Load versus separation for south face LVDT’s for Specimen 2	120
Figure 4.11	Load versus separation for north face LVDT’s for Specimen 2	121
Figure 4.12	Crack pattern for Specimen 3, north face.....	122
Figure 4.13	Photograph of Specimen 3, north face, after testing	123

Figure 4.14	Load versus column displacement during tensile loading for Specimen 3	124
Figure 4.15	Load versus separation for south face LVDT's during tensile loading for Specimen 3	124
Figure 4.16	Load versus slip during shear loading for Specimen 3	125
Figure 4.17	Load versus separation for south face LVDT's during shear loading for Specimen 3	125
Figure 4.18	Load versus column displacement during shear loading for Specimen 3	126
Figure 4.19	Photograph of stud failure surface for Specimen 4	126
Figure 4.20	Concrete void created by crushing for Specimen 4	127
Figure 4.21	Load versus west slip for Specimen 4	127
Figure 4.22	Load versus east slip for Specimen 4	128
Figure 4.23	Load versus separation for south face LVDT's for Specimen 4	128
Figure 4.24	Load versus separation for north face LVDT's for Specimen 4	129
Figure 4.25	Load versus column displacement for Specimen 4	129
Figure 4.26	Load versus slip for Specimen 5	130
Figure 4.27	Load versus separation for SF LVDT's for Specimen 5	130
Figure 4.28	Load versus separation for NF LVDT's for Specimen 5	131
Figure 4.29	Load versus column displacement for Specimen 5	131
Figure 4.30	Crack Pattern for Specimen 6, north face	132
Figure 4.31	Photograph of stud failure surface for Specimen 6	133
Figure 4.32	Load versus column displacement for Specimen 6	133
Figure 4.33	Load versus separation for south face LVDT's for Specimen 6	134
Figure 4.34	Load versus separation for north face LVDT's for Specimen 6	134
Figure 4.35	Load versus column displacement during tensile loading for Specimen 7	135
Figure 4.36	Load versus separation for south face LVDT's during tensile loading for Specimen 7	135
Figure 4.37	Load versus separation for north face LVDT's during tensile loading for Specimen 7	136
Figure 4.38	Load versus slip during shear loading for Specimen 7	136

Figure 4.39 Load versus separation for south face LVDT's during shear loading for Specimen 7	137
Figure 4.40 Load versus separation for north face LVDT's during shear loading for Specimen 7	137
Figure 4.41 Load versus column displacement during shear loading for Specimen 7 ..	138
Figure 4.42 Photograph of stud failure surface for Specimen 8	138
Figure 4.43 Load versus column displacement during tensile loading for Specimen 8	139
Figure 4.44 Load versus separation for south face LVDT's during tensile loading for Specimen 8.....	139
Figure 4.45 Load versus separation for north face LVDT's during tensile loading for Specimen 8.....	140
Figure 4.46 Load versus west slip during shear loading for Specimen 8	140
Figure 4.47 Load versus east slip during shear loading for Specimen 8	141
Figure 4.48 Load versus separation for south face LVDT's during shear loading for Specimen 8	141
Figure 4.49 Load versus separation for north face LVDT's during shear loading for Specimen 8	142
Figure 4.50 Load versus column displacement during shear loading for Specimen 8 ..	142
Figure 5.1 Load versus average slip for Specimen 1	143
Figure 5.2 Load versus average column displacement for Specimen 2.....	143
Figure 5.3 Load versus average slip for Specimen 3	144
Figure 5.4 Load versus average slip for Specimen 4	144
Figure 5.5 Progression of damage mechanisms for Cyclic Tests	145
Figure 5.6 Typical cycle for Specimen 4	145
Figure 5.7 Load versus average slip for Specimen 5	146
Figure 5.8 Load versus average column displacement for Specimen 6.....	146
Figure 5.9 Load versus average slip for Specimen 7	147
Figure 5.10 Load versus average slip for specimen 8.....	147
Figure 5.11 Typical cycle for Specimen 8	148

Figure 5.12 Acoustic emission activity for Specimen 1 at Sensor 1	148
Figure 5.13 Acoustic emission activity for Specimen 1 at Sensor 3	149
Figure 5.14 Acoustic emission activity for Specimen 1 at Sensor 4	149
Figure 5.15 Acoustic emission activity for Specimen 1 at Sensor 6	150
Figure 5.16 Acoustic emission activity for Specimen 2 at Sensor 1	150
Figure 5.17 Acoustic emission activity for Specimen 2 at Sensor 6	151
Figure 5.18 Acoustic emission activity for Specimen 3 at Sensor 1	151
Figure 5.19 Acoustic emission activity for Specimen 3 at Sensor 6	152
Figure 5.20 Acoustic emission activity for Specimen 4 at Sensor 2	152
Figure 5.21 Acoustic emission activity for Specimen 4 at Sensor 6	153
Figure 5.22 Acoustic emission activity for Specimen 5 at Sensor 1	153
Figure 5.23 Acoustic emission activity for Specimen 5 at Sensor 4	154
Figure 5.24 Acoustic emission activity for Specimen 5 at Sensor 9	154
Figure 5.25 Acoustic emission activity for Specimen 5 at Sensor 6	155
Figure 5.26 Acoustic emission activity for Specimen 5 at Sensor 10	155
Figure 5.27 Acoustic emission activity for Specimen 5 at Sensor 7	156
Figure 5.28 Acoustic emission activity for Specimen 6 at Sensor 1	156
Figure 5.29 Acoustic emission activity for Specimen 6 at Sensor 4	157
Figure 5.30 Acoustic emission activity for Specimen 6 at Sensor 6	157
Figure 5.31 Acoustic emission activity for Specimen 7 at Sensor 4	158
Figure 5.32 Acoustic emission activity for Specimen 8 at Sensor 10	158
Figure 6.1 Envelope curves for Specimens 4 and 8.....	159
Figure 6.2 Comparison to design formulas for Specimens 1 and 5.....	159
Figure 6.3 Comparison to design formulas for Specimens 2 and 6.....	160
Figure 6.4 Comparison to design formulas for Specimens 3 and 7.....	160
Figure 6.5 Comparison to interaction curves.....	161
Figure 6.6 Comparison to design formulas for Specimen 4	161
Figure 6.7 Comparison to design formulas for Specimen 8	162
Figure 6.8 Effective secant stiffness versus average slip for Specimens 1 and 5.....	162

Figure 6.9 Effective secant stiffness versus average column displacement for Specimens 2 and 6.....	163
Figure 6.10 Effective secant stiffness versus average slip for Specimens 3 and 7.....	163
Figure 6.11 Effective stiffness versus average slip for Specimens 4 and 8.....	164
Figure 6.12 Deformation Capacity	164
Figure 6.13 Normalized energy versus average slip for Specimens 1 and 5.....	165
Figure 6.14 Normalized energy versus average slip for Specimens 3 and 7.....	165
Figure 6.15 Cumulative normalized energy versus average slip for Specimens 4 and 8	166
Figure A.1 Degrees of freedom for panel translation and rotation.....	172
Figure A.2 Translation in the y-direction, Δ_y , for Specimen 1	172
Figure A.3 Translation in the y-direction, Δ_y , for Specimen 2	173
Figure A.4 Translation in the y-direction, Δ_y , for Specimen 3	173
Figure A.5 Translation in the y-direction, Δ_y , for Specimen 4	174
Figure A.6 Translation in the y-direction, Δ_y , for Specimen 5	174
Figure A.7 Translation in the y-direction, Δ_y , for Specimen 6	175
Figure A.8 Translation in the y-direction, Δ_y , for Specimen 7	175
Figure A.9 Translation in the y-direction, Δ_y , for Specimen 8	176
Figure A.10 Slip ratio versus average slip for Specimen 1	176
Figure A.11 Slip ratio versus average slip for Specimen 4	177
Figure A.12 Rotation about the z-axis, θ_z	178
Figure A.13 Rotation about the z-axis, θ_z , for Specimen 1	179
Figure A.14 Rotation about the z-axis, θ_z , for Specimen 2	179
Figure A.15 Rotation about the z-axis, θ_z , for Specimen 3	180
Figure A.16 Rotation about the z-axis, θ_z , for Specimen 4	180
Figure A.17 Rotation about the z-axis, θ_z , for Specimen 5	181
Figure A.18 Rotation about the z-axis, θ_z , for Specimen 6	181
Figure A.19 Rotation about the z-axis, θ_z , for Specimen 7	182

Figure A.20	Rotation about the z-axis, θ_z , for Specimen 8	182
Figure A.21	Translation in the x-direction, Δ_x , for Specimen 2	183
Figure A.22	Translation in the x-direction, Δ_x , for Specimen 4	183
Figure A.23	Translation in the x-direction, Δ_x , for Specimen 5	184
Figure A.24	Translation in the x-direction, Δ_x , for Specimen 6	184
Figure A.25	Translation in the x-direction, Δ_x , for Specimen 7	185
Figure A.26	Translation in the x-direction, Δ_x , for Specimen 8	185
Figure A.27	Rotation about the y-axis, θ_y	186
Figure A.28	Rotation about the y-axis, θ_y , for Specimen 2	186
Figure A.29	Rotation about the y-axis, θ_y , for Specimen 4	187
Figure A.30	Rotation about the y-axis, θ_y , for Specimen 5	187
Figure A.31	Rotation about the y-axis, θ_y , for Specimen 6	188
Figure A.32	Rotation about the y-axis, θ_y , for Specimen 7	188
Figure A.33	Rotation about the y-axis, θ_y , for Specimen 8	189
Figure A.34	True versus measured slip	189

1. Introduction

The aftermath from the 1994 Northridge, California earthquake sparked a growing concern regarding the seismic resistance of steel moment frames. The focus of this concern was the moment connection region. Fractures emanating from the girder flange-to-column flange weld and often propagating into the column flange and web led to costly repairs of existing structures.

The assessment of this problem has led researchers in several different directions in an effort to provide an effective, yet economical solution. Research has been done to assess the connection region itself. Recommendations such as removal of the backing bar, improved welding procedures, the utilization of weld material with a higher fracture toughness, and changes in connection geometry have been proposed.

Efforts have also been made to relieve the demand on this connection region. One popular method proposed is the introduction of “dog bones” to the flanges of the beams framing in the columns. This detail involves reducing the flange area for the purpose of moving the weakest point of the beam away from the connection region containing welds. Thus, plastic hinges are moved to an area in the beam void of any welding.

Another alternative involves utilizing a composite wall system. This report addresses an aspect of the behavior for steel frame-reinforced concrete infill wall (S-RCW) composite system, with emphasis placed on the interface region between the steel sections and the reinforced concrete infill panels.

1.1 Steel Frame with Reinforced Concrete Infill Walls System

The S-RCW infill system consists of steel frames with reinforced concrete infill walls. When idealizing the behavior of this system, gravity and a portion of the overturning forces are assumed to be resisted by the steel frame, while story (seismic) shear and the remainder of the overturning forces are assumed to be resisted by the reinforced concrete infill wall. There are several advantages associated with this type of system. One advantage is that the orientation of the infill wall is such that the wall provides excellent initial stiffness against sway. By improving the drift control of the frame, the deformation demands on the steel members are reduced. As a result, during an earthquake, the majority of the damage on the structure would be focused on the infill wall and not on the steel members. This is desirable since repairing damage to a concrete infill wall is more economical than repairing steel frame members. These infill repairs may comprise the injection of epoxy into the cracks, or even the complete replacement of the infill panels.

Another advantage of the steel frame-RC infill system is that the addition of a stiff and strong component such as a reinforced concrete infill wall will most likely result in the reduction of the steel member sizes, and possibly the replacement of some of the fully restrained moment connections in favor of less expensive partially restrained connections. In addition to improving the seismic resistance of the frame structure, reinforced concrete infill walls can be efficiently and economically constructed, with the wall forms placed in between the column and beam flanges, and high-slump concrete pumped into the infill panels.

In order for the composite wall system to function properly, composite action between the steel members and the infill wall must be attained. This can be achieved through headed shear studs welded to the beam and column flanges, and embedded in the infill wall. Shear studs are common in composite construction, and therefore provide an initial basis for investigation. In order to assess the degree of composite action in these

shear stud connections, the behavior of shear studs when subjected to the forces present in the S-RCW infill system must be known.

1.2 Behavioral Issues Concerning Shear Stud Connections

The primary issue to be addressed regarding connections in the S-RCW infill system is whether shear studs are a viable solution for establishing composite action between the steel members and the reinforced concrete infill wall. To evaluate this, the strength and deformation capacities of the shear studs are required in addition to knowing the strength and deformation demands on the studs. The research documented in this paper focuses on the capacity of the shear studs in the S-RCW infill system.

1.2.1 Forces on Shear Studs

In determining the strength and deformation capacities of shear studs for use in S-RCW infill systems, the forces resisted by the studs must be defined. During an earthquake, two major phenomena occur, sidesway and overturning of the frame. When subjected to cyclic loading, sway of the frame causes the infill wall and the frame columns to move relative to one another along the concrete-steel interface. This movement is opposed by the shear studs, so as to retain composite action in the frame. As a result, a large shear demand is placed on the shear studs. In addition to shear forces, curvature in the columns relative to the infill panel during cyclic loading subjects the shear studs to axial forces within each story, with the columns either trying to separate from the wall or bearing against it. Overturning of the infill panels also generates large axial tension stresses in the studs between the panels and the beams.

When comparing the forces acting on shear studs in infill walls to forces in studs found in composite beams, the main difference lies in the presence of significant axial tension in the former. Therefore, the strength and deformation capacity of shear studs for use with infill walls may be considerably different from studs in composite beams.

1.2.2 Shear Stud Orientation

Shear studs in infill walls are placed at a different orientation with respect to the geometry of the concrete panel than studs in composite beams. For infill walls, the line of shear studs are in the plane of the infill wall, whereas for composite beams they are normal to the plane of the concrete slab. As a result, the line of studs in an infill are parallel to the faces of the wall (i.e., parallel edges). Figure 1.1 shows the orientation of the studs with respect to the panel for a prototype S-RCW infill system. With the thickness of the wall being presumed to be fairly small, in the range of 20 to 36 cm (8 to 14 in.), these parallel edges are fairly close to the line of studs, which may considerably affect the behavior of the studs since the concrete provides little confinement in this case. For composite beams, parallel edges are non-existent, and the nearest edges are normal to the axis of the studs. Because there are no nearby parallel edges in composite beams, the concrete slabs generally serve to partially confine the studs. In an infill, the limited thickness of the panel cannot provide such confinement.

1.2.3 Infill Wall Reinforcement

Infill walls in composite wall systems contain steel reinforcement. This reinforcement is essential in maintaining the integrity of the infill wall. However, composite action between the wall and the steel members is achieved directly through the shear studs, or other form of suitable shear connection. As a result, there is a large concentration of stresses near the interface region, and there is a likelihood of localized concrete damage in the vicinity of the shear studs. Therefore, the addition of transverse steel reinforcement around the stud in the attempt of confining the concrete around the shear stud should improve the performance of the interface.

1.3 Objectives

The primary objective of this project is to determine through experiments the monotonic and cyclic strength and deformation capacity of headed shear stud connections between steel wide-flange members and reinforced concrete infill panels, subjected to combined shear and axial tension. The research will investigate the effects of the concrete infill wall edges parallel to the line of studs, and the addition of confining steel reinforcement around the shear stud, on the strength and deformation capacities of shear studs. Furthermore, the experimental data will be used for comparison with current design provisions for headed shear connectors. Therefore, a concerted effort in the form of an experimental program was made in order to assess the behavior of headed shear stud connections for infill walls, carefully taking into account the issues previously mentioned.

1.4 Organization of Report

In this report, a review of past research performed pertaining to shear stud behavior is presented in Chapter 2. Chapter 3 provides a description of the experimental program developed for this project, which includes information on the design and fabrication of the experimental test setup, panel reinforcement configurations, instrumentation of the specimens, and the loading procedure for each test. This is followed by the presentation of experimental observations for each test in Chapter 4. This includes observations made of each specimen during the load history and once testing had completed, as well as the presentation of the measured quantities obtained from the instrumentation scheme. In Chapter 5, the load versus primary displacement relationship is examined in depth. Further analysis of experimental data, such as energy dissipation, effective secant stiffness, and comparison to existing design estimates of stud strength, is included in Chapter 6. A summary of the project and conclusions drawn from it are provided in Chapter 7.

2. Review of Past Literature

Past research on shear connectors has predominantly dealt with composite behavior of concrete slabs in composite beam systems, where the line of shear studs is perpendicular to the slab. Also, most testing has been performed under monotonic loading. The cyclic loading experiments that have been conducted focus primarily on fatigue loading (low amplitude, high number of cycles), with only occasional emphasis given to seismic loading (high amplitude, low number of cycles). Past research relevant to the current project is summarized in this chapter.

2.1 Monotonic Shear Tests

Early studies of composite structures were performed by Viest (1956). Viest examined the behavior of shear studs for use in composite beam structures through an experimental program using “push-out” tests of shear studs. From these experiments, empirical equations were developed to predict the strength of shear studs for composite beams.

Research done by Ollgaard et al. (1971) investigated shear stud behavior under monotonic loading characteristics for composite beam structures. The experimental program associated with this research used push-out tests to determine the behavior of shear studs. Each specimen consisted of an I-beam with two or more shear studs welded to each flange. A portion of a concrete slab/deck was then attached to each flange. A total of 48 specimens were tested. Two primary failure modes were observed. These failure modes were shearing of the stud and concrete damage near the shear stud. It was also observed that cracking in the concrete slab did not occur until the ultimate load was

nearly achieved. The researchers concluded that the shear strength capacity of a single stud, Q_n , may be given by the following expression:

$$Q_n = 0.5 A_{sc} \sqrt{f'_c E_c} \leq A_{sc} F_u \quad (2.1)$$

where A_{sc} is the area of the shear stud in in.² [which, for the 3/4 inch headed shear studs used in this work equals 285 mm² (0.4418 in²)], f'_c is the concrete compressive strength in ksi [with a nominal value of 27.58 MPa (4 ksi) in this research], E_c is the modulus of elasticity of concrete in ksi [in this work computed as $E_c = w^{1.5} \sqrt{f'_c}$, where w , the density of concrete in pcf, is taken as 22.78 kN/m³ (145 pcf), giving a value of 24,080 MPa (3492 ksi)], and F_u is the tensile strength of the stud in ksi, taken in this work as a nominal value of 413.7 MPa (60 ksi). A formula was also developed relating load and displacement of a shear stud connector:

$$Q = Q_u \left(1 - e^{-18\Delta}\right)^{\frac{2}{5}} \quad (2.2)$$

where Q is the shear load on the stud in kips, Q_u is taken as the shear stud capacity, Q_n , given by Equation 2.1 in kips, and Δ is the slip in inches. For reloading of shear studs, the equation for the load-slip relationship was given as:

$$Q = Q_u \frac{80\Delta}{1 + 80\Delta} \quad (2.3)$$

Research was also done concerning how the stud behavior is affected when concrete cracks formed in composite beam structures under monotonic loading (Oehlers, 1989; Oehlers and Park, 1992). The experimental setup consisted of a concrete slab with shear studs welded to a steel plate, and embedded in the slab. The slab was of a small enough thickness such that a longitudinal splitting failure would be induced before the shear studs would fail. The experimental program also examined the usefulness of placing transverse steel reinforcement near the stud in an attempt to limit the propagation of these cracks towards the stud. The primary variables between tests were the amount of steel, bar size, and bar spacing. Findings from this research showed that there was a significant reduction in the shear stud capacity due to crack formation in the concrete slab. Experimental data showed that using little or no confining transverse steel resulted

in a reduction in the shear stud capacity by as much as 44 percent in slabs where longitudinal cracks are present. However, by adding approximately one percent of confining steel to the specimen, the load capacity nearly doubled when compared to using little or no confining steel. These results emphasize the need for some sort of transverse steel arrangement to limit crack propagation in a thin concrete slab.

2.2 Fatigue Shear Stud Tests

Several tests have been performed studying the shear stud behavior in composite beam systems under fatigue loading. Slutter and Fisher (1971) examined the effect of the minimum stress applied and the range of stresses used. The experimental program involved push-out testing of shear connectors, varying the minimum stress applied and the stress range. Results showed that when both of these variables were increased in magnitude, there was a degradation in the shear stud capacity, leading to failure in a fewer number of cycles. Of the two parameters, it appeared that the range of stresses applied possessed a stronger influence on the stud behavior than the minimum stress applied.

Other push-out tests of shear connectors subjected to fatigue loading were performed by Toprac (1965), and Oehlers (1990). Results from these experimental programs showed that a degradation in the shear stud strength occurred during fatigue loading. Concrete crushing damage near the shear connector in later cycles, causing larger increases in slip after each cycle, was believed to be a major factor in contributing to the strength degradation.

Static and fatigue push-out tests of L-shaped connectors were performed by Thürlimann (1959). Results from fatigue testing showed that there were a larger number of cycles to failure for the L-shaped connectors than for straight connectors. From this research, a design criteria was presented for L-shaped connectors for fatigue and static loading conditions.

Mainstone and Menzies (1967) examined the fatigue strength of different types of

shear connectors. Push-out specimens having U-shaped bar anchors, shear studs, and channels were tested. Results showed that shear studs possessed the lowest strength per connector, while channel sections had the highest strength per connector. The failure modes for both of these shear connector types was yielding of the connector, while when U-shaped bar anchors were used, failure was dictated by concrete failure.

Yen et al. (1997) also investigated shear stud behavior under fatigue loading for composite beams. For the experimental program, the shear studs were instrumented, and results from the composite beam tests showed that once concrete cracking occurred near the stud, the studs were more heavily stressed. The primary failure mechanism was a splitting crack along the entire length of the beam. From this, it was recommended that the steel reinforcement be well distributed throughout the slab, using welded-wire fabric for example.

2.3 Seismic Shear Stud Tests

Hawkins and Mitchell (1984) performed tests on shear connectors under seismic loading. This research was applicable to slabs in composite bridge elements. Both push and push-pull tests were performed on composite slab and composite deck systems. The primary variable investigated was shear stud spacing. Findings from the performed experiments showed that large stud spacing, between 305 and 457 mm (12 and 18 in.), and staggering the line of studs produced more stable hysteresis loops than when the studs were close together, between 76 and 114 mm (3 and 4.5 in.). Also, it was seen that when failure was initiated by concrete pullout, there was a more rapid deterioration in the peak shear strength with each passing cycle, while when shear stud failure governed, more stable hysteresis loops were present. When comparing the behavior of the cyclic shear tests to their companion monotonic shear tests, it was noticed that much less ductility was achieved in the cyclic tests than the monotonic tests.

Seismic push and push-pull tests on shear studs were also performed by Bursi and Ballerini (1996). The type of system targeted by these tests was once again composite

beam systems. Results showed that push-pull specimens exhibited less ductility than the push specimens. Also, the push-pull specimens failed at a lower load than the push specimens did. The shear studs themselves were instrumented with strain gauges near both the base and the head of the shear stud. Data provided by this instrumentation showed that larger strains were achieved close to the base of the shear stud.

Gattesco and Giuriani (1995) also investigated the seismic response of shear connectors. A new testing apparatus and specimen configuration was introduced as an alternative to commonly found “push-out” testing setups. This “direct shear” test involves testing a single shear connector at a time. The cyclic load is applied directly to steel bars attached to the steel element connected to the shear stud. This apparatus was described as being a more accurate model of the actual shear stud behavior found in the complete composite structure itself. As was present with fatigue loading experiments, Gattesco and Giuriani’s tests showed that with each passing load cycle, there was a steady increase in slip, resulting in a loss in load transfer from the steel element to the concrete element. Because individual studs in a small specimen were tested, no transverse reinforcement was provided.

McMullin and Astaneh-Asl (1994) examined the implementation of a metal skirt around the shear stud in composite beam structures subjected to seismic loading. This skirt provides an air void which allows the stud to flex without localized crushing of the concrete. The amount of desired flexural behavior in the shear stud can be controlled by adjusting the height of the skirt. Results from the experiments showed that using the skirt improved the ductility in the specimen. However, in achieving the improved ductility, much lower peak load values and stiffnesses were achieved.

Klingner et al. (1982) also investigated the behavior of anchor bolts when subjected to reversed cyclic shear loading. An experimental study was conducted testing single A307 anchor bolts embedded in concrete. Variables studied included the distance to a free edge in the direction of loading, the effect of use 180 degree hairpins wrapped around the anchor bolt, and the type of cyclic loading program. Counterpart monotonic shear specimens were also tested. Results from the testing program showed that cyclic

loading greatly reduced the ultimate strength reached, by as much as 50 percent. Also, small edge distances reduced the shear strength unless 180 degree hairpins were used, in which case the full anchor bolt shear strength was achieved. Results from monotonic shear tests at large edge distances where the failure mode was governed by steel failure showed that the full anchor bolt capacity, $A_s F_u$, was not achieved. This led to the authors' conclusion that the shear strength for steel failure should be reduced by 25 percent. However, based on the experimental results when steel failure governed, the average strength due to shear loading was approximately 91 percent of $A_s F_u$, with a standard deviation of 4 percent.

2.4 Combined Loading Shear Stud Tests

McMackin et al. (1973) studied the effect of headed steel anchors subjected to both shear and tension. The loading configuration for both of these forces was monotonic. From tests performed, the following equation was formulated describing the anchor capacity under combined loading:

$$\left(\frac{P / A_s}{\bar{P}_u / A_s} \right)^{5/3} + \left(\frac{S / A_s}{\bar{S}_u / A_s} \right)^{5/3} = 1 \quad (2.4)$$

where P is the applied tensile load, S is the applied shear load, \bar{P}_u is the anchor tensile capacity, \bar{S}_u is the anchor shear capacity, and A_s is the cross-sectional area of the anchor.

2.5 Infill Panel Tests

The majority of research studying the seismic behavior of steel frames with reinforced concrete infills has been done in Japan by Makino (1985) and Hayashi and Yoshinaga (1985, 1986, 1987, and 1994). Experiments were performed on single story, single bay steel frames with reinforced concrete infills at approximately a one-third scale. The principle variables examined included the orientation of the steel columns (strong

axis versus weak axis), the panel aspect ratio, and the stud spacing. In these tests, the shear studs were in place largely to preclude out-of-plane failure of the wall. The experiments showed that the infill system performed well when using the strong axis of the steel columns, but that when using the weak column axis, there was a significant decline in the peak load with each passing cycle. Furthermore, the shear stud spacing, generally large in these tests, appeared to have little or no impact on the behavior of the infill system. Push-out and push-pull shear stud tests were also conducted. From this experimental program, a stud strength formula was recommended as:

$$q = \phi 0.5 a_{sc} \sqrt{F_c E_c} \quad (2.5)$$

where q is the shear stud capacity, $\phi = \phi_l$, the edge reduction factor where $\phi_l = (a/15)^{1/2}$, a is the distance from the center of the stud to the edge of the panel in cm, a_{sc} is the area of the shear stud in cm^2 [2.85 cm^2 (0.4418 in^2) in this work], F_c is the concrete compressive strength in kg/cm^2 [having a nominal value of 281 kg/cm^2 (4 ksi) in this research], and E_c is the modulus of elasticity of concrete in kg/cm^2 [computed as $245,700 \text{ kg/cm}^2$ (3492 ksi)]. For the experiments in this work, a equals 12.7 cm (5 inches) and ϕ_l thus equals 0.92 . This formula provides values equivalent to Equation 2.1, where concrete failure governs, but with an additional term, ϕ , intended to reduce the stud capacity for the case of thin walls. This could result in the wall faces being close to the stud, reducing the amount of concrete confinement around the stud, which could result in a lower stud capacity. Note that Makino (1985) recommended taking an additional 40 percent reduction in the strength calculated by Equation 2.5. However, this reduction relates more specifically to his recommendations for design (e.g., functioning as a resistance factor), and the 40 percent reduction is neglected in this work so that a more direct comparison of experimental strength may be made to the values predicted by Equation 2.5.

2.6 Shear Stud Strength Equations for Design

2.6.1 American Institute of Steel Construction (AISC)

For the determination of the shear capacity of shear studs, AISC (1993) adopted Equation 2.1, proposed by Ollgaard et al. (1971) in its Load and Resistance Factor Design (LRFD) specification. A resistance factor, ϕ , equal to 1 is assumed in this equation. No provisions are provided with respect to shear studs subjected to tension loading only, or combined shear and tension loading.

2.6.2 Prestressed Concrete Institute (PCI)

For shear loading only, PCI in its manual of recommended practice, *PCI Design Handbook* (PCI, 1992), proposes that for failure dictated by failure of the shear stud, the following equation be used:

$$\phi V_s = \phi 0.75 A_b f_s \quad (2.6)$$

where V_s is the nominal stud shear strength due to steel failure in kips, $\phi = 1$, A_b is the cross-sectional area of the shear connector in square inches [285 mm² (0.4418 in²) in this work], and f_s is the tensile strength of the steel in ksi [taken as 413.7 MPa (60 ksi) in this work]. For failure initiated by concrete failure, the following equation exists based on the formation of a 45 degree shear cone:

$$\phi V_c = \phi 800 A_b \lambda \sqrt{f'_c} / 1000 \leq \phi 2\pi d_e^2 \lambda \sqrt{f'_c} / 1000 \quad (2.7)$$

where V_c is the stud shear strength due to concrete failure in kips, $\phi = 0.85$, λ is a correction factor for lightweight concrete (equal to 1.0 in this work), f'_c is the concrete compressive strength in psi, and d_e is the edge distance in the direction of the load in inches [taken as 177.8 mm (7 in.) in this work]. The cap of $\phi 2\pi d_e^2 \lambda \sqrt{f'_c} / 1000$ on ϕV_c in Equation (2.7) is from PCI (1985), but was removed in PCI (1992). It was included here for consideration because it accounts for potential edge condition effects (d_e), which are

potentially important in this application for shear connectors near the corners of the infill panels. The design shear strength is the lesser of Equations 2.6 and 2.7.

For the stud tensile strength, where steel failure governs, PCI (1992) uses the following equation:

$$\phi P_s = \phi 0.9 A_b f_s \quad (2.8)$$

where P_s is the nominal stud tensile strength due to steel failure in kips and $\phi = 1.0$.

When concrete failure governs, the following equation is used, assuming a 45 degree pullout cone forms in the concrete:

$$\phi P_c = \phi 12.6 \ell_e (\ell_e + d_h) \lambda \sqrt{f'_c} / 1000 = 10.7 \ell_e (\ell_e + d_h) \lambda \sqrt{f'_c} / 1000 \quad (2.9)$$

where P_c is the nominal stud tensile strength due to concrete failure in kips, $\phi = 0.85$, ℓ_e is the length of stud embedment in inches [127 mm (5 inches) in this work], and d_h is the diameter of the head of the shear stud in inches [31.75 mm (1.25 inches) in this work]. The design tensile strength is given as the lesser of Equations 2.8 and 2.9. PCI (1992) also provides adjustments to the stud tensile strength equations to take into account groups of studs and studs near a free edge.

For shear studs subjected to combined shear and tension, PCI (1992) uses the following equations:

$$\frac{1}{\phi} \left[\left(\frac{P_u}{P_s} \right)^2 + \left(\frac{V_u}{V_s} \right)^2 \right] \leq 1.0 \quad (2.10)$$

where $\phi = 1.0$, P_u is the factored tensile load and V_u is the factored shear load, and:

$$\frac{1}{\phi} \left[\left(\frac{P_u}{P_c} \right)^2 + \left(\frac{V_u}{V_c} \right)^2 \right] \leq 1.0 \quad (2.11)$$

where $\phi = 0.85$.

The PCI (1992) stud strength equations for shear, tension, and combined shear and tension where concrete failure governs are based on research done by Shaikh and Yi (1985). This work involved an analysis of the stud strength using a 45 degree cone surface, and performing a comparison with existing test results. From this analysis,

Shaikh and Yi (1985) proposed modifications and additions to the 1971 PCI Design Handbook, which were adopted into later revisions of the Handbook (Equations 2.7, 2.9, and 2.11).

Note that in Equation 2.6, the factor $0.75f_s$ is meant to represent the approximate yield strength in shear (as opposed to ultimate shear strength). Similarly, in Equation 2.8, the factor $0.9f_s$ is meant to represent the approximate tensile yield strength of the stud, as opposed to the ultimate tensile strength of the stud (PCI, 1992). Thus, if comparing these PCI equations with Equations 2.1, 2.5, 2.7, and 2.9 for tensile or shear loading conditions, Equations 2.6 and 2.8 will generally provide conservative strength predictions, as they are estimates of the yield strength, not the ultimate strength, of the stud.

2.6.3 National Earthquake Hazards Reduction Program (NEHRP)

The *NEHRP Recommended Provisions for Seismic Regulations for New Buildings* (1997) adopted equations similar to those used by PCI (1992) (Equations 2.6 through 2.11) in the chapter addressing concrete design. In addition, in the chapter concerning composite construction, for reinforced concrete infill walls with steel elements, the AISC LRFD equation is used (Equation 2.1) with a 25 percent reduction in the stud strength. This provision was adopted into the AISC Seismic Provisions (AISC, 1997), which is now referenced by NEHRP in the composite chapter.

2.6.4 Concrete Capacity Method (CC Method)

The Concrete Capacity Method, as presented in the design guide from the Comité Euro-International du Béton (CEB), gives different design equations for determining anchor strength (CEB, 1997). For shear resistance governed by steel failure, the following equation holds:

$$V_{Rk,s} = k_2 A_s f_{yk} \quad (2.12)$$

where $V_{Rk,s}$ is the anchor shear strength in N, $k_2 = 0.6$, A_s is the stressed cross-section of the anchor in the shear plane in mm^2 , and f_{yk} is the characteristic yield strength in MPa. For concrete failure for anchors, the anchor shear resistance is determined using a 35 degree shear cone as opposed to a 45 degree shear cone. The resulting equation for the shear capacity of a single anchor is as follows:

$$V_{Rk,c}^0 = k_4 d_{nom}^{0.5} (\ell_f / d_{nom})^{0.2} f_{ck}^{0.5} c_1^{1.5} \quad (2.13)$$

where $V_{Rk,c}^0$ is the shear resistance of the anchor without edge effects, small spacing or member thicknesses, and is not embedded in concrete that is cracked, in N, $k_4 = 0.5 \sqrt{\text{N/mm}}$, d_{nom} is the outside diameter of the anchor in mm, ℓ_f is the effective length of the connector under shear loading, f_{ck} is the characteristic compressive strength of concrete in MPa, and c_1 is the edge distance in the direction of the shear load in mm. Additional resistance reduction factors are specified in the CC Method to account for the change in the projected shear cone failure due phenomena such as cracked sections, close stud spacing, member thickness, and edge effects.

For the tensile strength of an anchor where steel failure governs, the CC Method provides the following equation:

$$N_{Rk,s} = A_s f_{yk} \quad (2.14)$$

where $N_{Rk,s}$ is the tension resistance of an anchor due to steel failure in N, A_s is the stressed cross-section of the anchor in the shear plane in mm^2 , and f_{yk} is the characteristic yield strength in MPa. For concrete failure, the tension resistance is also calculated using a 35 degree pullout cone. The tension resistance of a single anchor is as follows:

$$N_{Rk,c}^0 = k_1 f_{ck}^{0.5} h_{ef}^{1.5} \quad (2.15)$$

where $N_{Rk,c}^0$ is the tension resistance of a single anchor not influenced by edge effects or anchor spacing effects, and is not embedded in concrete that is cracked, in N, $k_1 = 7.5 \sqrt{\text{N/mm}^{0.5}}$, f_{ck} is the characteristic compressive strength of concrete in MPa, and h_{ef} is the effective anchor depth in mm. Additional resistance reduction factors are applied to account changes in the pullout cone geometry due to edge and spacing effects, small member thicknesses, as well as cracked sections.

For combined shear and tension, the CC Method uses the following equations:

$$N_{Sd} / N_{Rd} \leq 1 \quad (2.16)$$

$$V_{Sd} / V_{Rd} \leq 1 \quad (2.17)$$

$$\left(\frac{N_{sd}}{N_{Rd}} \right) + \left(\frac{V_{sd}}{V_{Rd}} \right) \leq 1.2 \quad (2.18)$$

where N_{Sd} is design value of the tension load in N, N_{Rd} is the characteristic tension resistance in N, V_{Sd} is design value of the shear load in N, V_{Rd} is the characteristic shear resistance in N. For Equations 2.16 through 2.18, the smallest values of the shear and tension resistance for the concrete-controlled and steel-controlled failure modes are used. Equation 2.18 provides a simplified interaction equation without exponentials. As a result, the values for N_{Sd} and V_{sd} are smaller. To adjust for this, a constant of 1.2 is utilized in order to extend the interaction curve to accommodate larger design capacities.

From the past literature previously discussed, the vast majority of investigation has dealt with the behavior of headed shear studs in composite beam or slab systems. Due to the different orientation of the shear studs with respect to the concrete panel, the problem exists concerning the applicability of current design recommendations for use in an infill wall system.

3. Experimental Program

An experimental test setup was designed to simulate the local behavior of headed shear stud connections between reinforced concrete infill walls and steel frame systems. Figure 1.1 shows a prototype composite steel frame-infill wall system. As previously mentioned, this test setup must be able to accommodate cyclic shear loading as well as axial tension.

3.1 Experimental Test Setup

3.1.1 General Test Setup Characteristics

Figures 3.1 through 3.3 show the test setup devised for the shear stud tests. This specimen is intended to represent the local behavior of the shear stud connection in reinforced concrete infill panels. A total of eight specimens were constructed in two series of four each. In order to secure the specimen to the strong floor during testing, the specimen was attached to a W14x211 foundation beam, which was bolted to the strong floor. Headed shear studs with 19 mm (0.75 in.) shank diameter, 31.75 mm (1.25 in.) head diameter, and 127 mm (5 in.) length were used for all tests. Two studs were placed along each wall-column interface at a center-to-center spacing of 356 mm (14 in.) in a single line. Stud size and spacing were selected based on an idealization of this structural system rather than an actual prototype. In addition, the stud spacing was selected to be large enough such that there would be no overlap in the vertical distribution of stresses

due to a 45 degree failure cone from each stud into the wall. The thickness of the wall was chosen as 254 mm (10 in.) on the basis of two criteria. First, the wall thickness should reflect realistic construction details. In addition, the thickness must be large enough such that edge effects would not interfere with stud behavior. The width of the wall was 610 mm (24 in), so to insure that the horizontal distribution of stresses at each wall-column interface would not affect the behavior of the opposite interface. The wall height was 711 mm (28 in.), which accommodates the 356 mm (14 in.) spacing between studs plus one-half the stud spacing from the stud to the top and bottom edges of the wall.

The steel sections used for the columns were W14x90 shapes. The steel grade was A36. In addition to possessing the required strength for the tests, the columns must also be of comparable size to what would be present in a low-to-mid rise steel frame structure in seismic zones to provide consistent proportions with respect to the infill panel. The shear studs were welded, using standard practice, to both flanges over the web of each of the columns, such that the columns could be turned around and reused for a second series of tests upon the completion of the first series.

To apply the shear loading, a large pin connection, which was free to rotate in the plane of the specimen, was bolted to the testing machine. An A36 steel built-up section with 51 mm (2 in.) thick flanges and 25 mm (1 in.) thick web was then bolted to the pin. When downward shear loading was applied to the wall, the built-up section loaded two 152 mm (6 in.) wide, 25 mm (1 in.) thick A36 steel load transfer plates, located at each end of the wall. These plates, which spanned the 254 mm (10 in.) thickness of the wall, were used to concentrate the distribution of the load over the region where the shear stud was embedded.

To accommodate fully-reversed shear loading, a threaded rod system was utilized. A total of four 38 mm (1.5 in.) diameter high-strength steel threaded rods were attached to the built-up section, and then to a 51 mm (2 in.) thick A36 steel transfer plate below the concrete portion of the specimen. When the load was reversed, the threaded rods would pull up on the bottom plate. Two additional 152 mm (6 in.) wide, 254 mm (10 in.) deep, and 25 mm (1 in.) thick A36 steel plates rested on the bottom plate, so that

the reversed shear load would be distributed over the same region as the downward shear load. The large thickness of the bearing plates and the flanges of the built-up section, as well as the large rod diameter of the threaded rod, were part of a concerted effort to limit the amount of displacement incurred when tension is applied to these components during reverse shear loading. Any displacements present as a result of bending or stretching of these components would be independent of slip between the wall and columns, and would therefore be undesirable. In order to install the reverse shear loading system, the wall needed to be elevated 343 mm (13.5 in.) with respect to the foundation beam to provide sufficient clearance for the necessary components.

A linear bearing system comprising of two Schneeberger HRB-65 bearing blocks consisting of multiple cylindrical bearings on a single rail was attached to the base plate of one of the columns (called the Actuator Column). This column included a pattern of holes to accept the free-end fixture of the horizontal actuator for those specimens that were tested with axial tension. This bearing system was needed to insure that the axial tensile load would be transferred completely to the wall, rather than to the column base connection by means of friction. With the linear bearing system installed, the actuator column attached to it was free to translate, greatly reducing the amount of horizontal load transferred to the column base connection. With the Actuator Column free to translate, the base plate of the opposite column (the A-Frame Column) was bolted to the foundation beam, and the top of the A-Frame Column was bolted to a diagonal A-brace, bolted in turn to the foundation beam. The rail of the bearing contained a hole pattern in a single line along the centerline of the rail. As a result, the web of the foundation beam prevented a direct connection between the bearing system and the foundation beam. To make the connection, a 51 mm (2 in.) thick A36 steel plate was used, in which holes were drilled and tapped in a pattern matching that of the bearing rail. The plate was then bolted to the flanges of the foundation beam. In addition, the Actuator Column base plate was thicker than the base plate of the A-Frame Column. This was designed to resist moments created by the two bearing blocks due to the eccentricity of the applied shear load relative to the centerline of the Actuator Column.

A framing system was implemented to support the horizontal actuator for cases in which axial tension was applied. It consisted of two W12x65 steel columns bolted to the strong floor, with a 305 mm (12 in.) by 305 mm (12 in.) by 13 mm (0.5 in.) thick steel tube placed between the columns and bolted to the column flanges. The columns were oriented with their weak axis opposing the horizontal force applied by the actuator, making it necessary to brace the columns. Therefore, two W8x31 diagonal braces were bolted to the web of each of the columns on one end, and to floor beams bolted to the strong floor on the other end.

3.1.2 Reinforcement Configurations

The main variable between Test Series 1 and 2 was the steel reinforcement configuration in the wall. Based on the space limitations present for this specimen, all reinforcement was treated as stirrups for the determination of hook extensions. Steel reinforcement must be able to carry stresses in the wall when the concrete is heavily damaged due to cracking. Unlike studs in composite beams, the shear studs in composite infill walls are in the plane of the infill wall. This results in different modes of failure for the concrete. Figure 3.4 shows the different modes of failure that are possible in an infill panel in addition to the typical pullout cone. One mode of failure involves a crack perpendicular to the plane of the wall and parallel to the interface at or just above the head of the shear studs (Crack A-A in Figure 3.4). When shear forces are applied, large stress concentrations develop in the stud embedment region. The stresses in the embedment region cause shearing in the wall, possibly resulting in extensive cracking. This type of longitudinal crack is also possible from axial tension in combination with a pullout failure in the wall. A second possible mode of failure consists of a splitting crack in the plane of the wall (Crack B-B in Figure 3.4). This is caused by the shear studs bearing on the surrounding concrete, possibly resulting in splitting of the wall to occur. A third failure mode is through cracking perpendicular to the plane of the wall, emanating from the shear connector and progressing, either vertically or diagonally

toward the interior region of the wall (Crack C-C in Figure 3.4). This is caused by the shear studs transferring stresses from the steel columns to the infill wall. Stresses in the concrete are concentrated in the vicinity of the stud, which may initiate cracking, but are more evenly distributed further away from the composite connection region. A reinforcement scheme is required which has the capability to intercept cracks forming in the wall, and allow the wall to carry the shear and tensile demands required.

To estimate stud shear strength, the formulas from AISC LRFD were used as given in Equation 2.1 (AISC, 1993). The first part of Equation 2.1 provides an estimate of the stud shear capacity based on concrete failure, while the second part assumes shear failure of the stud itself. Assuming normal weight concrete with a compressive strength of 27.58 MPa (4000 psi), a shear stud tensile strength of 413.7 MPa (60 ksi), and $E_c = w^{1.5} \sqrt{f'_c}$, where E_c is the concrete elastic modulus in ksi, w is the unit weight of concrete in pcf, and f'_c is the 28-day concrete compressive strength in ksi, Equation 2.1 predicts a stud shear strength of 116 kN (26.1 kips) per stud based on concrete failure (which controls), and 118 kN (26.5 kips) per stud based on steel failure. For design of the test setup, this value was increased by a factor of safety of 4/3 to give a design value of 156 kN (35 kips) per stud, so as to insure adequate strength and stiffness in the load frame.

The stud tensile capacity was determined using PCI formulas without resistance factors (PCI, 1992), since no stud tensile strength specifications exist in AISC LRFD. Equations 2.8 and 2.9, respectively, provide stud tensile capacities of approximately 106 kN (23.9 kips) and 111 kN (24.9 kips) per stud, with Equation 2.8 controlling.

Figures 3.5 and 3.6 show the reinforcement design for Series One. This series was designated as the “Perimeter Bar” reinforcement configuration. This design consists of tying two perimeter bars directly to each line of shear studs. This scheme was suggested by Makino in that by anchoring the wall reinforcement to the shear stud, it may be possible to provide better stress transfer from the steel columns to the concrete wall through the shear studs (Makino, 1985).

The perimeter bar scheme was adopted in this study because it was assumed to be

the simplest and most economical scheme that had any likelihood of performing well under the expected loading. The perimeter bars were located at a distance of approximately 25 mm (1 in.) from the head of the stud. This was done to prevent poor bonding of the concrete below the head of the shear stud. This location shown in Figure 3.5 is a compromise of the likely field location (up against the head of the stud) and the preferred location for structural performance (against the steel sections).

The amount and detailing of the reinforcing steel in the wall were for this scheme designed in accordance with the seismic specifications of ACI 318-95 (ACI, 1995). For a 25 mm (10 in.) thick wall or greater, it is recommended by ACI that two curtains of reinforcement be used. In order to tie the two curtains of reinforcing steel to the perimeter bars, the wall steel consisted of a 90 degree bend extending from the wall steel to the perimeter bar. A second 90 degree bend at the perimeter bar allowed for the wall steel to wrap around the perimeter bar. All reinforcement consisted of a hook with an extension of $6d_b$. This is based on ACI hook requirements for stirrups. For regular bars, a hook extension of $12d_b$ should be used (ACI, 1995). For walls or diaphragms, ACI Code specifies that a minimum of 0.25 percent steel reinforcement be used. However, this amount was doubled to assist in the control of cracking in the wall, which was also done for the infill panel experiments whose results were reported by Makino (Makino, 1985). Based on this, #4 reinforcing bars with center-to-center spacing at 8 in. in both horizontal and vertical directions provided this percentage. The ratio of reinforcing steel, ρ , is given by:

$$\rho = \frac{A_s}{st} \quad (3.1)$$

where A_s is the area of reinforcing steel in in.², s is the center-to-center spacing between wall steel bars in inches, and t is the wall thickness in inches.

In addition to meeting area of wall reinforcing ratio requirements, there was also a demand for the reinforcement to provide adequate strength for the forces in the interface region during testing. This was of primary concern when axial tension was applied due to the low tensile capacity of concrete along with a potential failure plane defined by

crack A-A in Figure 3.4. The tensile strength of the horizontal bars is given by $P_n = A_{st} f_y$, where A_{st} is the total area of reinforcing steel subjected to tension in in.² and f_y is the yield strength of the reinforcing bars in ksi. Assuming Grade 60 steel reinforcing bars, eight #4 bars provided 427 kN (96 kips), which exceeds the largest possible axial tension force, which is estimated as twice the tensile capacity of each shear stud augmented by a load factor of approximately 2 to insure adequate capacity. Furthermore, the tensile strength of the concrete alone along crack A-A in Figure 3.4 was also calculated using the ACI formula for the tensile capacity of concrete (ACI, 1995), or $P_n = 6.7 A_c \sqrt{f'_c}$, where P_n is the tensile capacity of the concrete in lb, A_c is the area of concrete subjected to the tensile force in in.², and f'_c is the 28-day concrete compressive strength in psi. From this last expression, the tensile capacity of the concrete panel, neglecting the reinforcement and applying a resistance factor equal to 0.7, is 596 kN (134 kips), well exceeding the applied axial tensile load. In the perimeter bar configuration, no reinforcement was provided to resist tension along crack type B-B.

Figures 3.7 and 3.8 shows the steel reinforcement detail for Series Two. This series was designated as the “confinement cage” reinforcement configuration. Similar criteria was used in designing the cage reinforcement scheme as was used in the perimeter bar scheme. The cage reinforcement scheme consisted of a steel cage containing the concrete around the shear studs. The cage was approximately 660 mm (26 in.) in length to provide ample cover from the top and bottom faces of the wall. The cage stirrups were #3 reinforcing bars bent into a 216 mm (8.5 in.) by 216 mm (8.5 in.) (outer diameter) square with the ends of the bars each having 135 degree hooks with proper extension. Uniform spacing of the stirrups at 89 mm (3.5 in.) center-to-center was used.

The stirrup spacing was selected on the basis of several criteria. One such criteria was to allow for enough stirrups to provide adequate strength when subjected to tensile forces along cracks A-A and B-B. A 89 mm (3.5 in.) spacing provided a total of eight stirrups per cage. From $P_n = A_{st} f_y$, the total tensile capacity of the stirrups in the cage is 427 kN (96 kips), which exceeds the tensile demand for testing. Another aspect

investigated with respect to the design of the stirrups was shear friction resistance with crack A-A being the potential failure plane. The shear friction formulas from the ACI code were used (ACI, 1995). The formula to calculate the amount of shear friction is as follows:

$$V_n = \phi A_{vf} f_y \mu \quad (3.2)$$

where V_n is the shear friction force to transfer shear stress in kips, ϕ is the resistance factor equal to 0.85, A_{vf} is the area of concrete enclosed by the stirrups in in.², f_y is the yield stress of the reinforcement in ksi, and μ is a factor based on the surface of the reinforcement, equaling 1.4 as per ACI (1995). In this equation, V_n is replaced by the design stud shear strength, V_{stud} , multiplied by a load factor of 1.2 to insure adequate capacity, and A_{vf} can be represented by:

$$A_{vf} = A_{vbf} \left(\frac{s_t}{s_v} \right) \quad (3.3)$$

where A_{vbf} is the area of shear friction reinforcement placed at a spacing between stirrups which is twice the area of the stirrup bar, A_{bar} , in in.², s_v is the spacing between stirrups in inches, and s_t is the spacing between studs in inches. The resulting expression for the stirrup spacing is:

$$s_v = \frac{\phi(2A_{bar})s_t f_y \mu}{1.2V_{stud}} \quad (3.4)$$

From this equation, and using a steel yield stress of 413.7 MPa (60 ksi) and #3 reinforcing bars, the maximum stirrup spacing is calculated as 95 mm (3.74 in.). Therefore, a stirrup spacing of 89 mm (3.5 in.) on center was used. In addition, the stirrup spacing needed to be tight enough to intercept cracks originating from the studs before they could be substantially developed in the wall. The final criteria was that the 89 mm (3.5 in.) stirrup spacing was readily divisible by the shear stud spacing and the wall height, allowing each shear stud to be centered between stirrups.

A #4 longitudinal reinforcing bar was placed in each stirrup corner extending the entire length of the cage. In addition to providing the means by which to assemble the

cage, the longitudinal bars were also designed to arrest crack types B-B and transfer the shear force from one stud over a shear crack. This criteria was check using the following equation:

$$A_s = \frac{Q_n}{4f_y} \quad (3.5)$$

where A_s is the required amount of reinforcing steel per bar in in.², and Q_n is the design stud shear strength, 35 kips. From Equation 3.5, the required area of steel is 95 mm² (0.146 in.²), indicating that #4 reinforcing bars are sufficient.

Two longitudinal perimeter bars were placed inside the cage, and were tied to the stirrups at the bottom of the cage between corner bars. The clear spacing between the perimeter bars was the diameter of the head of the stud to allow cage to be fully assembled before being placed over the shear studs. As a result, only one of the perimeter bars could be tied near the shear studs. To account for this, the perimeter bars were offset from the center of the cage to insure that the cage would be centered about the shear studs. These perimeter bars served several purposes. First, the perimeter bars provided reinforcement near the line of shear studs. In addition, the perimeter bars were the primary means by which the cage was securely tied near the base of the shear studs. Finally, the perimeter bars and the bottom corner bars serve to provide a bearing “surface” for the concrete cones when the studs were subjected to tension.

It was necessary for wall reinforcing steel to be present in the specimen in addition to the cages. Three horizontal #4 reinforcing bars spaced 203 mm (8 in.) center-to-center in two curtains served as the wall steel as opposed to the perimeter bar scheme, in which four horizontal #4 reinforcing bars were used. The wall steel was placed inside the cages to prevent them from being present within the cover. They extended to the extreme ends of the two cages to insure adequate anchorage. Due to the longitudinal bars in the cage, no additional vertical wall reinforcing steel was added.

When comparing the two reinforcement configurations, the perimeter bar scheme served as a benchmark of the minimum reinforcing scheme that should be used to resist cyclic loading in composite reinforced concrete infill wall-steel frame connections. The

perimeter bars allow the wall steel to be anchored to the shear studs. However, the reinforcement scheme does not address all of the possible failure modes previously discussed, namely crack types B-B and C-C. In addition, the wall reinforcement ends 38 mm (1.5 in.) from the head of the shear stud, leaving the remaining concrete near the steel column unreinforced. This makes this region susceptible to concrete damage from cracking, especially in situations where axial tension is present. The confinement cage reinforcement configuration was designed specifically to address issues involving all likely failure modes in the infill walls. The failure modes are primarily due to cracking from high stress concentrations close to the shear studs. Consequently, the reinforcing cage was utilized to prevent concrete damage from extending from the shear stud, allowing the wall system to remain predominantly intact.

3.2 Fabrication of Test Specimens

All steel components of the test setup were fabricated by LeJeune Steel Company, Minneapolis, Minnesota in accordance with design specifications provided by the University of Minnesota researchers. With respect to the shear stud connectors, it was not possible to obtain mill report values on specific studs. However, typical mill report values for the $\frac{3}{4}$ inch studs used at LeJeune Steel Company consistently have a yield stress value of approximately 53 ksi and an ultimate tensile strength of approximately 71 ksi. The steel reinforcement was cut and bent to design specifications by Ambassador Steel, Minneapolis, Minnesota. Tension tests were performed on straight bars of each size, cut from the same bar stock as was used in fabricating the reinforcement for the test specimens. The tests were performed in accordance with ASTM A 370-96 and E 111-82 (ASTM, 1996). The results from the bar tests are summarized in Table 3.1. The concrete was mixed and delivered by Cemstone, Minneapolis, Minnesota. The mix ordered was a standard 28 MPa (4000 psi) floor slab mix, because it was assumed that such would be the grade and quality of concrete for use in an infill wall system. A slump of 101 mm (4 in.) was requested, and smooth, rounded aggregate was used with a maximum diameter

of 19 mm (0.75 in.). The mix design for the concrete mix is given in Table 3.2. Concrete properties for the two test series are listed in Tables 3.3 and 3.4. For Series 2, 3 gallons of water was added to get the initial slump to 152 mm (6 in.) as was measured for Series 1. Compressive cylinders were made, cured, and tested in accordance with ASTM C 31-95 and C 39-94 (ASTM, 1994, 1995).

3.2.1 Specimen Construction

In preparation for pouring the wall specimens, a formwork system was required. Each series of tests, comprised of four specimens, were poured from the same concrete batch. The wall forms were constructed of 19 mm (0.75 in.) thick concrete form grade plywood and 2 by 4 wood studs. The wall was elevated 343 mm (13.5 in.) from the foundation beam to allow for the reverse shear loading apparatus to be installed. Therefore, four bottom form blocks were fabricated using construction lumber and concrete form grade plywood. Also, four spacers for the linear bearing system were required. This spacer, which supported the Actuator Column during casting, was constructed by gluing solid oak planks in a stack. The top and bottom surfaces of the glued blocks were milled to size, and a hole pattern matching that of the actuator column base plate was drilled into each oak spacer. Oak was chosen due to its high density and superior dimensional stability. This provided greater resistance to creep effects and moisture damage to insure more precise placement of the steel columns for casting, relative to their final position in the actual test setup.

The specimen was placed onto a casting beam, which were W27x94 steel sections. These steel sections were placed on their sides, and the specimens were placed on the web of the sections. Hole patterns matching those in the two column base plates were drilled into the webs of the casting beams so the specimen columns could be securely bolted to the casting beam. An additional hole was drilled into the casting beam to permit bolting to the strong floor.

Once the specimens were secured to the casting beams and the strong floor, the bottom form blocks were installed and the steel reinforcement was tied. For the perimeter bar specimens, the reinforcement was tied in place. For the cage reinforcement scheme, the cages were fully constructed first, and were then tied to the shear studs. Since the wall reinforcement for the cage scheme was placed inside the cages, it was necessary to unbolt one of the columns and move it away from the other column, so the wall steel could fit between the cages. With the wall steel not tied to the cages, but resting on the stirrups, the column was moved back into place.

Once the steel reinforcement was in place, the wall forms were installed. The bottom of the wall form was bolted to the bottom form block. For the perimeter bar specimens, steel angle sections were used to support the top of the form. One leg of the angle supported the wall form perpendicular to the plane of the wall, while the remaining angle was clamped to the flange of the column. In addition, 4.76 mm (3/16 in.) threaded rod served as ties to connect the two wall forms. This clamping system caused difficulty in producing a flat top surface because the clamps interfered with the screeds during casting. To avoid this problem, the clamping system for the cage specimens was modified, with the clamps attached directly to the edge of the 2x4 studs of the wall form. Also, from observations made during the concrete pour of the perimeter bar specimens, the 2 mm (0.0625 in.) steel ties were omitted.

In addition to pouring the wall specimens, thirty 152 mm (6 in.) diameter concrete cylinders were prepared for use in standard tests of concrete strength (compressive tests, split tensile tests, and modulus of elasticity tests) for each series. In addition, three 152 mm (6 in.) by 152 mm (6 in.) by 305 mm (12 in.) modulus of rupture (MOR) beams were also poured.

Each wall specimen was poured in two layers, with each layer filling the wall halfway. After the first layer was placed in each wall specimen, the concrete was then vibrated to insure proper consolidation. The second layer was then placed for each wall, and was promptly vibrated. The top surfaces of the walls were screeded, floated, and finished. Once the top surfaces of the walls were firm to the touch, wet burlap and plastic

were placed over the top surfaces to keep them moist. The wet burlap and plastic remained on the wall specimen until forms were removed. Approximately six hours upon completion of the concrete pour, the bolts of the A-frame column were removed. This was done in an effort to prevent cracking or wall separation from the steel column due to concrete shrinkage effects. Four days after the concrete pour, wall specimen forms, cylinder molds, and modulus of rupture forms were removed. The moist-cured cylinders were placed in a water bath after form removal.

3.3 Loading Procedure

3.3.1 Load Combinations

Each of the four specimens within each test series was subjected to different loading, as shown in Tables 3.5 and 3.6. To provide a benchmark with which to compare to existing design equations, tests with applied monotonic shear force only were performed on both steel reinforcement configurations. These tests also assisted in the determination of the target slips used in the formulation of the cyclic slip history for the cyclic tests. Tests with only monotonic axial tension were also performed on both reinforcement configurations for comparison with existing design equations. Both of these schemes also provide the critical anchor values for the envelope where the effects of combined shear and tension would be investigated.

A third test involved first the application of a constant axial tension force equal to approximately one-half the estimated stud tensile capacity for two studs. Once the constant axial load target was reached, monotonic shear was then applied. This test was also performed on both steel reinforcement configurations. This procedure provided more similarity to the actual demands on shear studs in an infill wall than a monotonic shear only test does. The fourth load combination involved the application of cyclic shear with no axial tension present. This was performed on the perimeter bar scheme only. No constant axial tension was applied due to the fact that the monotonic axial

tension and the monotonic shear with constant axial tension tests exhibited relatively poor tension resistance, and applying tension in the cyclic test would have resulted in an early failure. The final load combination involved applying a constant axial tension force equal to one-half the estimated stud tensile strength for two shear studs, followed by the application of cyclic shear. This was used for the cage specimen configuration only. This loading procedure best simulates the seismic demands placed on the shear studs in an infill wall system.

For the tests where shear loading was present, 2 mm (0.0625 in.) teflon pads were placed between the top and bottom surfaces of the concrete panel and the load transfer plates, with the exception of Specimen 1. These pads served to reduce the amount of friction between the concrete and the crosshead of the testing machine. Also, for monotonic shear tests other than Specimens 1 and 3, a small hydrocal mortar bed was placed on the top surfaces of the concrete, and the crosshead was lowered until the built-up section squeezed out a small amount of excess wet hydrocal. The crosshead was then raised to allow the hydrocal to harden. This was to provide a uniform bearing surface for shear loading. For Specimens 6 through 8, a 2 mm (0.0625 in.) thick steel plate was placed under the A-Frame Column in an effort to reduce the amount of initial separation present resulting from tightening the bolts connecting the two columns to the foundation beam.

For the application of shear loading, a 2670 kN (600 kip) MTS actuator was used with an MTS 458 test controller. The axial tensile force for the pullout tests was applied by an MTS 342 kN (77 kip) actuator with a MTS 407 controller. A 156 kN (35 kip) MTS actuator with a MTS 406 controller was used to apply the axial tensile force for the combined shear and tension tests.

A labeling system was devised to reference the different specimens and their respective load combinations in a more simplified manner. The template for the labeling system is A-XX-YY-B. Table 3.5 provides the definitions for this template, and Table 3.6 provides the specimen labels for each test performed, as well as the test parameters.

3.3.2 Instrumentation and Data Collection

Figures 3.9 through 3.12 and Tables 3.7 through 3.9 show the instrumentation scheme used for data collection, as well as the location of each instrument. The primary phenomena that needed to be measured during the tests was slip and separation of the concrete panel relative to the steel columns. For this, two 13 mm (0.5 in.) LVDT's were attached to both the column flange and the concrete wall on both concrete-steel interfaces on the south face (Figure 3.9 and Table 3.7). These instruments are referred to as "slip" LVDT's. Specimen orientation is provided in Figure 3.2, and the location is given in Table 3.7.

A second measurement of interest was separation between the wall and the column. To measure this displacement, initially four 3 mm (0.1 in.) LVDT's were placed on the south face at the location of each of the four shear studs (Figure 3.9 and Table 3.7). Since the wall would be displacing vertically, these "separation" LVDT's were attached to the wall, and a spring system set the LVDT extension rod against the steel column. The extension rods were then prevented from vertical translation on the wall by epoxying posts on the wall above and below the LVDT extension rod. This system allowed the wall to move with respect to the columns without vertical translation in the rods of the separation LVDT's. In early tests (Specimens 1 and 3), it was noticed that there were different amounts of separation visible on the north face versus the south face. As a result, four additional separation LVDT's were placed on the north face of the wall for subsequent tests (Figure 3.10 and Table 3.8).

Two 25 mm (1 in.) LVDT's were placed on the Actuator Column (Figure 3.12). The vertical placement of these instruments was the same as the location of the top and bottom faces of the wall. These LVDT's were used to measure any rotation of the Actuator Column. The final LVDT used was a 25 mm (1 in.) LVDT attached to the foundation beam, and then to the bottom center of the wall (Figure 3.12). This served as a backup to the two slip LVDT's. Examination of the results from the first two tests indicated little difference between this LVDT signal and those of the slip LVDT's. Thus,

it was removed. Two dial gages were used to measure any base translation in the A-Frame Column, and out-of-plane behavior of the wall (Figure 3.12).

To detect internal cracking in the specimen, an Acoustic Emissions monitoring system was utilized (Figure 3.11 and Table 3.9). The equipment used was manufactured by Physical Acoustics Corporation. A Mistras 2001 data acquisition system, 1220A preamplifiers, and R15 transducers were utilized. For the first test, four acoustic emission transducers were placed in two lines, with each line being approximately 89 mm (3.5 in.) from each wall-column interface. After the first test, an additional transducer was placed between the two sensors of each line to provide greater sensitivity in the detection of internal cracks. For Series 2, additional sensors were placed on the inside flange of the two steel columns near the web to detect any stud failures. For the first seven tests, transducers were attached to the specimen by applying a thin layer of silicone rubber on the transducer, and then attaching the transducer to the specimen. This method increased the risk of damaging the transducers when they were removed from the specimen. Based on the recommendation of the manufacturer, the silicon rubber was replaced by melted glue for the final test.

An Optim computerized data collection system was used to collect the measurements from the instrumentation. The data collection rate was set to 10 Hz for the tests in Series 1, except for Specimen 4. The rates were modified for Specimen 4 in order to extend the maximum data collection time before exceeding the buffer capacity of the data collection system memory. The data collection rates for Specimen 4 is given in Table 3.10. The data collection rate was 5 Hz for all of the tests in Series 2.

3.3.3 Test Control and Loading Procedure

The monotonic and cyclic shear load applications were performed under displacement control. This was done in order to better observe the specimen failure. The displacement rate used corresponded to the displacement rate of stroke of the MTS actuator, not the LVDT's, although targets of slip were used for the cyclic tests. The

constant axial tension was applied under load control, so as to provide a more consistent force throughout the test. The monotonic shear displacement rate was selected as displacing 0.03 mm (0.001 in.) in five seconds. This displacement rate was selected such that significant strain rate effects would not be present. This loading rate was not used for Specimen 1. Rather, a displacement rate of 0.03 mm (0.001 in.) in three seconds, followed by a five second pause was used. This was selected for the first test because predefined pauses in applied displacement at every 0.3 mm (0.01 in.) of specimen slip was desired. Additional data was collected for the first five seconds of every hold. Also, these holds were used to make observations and take photographs of the specimen condition. It was believed that a five second pause was required to allow time to check if the slip target was reached. These predefined targets and five second pauses were eliminated in subsequent tests.

For the monotonic axial tension tests, a displacement rate of 0.03 mm (0.001 in.) in ten seconds was used. This was based on the fact that the estimated ultimate tensile capacity was about 50 percent the estimated ultimate shear capacity. Therefore, with the expected peak in load being 50 percent less for the pullout tests, the displacement rate was reduced by 50 percent.

For the cyclic tests, a slip history was determined in addition to the displacement rates. Figures 3.13 and 3.14 show the slip history used for Specimens 4 and 8. The targets for the history were initially based on the behavior obtained from the monotonic companion tests from the same series (Specimens 1 and 7). The first three targets were based on load, although the test was performed under displacement control. Once the target load was reached (as per the digital readout on the test controller), the cycle was reversed. Loads were used as targets due to the extremely small magnitude of the slips associated with these loads. The first two load targets were selected based on observations from the monotonic tests, where the specimen remained in its elastic range, and no visible cracking was observed on the specimen. The third target for Specimen 4 was near the displacement for Specimen 1 where visible concrete cracking was observed,

while the third target for Specimen 8 was at a displacement where strong nonlinearity was present in Specimen 7.

The remaining targets were slip values. The slip targets were monitored based on the averages of the slip displacements measured using the LVDT's on the specimen. These slips were monitored, and once the slip target had been reached, the cycle was reversed. The first slip target was estimated as twice the slip of the preceding load target. The next slip target was twice its predecessor, and all subsequent slip targets were 1.5 times greater than the preceding slip target. The loading rates for the two cyclic tests are given in Tables 3.11 and 3.12. The loading rate was initially the same as the monotonic shear tests, however, the rates were increased for targets with larger slips. This was done so that data collection could continue for a half cycle of loading without having to interrupt the process to permanently store data that had been collected in the computer memory. This allowed for a pause in testing at a point of approximately zero load and slip.

4. Experimental Observations

The following chapter includes a summary of specimen performance through observations made during the testing of each specimen, examination of each specimen after the completion of testing, and general remarks of the load versus displacement plots of the data collected during testing. The ultimate values of load as well as the displacement at ultimate failure are given in Table 4.1. Table 4.1 shows the ultimate shear load and slip displacement for Specimens 1, 3, 4, 5, 7, and 8, and the ultimate tensile load and separation displacement for Specimens 2 and 6. Specimens 3, 7, and 8 also had 127 kN (28.5 kips) of tensile load applied prior to application of the shear loading.

4.1 Specimen 1 (1-PB-MS-0)

Specimen 1 features the perimeter bar reinforcement scheme, and was tested under pure monotonic shear. Prior to testing, it was observed that there was a small amount of separation between the concrete panel and the steel columns. These joints opened as a result of torquing the bolts connecting the two columns to the foundation beam, indicating a small difference in height between the two columns. In addition, it was noticed throughout the test that the load transfer plates were not flush with the top surface of the wall, due to an uneven concrete surface caused by the inability to properly screed the top concrete surface, as described in Chapter 3.

4.1.1 Observed Response to Load History

During testing, a visible crack was first noticed on the north face of the specimen in the vicinity of the top west stud. Figure 4.1 shows the crack pattern for Specimen 1. Upon initial formation, the first crack extended from the wall-column interface in a horizontal orientation approximately 51 mm (2 in.) towards the center of the panel, but as it propagated away from the panel, the crack assumed 45 degree inclination towards the top center of the wall. This crack formation corresponded with a shear load of about 289 kN (65 kips). At about 334 kN (75 kips), a new branch of the crack began to propagate downward towards the west wall-column interface. At a shear load of approximately 376 kN (84.5 kips), a new crack developed on the east wall-column interface in the vicinity of the east top shear stud. This crack angled 45 degrees towards the top and center of the panel. By this time, there was extensive cracking at the top west region of the panel. The amount of cracking in the top east region of the panel was not as pronounced as that of the top west region. At a shear load of 392 kN (88.2 kips), cracks were observed originating from the panel-column interfaces at both the bottom west and east shear studs. The amount of crack propagation at these locations was not as extensive as in the top west or top east regions.

Loading was terminated once the measured loads dropped below 75 percent of the previous peak load. Figure 4.2 shows a photograph of the specimen after testing. For this test, the peak load was 400 kN (89.9 kips), while the maximum average slip at the end of the test was 13 mm (0.5 in.).

4.1.2 Condition after Testing

A coring drill with a 51 mm (2 in.) coring bit was used to remove the concrete surrounding the head of the shear studs, thus allowing disassembly of the columns and the panel. Once the panel and the columns were separated, it was noticed that the bottom west shear stud had completely fractured at the base of the stud just above the weld collar. The fracture surface was relatively smooth, but not flat. The fracture surface near the top of the shear stud was closer to the base of the stud, with the fracture surfaces near the bottom of the stud approximately 2 mm (0.0625 in.) further away from the base of the shear stud. The remaining shear studs were still attached to the columns. However, fractures existed in all three. The top of each of the shear studs had a tearing fracture at the weld collar. Also, the east side studs had a visible hairline crack around the remaining circumference of the studs. The attached shear studs were also permanently deformed. Figure 4.3 shows a picture of the deformed stud. The permanent deformations were largely concentrated near the base of the shear studs, with little curvature present further away from the base. The deformed portion of the studs had a length of approximately two times the stud diameter.

When examining the east and west concrete surfaces, longitudinal cracks were present between the location of the shear studs, as well as extending above and below the shear studs. There were also horizontal cracks extending from the location of the shear studs to the edges of the wall. There was extensive visible concrete crushing around the location of the studs. The approximate depth of concrete crushing damage was comparable to the length of the deformed portion of the stud.

4.1.3 Measured Response

Figure 4.4 shows the graph of load versus slip for Specimen 1 for the east and west slip LVDT's and the center LVDT. This figure shows that there is good agreement between the three instruments in measuring the displacement of the concrete panel relative to the steel columns. The load versus slip curve shows a very large initial stiffness, followed by a plateau which was maintained over a large amount of slip.

Figure 4.5 gives the load versus separation graph for the south face separation LVDT's, noting that there were no north face separation LVDT's for this test. This figure shows a fairly small amount of separation initially until higher loads were achieved. The exception was in the separation LVDT in the top west region of the panel, which is where the most prominent concrete damage existed. Figure 4.6 shows the load versus column displacement graph. In this figure, there is a strong agreement between the top and bottom column LVDT's, indicating that the linear bearing system was functioning as it was intended.

4.2 Specimen 2 (1-PB-NS-1)

Specimen 2, which also featured the perimeter bar reinforcement configuration, was tested in pure axial tension. Prior to testing, small initial wall separations were noted as a result of bolt tightening upon connecting the steel columns to the foundation beam.

4.2.1 Observed Response to Load History

Upon application of the axial tensile load, audible popping and pinging sounds were observed at loads ranging from 67 kN to 89 kN (15 to 20 kips). There was also a noticeable difference in the wall separations on the north face east panel-column interface compared to the south, with little or no separation seen on the south face, and the north face having noticeable wall separations. There also did appear to be some differential north versus south separation on the west side of the specimen as well.

A crack formed in the bottom east region of the wall near the vicinity of the bottom east shear stud at a load of approximately 120 kN (27 kips). The crack pattern for this specimen is given in Figure 4.7. The crack started horizontally extending outward from the panel-column interface, and was followed by the formation of slightly inclined vertical cracks near the head of the bottom east shear stud. The vertical cracks propagated upward and towards the wall column interface. Horizontal and vertical

cracks formed in the top west region of the wall at a tensile load of approximately 142 kN (32 kips), the ultimate load achieved, followed by a load drop of about 13 kN (3 kips). As loading then increased, the top west crack propagated downward, while the bottom east crack continued to extend upward. Cracks developed in the bottom west region of the wall at an axial tensile load of 133 kN (30 kips). Testing ended when specimen failure occurred, which was characterized by the west top crack extended downward to the bottom of the panel and through the thickness of the panel, at which time the specimen lost most of its load carrying capacity. Figure 4.8 provides a photograph of the specimen after loading was stopped. The portion of the panel west of the crack was separated from the remainder of the panel. The location of the concrete rupture was in the vicinity along the line of the perimeter bars, and the portion of the wall still attached to the Actuator Column was devoid of reinforcement. Once the splitting failure had transpired, the specimen still carried about 36 kN (8 kips). This was a result of the resistance provided by mechanical interaction between the perimeter bars and the heads of the shear studs. In order for further lateral displacement to occur, it would have been necessary for the perimeter bars to bend away from the studs to allow the heads of the shear studs to pass between the perimeter bars.

4.2.2 Condition after Testing

Upon completion of the coring process all four shear studs were examined. The shear studs displayed no noticeable permanent curvature, and were in good condition. The west face of the wall was also examined. A small amount of concrete crushing damage was noticed around the embedment region of each stud. The depth of this damage was small, less than one half the stud diameter. Also, horizontal cracks extending to both the north and south wall faces from the west bottom shear stud were also present. A small amount of vertical cracking was present on the east face originating from the east bottom shear stud and extending upward and out towards the north and south faces of the panel.

4.2.3 Measured Response

Figure 4.9 shows the load versus column displacement graph for Specimen 2. From Figure 4.9, there is good agreement between the top and bottom column LVDT's, indicating that the linear bearing system was functioning properly, and that the axial tensile force was being transferred from the Actuator Column to the concrete panel, and not to the base of the Actuator Column. Figures 4.10 and 4.11 show the load versus separation curves for the separation LVDT's on the south and north faces, respectively. The curves on these graphs appear to be erratic, with the top west separation on the north face turning negative once the peak load was achieved. However, with the load drop occurring due to specimen failure, the load was redistributed, and studs located in damaged regions in the panel began to unload, causing unusual separation measurements.

4.3 Specimen 3 (1-PB-MS-1)

Specimen 3 utilized the perimeter bar reinforcement scheme, and was tested in monotonic shear with a constant axial tension load. Prior to testing, there was initial separation of the panel and the columns as a result of tightening the bolts that connect the column base plates to the foundation beam and bearing assembly.

4.3.1 Observed Response to Load History

The loading sequence first had axial load applied to the specimen by the horizontal actuator. During application of the load, some panel-column separation was noticed. Furthermore, it was noticed that the separation displacements between the north and south faces of the same panel-column interfaces were different. This was observed

for both the east and west panel-column interfaces. For the east panel-column interface, the separation displacements on the north face were noticeable, whereas there was no noticeable separation on the south face. The opposite held true for the west panel-column interface, although not to as large an extent, where the south face exhibited visible panel separations, and the north face exhibited little movement relative to the column. This could be an indication that there was some eccentricity present, possibly between the two lines of shear studs, or in the orientation of the steel columns with respect to one another and to the horizontal actuator. This is discussed further in Appendix A.

Application of an axial tensile load of 133 kN (30 kips) was initially targeted, being approximately 60 percent of the calculated tensile strength of two studs, based on Equation 3.3. At a horizontal force of 124 kN (27.9 kips), visible cracks appeared in the upper east and lower west portions of the specimen near the studs in those regions, as shown in the crack pattern provided in Figure 4.12. The crack in the upper west end was horizontal and originated at the panel-column interface near the top west shear stud. This crack branched out into a series of vertical cracks extending above and below the horizontal crack. The crack in the bottom east region was also horizontal, and it originated at the panel-column interface in the vicinity of the bottom east shear stud. The extent of cracking in the top west portion of the wall was more severe than that of the bottom east portion. At this point in the load history, a pause in loading was taken for further examination of the specimen. It was decided that the total axial load to be applied to the specimen would be set at 127 kN (28.5 kips), instead of 133 kN (30 kips), due the cracking which occurred during the horizontal load application. Subsequently, loading resumed, and the new target of 127 kN (28.5 kips) was reached.

Once the constant axial load was attained, the shear loading history began. It was noticed that the built-up section did not lie flush with the load transfer plates on the top of the specimen wall. This was due to an uneven top concrete surface, as well as to possible inclination in the built-up section perpendicular to the plane of the panel. During shear loading, the cracks in the top west portion of the panel propagated downward. The crack

in the bottom east region propagated downward and towards the middle of the wall. Specimen failure occurred in a sudden manner as a vertical splitting crack extended over the entire height and through the thickness of the panel on the west side of the specimen, as shown in Figure 4.13. As with Specimen 2, the splitting occurred immediately to the west of the perimeter bars, and where no steel reinforcement existed except for the studs. The maximum shear load achieved was approximately 231 kN (52 kips), and the total slip was approximately 2 mm (0.072 in.).

4.3.2 Condition after Testing

After the coring procedure was completed, all of the shear studs were examined. No visible fractures were present in any of the shear studs. The shear studs on the west side showed no noticeable permanent deformation at all, while small permanent deformations were present near the base of the studs on the east side. The approximate length of the permanently deformed stud was one stud diameter. Upon inspection of the east wall surface, it was noticed that concrete crushing damage was present around the vicinity of the shear studs. The approximate depth of concrete damage was comparable to the length of the deformed portion of the stud. Also, a vertical crack existed between the shear studs, and above the top east shear stud to the top of the wall. Cracks also extended horizontally from the bottom east shear stud to both the north and south panel faces, while a crack extended horizontally only to the north face from the top east shear stud.

4.3.3 Measured Response

Figure 4.14 shows the load versus column displacement during the application of the axial load. From this figure, it is noticed that there is reasonably good agreement between the top and bottom column LVDT's. Furthermore, even once the desired axial load was reached and held constant, the Actuator Column continued to displace. This

can also be seen in the load versus separation curves for the south face LVDT's, shown in Figure 4.15. From Figure 4.15, the east side separation LVDT's also continued to displace once the axial load was held constant. However, only a small amount of separation was present on the west side. A discussion of this phenomenon is given in Appendix A. Figure 4.16 gives the shear load versus slip graph during the shear load history for the east and west slip LVDT's in addition to the center LVDT. Again, there is a fairly good correlation between these LVDT's, with the west slip LVDT providing slightly less slip. The amount the ductility achieved by Specimen 3 was small, not exceeding 3 mm (0.10 in.) in displacement.

Figure 4.17 shows the load versus separation graph during shear loading. The separation continued to increase on the east panel-column interface, although the separation at the west panel-column interface remained small. Figure 4.18 shows the load versus column displacement graph during shear loading. The column displacement continued to increase during shear loading, and once failure occurred, the Actuator Column displaced to a large magnitude because it was no longer connected to the rest of the specimen.

4.4 Specimen 4 (1-PB-CS-0)

Specimen 4, the last specimen using the perimeter bar reinforcement scheme, was tested in cyclic shear. No axial tension was applied. Figure 3.13 reports the shear loading history for this test. Prior to testing, initial wall separations were present due to bolt tightening.

4.4.1 Observed Response to Load History

During the 267 kN (60 kips) cycles (see Figure 3.13), small pinging sounds were heard originating from the specimen. In the reversed cycle of the second 267 kN (60 kips) cycle, a small horizontal hairline crack in the west bottom region of the wall

appeared. The crack was well below the location of the west bottom shear stud, and did not propagate past its original length. This was the only crack observed during testing, and therefore no crack pattern was provided. During the second 1 mm (0.04 in.) cycle, full wall separation at both the east and west panel-column interfaces was observed. A small amount of crushing damage in the corners of the panel was also observed. During the 2 mm (0.08 in.) cycles, it was observed that there was degradation in maximum load achieved for each passing cycle. In the reversed shear, quarter cycle of the third 2 mm (0.08 in.) cycle, a loud metallic “pinging” sound was heard in the vicinity of the top west region of the wall. The pinging sound corresponded to a shear load of approximately 156 kN (35 kips), about 60 percent of the maximum load achieved for that particular quarter cycle. Also, following the loud pinging sound, the out-of-plane dial gage moved significantly, approximately 0.3 mm (0.013 in.). Just prior to the completion of the first quarter cycle of the first 3 mm (0.12 in.) cycle, a second loud metallic “pinging” sound was heard, immediately followed by a drop in shear load. In the second shear quarter cycle of the same 3 mm (0.12 in.) cycle, a third loud metallic “pinging” sound occurred, and the entire panel visibly shifted relative to the steel columns. In the following quarter cycle of the second 3 mm (0.12 in.) cycle, it was observed that the specimen was only able to carry approximately 50 percent of the shear load it carried in the first 3 mm (0.12 in.) cycle, 111 kN (25 kips) compared to 240 kN (54 kips). In the reverse shear, quarter cycle of the second 3 mm (0.12 in.) two more loud pinging sounds occurred, and following this point the specimen was able to carry very little load, and thus testing was concluded. The maximum load achieved was approximately 383 kN (86 kips) in the forward shear, quarter cycle of the first 2 mm (0.08 in.) cycle. It was assumed that the loud metallic “pinging” sounds heard during testing corresponded to stud failures.

4.4.2 Condition after Testing

Since all four studs had fractured, no coring was required. Figure 4.19 shows the stud failure surface for Specimen 4. Figure 4.20 shows a void created by concrete

crushing damage due to the stud bearing on the panel. Examination of the panel after testing showed that the concrete was in good condition. However, on both the east and west faces of the panel, vertical hairline cracks existed between the studs, as well as above and below the studs to top and bottom ends of the panel. The studs themselves had fractured just above the weld collar.

4.4.3 Measured Response

Figures 4.21 and 4.22 show the load versus slip plots for the west and east slip LVDT's, respectively. From these curves, it is noticed that there is a shift in the load-slip relationship between the two LVDT's. The west slip LVDT produced slip values larger in the negative slip direction than did the east slip LVDT. An analysis of this slip differential is given in Appendix A. Also, a load drop is present in the first 3 mm (0.12 in.) cycle in the reversed shear (positive slip) direction, which corresponds to the loud "pinging" sound observed during testing. Figures 4.23 and 4.25 show the load versus separation and load versus column displacement graphs for the top west separation LVDT on the south face and the top column LVDT, respectively. These figures indicate that the separations and column displacements continued to increase as the test progressed, although there was a small recovery in separation and column displacement during the unloading portion of each cycle.

4.5 Specimen 5 (2-CG-MS-0)

Specimen 5 was reinforced with the confinement cage scheme, and it featured pure monotonic shear loading. Prior to testing, separation displacements in the panel-column interface were present as a result of bolt tightening connecting the column base plates to the foundation beam.

4.5.1 Observed Response to Load History

Throughout the test, no visible cracking was present. Therefore, no crack pattern was provided. At a load of 445 kN (100 kips), separations along the east panel-column interface were present along the full height of the panel. At a load of 498 kN (112 kips), a loud “pinging” sound was observed originating from the top west portion of the specimen. A large load drop immediately followed. The load then began to increase until a second “pinging” sound originating from the top east portion of the panel was observed. Another load drop immediately followed. Again the load began to increase to approximately 294 kN (66 kips) until a third “pinging” sound in the bottom west vicinity of the specimen occurred, immediately followed by a load drop. After this third “pinging” sound, the west slip LVDT was no longer operative. A fourth and final “pinging” sound was observed at a load of approximately 120 kN (27 kips), and marked specimen failure. After the fourth “pinging” sound, the panel was no longer connected to either of the columns, and rested on blocks placed on the foundation beam. The ultimate load achieved was 503 (113 kips), and the average slip at failure was 11 mm (0.45 in.). Again, these loud “pinging” sounds were believed to correspond to stud failures.

4.5.2 Condition after Testing

Since the specimen was no longer connected to the columns, the coring procedure was not necessary. Examination of the panel showed that no visible cracks were present on any of the panel faces. All four studs had fractured just past the weld collar, similar to the stud failures for Specimen 4 (Figure 4.19).

4.5.3 Measured Response

Figure 4.26 shows the load versus slip plot for Specimen 5. From this figure, there is a strong agreement between the west and east slip LVDT’s. Also shown is the

load drops corresponding to the “pinging” sounds observed. Figures 4.27 and 4.28 show the load versus separation graphs for the south face and north face separation LVDT’s, respectively. Larger separations were recorded on the east panel-column interface on the south face than on the west panel-column interface. However, the opposite held true on the north face, where larger separations were present at the west panel-column interface than on the east panel-column interface. This is an indication that there was some eccentricity or rotation of the specimen in the north-south direction. This phenomenon is addressed in Appendix A. Figure 4.29 gives the load versus column displacement graph. From this figure, there is good agreement between the top and bottom column LVDT’s, indicating once again that the linear bearing system was functioning properly.

4.6 Specimen 6 (2-CG-NS-1)

Specimen 6 was the second specimen to feature the confinement cage reinforcement scheme, and was loaded in pure axial tension.

4.6.1 Observed Response to Load History

At a load of 205 kN (46.2 kips), a horizontal crack was observed in the top west region of the panel near the top west stud on both the north and south faces of the panel, as shown in Figure 4.30. This crack branched and propagated at a 45 degree inclination. A horizontal crack in the bottom west portion of the panel was also observed at this load. At a load of 214 kN (48 kips), a horizontal crack formed in the bottom east portion of the panel. There was little propagation of this crack. At a load of 222 kN (49.9 kips), a new horizontal crack formed in the upper east portion of the panel in the vicinity of the top east stud. Some branching of this crack occurred, with the crack extending upward at a 45 degree angle. Large separations were observed at both panel-column interfaces to the extent where the separation LVDT’s were no longer in contact with the columns at loads in excess of 245 kN (55 kips). Specimen failure occurred when the two east studs failed

in tensile fracture. The ultimate load achieved was 281 kN (63.16 kips), and the average column displacement at failure was 28 mm (1.1 in.).

4.6.2 Condition after Testing

The two west studs were removed by coring. All four studs exhibited large permanent axial deformations (i.e., elongation), originating from the weld collar, with the diameter of the two fractured studs being reduced to as little as 13 mm (0.5 in.) from its original diameter of 19 mm (0.75 in.). The fracture itself occurred approximately 25 mm (1 in.) from the weld collar. The length of the permanently deformed region was approximately two stud diameters. Figure 4.31 shows the deformed, fractured stud for Specimen 6. The east and west concrete faces showed some localized crushing in the vicinity of the studs, but no cracking was visible. The depth of concrete crushing damage was similar to that of the deformed region of the stud.

4.6.3 Measured Response

Figure 4.32 shows the load versus column displacement graph for Specimen 6. The two column LVDT's recorded similar behavior with respect to one another, indicating that the linear bearing system was working properly, and that the axial load was being transferred to the concrete panel and not to the base of the Actuator Column. Figures 4.33 and 4.34 show the load versus separation plots for the south face and north face separation LVDT's, respectively, and it is noted that the separation LVDT's were no longer in contact with the columns at loads in excess of 55 kips. The south face separation LVDT's produced similar results when compared to one another. The north face separation LVDT's also produced similar readings, with the exception of the west separation LVDT's, which exhibited a more pronounced degradation in stiffness.

4.7 Specimen 7 (2-CG-MS-1)

Specimen 7 also used the confinement cage reinforcement scheme, but was loaded in monotonic shear and constant axial tension.

4.7.1 Observed Response to Load History

The axial load was applied first with the horizontal actuator. Soft “popping” sounds near the two panel-column interfaces were observed throughout the application of this load. No visible cracking was present during this load history. An axial load of 127 kN (28.5 kips) was attained in preparation for the shear load history.

After the axial target was attained, the shear loading history commenced. Visible panel-column separations were present at each interface early in the load history. No visible cracking was noticed. The panel-column separations continued to increase in magnitude up to the initiation of specimen failure, marked by the failure of the two east studs by fracture. The ultimate load achieved was 306 kN (68.82 kips), and the average slip at failure was 6 mm (0.23 in.).

4.7.2 Condition after Testing

The west studs were cored, and exhibited some permanent shear deformation near the weld collar, with the approximate length of this deformation being one stud diameter. The fractures on the east studs occurred just passed the weld collar, similar to Specimen 4 (Figure 4.19). No cracking was present on the west and east faces of the panel, although some localized crushing was present in the concrete surrounding the studs, in which the depth of concrete crushing was similar to the deformed portion of the stud.

4.7.3 Measured Response

Figure 4.35 shows load versus column displacement during the axial load application. The shape of the curve is nearly linear, with the Actuator Column continuing to displace even when the axial target was attained (as shown in Figure 4.35). Again, the measurements from the two instruments are fairly similar, indicating good performance of the linear bearing system. Figures 4.36 and 4.37 show the axial tension load versus separation curves when applying the axial load for the south face and north face separation LVDT's, respectively. The curves for the south face separation displacements are fairly similar to one another, showing significant separations during the application of the axial load. The north face separations showed some disparity, however, with the west separations being larger than the east separations.

Figure 4.38 shows the load versus slip graph during shear loading. The west and east slip LVDT's produced similar measurements. Only a small amount of specimen ductility was exhibited up to failure. Figures 4.39 and 4.40 show the load versus separation curves during shear loading. These figures show little increase in separation until a load of approximately 178 kN (40 kips), at which point the separations increased at a steady rate. Figure 4.41 shows the load versus column displacement graph during shear loading. Again, there is little increase in column displacement until a load of approximately 222 kN (50 kips), where the column displacement begins to increase steadily.

4.8 Specimen 8 (2-CG-CS-1)

Specimen 8 was the fourth specimen featuring the confinement cage reinforcement scheme, and it was tested in cyclic shear with a constant axial tensile load. Figure 3.14 reports the shear loading history for this specimen.

4.8.1 Observed Response to Load History

The axial load was applied first with the horizontal actuator. No visible cracking was present during the axial load application. Axial load was reached and maintained at the target of 127 kN (28.5 kips).

Once the axial load was attained, the shear loading history was initiated. The initial cycles exhibited no signs of damage, with the loads and slips within each set of cycles being comparable. During the 0.5 mm (0.02 in.) cycles (See Figure 3.14), however, the load attained at each slip target began to decrease from the first to third cycle at the 0.5 mm (0.02 in.) target. The load did though increase when moving to the next target of 1 mm (0.04 in.). When proceeding from the 1 mm (0.04 in.) target to the 2 mm (0.08 in.) target, the load achieved dropped by as much as 4.5 percent. Throughout the test, no visible cracking was present. There was a steady and significant increase in panel-column separation for both panel-column interfaces. Specimen failure occurred in the first 2 mm (0.08 in.) cycle during reversed shear loading when the two east studs failed simultaneously by fracture. The maximum load achieved was 256 kN (57.65 kips), and the largest slip target reached was the 2 mm (0.08 in.) target.

4.8.2 Condition after Testing

The west studs were cored, and examination of these studs showed that there was permanent stud deformation near the weld collar, with the diameter of the stud at this location being reduced by as much as 2 mm (0.0625 in.). The approximate length of the deformed portion of the stud was one stud diameter. The east side studs had fractured during testing just past the weld collar at the center of the stud. However, the fracture surface angles towards the column further away from the center of the stud, as shown in Figure 4.42. No visible concrete cracking was present on any of the panel faces. There was, however, some localized crushing of the concrete surrounding each stud, whose depth was comparable to the permanently deformed portion of the stud.

4.8.3 Measured Response

Figure 4.43 shows the graph of load versus column displacement during axial loading. This figure shows a bilinear trend during the application of the axial load. In addition, the Actuator Column continued to displace even once the axial load target was achieved and held constant. Figure 4.44 shows the load versus separation curve during the application of the axial load for the south face separation LVDT's. From this figure, it can be observed that there is a small amount of disparity between separation displacements. Figure 4.45 shows the load versus separation curve for the north face separation LVDT's when the axial load was applied. From this figure, there is a large difference in separation displacements between the east and west panel-column interfaces, with larger separations present at the west interface, possibly evidence of some eccentricity or rotation of the panel. This is discussed further in Appendix A.

Figures 4.46 and 4.47 show the load versus slip graphs for the west and east slip LVDT's. From these graphs, a shift in the slip displacements is seen from the west side to the east side in the negative slip direction. There is also significant degradation in the load-slip relationship during the 2 mm (0.08 in.) cycle. Figures 4.48 through 4.50 show the graphs for load versus separation on the south face and north face separation LVDT's, respectively, and load versus column displacement for the column LVDT's. These curves show a steady increase in panel-column separation and Actuator Column displacement throughout the test, with only a small displacement recovery during the unloading portions of each cycle.

5. Assessment of Load-Displacement Behavior

The following chapter evaluates the detailed specimen behavior for the series of eight steel frame-RC infill connection specimens tested. The primary mode of behavior investigated is the load versus average displacement relationship for each test.

Figures 5.1 to 5.11 show load versus displacement graphs for each test in addition to the graphs for a typical cycle for the two cyclic tests conducted, Specimens 4 and 8. Figures 5.12 through 5.32 show the corresponding results from the acoustic emission sensors for each test.

Also provided in Figures 5.1 to 5.11 are “Key Points” representing changes in load versus average displacement behavior that are reconciled with experimental observations made during the test and with acoustic emission data collected. These Key Points are identified by an Arabic numeral referring to their relative occurrence during the test. Also shown for the shear tests is the comparison to the load versus displacement relationship proposed by Ollgaard et al. (1971) in Equation 2.2, using the corresponding experimental peak shear strengths (reported in Table 4.1) for Q_u in Equation 2.2 (denoted Ollgaard w/ experiment).

5.1 Specimen 1 (1-PB-MS-0)

Figure 5.1 shows the load versus average slip graph with Key Points for Specimen 1, a monotonic shear test using the perimeter bar configuration. Key Point 1 and those with smaller slip displacements represent a region on the load versus average slip graph where an extremely large, nearly infinite stiffness exists. This can be attributed mostly to adhesion and friction between the steel columns and the concrete panel which dissipates energy somewhat after Key Point 1. Key Point 2 signifies a point where the load-slip relationship becomes markedly nonlinear. This change in behavior was the result of cracking of top west region of the panel in the vicinity of the top west

stud. This was confirmed through visual observations of the panel during testing. In addition, acoustic emission data also confirmed the presence of concrete damage in the top west region of the panel. The Ollgaard curve, using the experimental peak strength for Q_u in Equation 2.2, correlates well with the experimental load-deformation response.

Figure 5.12 shows the graph of the cumulative number of acoustic emission hits versus stroke for Sensor 1, located in the top west region of the panel (Figure 3.11). This figure shows a significant increase in acoustic emission activity in this sensor at an average slip of 1 mm (0.03 in.), which relates to a load of approximately 289 kN (65 kips). The acoustic emission activity begins to plateau at an average slip of approximately 3 mm (0.12 in.), although crack propagation was occurring, as evident through visual observation during testing. This is explained through the heavy degree of concrete damage surrounding Sensor 1, resulting in the isolation of this sensor from the panel. Figure 5.13 shows the acoustic emission activity for Sensor 3, located in the bottom west region of the panel. This sensor does not exhibit the large increase of acoustic emission activity that Sensor 1 does at an average slip of 1 mm (0.03 in.) due to the location of the crack relative to the two sensors, but does show the progression of cracking through a steady increase in acoustic emission activity throughout the test.

Key Point 3 marks the beginning of the plateau in load resistance (Figure 5.1). Furthermore, there is also a drop in load in this region. New cracking in the top east region of the panel at this point during testing is the most probable cause for this load drop. This new concrete damage was confirmed through visual observations made during testing, as well as through the analysis of the acoustic emission data. Figure 5.14 shows the acoustic emission activity for Sensor 4, located in the top east region of the panel. There is a large increase in acoustic emission activity at an average slip of 3 mm (0.12 in.), which corresponds to the load drop. Acoustic emission activity steadily increases after the large rise, indicating that the crack continued to propagate.

Key Point 4 is the point where the ultimate load has been reached. At this point, all studs have fully yielded, and are undergoing plastic deformations.

Key Point 5 represents the beginning of a steady drop in load, leading to specimen failure (Figure 5.1). New cracking in the bottom east region of the panel was visible during testing at this point. Figure 5.15 shows the acoustic emission activity for Sensor 6, located in the bottom east region of the panel near the bottom east stud. This plot shows a large increase in acoustic emission activity at an average slip of about 7 mm (0.28 in.), indicating new cracking in the bottom east region of the panel. At this point, the amount of damage in the specimen is such that the load can no longer be maintained, resulting in a steady decrease in load.

5.2 Specimen 2 (1-PB-NS-1)

Figure 5.2 shows the curve for load versus average column displacement for Specimen 2, a pullout test using the perimeter bar configuration. The behavior up to Key Point 1 represents a region of high initial, near linear stiffness. No noticeable concrete damage was present up to this point. Key Point 2 corresponds to a large drop in load caused by a large crack opening in the top west region in the panel. This crack was observed visually during the test, and acoustic emission data also supports the presence of concrete damage at this point.

Figure 5.16 shows the acoustic emission activity for Sensor 1. A steady rise in acoustic emission activity detected by this sensor occurred up to an average column displacement of approximately 2 mm (0.08 in.), which is where the load drop occurred. Then there is a plateau where little acoustic emission activity was detected. This is over the range of column displacements where the load drop occurred. Once the load began to increase again, large increases in acoustic emissions activity were measured, indicating a redistribution of stresses in the panel. Prior to the drop in load between Key Point 2 and Key Point 3, there is a marked nonlinearity present in the load-displacement relationship (Figure 5.2). This is caused by the cracking present in the bottom east region of the specimen near the bottom east stud, just prior to the crack forming in the top west region of the panel. Visual observations made during the test confirmed the presence of this

cracking. Furthermore, acoustic emission data also supports the notion of concrete damage in this region at Key Point 2 during testing, as shown in Figure 5.17, showing the graph of acoustic emission activity for Sensor 6.

From Figure 5.17, there is a steady increase in acoustic emission activity starting at an average column displacement of approximately 2 mm (0.08 in.), which relates to Key Point 2. It is past Key Point 2 where the significant nonlinear behavior begins. Key Point 3 marks the failure of the specimen due to the propagation of the crack in the top west region vertically down along where the perimeter bars in the specimen are located, resulting in a pullout failure at the west side of the panel.

5.3 Specimen 3 (1-PB-MS-1)

Figure 5.3 shows the load versus average slip graph for Specimen 3, monotonic shear loading with constant axial tension using the perimeter bar configuration. Because adhesion is lost during axial load application, there is no region of nearly infinite stiffness. Key Point 1 represents the beginning of the application of the shear load. The constant axial tension of 127 kN (28.5 kips) had already been applied, and during the application, cracks had formed in the top west and bottom east regions of the panel in the vicinity of the top west and bottom east studs, respectively.

Key Point 2 marks the start of significant nonlinearity in the load-average slip relationship. This is due to further damage in the concrete panel through the branching and further opening of the preexisting cracks. Visual observations of the panel made during testing support this argument. In addition, steady increases in acoustic emission activity during testing further support the evidence of crack propagation throughout the test. Figures 5.18 and 5.19 show the steady increase of acoustic emission activity up to failure for Sensors 1 and 6, respectively, with Sensor 1 monitoring acoustic emission activity for the crack in the top west region, and Sensor 6 monitoring crack propagation originating from the bottom east region.

Key Point 3 marks the failure of Specimen 3, with the mode of failure being nearly the same as that in Specimen 2, with the crack in the top west region of the panel propagating downward and through the thickness of the panel. Figures 5.18 and 5.19 also show the concrete pullout failure on the west side of the specimen with a large increase in acoustic emission activity in Sensors 1 and 6 towards the end of the test.

The Ollgaard curve, using the experimental peak strength for Q_u in Equation 2.2, correlates well with the experimental load-deformation response for lower levels of loading (before Key Point 2). However, the specimen retains stiffness for longer than predicted by the Ollgaard curve, although after Key Point 3, the loss of strength is sudden. The Ollgaard curve, which was developed to predict the behavior of shear connectors in composite beams, was not intended to predict the response of a shear connection subjected to combined tension and shear. The deviation between the two curves is likely due to the reduction in the strength and ductility of this specimen relative to Specimen 1, which was subjected to pure shear. Had the specimen load-deformation response continued to a strength approximately equal to that of Specimen 1, it is likely that the Ollgaard curve would have matched the load-deformation response well for the full scope of loading prior to the peak. The Ollgaard curve can thus not be considered a reliable prediction of load-deformation response near the peak strength of shear connectors subjected to combined tension and shear.

5.4 Specimen 4 (1-PB-CS-0)

Figure 5.4 shows the curve for load versus average slip for Specimen 4, which was subjected to cyclic shear loading using the perimeter bar scheme. Figure 5.5 shows sketches of the progression of cyclic damage addressed in this section. Figure 5.6 shows a typical set of cycles at a given target slip of 1 mm (0.04 in.). From Figure 5.6, Key Point 1 represents the initiation of significant nonlinear behavior due to stud contact with the surrounding concrete. This behavior is present only in the first cycle for each target displacement, and begins at the maximum previous slip obtained in the previous set of

cycles. Up to Key Point 1, the stud is deforming through surrounding concrete that has already been damaged (crushed) from cycles at the previous target slip. Once the maximum previous slip is surpassed, additional concrete crushing transpires, resulting in nonlinear behavior in the load-average slip relationship. This damage is shown through Figure 5.20, which gives the acoustic emission activity versus time for Sensor 2, located in the center west region of the panel (Figure 3.11). The parametric stroke in this figure represents the testing machine actuator stroke, which is not equivalent to slip. The “X’s” superimposed on the actuator stroke curve in Figure 5.20 indicate acoustic emission activity measured. This figure shows an increase in acoustic emission activity at the peak deformations of the first cycles, indicating further concrete damage, while the degree of activity tapers upon unloading and the subsequent two cycles. This pattern of acoustic emission activity is especially prominent in third set of cycles (267 kN, 60 kips) in Figure 5.20 from between 100 and 200 minutes, as seen in the cumulative number of hits plotted, which plateaus somewhat in the second and third cycles at this target load, as well as in the next set of cycles.

Key Point 2 refers to unloading of the half cycle, where concrete and stud elastic deformations are recovered. Key Point 3 represents a region on the load versus average slip curve where the stud is deforming through a void in the concrete caused by concrete crushing produced in previous cycles. This void was visually observed during the examination of the specimen once the steel columns were separated from the concrete panel, and is shown in Figure 4.20.

Key Point 4 marks both the stud and concrete panel being reloading elastically up to Key Point 5, which represents the same nonlinear behavior as that associated with Key Point 1, except now the direction of the applied shear is reversed. Also, the subsequent cycles at the same target produced lower peak loads than the preceding cycles. This is most likely a result of cumulative concrete damage in the panel. Figure 5.20 shows the steady increase in acoustic emission activity during testing, especially beginning at the fourth set of cycles (1 mm, 0.04 in.), which corresponds to an actuator stroke of approximately 4 mm (0.15 in.). Figure 5.21, showing acoustic emission activity for

Sensor 6, also shows a steady increase in acoustic emission activity, indicating the presence of continuing concrete damage.

Key Point 6 marks the beginning to the next cycle at the same target. It is noticed that there was not a significant change in the slope of the load versus average slip curve as was present in the previous cycle. This is due to the fact that the specimen had already been subjected to the same displacement in the first cycle. As a result, concrete crushing had already taken place, and significant nonlinear behavior was not present in subsequent cycles at that slip target.

5.5 Specimen 5 (2-CG-MS-0)

Figure 5.7 shows the graph of load versus average slip for Specimen 5, a monotonic shear test using the confinement cage. Key Point 1 represents the point up to which the specimen exhibited an extremely large, nearly infinite stiffness mostly caused by adhesion, as well as friction between the concrete panel and the steel columns. These mechanisms broke down as the curve approached Key Point 2, which represents the point where the load-average slip relationship becomes markedly nonlinear, although no visible concrete damage was present. Key Point 3 marks the beginning of where much more prominent nonlinear behavior occurs, marking the beginning of a plateau. Again, with little concrete damage existing, it is believed that the studs had fully yielded, and had begun to undergo strain hardening effects. Key Point 4 marks the first stud fracture of the top west stud, as indicated by a loud “pinging” sound in that region, followed by a large reduction in load.

Acoustic emission data also verifies the top west stud fracturing as shown in Figure 5.22, which provides the acoustic emission activity for Sensor 1. Figure 5.22 shows a pronounced increase in acoustic emission activity at an average slip of approximately 9 mm (0.36 in.), which relates to the first stud fracture. Key Point 5 marks the failure of the top east stud, as evidenced through a second loud “pinging” sound in that area of the panel. This is further verified through the examination of the acoustic

emission data at Sensors 4, 9, and 10 whose plots showing acoustic emission activity are shown on Figures 5.23, 5.24, and 5.26, respectively. Sensor 4, located in the top east region of the panel, shows a rise in hits at an average slip of approximately 10 mm (0.38 in.), which corresponds to the second stud fracture (Figure 5.23). Sensor 9, located on the east column in the vicinity of the top east stud (Figure 3.11), also recorded a rise in hits at the same average slip. Sensor 10 shows a large increase in acoustic emission activity also at the same average slip, indicating a disturbance on the east side of the specimen. Furthermore, due to the extreme increase in acoustic emission activity at Sensor 10, it is believed that the jolt caused by the fracturing of the top east stud disturbed the seating of this sensor, which was located on the east column, resulting in an abnormal rise in acoustic emission activity.

Key Point 6 marks the third stud failure of the bottom west stud. In addition to the audible “ping” sound heard, acoustic emission data picked up the fracture as well. Figure 5.27 shows the acoustic emission activity for Sensor 7, located on the west column near the top west stud. This figure shows an increase in activity at Sensor 7 at an average slip of approximately 11 mm (0.45 in.), which corresponds to the third stud failure. Key Point 7 relates to the final stud fracture of the bottom east stud, heard audibly. This Key Point is not shown on the load versus average slip plot because one of the slip LVDT’s was disturbed by the previous stud fractures, and was no longer operating. Figure 5.25 shows the acoustic emission activity for Sensor 6, located in the bottom east region of the panel. From Figure 5.25, there is a rise in acoustic emission activity just prior to the end of the test, thus verifying the location of the final stud fracture.

The Ollgaard curve, using the experimental peak strength for Q_u in Equation 2.2, correlates well with the experimental load-deformation response for lower levels of loading (before Key Point 2). However, the confinement from the cage causes an increase in strength (i.e., a retention of stiffness) in the specimen well beyond what was seen in Specimen 1 (which had no confining cage), thus leading to a load-deformation response that exhibits no flat slope as is predicted by the Ollgaard curve. Had the

specimen load-deformation response leveled off after Key Point 3 in the presence of less confinement, it is likely that the Ollgaard curve would have matched the load-deformation response well for the full scope of loading prior to the peak. The Ollgaard curve was not intended to predict response of a shear connection that has significant confinement, as it will tend to underpredict the stiffness of the shear connector as it approaches its ultimate strength.

5.6 Specimen 6 (2-CG-NS-1)

Figure 5.8 shows the load versus average column displacement curve for Specimen 6, a tension pullout test using the confinement cage. The initial stiffness is finite due to the lack of adhesion between the steel and the concrete as a result of the presence of axial tension. Behavior in the region of Key Point 1 represents a region of high initial stiffness with little specimen damage. At Key Point 2, significant nonlinearity in the load-displacement relationship occurs. This is a result of stud yielding. Furthermore, Key Point 2 coincides with the initiation of visible cracking in the panel.

Visible cracking was first observed in the top west region of the panel near the top west stud. Figure 5.28 shows acoustic emission activity for Sensor 1. At a column displacement of approximately 4 mm (0.15 in.), there was an increase in acoustic emission activity, which correlates to the stroke where cracking was observed, and where significant nonlinear load-displacement begins. Acoustic emission data for Sensor 4, given in Figure 5.29, shows additional new cracking in the top east region of the panel at a stroke of 5 mm (0.2 in.). This is also confirmed through visual observations made during testing. Key Point 3 represents a region where the load-displacement response begins to plateau. Due to the extremely large separations between the concrete panel and the steel columns, it is evident that large inelastic stud deformation had taken place. Examination of the studs after the panel had been separated from the steel columns showed that the studs did, in fact, undergo large inelastic deformations, as seen in Figure

4.31. Key Point 4 marks the failure of the specimen, where the two east studs failed simultaneously through fracture in tension. Figure 5.30, showing the acoustic emission activity for Sensor 6 located in the bottom east region of the panel, indicates a large increase in acoustic emission activity towards the end of the test, marking the stud fractures.

5.7 Specimen 7 (2-CG-MS-1)

Figure 5.9 shows the graph of load versus average slip for Specimen 7, a monotonic shear test with constant axial tension using the confinement cage. Key Point 1 represents the region up to which there is high initial stiffness. Key Point 2 relates to a large degree of nonlinear behavior in the load-average slip relationship. This is a result of yielding of the studs, as evident through large separations between the concrete panel and the steel columns on both the west and east sides. Furthermore, no visible cracking in the panel was present. Key Point 3 marks specimen failure in the form of simultaneous fracturing of the two east studs. Figure 5.31 shows acoustic emission data for Sensor 4, located in the top east region of the panel. This data shows a steady and gradual increase in acoustic emission activity, leading to a large rise in acoustic emission activity marking the stud fractures.

The Ollgaard curve, using the experimental peak strength for Q_u in Equation 2.2, correlates well with the experimental load-deformation response. The loss of strength and ductility due to the addition of tension (relative to Specimens 1 and 5) tends to be offset by the increase in strength and stiffness due to the addition of the confinement cage (relative to Specimens 1 and 3), thus resulting in strong correlation. This may be considered somewhat serendipitous, as the Ollgaard curve was not intended to predict the response of either a well-confined shear connector or a shear connector subjected to tension combined with shear.

5.8 Specimen 8 (2-CG-CS-1)

Figure 5.10 shows the curve for load versus average slip for Specimen 8, a cyclic shear test with a constant axial tensile load using the confinement cage. Figure 5.11 shows a typical set of cycles at a given target slip of 0.5 mm (0.02 in.). Cycle behavior for Specimen 8 largely resembles that of Specimen 4 with respect to key features. Key Point 1 represents nonlinear behavior due to stud contact with the surrounding concrete. This behavior is present only in the first cycle for each target, and begins at the maximum previous slip obtained in the previous set of cycles. Up to Key Point 1, the stud is deforming through surrounding concrete that has already been damaged (crushed) from cycles at the previous target. Once the maximum previous slip is surpassed, additional concrete crushing transpires, resulting in nonlinear behavior in the load-average slip relationship. Indications of this damage is shown through Figure 5.32, which gives the acoustic emission activity for Sensor 10, located on the east column near the bottom east stud. This figure shows an increase in acoustic emission activity for the first cycle of each target, indicating further concrete damage, while the activity begins to taper when unloading occurs and during the final two cycles for the target.

Key Point 2 refers to unloading of the half cycle, where concrete and stud elastic deformations are recovered. Key Point 3 represents a region on the load versus average slip curve where the stud is deforming through a void in the concrete caused by concrete crushing produced in previous cycles. This void was visually observed during the examination of the specimen once the steel columns were separated from the concrete panel. Key Point 4 marks both the stud and concrete panel being reloading elastically up to Key Point 5, which represents the same nonlinear behavior as that associated with Key Point 1, except now on the reverse portion of the cycle. Also, the subsequent cycles at the same target produced lower peak loads than the preceding cycles. This is most likely a result due to the cumulative concrete damage in the panel. Figure 5.32 shows the accumulation of concrete damage occurring.

Key Point 6 marks the beginning of the next cycle at the same target. It is noticed that there is not a significant change in the slope of the load versus average slip curve, as was present in the previous cycle. The specimen had already reached the same displacement as in the first cycle. As a result, concrete crushing had already taken place in the first cycle, and significant nonlinear behavior is not present in subsequent cycles at that slip target.

6. Data Analysis

In this chapter, comparisons are made between measured stud strengths and predictions obtained from existing design equations. In addition, discussion is provided regarding the differences in calculated and measured stud capacities. This chapter also includes an assessment of the stiffness decay for each specimen. Furthermore, aspects such as deformation capacity and energy dissipation capacity of the studs are also addressed. Another aspect of specimen behavior examined is an attempt to formulate a trilinear representation of the load versus average displacement curve for each specimen. The first break point in this idealization is the point where appreciable deviation from linearity is observed. The second trilinear break point represents a second and marked change in the load versus average displacement relationship, beyond which load remains relatively constant or decreases, i.e., stud yielding and the onset of plastic behavior of the stud. Tables 6.1 and 6.2 provide the load and displacement values obtained from this idealization. It should be noted that the average of the ratio of the first trilinear break point load with the ultimate load is approximately 50 percent for all of the specimens, and that the ratio for the second trilinear break point is approximately 80 percent. For the two cyclic shear tests, the trilinear break points were determined from the cyclic envelope curves, shown in Figure 6.1. The envelope was determined by plotting the shear load versus the maximum previous average slip in both shear directions.

6.1 Comparison to Current Design Equations

Comparisons of the stud strengths obtained from the eight panel-column connection tests are made with the stud strength formulas found in AISC LRFD (1993) and PCI (1992) in Figures 6.2 to 6.7. For monotonic and cyclic shear tests without axial tension, Equations 2.1, 2.6, and 2.7 were used without applying any resistance factors. Furthermore, for the monotonic shear tests, the shear stud strength formula developed in Japan, given in Equation 2.5, was also compared, denoted AIJ in Figure 6.2 (Makino, 1985). For the monotonic tension tests, Equations 2.8 and 2.9 in PCI (1992) were used. For tests where axial tension plus shear was applied, the PCI interaction equations were used (Equations 2.10 and 2.11) For clarity of the comparison with these design equations, all equations of Chapter 2 were computed assuming nominal, rather than measured, values for the material properties. These nominal values are reported in Chapter 2. The resistance factor, ϕ , was taken as 1.0 for all of these calculations. The experimental peak strengths, as well as the design equation values using nominal material properties, are reported in Table 6.3. It should be noted that, with the exception of Equation 2.5, the stud formulas used were not intended for infill walls, but for composite beams or for anchorage in concrete well away from nearby edges. As a result, the effects of parallel edges due to the lines of studs being in the plane of the panel are not taken into account in these specific equations. In addition, these existing design formulas do not include the influence of cyclic loading on stud strength.

6.1.1 Shear Strength of Headed Shear Studs in Wall Panels

For Specimen 1, the governing failure mode was concrete failure. From Figure 6.2, the PCI (1992) formula for the monotonic shear stud capacity when concrete failure governs (Equation 2.7) best fits the experimental results obtained for Specimen 1, and is, in fact, on the conservative side. However, the AISC LRFD formula (Equation 2.1), which is governed by concrete failure, overestimates the stud capacity for Specimen 1. Equation 2.7 also includes a term taking into account the edge distance in the direction of loading, which helps to produce stud strengths closer to the experimental results from

Specimen 1. It should be noted that both the AISC and PCI formulas correctly predicted that a concrete model of failure governs, although the corresponding assessment of shear strength assuming stud failure provided values that were only slightly higher than the corresponding concrete failure strengths. It should also be noted that the load transfer plates were not seated in the hydrocal mortar bed, possibly leading to unsymmetric loading of Specimen 1, which could produce a lower than typical stud strength. In addition, the unsymmetric damage pattern produced more damage on some studs, possibly leading to their failure before other studs attained peak strength. Thus, it would not be possible to attain a specimen strength equal to the sum of the peak strengths of all four studs, which is what is plotted for the formulas in the figure.

When examining Figure 6.2 for Specimen 5, in which failure was dictated by steel failure, the AISC LRFD formula (Equation 2.1), which was governed by concrete failure by a small amount, proved to correlate better with the stud strength, while the PCI shear strength formulas (Equations 2.6 and 2.7, with concrete failure controlling by a small amount) appear to be overly conservative for this case. The utilization of the confinement cage, in addition to a more uniform and symmetric loading surface through the use of the hydrocal mortar bed, produced larger strengths and a change in failure mode from concrete failure to steel stud failure. The confinement cage greatly reduced crack propagation, maintaining specimen integrity. However, when Klingner et al. (1982) tested A307 anchor bolts embedded in concrete, for shear failures governed by bolt failure, none of the strength values reached the specified ultimate tensile strength for an A307 bolt, with the mean percent reduction of 9 percent present, indicating that the full tensile strength cannot be reached in shear. Furthermore, this concept was supported in a study performed by Fisher et al. (1978), in which data obtained from tests previously conducted on A325 and A490 bolts was analyzed. From this analysis, it was concluded that bolts subjected to shear will not achieve their ultimate tensile strength. In addition, previous research has shown that there is variability in the ultimate tensile strength of shear studs. Pullout tests which had stud failures, as performed by McMackin et al. (1973), showed that the stud tensile strength well exceeded the specified ultimate tensile

strength. For this testing program, no tests on the studs themselves were performed. However, from Specimens 5 and 6, which were, respectively, pure shear and tension tests where steel failure governed, the experimental strength exceeded the nominal tensile strength of the studs (413.7 MPa or 60 ksi). This would lead to speculation that the actual ultimate tensile stress is larger than what was nominally specified. Based on previous experimental research showing that the specified tensile strength of the stud cannot be reached in shear, a reduction in strength to account for shear may be appropriate. However, this past research is based on research on bolts and not studs, and the results from Specimen 5 may suggest that the reduction in strength due to shear loading is not as large for studs as is the case for bolts. This is further supported by the research conducted by Ollgaard et al. (1971), where there were cases where the ultimate tensile strength was nearly reached or exceeded for shear studs. In addition, as indicated at the beginning of the chapter, Equation 2.6 predicts the yield shear strength, not the ultimate shear strength, of a stud failing in the steel. Thus, with respect to steel stud strength in shear, it would be appropriate to decrease the shear strength prediction relative to the stud tensile strength prediction, although it is acknowledged that the actual stud tensile strength will often be larger than the nominal value, and that the reduction of Equation 2.6 as compared to Equations 2.1 or 2.8 may be excessive for a well confined shear connector. With respect to the concrete stud strength in shear, increasing the shear strength prediction for concrete failure in the presence of confined concrete from that predicted by Equation 2.7, and possibly even Equation 2.1, may aid in increasing the predicted strength and in predicting the correct mode of failure for a wide range of infill wall conditions.

When comparing the experimental strength from Specimens 1 and 5 to the stud strength equation used in Japan for concrete failure (Equation 2.5), the stud strength calculated from Equation 2.5 exceeded the experimental strength for Specimen 1 (concrete failure) but predicted conservatively the strength of Specimen 5 (steel failure, with little evidence of detrimental effects from parallel edges). Equation 2.5 is equivalent to Equation 2.1 for concrete-governed failure, with the addition of a term to

take into account parallel edge effects for concrete governed failure. This factor was calculated to be 0.92. The actual reduction in strength between Specimens 1 and 5 was approximately 20 percent. As a result, the reduction in strength due to the presence of parallel edges as predicted by Equation 2.5 proved not to be large enough when comparing to the results obtained from this testing program. Thus, increasing the predicted strength of concrete failure for well confined concrete, coupled with using a larger reduction factor to account for parallel walls in poorly confined concrete, may be helpful in accurately assessing the peak strength due to concrete failure in infill walls. When examining Specimen 4 in Figure 6.6, the PCI stud shear strength formulas, Equations 2.6 and 2.7 [which are similar to the NEHRP (1997) shear stud seismic strength equations as specified for concrete design] produced a very accurate strength prediction with respect to the experimental result, albeit through incorrect prediction of the mode of failure (however, the equations for the steel and concrete shear failure modes produced very similar values). The AISC LRFD stud shear capacity formulas (Equation 2.1) overestimated the stud shear capacity for this cyclic application, and incorrectly predicted the failure mode (although the nominal strength due to concrete failure was close to that of steel failure). This points to some reduction in the shear strength predicted by Equation 2.1 as being appropriate, with the 25 percent reduction in strength specified in the NEHRP (1997) composite design chapter working well here, although better assessment of the mode of failure may be required in these design equations. The actual strength reductions for this experimental program showed that for Series 1, the reduction due to cyclic loading was 5 percent (Specimen 4 versus Specimen 1), although the strength of Specimen 1 may have been low for the reasons previously discussed.

6.1.2 Tensile Strength of Headed Shear Studs in Wall Panels

When comparing Specimens 2 and 6 to the PCI pullout stud capacity formulas (Equations 2.8 and 2.9), Figure 6.3 shows that the PCI formula greatly overestimates the stud pullout capacity for Specimen 2. However, when compared to Specimen 6 in Figure

6.3, the PCI stud pullout capacity formulas appear to be conservative. When examining this case, it should be noted that Specimen 2 used the perimeter bar reinforcing scheme, and failure occurred in the unreinforced portion of the concrete where the perimeter bars were terminated. This, in combination with the inclusion of parallel edges, produced stud strengths much lower than what was predicted by PCI. Specimen 6, on the other hand, utilized the confinement cage, which suppressed crack formation and propagation. This allowed for specimen performance to overcome the problems associated with parallel edges. Failure was through fracture of the studs in tension, which was correctly predicted by the PCI design formula. Note, however, that this would not be the case using the corresponding PCI values for the ϕ factors, as the nominal tensile strengths without ϕ factors are approximately equal for both the steel and concrete failure modes, as seen in the figure. In addition, as mentioned at the beginning of the chapter, Equation 2.8 is intended to predict the yield tensile strength rather than the ultimate tensile strength of the stud. Using a higher estimate for the ultimate tensile strength of the stud may thus be appropriate, as the strength exceeded the PCI prediction strength by 32 percent. However, only if the concrete strength predicted by Equation 2.9 were increased similarly would the correct failure mode be predicted. However, as a concrete mode of failure in the presence of adequate confinement was not exhibited in this test program, the amount of this increase cannot be assessed. In contrast, applying tensile load to a stud in a wall without proper reinforcement yields a tensile strength that is very low and most likely not easily quantifiable.

6.1.3 Combined Shear and Tension Strength of Shear Studs in Wall Panels

The strengths of Specimens 3, 7, and 8 are compared with the PCI interaction formulas for studs subjected to combined shear and tension in Figures 6.4, 6.5, and 6.7. The calculated strengths from the PCI equations were used for P_c , P_s , V_c , and V_s in the interaction formula (Equations 2.10 and 2.11). The two equations give nearly identical results using nominal material strengths (note that the concrete failure mode would have

given a lower strength prediction had the PCI ϕ factors been used). When compared to Specimen 3 in Figure 6.4, the PCI interaction formulas produce a stud shear capacity larger than the experimental result. This results from using the perimeter bar reinforcing scheme, where the effects of parallel edges with respect to stud strength are not addressed. For Specimen 3, specimen failure occurred due to heavy concrete damage where the perimeter bars were terminated. For Specimen 7 in Figure 6.4, the PCI interaction formulas provide a stud shear capacity slightly lower, but very close to the experimental ultimate load. For this test, a confinement cage was used to lessen the impact of parallel edges. Furthermore, the shear loading was monotonic in nature, which in combination with using the confinement cage, produced a stud strength that was in good agreement with the PCI prediction. This leads to the conclusion that the PCI interaction should be sufficient when adequate confining reinforcement is provided. In particular, Specimen 3 had an applied axial tensile load of 89 percent of its experimental pullout strength, but only 67 percent of the calculated pullout strength. However, as with the discussion of the monotonic shear tests, an increase in the PCI shear strength governed by concrete failure (Equation 2.7) to account better for the effects of confinement may insure better prediction of the failure mode being in the steel.

Figure 6.5 graphs the interaction curves from McMackin et al. (1973) (Equation 2.4), the PCI interaction curves (PCI, 1992) (Equations 2.10 and 2.11), a linear interaction relationship, and the experimental results from the eight tests. All of the values for shear and axial tension are normalized by $A_s F_u$, as defined in Chapter 2. From this figure, it may be concluded that only the linear interaction curve was appropriate for Specimen 3, while both PCI interaction curves somewhat underpredicted the results of Specimen 7 (both interaction curves give relatively similar results for the nominal values of material strengths as reported in Chapter 2). Note that if the PCI ϕ factors had been used, a concrete mode of failure would have incorrectly been predicted for Specimen 7. In addition, the PCI interaction curve assuming concrete failure (Equation 2.11) overestimated the strength for Specimen 3, in which concrete failure governed and the perimeter bar scheme was utilized. This indicates that without confinement, the PCI

concrete interaction curve does not provide an accurate strength prediction for parallel edges, and that with confinement, it provides a conservative estimate of the strength, but not necessarily the correct prediction of the failure mode.

When examining Specimen 8 in Figure 6.7, a confinement cage was used, and as a result, crack propagation was controlled, eliminating the parallel edge effect. However, the application of cyclic loading reduced the stud strength by 17 percent when compared to Specimen 7, producing a strength lower than the PCI prediction, which is similar to the NEHRP (1997) formulas found in the concrete design chapter. This overprediction indicates that the PCI interaction formula does not necessarily provide an adequately conservative estimate of the stud strength or failure mode when cyclic loading is applied. However, the composite design chapter in NEHRP requires a 25 percent reduction in stud shear strength from that predicted by Equation 2.1 (this would yield a strength equivalent to that predicted by Equation 2.6), and as was the case for Series 1, this reduction exceeds the 17 percent reduction found experimentally in Series 2. Thus, the overprediction of interaction strength for Specimens 7 and 8 indicates not so much a problem with the prediction of the tension and shear strengths (i.e., the anchor points of the interaction curves), but possibly with the form of the interaction equations themselves. For example, for shear connectors with adequate confinement, increasing the prediction of shear and tensile strength due to failure in either steel or concrete, coupled with a change in the interaction formula to be linear, may yield a more consistent prediction of interactive strength and failure mode.

6.2 Effective Secant Stiffness

Figures 6.8 through 6.11 show the effective secant stiffness versus displacement graphs for the eight tests. The effective secant stiffness was determined by tracing secant lines to periodic points on the load versus average displacement graphs. Effective secant stiffnesses for the cyclic tests were determined by dividing the sum of the peak loads for each cycle by the sum of their corresponding average slips. Also shown in Figures 6.8

through 6.11 are effective secant stiffnesses using the load-slip relationship proposed by Ollgaard et al. (1971) in Equations 2.2 and 2.3 using Equation 2.1 as Q_u for the monotonic shear tests (denoted Ollgaard w/ AISC), and the PCI interaction formula (Equations 2.10 and 2.11) for the combined shear and tension tests (denoted Ollgaard w/ PCI). All calculations assume nominal values for the material strengths and resistance factors, ϕ , equal to 1.0.

From these figures, several conclusions can be drawn. When examining the monotonic shear tests in Figure 6.8 for Specimens 1 and 5, the secant stiffness versus average slip relationships are nearly identical. There is an extremely large initial secant stiffness (i.e., nearly infinite relative to stiffness at finite slip displacements) for the two monotonic tests, followed by a sharp decay in stiffness. This corresponds to the loss of adhesion between the steel columns and the concrete panel early in the loading history. Also, the confinement cage does not affect the secant stiffness in pure shear since confinement does not influence the elastic properties of concrete (namely the modulus of elasticity), as well as friction/adhesion. The effective secant stiffnesses calculated using the envelope proposed by Ollgaard et al. (1971), compare well with the experimental results, particularly in the later stages of loading.

Figure 6.9 shows the effective secant stiffnesses for the two axial tension tests for Specimens 2 and 6, respectively. Both specimens exhibit similar initial secant stiffnesses, however, there is a more pronounced stiffness decay in Specimen 2, whereas Specimen 6 provides a more gradual stiffness decay. This is due to the lack of confinement for the perimeter bar reinforcement configuration used in Specimen 2, while Specimen 6 had the positive confinement from the reinforcement cage. As a result, parallel edge effects were responsible for the sharp secant stiffness decay for Specimen 2, while the confinement cage assisted in maintaining specimen integrity, allowing for a more gradual reduction in effective secant stiffness in Specimen 6. It should be noted that the mechanism in tension differs from that in shear. For tension, there is crushing (crumbling) of the concrete below the head of the stud, as well as large openings in cracks in the concrete. Also, when compared to the initial secant stiffnesses for the

monotonic shear tests, the initial tensile secant stiffness is much less than the initial shear secant stiffness, by as much as 96 percent. For pure tension, the confinement cage does affect the effective secant stiffness modestly.

Comparisons for the combined shear and tension tests for Specimens 3 and 7 are made in Figure 6.10. These figures show that there is a slightly larger initial secant stiffness for Specimen 7 than there is for Specimen 3. This is a result of the confinement cage used in Specimen 7 maintaining good specimen integrity during the application of the constant axial tensile load, while cracking had already initiated during the axial load history for Specimen 3, which used the perimeter bar reinforcement configuration. Both specimens exhibited a gradual decay of stiffness, with the stiffness decay extending to larger slips for Specimen 7 since a larger ductility was achieved from that test. Also, when comparing with tests having only the monotonic shear load (Figure 6.8), the addition of axial tension softens the specimens, resulting in lower initial effective secant stiffnesses. As was the case for pure tension, the use of the confinement cage affected the effective secant stiffness.

When comparing the effective secant stiffnesses for the two experiments with the envelope curve proposed by Ollgaard et al. (1971) using the PCI interaction strength predictions, Specimen 7 correlates more accurately than does Specimen 3. This can be explained in that the envelope curve implicitly assumes confinement by the concrete, as is the case in a composite beam. However, this is not always the case for an infill wall. Specimen 7 had a confinement cage to overcome the parallel edges, while Specimen 3 does not use the confinement cage, resulting in no confinement provided to the studs.

Figure 6.11 compares the cyclic tests of Specimens 4 and 8. For Specimen 4, the initial secant stiffness is much larger than that for Specimen 8, by as much as 70 percent. This is a result of the softening effect produced by the application of the constant axial tensile load in Specimen 8. No axial tension was applied to Specimen 4, so this softening effect is not present. For Specimen 4, a sharp drop in effective stiffness occurs at an average slip in the order of 0.3 mm (0.01 in.) to 0.6 mm (0.02 in.). This is a result of the loss of adhesion between the concrete panel and the steel column. No such adhesion

exists in Specimen 8 because of the axial load applied initially, resulting in a reduced initial stiffness. After this point, the effective stiffnesses begin to gradually decay for both specimens, and are relatively similar. The envelope curve proposed by Ollgaard overpredicts the stiffness of both specimens. This indicates that degradation in stiffness due to cyclic action occurs relative to behavior from monotonic loading, for which Equation 2.2 was developed.

6.3 Deformation Capacity

Table 6.4 summarizes the deformation capacities for each of the eight tests. The deformation capacity was taken as the average displacement (from all gages measuring the displacement) corresponding to a post-peak load that was equal to 80 percent of the ultimate load (Figure 6.12). From Table 6.4, for the monotonic shear tests (Specimens 1 and 5), Specimen 1 had a larger deformation capacity than did Specimen 5, although both specimens exhibited large deformation capacities. This could be due to the fact that Specimen 1 used the perimeter bar reinforcement scheme, which resulted in greater concrete damage than was present in Specimen 5, which used the confinement cage. This premature concrete damage present in Specimen 1 (from either parallel edges or an unsymmetric loading surface) interfered with the definition for deformation capacity since there was an absence of bearing on the concrete by the stud. As a result, additional slip displacements were recorded, while there was little additional deformation of the stud itself.

For the two pullout tests, Specimens 2 and 6, the deformation capacity for Specimen 6 was approximately 86 percent larger than that for Specimen 2. This can be attributed to the use of the confinement cage for Specimen 6, which effectively controlled crack propagation, allowing for the mode of failure to be steel tension fracturing, as opposed to concrete failure as was the case for Specimen 2.

Comparison of the combined loading tests, Specimens 3 and 7 shows that the latter had a deformation capacity that was 65 percent larger than the former. The mode

of failure changed with concrete-controlled failure giving way to steel failure from Specimen 3 to Specimen 7. Again, the addition of the confinement cage was responsible for this change in failure mode. Furthermore, while the applied axial load for both tests was 127 kN (28.5 kips), this target represented 89 percent of the experimental pullout capacity for Specimen 3, while only 45 percent of the pullout capacity for Specimen 7. The increased intensity in tensile loading relative to the pure pullout capacity resulted in Specimen 3 being brought close to failure merely with the application of the axial load.

For the two cyclic tests, Specimens 4 and 8, the deformation capacity was calculated for both shear loading directions using the cyclic envelopes. For Specimen 4, the deformation capacity for both directions was 2 mm (0.08 in.). For Specimen 8, the deformation capacity was 2 mm (0.08 in.) in the negative shear direction (the initial loading direction of shear load), and 1 mm (0.05 in.) in the opposite shear direction, resulting in an average deformation capacity of 1.7 mm (0.07 in.). Upon reversing the loading direction, the deformation capacity was lowered due to the amount of damage incurred by the specimen during the previous half-cycle.

6.4 Energy Dissipation Capacity

An additional method for comparing the effect of test parameters is through energy dissipation. The energy dissipated during each test was taken as the area under the load versus average slip displacement curve using the trapezoidal rule. The computed energies were then normalized by the product of one-half of the load and the slip at the second trilinear point, as identified in Table 6.2. This point was taken as a pseudo-yield point, and normalization with respect to elastic energy at yield allows comparison of energy dissipation capacities among various specimens. A comparison of the energy dissipated by Specimens 2 and 6 was not made since they are both pure pullout tests.

When comparing the energy dissipated for the two monotonic specimens, Specimens 1 and 5 in Figure 6.13, the two specimens dissipated roughly the same amount of total energy. However, the energy was dissipated at a faster rate for Specimen 5 than

for Specimen 1. This is due to the fact that Specimen 5 developed stud fractures that resulted in large load reductions late in the loading history, but the ultimate load was greater. Specimen 1, however, did not reach the magnitude of load that Specimen 5 did due to the amount of concrete damage resulting from the lack of adequate confining reinforcement and an unsymmetric loading surface. Yet, it did maintain its peak load over large slips.

The energy dissipated for Specimens 3 and 7 is shown in Figure 6.14. The relationship between the energy dissipated and the average slip is similar between these two specimens. However, there is significantly more energy dissipated by Specimen 7. This is due to the small amount of deformation capacity in Specimen 3, preventing any significant amount of energy dissipation. Furthermore, concrete damage was the primary failure mode in Specimen 3, with no signs of stud yielding, while stud failure governed for Specimen 7. Since a large amount of energy is dissipated through stud yielding, Specimen 3 was unable to dissipate the amount of energy dissipated by Specimen 7. In conclusion, the presence of confining reinforcement greatly enhances the energy dissipation capacity for combined shear and tension loading, primarily because it increases ductility.

When comparing the cumulative energy dissipated for the two cyclic tests, Specimens 4 and 8 in Figure 6.15, the total amount of energy dissipated by the end of the tests are comparable with one another. However, Specimen 4 dissipates energy over a larger range of displacements, and Specimen 8 shows much more energy dissipation at lower values of slip than does Specimen 4. Since most of the energy is dissipated by the yielding of the studs, the studs in Specimen 8 were driven to larger inelastic strains earlier in the load history than did the studs in Specimen 4.

7. Summary and Conclusions

An experimental program was undertaken to gain a better understanding of the behavior of headed shear studs under multi-axial loading for use in the connection of reinforced concrete infill walls to steel frames for seismic applications. A test setup was developed that accurately simulates the forces and deformations in the connection region of the S-RCW infill system. A total of eight stud tests of steel frame-RC infill subassemblages were conducted. This chapter summarizes the results of this experimental research and draws conclusions.

7.1 Experimental Procedure

To understand the behavior of shear studs for use in steel frames with reinforced concrete infill walls, the forces resisted by such shear studs must be identified and simulated in a laboratory setting. While the response of the studs and surrounding concrete was monitored, the shear studs are subjected to shear forces arising from the relative movement between the interfaces of the steel and concrete components, i.e., slip and gap/contact. For seismic applications, this shear force is cyclic in nature. In addition, due to curvature of the frame members and overturning of the system, shear studs are also subjected to axial tension/compression forces, with axial tension being the most detrimental.

7.1.1 Test Setup

The traditional “push-out” test setup for monotonic shear tests of headed shear studs was modified to meet the needs listed above. This setup represents a micro-model, a model of a localized portion of a steel frame- RC infill interface. The first change was to use two steel (column) sections and one concrete member as opposed to a more typical arrangement of two concrete slabs and one steel (beam) section. Also, load transfer plates were placed on top of and below the concrete panel near the column-panel interface, separated from the concrete by teflon pads. This measure was taken to concentrate the load over a more localized portion of the panel as shown in Figure 3.1, namely over the stud embedment region. This prevented the transfer of stresses to regions of the panel away from the interface and the resulting eccentric loading of the studs. Judging from the testing program, the majority of the concrete damage was observed in the region below the load transfer plates, with virtually no damage near the center of the panel, indicating the success of this measure.

Another modification made to the pushout specimen involved the attachment of a horizontal actuator for the application of axial tensile load to one of the steel columns. To transfer the tension forces from the column to the infill panel, and not to the connection of the column base plate, a linear bearing system was used to provide a nearly frictionless column base connection in the in-plane lateral direction. In addition, the other steel column was equipped with an A-brace to provide lateral sway resistance to this column. On the basis of the data collected from the two LVDT’s on the actuator column, the linear bearing system performed well, with little column rotation present and the proper transfer of stresses from the actuator column to the infill panel.

A threaded rod system was implemented to accommodate cyclic loading using a universal testing machine. When reversed shear was applied, these rods pulled up on a steel bearing plate which loaded the bottom of the concrete panel (Figure 3.1). This system avoided the possibility of tension being applied to the panel during the reversed shear cycles. From the results of the cyclic tests, the reversed shear loading system

worked well, as evident through the similarity between load and slip peaks for corresponding shear and reversed shear cycles. The only negative feature of the system is that slip displacement between concrete and steel is not identically equal to the movement of the crosshead. This is due to the flexibility introduced by the threaded rods.

7.1.2 Instrumentation and Loading

The design of the instrumentation scheme was crucial in determining the behavior of the shear studs in infill wall systems. A primary measurement was slip, i.e., the relative movement between each steel column and the concrete panel. This measurement was also important in the control of the cyclic tests. Displacement history targets were based on slip, not on testing machine (actuator) stroke, because in the reversed shear cycles, phenomena such as stretching of the threaded rods and bolts, as well as bending of the bearing plate were included in the stroke. These additions to the stroke were not present in the forward shear cycles. As a result, displacement history targets based on slip provided a symmetric load versus slip relationship.

Separation LVDT's were used to measure the gap between the steel and the concrete. These gaps grew due to the presence of axial tension on the specimen. In addition, any yielding of the studs, even in specimens with shear loading only, mobilizes increases in the gap opening. Judging from visual observations made in early tests, as well as data collected in later tests, it was important to instrument both faces of the panel to monitor any rotation of the panel.

Additional instrumentation used in the testing program was an acoustic emission monitoring system. Acoustic emission instrumentation was extremely useful since the shear studs were embedded in the concrete panel and cannot be observed during testing. Acoustic emission data collected was essential in explaining some of the changes in the load versus displacement relationship for each of the eight tests performed, as indicated in Chapter 4.

7.2 Test Results

The experimental program was designed to assess the impact of three primary test variables. These variables included the type of shear loading (monotonic versus cyclic), the presence of axial tension, and the reinforcement configuration for the perimeter of the panel (perimeter bars versus confinement cage). A total of eight specimens were fabricated and tested, including four with the perimeter bar detail (Figure 3.5), and the remaining four with the confinement cage detail (Figure 3.7).

7.2.1 Monotonic Shear Behavior

The greatest factor affecting the monotonic stud shear behavior was the presence of axial tension. When a constant axial tensile load of 127 kN (28.5 kips) was applied, the monotonic shear strength of the studs was reduced by nearly 40 percent for both the perimeter bar and confinement cage specimens (Specimen 3 versus Specimen 1 and Specimen 7 versus Specimen 5). The maximum slip achieved was also reduced when axial tension was present, 84 percent for the perimeter bar specimens, and 48 percent for the specimens using the confinement cage. This magnitude of axial tension force represents 89 percent of the peak tensile strength exhibited by the perimeter bar scheme and 45 percent of that for the confinement cage.

The type of reinforcement configuration also contributed to the monotonic shear behavior. When no axial tension was present, the monotonic shear strength was increased by 26 percent for the specimen with the confinement cage over that for the perimeter bar scheme (Specimen 5 versus Specimen 1). It should be noted, however, that a portion of this increase in shear strength could be the result of an unsymmetric loading surface present for the perimeter bar specimen (Specimen 1).

The type of reinforcement configuration was also an important contributing factor for the tests in which axial tension was applied prior to monotonic shear. The monotonic

shear strength was 27 percent larger when a confinement cage was used (Specimen 7 versus Specimen 3). The maximum slip achieved using the confinement cage configuration (Specimen 7) was approximately three times larger than the maximum slip achieved using the perimeter bar reinforcement configuration (Specimen 3) when axial tension was applied.

7.2.2 Monotonic Axial Tension Behavior

For the monotonic axial tension tests, the only variable considered was the type of reinforcement configuration used, which proved to have a large impact on specimen behavior. When the confinement cage was used (Specimen 6), the axial tension strength was approximately three times larger than that for the specimen utilizing the perimeter bar scheme (Specimen 2). The corresponding ductility was over seven times larger when using the confinement cage. This relates to the effect of parallel edges on the degree of confining pressure in thin infill walls. For the perimeter bar specimens, the small thickness of the wall does not provide adequate confinement around the stud. Thus the concrete cracks before the stud strength is fully developed. However, the use of a confinement cage can provide enough confinement around the stud to overcome the parallel edge effect of the wall.

7.2.3 Cyclic Loading

The introduction of cyclic loading did not translate to a large loss in stud strength. Only a 5 percent reduction in stud strength of the cyclic specimen using the perimeter bar configuration (Specimen 4), and 17 percent for the specimen with the confinement cage (Specimen 8), were observed, although this comparison is not entirely appropriate because Specimen 8 was subjected to cyclic shear with constant axial tension, whereas Specimen 4 did not resist axial tension. While the confinement cage specimen exhibited a larger strength degradation with cyclic loading, the mobilizing mechanism for the

larger loss was almost certainly the axial tension loaded applied prior to the cyclic shear load.

The greatest impact of cyclic loading was in the large reductions in the amount of displacement ductility displayed by the specimens. For the perimeter bar specimens, the ratio of the slip at failure for cyclic shear to the slip at failure for monotonic shear was 0.24. For the confinement cage specimens, the ratio of the maximum slip for the cyclic shear test with constant axial tension to the maximum slip for the monotonic shear test with constant axial tension was 0.34. These low slip ratios result from a low-cycle fatigue failure in the shank of the shear studs when subjected to cyclic loading. This was the governing failure mode for both cyclic tests, with little damage occurring in the concrete. This complication cannot be addressed through the detailing of the reinforcement, since stud failure controls at small slips. Ductility of the shear stud may be enhanced by use of a skirt or similar device at the base of the stud (McMullin et al., 1994), but with substantial losses in strength and stiffness also occurring. However, until the cyclic slip demand on studs is defined for S-RCW infill systems, it will not be clear whether the studs will have sufficient ductility. This is being addressed in related research on this project (Tong et al., 1998).

7.3 Design Recommendations

When comparing the results of the eight tests to strength estimates from existing design formulas, as shown in Figures 6.2 through 6.7, the PCI (1992) formulas for concrete failure due to shear loading proved to better predict the experimental strength for the test controlled by concrete failure (Specimen 1). Both the magnitude and the failure mode was predicted well by the Equation 2.7. The AISC LRFD (1993) formula (Equation 2.1, governed by concrete failure) proved to be unconservative when compared to the experimental results. It should be noted that there was an unsymmetric loading surface for the specimen where concrete failure governed (Specimen 1), which could lead to uncharacteristically lower strengths. When steel failure governed (Specimen 5), the

AISC LRFD equation for steel failure correlated better with the experimental results than the PCI formula for steel failure (Equation 2.6), the latter of which proved to be overconservative. Thus, an increase in the predicted PCI shear strength due to failure in the steel may be warranted. For example, the ratio of the experimental strength per stud in shear (Specimen 5) versus in tension (Specimen 6) is 90%. Both the AISC and PCI equations, however, incorrectly predicted the failure mode. This is best remedied by increasing the predicted strength due to failure in the concrete of a well confined shear connector. The Japanese stud strength correction factor for parallel edges (Equation 2.5) overestimated the stud strength when concrete failure governed, as was the case for Specimen 1, indicating that this factor possibly does not represent accurately the influence of parallel edges on stud strength in this testing program. The reduction factor used assumes that a 30 cm (11.8 in.) wall will provide as much confinement as would a concrete slab. The experimental results show that the confinement provided by a 25 cm (10 in.) thick wall was not sufficient. Using the Japanese parallel edge correction factor formula, but modifying the denominator to match the results from Specimen 1, the modified reduction factor equation would be $\phi_I = (a/17)^{1/2}$, as compared to $(a/15)^{1/2}$ in Equation 2.5. Note, however, that because of unsymmetric loading, the shear strength of Specimen 1 may be low, and the existing factor of $(a/15)^{1/2}$ may in fact be adequate. A more important conclusion is that, from the results of Specimen 5, which has adequate confinement and which was underpredicted by Equation 2.5, no reduction factor due to parallel edge effects may be required. Instead, increasing the predicted shear strength due to failure in the concrete from what is predicted by Equations 2.1 or 2.7 may be warranted for well confined shear connectors.

The influence of confinement was especially evident for the case when axial tension was applied, in which the specimens using the confinement cage performed considerably better than those with the perimeter bar detail. For the case when only axial tension was applied, the strength and ductility were 98 and 632 percent larger, respectively, for the specimen using the confinement cage (Specimen 6) over that with the perimeter bar scheme (Specimen 2). For Specimen 6, the PCI formulas (Equations

2.8 and 2.9) correctly predicted the failure mode, and conservatively predicted the peak tensile strength of the experimental results. A small increase in the tensile strength due to steel failure (Equation 2.8), and a more substantial increase in the strength due to failure in the concrete (Equation 2.9), may be warranted. The estimated strength from Equation 2.8 was 75% of the actual strength; the estimated strength from Equation 2.9 was 79% (all with $\phi = 1$).

For the combined shear and tension tests, a similar trend was observed, in which the strength and ductility for the specimen utilizing the confinement cage (Specimen 7) were 27 and 193 percent larger, respectively, than those for the specimen relying on the perimeter bar scheme (Specimen 3). However, it is possible that the shape of the PCI interaction equations (Equations 2.10 and 2.11) themselves may be unconservative when a concrete failure mode dominates in an infill wall, as is the case for Specimen 3, whose combined strength was overpredicted. A linear interaction curve, coupled with the increase in predicted strengths discussed above, may yield a more consistently accurate strength prediction.

For the cyclic tests (Specimens 4 and 8), the NEHRP (1997) design shear strengths from the concrete design chapter are equivalent to the PCI (1992) shear strength predictions. For the case when no axial tension was present (Specimen 4), the NEHRP (i.e., PCI) stud strength is reached, based on Equations 2.6 and 2.7. In addition, the monotonic strength according to AISC (1993) greatly overpredicts the results. The experimental reduction in shear strength was only 5 percent from Specimens 1 to 4, not 25 percent, due partially to a lower shear strength possibly being achieved in Specimen 1 due to unsymmetric loading. Nevertheless, taken together, Specimens 1, 4, and 5 point to the possibility of needing a prediction for monotonic shear strength that is greater than the PCI prediction (Equations 2.6 and 2.7), yet less than the AISC prediction (Equation 2.1), particularly for the formulas related to concrete failure. An adequate reduction formula similar to that included in Equation 2.5, but which accounts for the presence of confining steel, may work well. If Equation 2.7, predicting concrete failure, were modified to account for confinement, and Equation 2.6 were increased slightly for the

prediction of failure in the steel, then the additional reduction due to the presence of cyclic action in an infill wall could be less than 25 percent as specified in NEHRP (1997), and more in line with the reductions seen in these experiments.

For the case when axial tension was present in conjunction with cyclic shear (Specimen 8), the NEHRP strength using the PCI interaction formulas (Equations 2.10 and 2.11, using the PCI calculated nominal values for the monotonic shear and tension capacities), overestimate the stud strength. These same equations conservatively predict the monotonic results of Specimen 7. For the composite design chapter, the NEHRP (1997) specification requires a 25 percent reduction in the AISC LRFD (1993) stud strength formulas for shear loading of studs. However, this reduction exceeded the strength reductions in the two cyclic tests, which were 5 percent for Specimen 4, and 17 percent for Specimen 8. As a further reduction in the cyclic shear strength seems unwarranted, it may be necessary to alter the shape of the interaction equations themselves (Equations 2.10 and 2.11) to capture behavior as evidenced in Specimen 8. Such a change in these equations would similarly benefit the prediction of Specimen 3.

Based on the preceding discussions, for studs in S-RCW infill systems where parallel edges greatly affect stud strength, confining reinforcement around the stud is essential to develop the full strength and ductility of the studs, especially when axial tension is present. In such cases, the AISC LRFD (1993) and PCI (1992) strength capacities are reached. However, the possibility exists that the nominal ultimate tensile strength of the stud for this testing program, as well as in previous testing programs, is variable with respect to the specified nominal stud tensile strength. For Specimens 5 and 6, the experimental results had stud strengths that exceeded the specified nominal ultimate tensile strength (i.e., $A_s F_u$ of the stud). In addition, concrete strength is variable. Comparing the eight specimens to predicted values using measured material properties may thus yield different conclusions, both with respect to the predicted strength and failure mode. Such analysis is beyond the scope of this work.

Nevertheless, some conclusions may be drawn based upon use of nominal material values for predicting stud strength. The PCI strength formula for steel failure

(Equation 2.6) accounts for shear loading with a 25 percent reduction in the stud shear strength for steel-controlled failure (while AISC LRFD, Equation 2.1, requires no such reduction), perhaps due to the fact that axial and bending stresses are present in addition to shear stresses. Based on the results from other experimental programs for bolts, a reduction in strength to account for shear loading when steel failure governs is necessary, although from this and other testing programs, a 25 percent reduction in the monotonic shear strength appears to be overly conservative in the application to shear studs. In addition, better accounting for the presence of confining steel is required for the equations that predict concrete failure (Equations 2.1 and 2.7). In contrast, for cyclic loading, the NEHRP (1997) composite reduction in strength is also overly conservative, indicating this reduction more than takes in account the effect on cyclic loading. As a lower bound, a reduction of approximately 17 percent, which was the case for Specimen 8, would be more representative of this experimental program (or a smaller reduction of 10 to 15 percent if the monotonic shear strength prediction is reduced from Equation 2.1, e.g., using a reduction factor similar to that used in Equation 2.5). The tensile strengths, on the other hand, appear to be adequately predicted well, if somewhat conservatively, by the PCI formulas (Equations 2.8 and 2.9). Finally, the interaction formulas of Equations 2.10 and 2.11 may be somewhat unconservative both for monotonic and cyclic loading.

Based on the results obtained from this experimental program, the following conclusions can be drawn:

- For monotonic shear loading where steel failure governs, the AISC LRFD equations for steel failure is an accurate representation of the stud behavior (i.e., the nominal ultimate tensile strength can be achieved in shear for studs). However, previous research has indicated that the ultimate tensile strength cannot be developed in shear for bolts, thus indicating the possible need for a reduction in strength due to shear loading. More experiments focusing solely on shear loading applied to shear studs in infill walls are needed to fully understand the behavior for steel-controlled stud failures.

- For monotonic shear loading where concrete failure governs, the PCI equations for concrete failure should be used. For the Japanese equation accounting for parallel edge effects (Equation 2.5), more accurate assessment of the amount of confining steel is warranted in the reduction factor accounting for parallel edge effects, resulting in an increase in the predicted shear strength due to concrete failure. With such an assessment, the evidence shows that both the shear strength and the shear failure mode may be better predicted.
- For monotonic axial tension loading where steel failure governs, a strength prediction equivalent to $A_s F_u$ should be used (i.e., the nominal ultimate tensile strength can be achieved for studs).
- For monotonic axial tension loading where concrete failure governs, the concrete splitting failure present for Specimen 2 should be avoided due to poor strength and deformation capacity by providing adequate confinement to the stud. If confinement is added to avoid this type of failure, and to develop instead a 45 degree cone failure, the stud behavior cannot be quantified from this experimental program since there was no test in which this type of concrete failure was present, although it is likely that the strength is above that predicted by Equation 2.7 as little damage in the concrete was seen at the time of failure in the stud in Specimen 6, and Equations 2.6 and 2.7 yielded similar nominal strengths.
- For monotonic shear with constant axial tension applied, when steel failure governs, the PCI interaction equation for steel failure should be used. However, a linear interaction equation may yield more consistent results of strength prediction.
- For monotonic shear with constant axial tension applied, when concrete failure governs, as was the case for monotonic axial tension where concrete failure governs, the concrete splitting mode of failure yields poor strength and deformation capacities, and should be avoided through avoided through

providing adequate confinement to the studs. If this failure mode is avoided, and a concrete failure mode consisting of a shear or pullout cone develops instead, the stud behavior cannot be assessed from this experimental program since no specimen failed in this manner.

- To account for cyclic loading, a reduction in the monotonic shear strength of at least 15 percent should be assumed for shear connections in infill walls. This is based on the results from Specimens 7 and 8, as opposed to Specimens 1 and 4, in which Specimen 1 possessed an unsymmetric loading surface and may have failed prematurely, resulting in a lower reduction due to cyclic loading.

7.4 Further Research

The research presented provides a better understanding of the behavior of shear studs in S-RCW infill systems. However, there are several aspects that need further investigation.

1) For all of the tests conducted as part of this research, the combined shear and tension tests had the tension force held at a constant value. In the actual S-RCW infill system, the axial load is cyclic in nature (both in tension and compression) as is the shear load. A constant axial tension load was used for simplicity and because it represents a worst case scenario. Even though it is possible that cyclic tension yields the same results (strengths) as constant tension due to that the tension at peak shear is most crucial, the stud behavior under both cyclic shear and cyclic tension/compression should also be investigated.

2) Another area that needs further investigation is the problem of low-cycle fatigue failure of the studs under cyclic loading. This mode of failure governed both of the cyclic shear tests in this research. It is important to address the severity of this problem by first defining the demand on the shear studs for this structural system, which is being addressed in related research on this project (Tong et al., 1998). If the demand is

as high as the load histories for the tests performed, a low-cycle fatigue design criterion will need to be implemented.

3) In addition, methods for constructing the confinement cage should be investigated. For this project, the confinement cages were hand-tied using bent reinforcement. Alternative methods, such as three-dimensional cages made of fiber reinforced plastics or welded wire fabric, should be investigated. For this reinforcement, it is unlikely that substantial ductility of the bars is required.

4) Furthermore, alternative anchors could be implemented. For composite beams and a variety of precast systems, alternative anchors such as deformed bar anchors, channel sections, and perforated steel plates have been investigated. These and other alternative anchors should be evaluated to determine their applicability in S-RCW infill systems.

References

American Concrete Institute (ACI) Committee 318 (1995). *Building Code Requirements for Structural Concrete* (ACI 318-95) and *Commentary* (ACI 318R-95), American Concrete Institute, Detroit, Michigan.

American Institute of Steel Construction (AISC) (1997). *Seismic Provisions for Structural Steel Buildings*, AISC, Chicago, Illinois.

American Institute of Steel Construction (AISC) (1993). *Load and Resistance Factor Design for Structural Steel Buildings*, Second Edition, AISC, Chicago, Illinois.

Bursi, O. S. and Ballerini, M. (1996). "Behavior of a Steel-Concrete Composite Substructure with Full and Partial Shear Connection." *Proceedings of the Eleventh World Congress on Earthquake Engineering*, Paper No. 771, Acapulco, Mexico, 23-28 June 1996, Elsevier, New York.

Comité Euro-International du Béton (CEB) (1997). *Design of Fastenings in Concrete*, Thomas Telford, London, England.

Fisher, J. W., Galambos, T. V., Kulak, G. L., and Ravindra, M. K. (1978). "Load and Resistance Factor Design Criteria for Connectors." *Journal of the Structural Division*, ASCE, 104(ST9), September, 1427-1441.

Gattesco, N. and Giuriani, E. (1996). "Experimental Study on Stud Shear Connectors Subjected to Cyclic Loading." *Journal of Constructional Steel Research*, 38(1), 1-21.

Hawkins, N. M. and Mitchell, D. (1984). "Seismic Response of Composite Shear Connections." *Journal of Structural Engineering*, ASCE, 110(9), 1-10.

Hayashi, M. and Yoshinaga, K. (1985). "An Experimental Study on Practical Application of Composite Structures of a Frame and an Earthquake-Resistant Wall 1." *Synopses of the Conference of the Architectural Institute of Japan*, Architectural Institute of Japan (AIJ), Tokyo, Japan, October, 1335-1336.

Hayashi, M. and Yoshinaga, K. (1986). "An Experimental Study on Practical Application of Composite Structures of a Frame and an Earthquake-Resistant Wall 2." *Synopses of the Conference of the Architectural Institute of Japan*, AIJ, Tokyo, Japan, August, 1367-1368.

Hayashi, M. and Yoshinaga, K. (1987). "An Experimental Study on Practical Application of Composite Structures of a Frame and an Earthquake-Resistant Wall 3."

Synopses of the Conference of the Architectural Institute of Japan, AIJ, Tokyo, Japan, October, 1317-1318.

Hayashi, M. and Yoshinaga, K. (1994). "An Experimental Study on Practical Application of Composite Structures of a Frame and an Earthquake-Resistant Wall 9." *Synopses of the Conference of the Architectural Institute of Japan*, AIJ, Tokyo, Japan, September, 1617-1618.

Klingner, R. E., Mendonca, J. A., and Malik, J. B. (1982). "Effect of Reinforcing Details on the Shear Resistance of Anchor Bolts under Reversed Cyclic Loading." *Journal of the ACI*, January-February, 3-12.

Mainstone, R.J. and Menzies, J. B. (1967). "Shear Connectors in Steel-Concrete Composite Beams for Bridges. Part 1: Static and Fatigue Tests on Pushout Specimens." *Concrete*, 1(9), 291-302.

Makino, M. (1985). "Design of Framed Steel Structures with Infill Reinforced Concrete Walls." *Composite and Mixed Construction*, Roeder, C. W. (ed.), ASCE, New York, New York, 279-287.

McMackin, P. J., Slutter, R. G., and Fisher, J. W. (1973). "Headed Steel Anchors under Combined Loading." *Engineering Journal*, AISC, 10(2), 43-52.

McMullin, K. and Astaneh-Asl, A. (1994). "Cyclical Behavior of Welded Steel Shear Studs." *Structures Congress XII: Proceedings of Papers Presented at the Structures Congress '94*, Atlanta, Georgia, 24-28 April 1994, 1024-1029.

National Earthquake Hazard Reduction Program (NEHRP) (1997). *Recommended Provisions for the Development of Seismic Regulations for New Buildings. Part 1—Provisions. Part 2—Commentary*, Report No. 302 and 303, Building Seismic Safety Council, Federal Emergency Management Agency, Washington, D. C.

Oehlers, D. J. (1989). "Splitting Induced by Shear Connectors in Composite Beams." *Journal of Structural Engineering*, ASCE, 115(2), 341-362.

Oehlers, D. J. (1990). "Deterioration in Strength of Stud Connectors in Composite Bridge Beams." *Journal of Structural Engineering*, ASCE, 116(12), 3417-3431.

Oehlers, D. J. and Park, S. M. (1992). "Shear Connectors in Composite Beams with Longitudinally Cracked Slabs." *Journal of Structural Engineering*, ASCE, 118(8), 2004-2022.

Ollgaard, J. G., Slutter, R. G., and Fisher, J. W. (1971). "Shear Strength of Stud Connectors in Lightweight and Normal-Weight Concrete." *Engineering Journal*, AISC, April, 55-64.

Prestressed Concrete Institute (PCI) (1985). *PCI Design Handbook*, Third Edition, PCI, Chicago, Illinois.

Prestressed Concrete Institute (PCI) (1992). *PCI Design Handbook*, Fourth Edition, PCI, Chicago, Illinois.

Shaikh, F. A., and Yi, W. (1985). "In-Place Strength of Welded Headed Studs." *PCI Journal*, 30(2), 56-81.

Slutter, R. G. and Fisher, J. W. (1966). "Fatigue Strength of Shear Connectors." *Highway Research Record*, No. 147, 65-68.

Thürlimann, B. (1959). "Fatigue and Static Tests of Stud Shear Connectors." *Journal of the ACI*, 30(12), 1287-1302.

Tong, X., Hajjar, J. F., and Schultz, A. E. (1998), "Prototype Design of Steel Frames with Reinforced Concrete Infill Walls," *Structural Engineering Report No. ST-98-1*, Department of Civil Engineering, University of Minnesota, Minneapolis, Minnesota, January, 40 pp.

Toprac, A. A. (1965). "Fatigue Strength of $\frac{3}{4}$ -Inch Stud Shear Connectors." *Highway Research Record*, No. 103, 53-77.

Viest, I. M. (1956). "Investigation of Stud Shear Connectors for Composite Concrete and Steel T-Beams." *Journal of the ACI*, 27(8), 875-891.

Yen, R. J. Y., Lin, Y., and Lai, M. T. (1997). "Composite Beams Subjected to Static and Fatigue Loads." *Journal of Structural Engineering*, ASCE, 123(6), 765-771.

Table 3.1 Steel reinforcement properties

	#3 Bars		#4 Bars	
	ksi	MPa	ksi	MPa
Yield Strength				
Sample 1	84.50	582.6	74.54	514.0
Sample 2	84.44	582.2	74.98	517.0
Average	84.47	582.4	74.76	515.5
Standard Deviation	0.04	0.28	0.31	2.1
Ultimate Tensile Strength				
Sample 1	124.4	857.7	-	-
Sample 2	124.3	857.0	115.3	795.0
Average	124.4	857.7	-	-
Standard Deviation	0.04	0.28	-	-
Elastic Modulus				
Sample 1	27480	189480	27713	191080
Sample 2	28091	193690	27506	189650
Average	27786	191580	27610	190370
Standard Deviation	432.0	2979	146.4	1009
Ultimate Strain (%)	11.3		12.2	

Table 3.2 Mix design for concrete mix

	Weight (lb.)	Mass (kg)
Cement	400	181
Fly Ash	71	32
Sand	1484	673
Gravel, 19 mm (0.75 in.)	1764	800
Water	295	134
Total Air, %	2	2

Table 3.3 Concrete material properties for Series 1

	Sample			Average	Standard Deviation
	1	2	3		
Initial Slump	15.2 cm (6 in.)	-	-	-	-
Air Content (%)	1.7	-	-	-	-
28 Day f'_c (Air Cured)	32.98 MPa (4783 psi)	31.04 MPa (4502 psi)	32.35 MPa (4692 psi)	32.12 MPa (4659 psi)	0.989 MPa (143.4 psi)
28 Day f'_c (Moist Cured)	31.73 MPa (4602 psi)	31.57 MPa (4578 psi)	32.04 MPa (4647 psi)	31.78 MPa (4609 psi)	0.242 MPa (35.03 psi)
f'_c at Test 1 (49 Days-Air Cured)	37.16 MPa (5390 psi)	32.65 MPa (4736 psi)	34.67 MPa (5028 psi)	34.83 MPa (5051 psi)	2.26 MPa (327.6 psi)
f'_c at Test 2 (126 Days-Air Cured)	34.03 MPa (4935 psi)	32.73 MPa (4747 psi)	35.83 MPa (5196 psi)	34.19 MPa (4959 psi)	1.55 MPa (225.5 psi)
f'_c at Test 3 (89 Days-Air Cured)	32.77 MPa (4753 psi)	33.99 MPa (4930 psi)	37.10 MPa (5381 psi)	34.62 MPa (5021 psi)	2.23 MPa (323.8 psi)
f'_c at Test 4 (163 Days-Air Cured)	33.44 MPa (4850 psi)	33.91 MPa (4918 psi)	33.81 MPa (4903 psi)	33.72 MPa (4890 psi)	0.246 MPa (35.73 psi)
Modulus of Rupture (28 Days-Air Cured)	3.52 MPa (511 psi)	3.25 MPa (471 psi)	3.56 MPa (516 psi)	3.44 MPa (499.3 psi)	0.170 MPa (24.66 psi)
Split Tensile Strength (32 Days-Air Cured)	3.28 MPa (476.1 psi)	3.94 MPa (571.4 psi)	2.95 MPa (427.9 psi)	3.39 MPa (491.8 psi)	0.503 MPa (73.02 psi)
Elastic Modulus (28 Days-Air Cured)	29993 MPa (4350 ksi)	30338 MPa (4400 ksi)	- -	30166 MPa (4375 ksi)	243.8 MPa (35.36 ksi)

Table 3.4 Concrete material properties for Series 2

	Sample			Average	Standard Deviation
	1	2	3		
Initial Slump	15.24 6	-	-	-	-
Air Content (%)	1.5	-	-	-	-
28 Day f'_c (Air Cured)	32.08 MPa (4652 psi)	31.26 MPa (4533 psi)	33.04 MPa (4792 psi)	32.12 MPa (4659 psi)	0.89 MPa (129.6 psi)
28 Day f'_c (Moist Cured)	33.85 MPa (4909 psi)	34.70 MPa (5032 psi)	33.02 MPa (4789 psi)	33.85 MPa (4910 psi)	0.84 MPa (121.5 psi)
f'_c at Test 1 (59 Days-Air Cured)	29.88 MPa (4334 psi)	31.22 MPa (4528 psi)	30.96 MPa (4490 psi)	30.69 MPa (4451 psi)	0.71 MPa (102.8 psi)
f'_c at Test 2 (66 Days-Air Cured)	30.54 MPa (4430 psi)	30.22 MPa (4383 psi)	30.71 MPa (4454 psi)	30.49 MPa (4422 psi)	0.25 MPa (36.12 psi)
f'_c at Test 3 (91 Days-Air Cured)	29.06 MPa (4214 psi)	29.24 MPa (4241 psi)	27.89 MPa (4045 psi)	28.73 MPa (4167 psi)	0.73 MPa (106.2 psi)
f'_c at Test 4 (101 Days-Air Cured)	27.26 MPa (3953 psi)	29.37 MPa (4260 psi)	29.57 MPa (4289 psi)	28.73 MPa (4167 psi)	1.28 MPa (186.2 psi)
Modulus of Rupture (28 Days)	4.66 MPa (676 psi)	4.65 MPa (674 psi)	5.12 MPa (743 psi)	4.81 MPa (697.7 psi)	0.27 MPa (39.27 psi)
Split Tensile Strength (28 Days)	3.05 MPa (442.1 psi)	3.01 MPa (437.1 psi)	3.03 MPa (440.0 psi)	3.03 MPa (439.7 psi)	0.017 MPa (2.53 psi)
Elastic Modulus (28 Days)	26891 MPa (3900 ksi)	27580 MPa (4000 ksi)	- -	27235 MPa (3950 ksi)	487.6 MPa (70.71 ksi)

Table 3.5 Specimen labeling system

Symbol	Definition
A	Experimental Series
	1=Series 1
	2=Series 2
XX	Reinforcement Configuration
	PB=Perimeter Bar Configuration
	CG=Cage Configuration
YY	Shear Application
	MS=Monotonic Shear
	CS=Cyclic Shear
	NS=No Applied Shear
B	Axial Tension Application
	0=No Axial Tension Applied
	1=Constant Axial Tension Applied

Table 3.6 Schedule of tests

Series	Specimen	Reinforcement Configuration	Shear Loading	Axial Tensile Loading
1	1	Perimeter Bar	Monotonic	-
1	2	Perimeter Bar	-	Monotonic
1	3	Perimeter Bar	Monotonic	Constant-127 kN (28.5 kips)
1	4	Perimeter Bar	Cyclic	-
2	5	Cage	Monotonic	-
2	6	Cage	-	Monotonic
2	7	Cage	Monotonic	Constant-127 kN (28.5 kips)
2	8	Cage	Cyclic	Constant-127 kN (28.5 kips)

Table 3.7 South face instrumentation

	Specimen							
Instrument	1	2	3	4	5	6	7	8
SLIP-WEST								
x ₁	38 mm (1.5 in.)	41 mm (1.625 in.)	41 mm (1.625 in.)	48 mm (1.875 in.)	48 mm (1.875 in.)	46 mm (1.813 in.)	44 mm (1.75 in.)	46 mm (1.813 in.)
y ₁	395 mm (15.56 in.)	362 mm (14.25 in.)	413 mm (16.25 in.)	411 mm (16.19 in.)	419 mm (16.5 in.)	414 mm (16.31 in.)	419 mm (16.5 in.)	418 mm (16.44 in.)
SLIP-EAST								
x ₂	48 mm (1.875 in.)	44 mm (1.75 in.)	44 mm (1.75 in.)	43 mm (1.688 in.)	41 mm (1.625 in.)	40 mm (1.563 in.)	41 mm (1.625 in.)	41 mm (1.625 in.)
y ₁	398 mm (15.69 in.)	359 mm (14.13 in.)	408 mm (16.06 in.)	408 mm (16.06 in.)	416 mm (16.38 in.)	418 mm (16.44 in.)	416 mm (16.38 in.)	418 mm (16.44 in.)
SEP-SFWT								
x ₁	64 mm (2.5 in.)	67 mm (2.625 in.)	62 mm (2.438 in.)	52 mm (2.063 in.)	64 mm (2.5 in.)	65 mm (2.563 in.)	57 mm (2.25 in.)	56 mm (2.188 in.)
y ₁	175 mm (6.875 in.)	171 mm (6.75 in.)	179 mm (7.063 in.)	181 mm (7.125 in.)	178 mm (7 in.)	178 mm (7 in.)	178 mm (7 in.)	176 mm (6.938 in.)
SEP-SFWB								
x ₁	62 mm (2.438 in.)	67 mm (2.625 in.)	59 mm (2.313 in.)	51 mm (2 in.)	65 mm (2.563 in.)	65 mm (2.563 in.)	57 mm (2.25 in.)	57 mm (2.25 in.)
y ₂	175 mm (6.875 in.)	178 mm (7 in.)	168 mm (6.625 in.)	175 mm (6.875 in.)	178 mm (7 in.)	179 mm (7.063 in.)	175 mm (6.875 in.)	178 mm (7 in.)
SEP-SFET								
x ₂	54 mm (2.125 in.)	64 mm (2.5 in.)	64 mm (2.5 in.)	52 mm (2.063 in.)	64 mm (2.5 in.)	64 mm (2.5 in.)	57 mm (2.25 in.)	56 mm (2.188 in.)
y ₁	178 mm (7 in.)	178 mm (7 in.)	184 mm (7.25 in.)	171 mm (6.75 in.)	179 mm (7.063 in.)	181 mm (7.125 in.)	178 mm (7 in.)	179 mm (7.063 in.)
SEP-SFEB								
x ₂	62 mm (2.438 in.)	67 mm (2.625 in.)	59 mm (2.313 in.)	52 mm (2.063 in.)	65 mm (2.563 in.)	64 mm (2.5 in.)	57 mm (2.25 in.)	57 mm (2.25 in.)
y ₂	181 mm (7.125 in.)	178 mm (7 in.)	162 mm (6.375 in.)	178 mm (7 in.)	176 mm (6.938 in.)	179 mm (7.063 in.)	175 mm (6.875 in.)	178 mm (7 in.)

Table 3.8 North face instrumentation

Instrument	Specimen							
	1	2	3	4	5	6	7	8
SEP-NFWT								
x ₂	-	65 mm (2.563 in.)	-	52 mm (2.063 in.)	65 mm (2.563 in.)	65 mm (2.563 in.)	57 mm (2.25 in.)	56 mm (2.188 in.)
y ₁	-	178 mm (7 in.)	-	181 mm (7.125 in.)	178 mm (7 in.)	179 mm (7.063 in.)	178 mm (7 in.)	178 mm (7 in.)
SEP-NFWB								
x ₂	-	64 mm (2.5 in.)	-	52 mm (2.063 in.)	65 mm (2.563 in.)	65 mm (2.563 in.)	57 mm (2.25 in.)	57 mm (2.25 in.)
y ₂	-	178 mm (7 in.)	-	179 mm (7.063 in.)	176 mm (6.938 in.)	179 mm (7.063 in.)	178 mm (7 in.)	178 mm (7 in.)
SEP-NFET								
x ₁	-	65 mm (2.563 in.)	-	54 mm (2.125 in.)	65 mm (2.563 in.)	64 mm (2.5 in.)	57 mm (2.25 in.)	56 mm (2.188 in.)
y ₁	-	178 mm (7 in.)	-	178 mm (7 in.)	176 mm (6.938 in.)	178 mm (7 in.)	178 mm (7 in.)	176 mm (6.938 in.)
SEP-NFEB								
x ₁	-	65 mm (2.563 in.)	-	52 mm (2.063 in.)	64 mm (2.5 in.)	64 mm (2.5 in.)	57 mm (2.25 in.)	57 mm (2.25 in.)
y ₂	-	178 mm (7 in.)	-	179 mm (7.063 in.)	184 mm (7.25 in.)	181 mm (7.125 in.)	178 mm (7 in.)	178 mm (7 in.)

Table 3.9 Acoustic emission instrumentation

Instrument	Specimen							
	1	2	3	4	5	6	7	8
AE-1								
x ₁	92 mm (3.625 in.)	89 mm (3.5 in.)	92 mm (3.625 in.)	76 mm (3 in.)	89 mm (3.5 in.)	82 mm (3.25 in.)	89 mm (3.5 in.)	76 mm (3 in.)
y ₁	87 mm (3.438 in.)	89 mm (3.5 in.)	82 mm (3.25 in.)	89 mm (3.5 in.)				
AE-2								
x ₁	-	89 mm (3.5 in.)	90 mm (3.563 in.)	76 mm (3 in.)	-	-	-	-
y ₁	-	305 mm (12 in.)	362 mm (14.25 in.)	305 mm (12 in.)	-	-	-	-
AE-3								
x ₁	62 mm (2.438 in.)	89 mm (3.5 in.)	92 mm (3.625 in.)	76 mm (3 in.)	89 mm (3.5 in.)	82 mm (3.25 in.)	89 mm (3.5 in.)	76 mm (3 in.)
y ₁	645 mm (25.38 in.)	622 mm (24.5 in.)	628 mm (24.75 in.)	622 mm (24.5 in.)				
AE-4								
x ₂	92 mm (3.625 in.)	89 mm (3.5 in.)	90 mm (3.563 in.)	76 mm (3 in.)	89 mm (3.5 in.)	82 mm (3.25 in.)	89 mm (3.5 in.)	76 mm (3 in.)
y ₁	79 mm (3.125 in.)	89 mm (3.5 in.)	89 mm (3.5 in.)	89 mm (3.5 in.)	89 mm (3.5 in.)	89 mm (3.5 in.)	89 mm (3.5 in.)	89 mm (3.5 in.)
AE-5								
x ₂	-	89 mm (3.5 in.)	90 mm (3.563 in.)	76 mm (3 in.)	-	-	-	-
y ₁	-	305 mm (12 in.)	365 mm (14.38 in.)	305 mm (12 in.)	-	-	-	-
AE-6								
x ₂	70 mm (2.75 in.)	89 mm (3.5 in.)	89 mm (3.5 in.)	76 mm (3 in.)	89 mm (3.5 in.)	82 mm (3.25 in.)	89 mm (3.5 in.)	76 mm (3 in.)
y ₁	641 mm (25.25 in.)	622 mm (24.5 in.)	651 mm (25.63 in.)	622 mm (24.5 in.)				
AE-7								
x ₁	-	-	-	-	0	0	0	0
y ₁	-	-	-	-	89 mm (3.5 in.)	89 mm (3.5 in.)	89 mm (3.5 in.)	89 mm (3.5 in.)
AE-8								
x ₁	-	-	-	-	0	0	0	0
y ₁	-	-	-	-	622 mm (24.5 in.)	622 mm (24.5 in.)	622 mm (24.5 in.)	622 mm (24.5 in.)
AE-9								
x ₂	-	-	-	-	0	0	0	0
y ₁	-	-	-	-	89 mm (3.5 in.)	89 mm (3.5 in.)	89 mm (3.5 in.)	89 mm (3.5 in.)
AE-10								
x ₂	-	-	-	-	0	0	0	0
y ₁	-	-	-	-	622 mm (24.5 in.)	622 mm (24.5 in.)	622 mm (24.5 in.)	622 mm (24.5 in.)

Table 3.10 Data collection rates for Specimen 4

Target	Data Collection Rate
89 kN (20 kips)	10 Hz
178 kN (40 kips)	10 Hz
267 kN (60 kips)	10 Hz
1 mm (0.04 in.)	5 Hz
2 mm (0.08 in.)	5 Hz
3 mm (0.12 in.)	5 Hz

Table 3.11 Loading rates for Specimen 4

Target	Loading Rate
89 kN (20 kips)	0.025 mm (0.001 in.) in 5 sec.
178 kN (40 kips)	0.025 mm (0.001 in.) in 5 sec.
267 kN (60 kips)	0.025 mm (0.001 in.) in 5 sec.
1 mm (0.04 in.)	0.05 mm (0.002 in.) in 5 sec.
2 mm (0.08 in.)	0.05 mm (0.002 in.) in 5 sec.
3 mm (0.12 in.)	0.1 mm (0.004 in.) in 5 sec.

Table 3.12 Loading rates for Specimen 8

Target	Loading Rate
89 kN (20 kips)	0.013 mm (0.0005 in.) in 5 sec.
178 kN (40 kips)	0.025 mm (0.001 in.) in 5 sec.
0.5 mm (0.02 in.)	0.025 mm (0.001 in.) in 5 sec.
1 mm (0.04 in.)	0.05 mm (0.002 in.) in 5 sec.
2 mm (0.08 in.)	0.05 mm (0.002 in.) in 5 sec.

Table 4.1 Ultimate values for load and displacement

Specimen	Ultimate Load	Displacement at Failure
1	400 kN (89.90 kips)	13 mm (0.5 in.)
2	142 kN (31.88 kips)	4.6 mm (0.18 in.)
3	241 kN (54.18 kips)	2.0 mm (0.08 in.)
4 Shear	381 kN (85.72 kips)	3.0 mm (0.12 in.)
4 Reversed Shear	370 kN (83.08 kips)	3.0 mm (0.12 in.)
5	503 kN (113.1 kips)	11 mm (0.45 in.)
6	281 kN (63.16 kips)	28 mm (1.1 in.)
7	306 kN (68.82 kips)	5.8 mm (0.23 in.)
8 Shear	253 kN (56.78 kips)	2.0 mm (0.08 in.)
8 Reversed Shear	256 kN (57.65 kips)	2.0 mm (0.08 in.)

Table 6.1 Load and displacement values for the first trilinear break point

Specimen	Max Load (kN)	Max Load (kips)	Load (kN)	Load (kips)	Ratio to Max Load	Displacement (mm.)	Displacement (in.)	Ratio to Stud Diameter
1	399.9	89.90	222.4	50	0.556	0.4140	0.0163	0.022
2	141.8	31.88	80.06	18	0.565	0.7874	0.0310	0.041
3	241.0	54.18	102.304	23	0.425	0.2616	0.0103	0.014
4	381.3	85.72	182.4	41	0.478	0.2159	0.0085	0.011
5	503.0	113.1	266.9	60	0.531	0.4953	0.0195	0.026
6	280.9	63.16	111.2	25	0.396	1.1303	0.0445	0.059
7	306.1	68.82	160.1	36	0.523	0.2794	0.0110	0.015
8	252.6	56.78	129.0	29	0.511	0.1994	0.0079	0.010
Average					0.498			

Table 6.2 Load and displacement values for the second trilinear break point

Specimen	Max Load (kN)	Max Load (kips)	Load (kN)	Load (kips)	Ratio to Max Load	Displacement (mm.)	Displacement (in.)	Ratio to Stud Diameter
1	399.9	89.9	343.074	77.13	0.858	1.5418	0.0607	0.081
2	141.8	31.877	120.10	27	0.847	1.3843	0.0545	0.073
3	241.0	54.18	213.504	48	0.886	1.0643	0.0419	0.056
4	381.3	85.72	311.4	70	0.817	0.6350	0.0250	0.033
5	503.0	113.08	364.7	82	0.725	1.3919	0.0548	0.073
6	280.9	63.16	209.056	47	0.744	0.3861	0.0152	0.020
7	306.1	68.82	253.5	57	0.828	1.2598	0.0496	0.066
8	252.6	56.78	191.3	43	0.757	0.3810	0.0150	0.020
Average					0.808			

Table 6.3 Comparison of peak strengths from measured and predicted results

Spec.	Experimental Results [kN (kips)]		Predicted Results [kN (kips)] Based Upon Nominal Material Strengths							
	Shear Load	Tensile Load	Eq. 2.1	Eq. 2.5	Eq. 2.6	Eq. 2.7	Eq. 2.8	Eq. 2.9	Eq. 2.10	Eq. 2.11
1	400 (89.90)	-	464 (104.4)	427 (96.07)	354 (79.58)	346 (77.79)	-	-	1.28	1.34
2	-	142 (31.88)	-	-	-	-	212 (47.71)	222 (49.81)	0.45	0.41
3	241 (54.18)	127 (28.50)	464 (104.4)	427 (96.07)	354 (79.58)	346 (77.79)	212 (47.71)	222 (49.81)	0.82	0.81
4	381 (85.72)	-	464 (104.4)	427 (96.07)	354 (79.58)	346 (77.79)	-	-	1.16	1.21
4 (reversed)	370 (83.08)	-	464 (104.4)	427 (96.07)	354 (79.58)	346 (77.79)	-	-	1.09	1.14
5	503 (113.1)	-	464 (104.4)	427 (96.07)	354 (79.58)	346 (77.79)	-	-	2.02	2.11
6	-	281 (63.16)	-	-	-	-	212 (47.71)	222 (49.81)	1.75	1.60
7	306 (68.82)	127 (28.50)	464 (104.4)	427 (96.07)	354 (79.58)	346 (77.79)	212 (47.71)	222 (49.81)	1.10	1.11
8	253 (56.78)	127 (28.50)	464 (104.4)	427 (96.07)	354 (79.58)	346 (77.79)	212 (47.71)	222 (49.81)	0.87	0.86
8 (reversed)	256 (57.65)	127 (28.50)	464 (104.4)	427 (96.07)	354 (79.58)	346 (77.79)	212 (47.71)	222 (49.81)	0.88	0.88

Table 6.4 Deformation capacities

Specimen	Deformation Capacity	Normalized by Stud Diameter
1	11 mm (0.46 in.)	0.61
2	3.8 mm (0.15 in.)	0.20
3	2.0 mm (0.08 in.)	0.10
4 Shear	2.0 mm (0.08 in.)	0.10
4 Reversed Shear	2.0 mm (0.08 in.)	0.10
4 Average	2.0 mm (0.08 in.)	0.10
5	9.2 mm (0.36 in.)	0.48
6	28 mm (1.10 in.)	1.5
7	5.8 mm (0.23 in.)	0.31
8 Shear	2.0 mm (0.08 in.)	0.11
8 Reversed Shear	1.2 mm (0.05 in.)	0.06
8 Average	1.7 mm (0.07 in.)	0.09

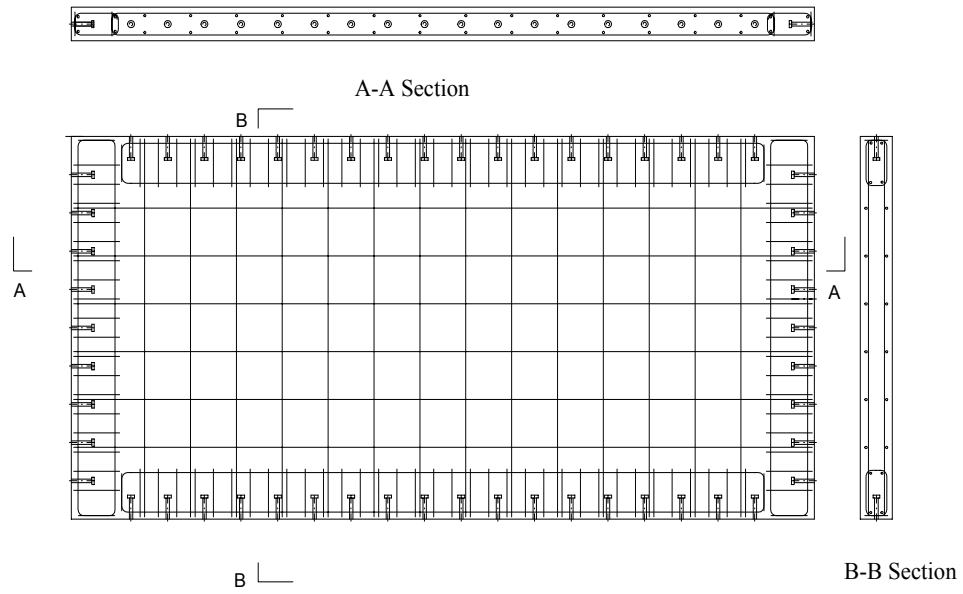


Figure 1.1 Prototype infill wall-steel frame system

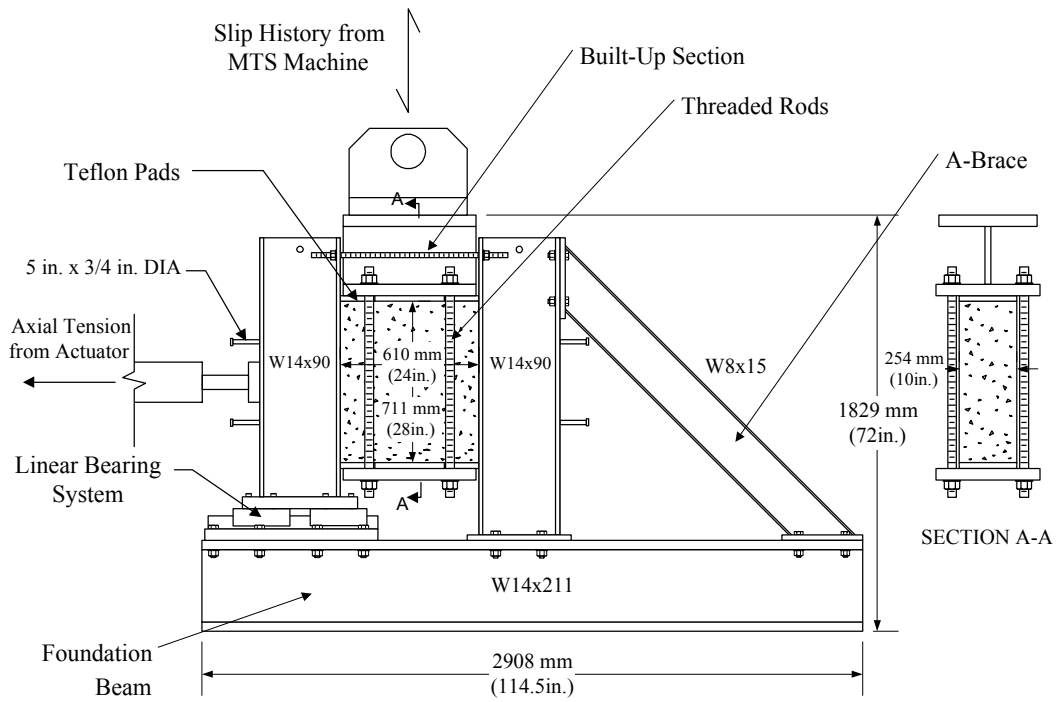


Figure 3.1 Elevation of the experimental test setup

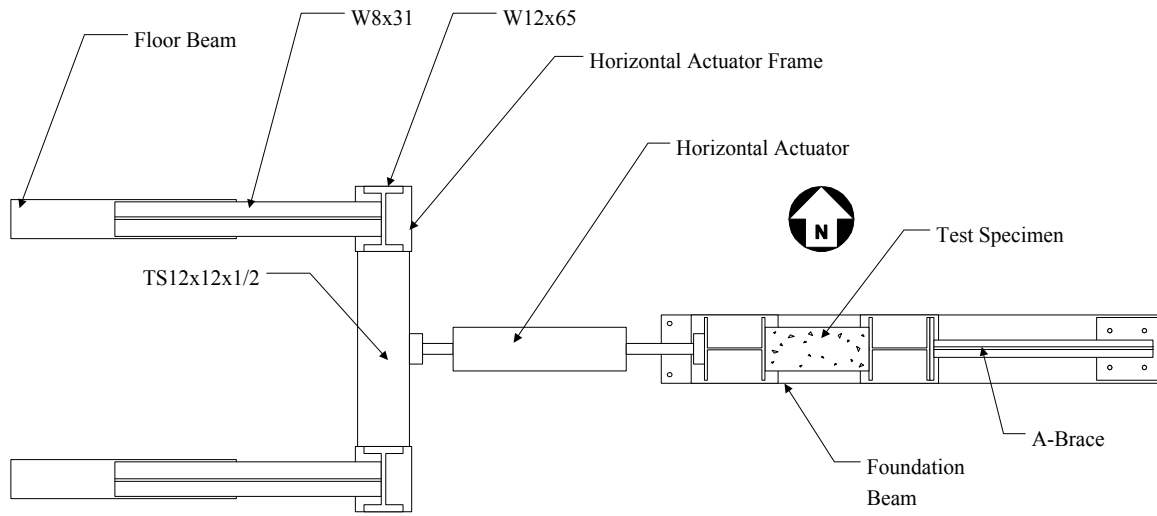


Figure 3.2 Plan view of the experimental test setup

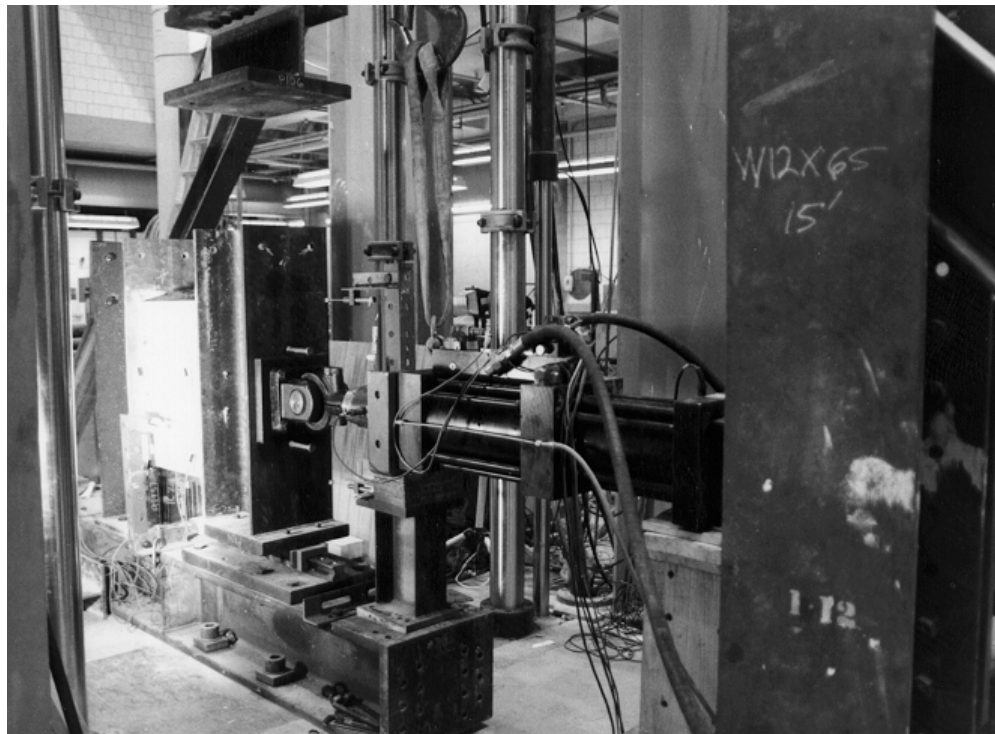


Figure 3.3 Photograph of the experimental test setup



Figure 3.6 Photograph of the “Perimeter Bar” steel reinforcement configuration

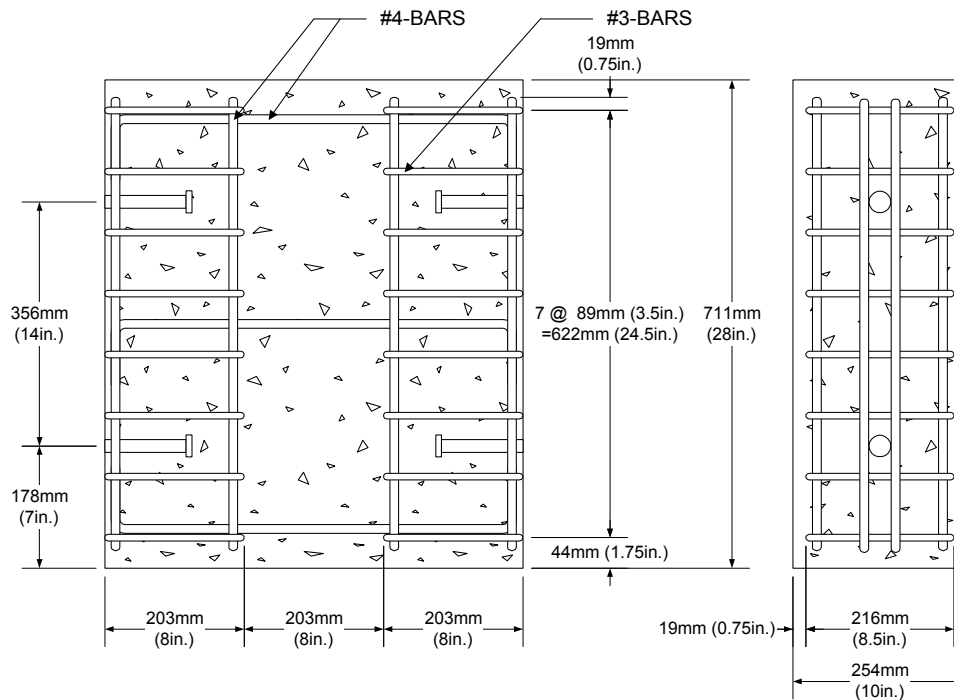


Figure 3.7 “Cage” steel reinforcement configuration

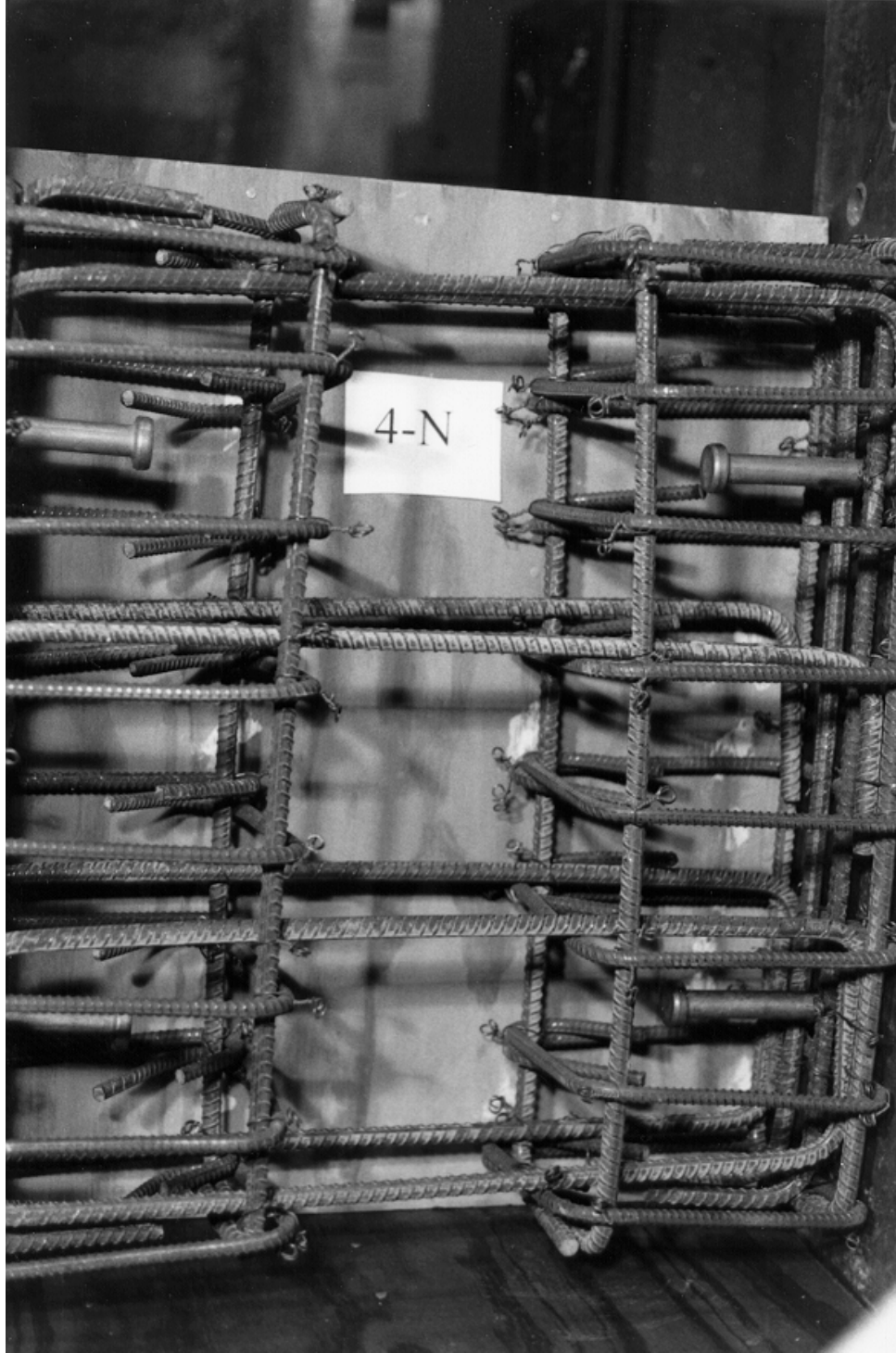


Figure 3.8 Photograph of the “Cage” steel reinforcement configuration

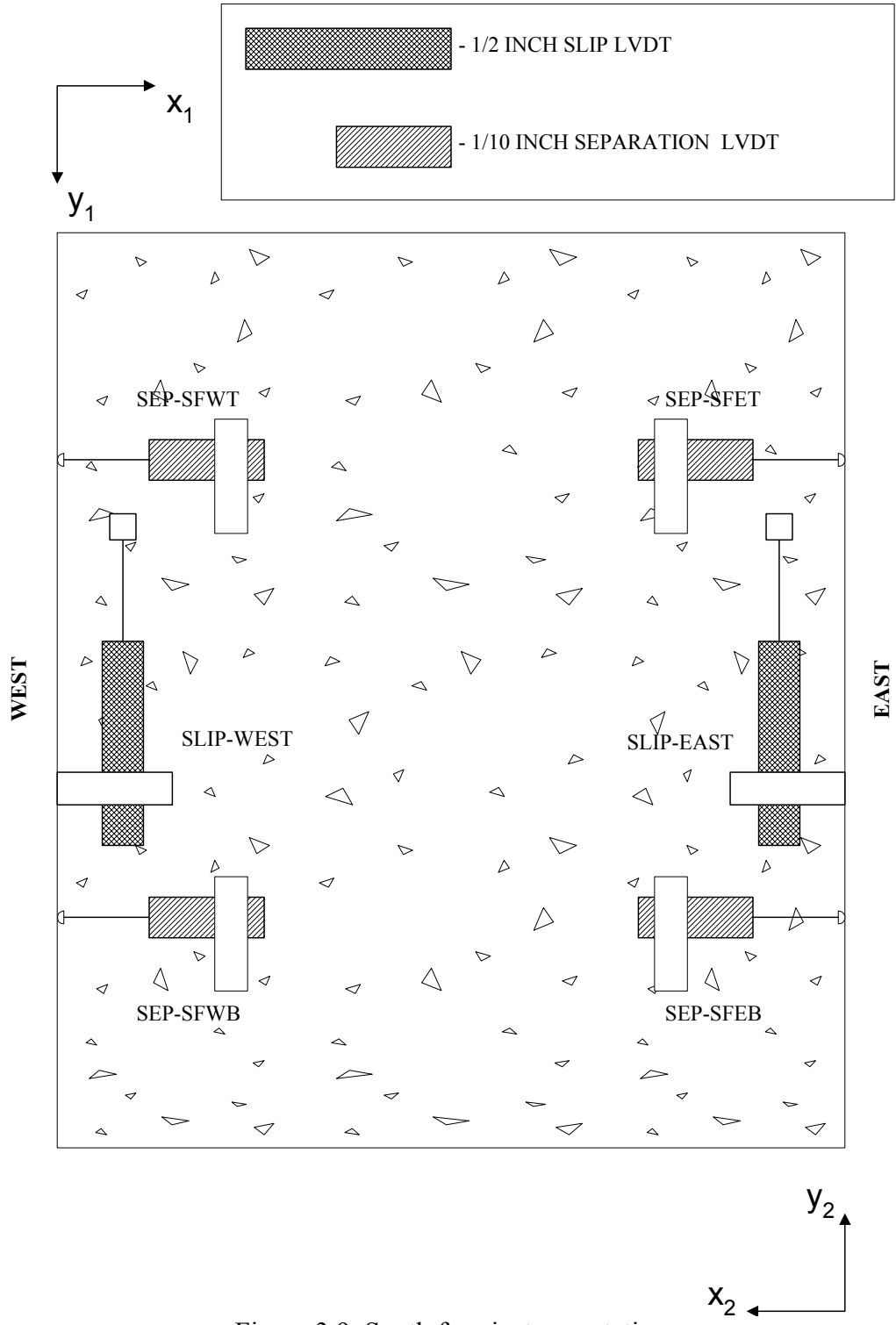


Figure 3.9 South face instrumentation

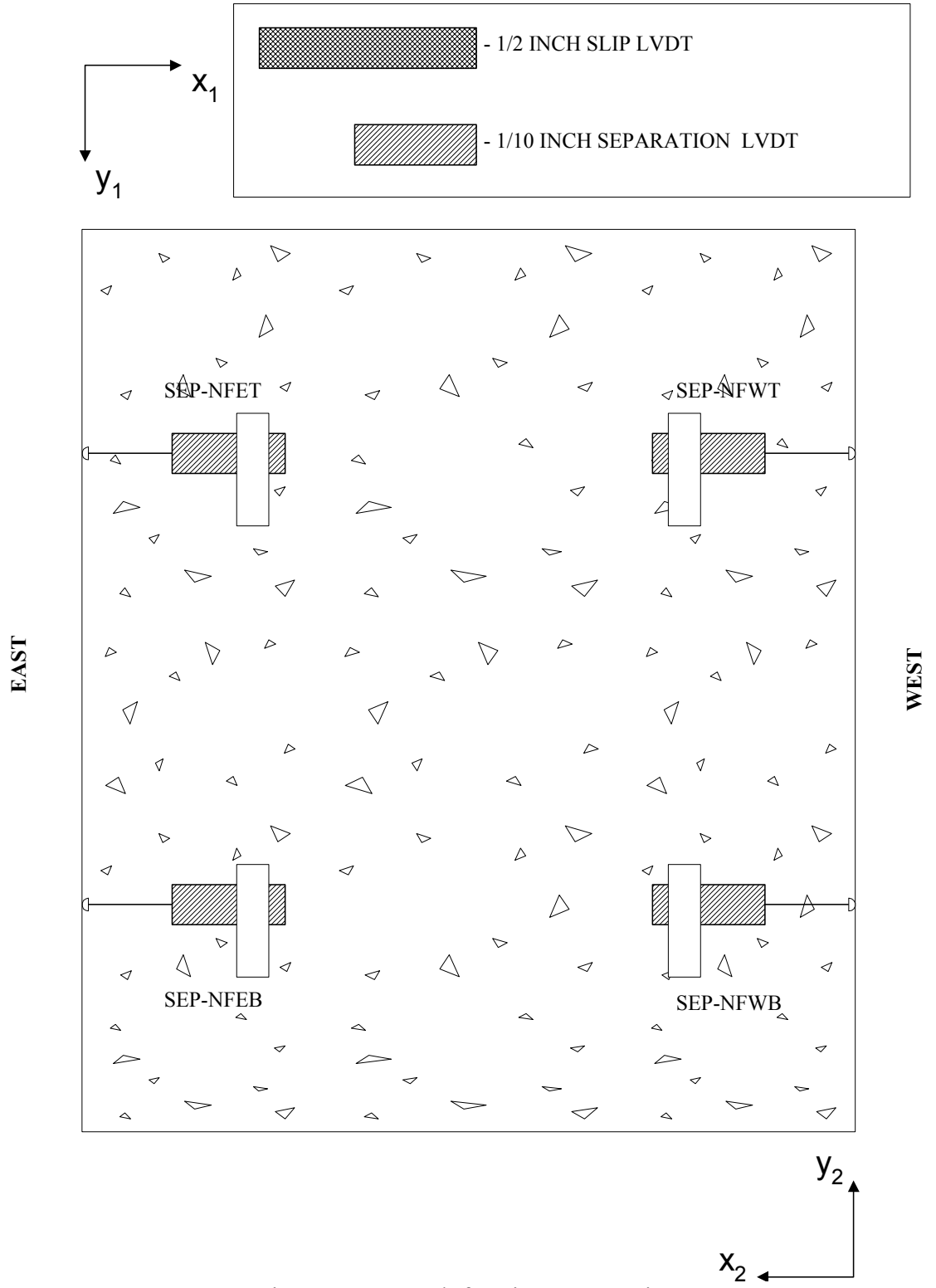


Figure 3.10 North face instrumentation

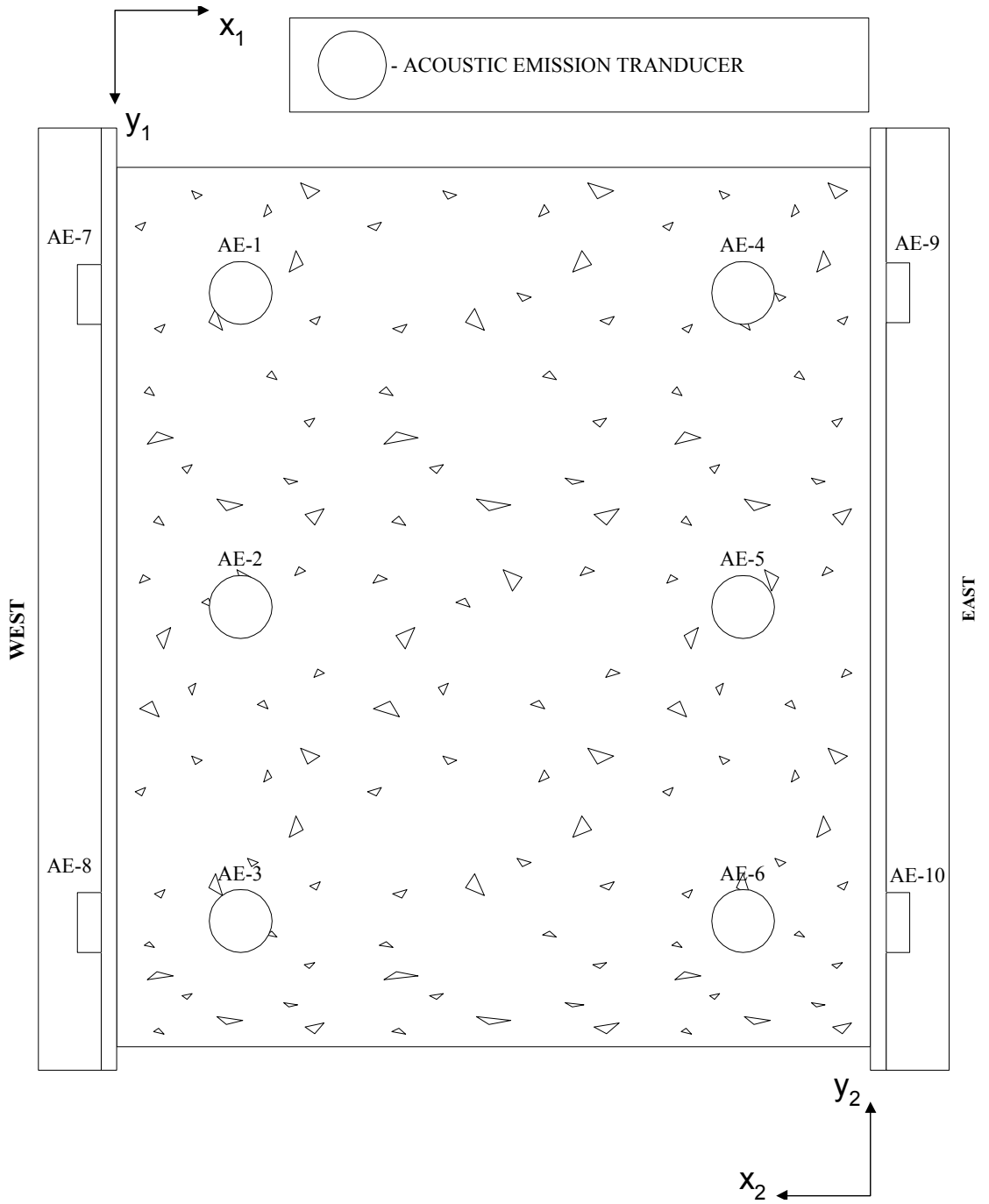


Figure 3.11 Acoustic emission instrumentation

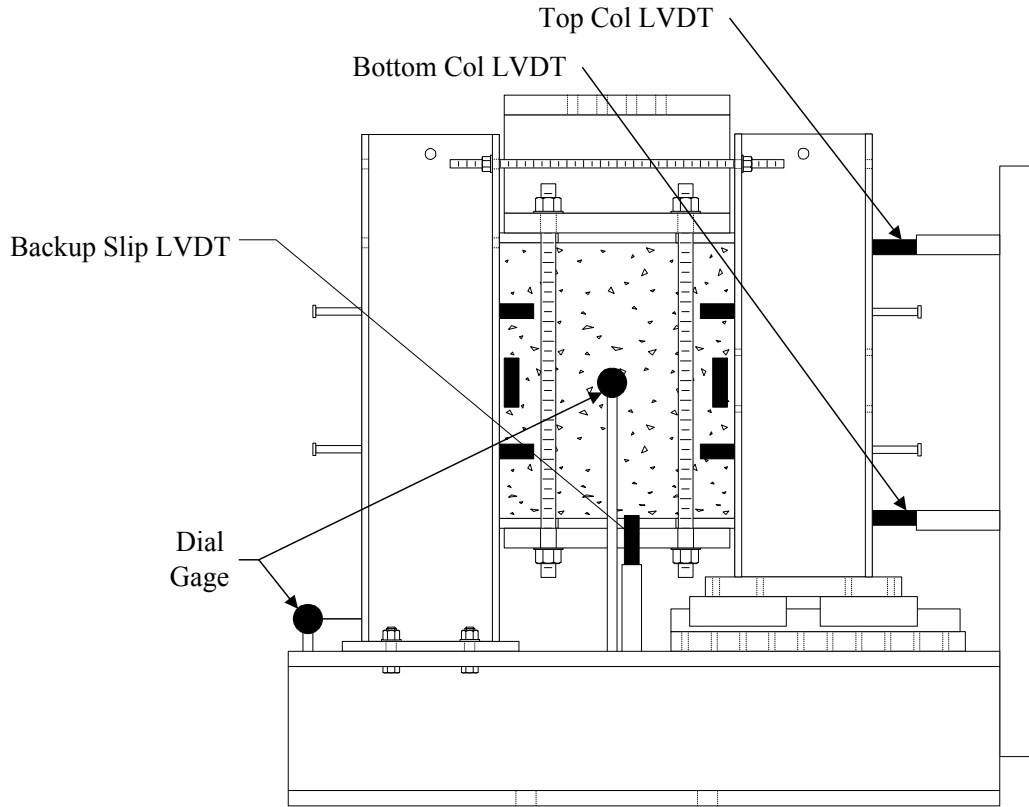


Figure 3.12 Other LVDT's and dial gages

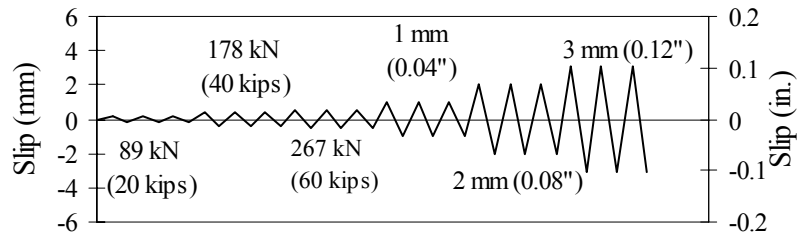


Figure 3.13 Cyclic slip history for Specimen 4

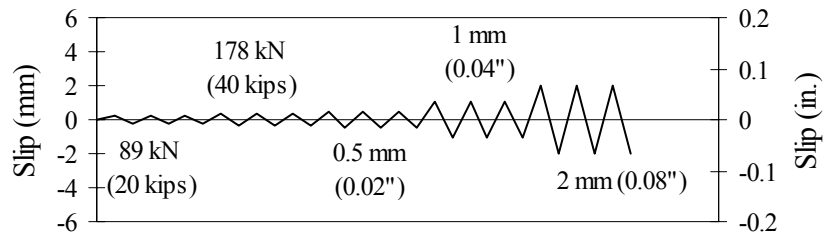


Figure 3.14 Cyclic slip history for Specimen 8

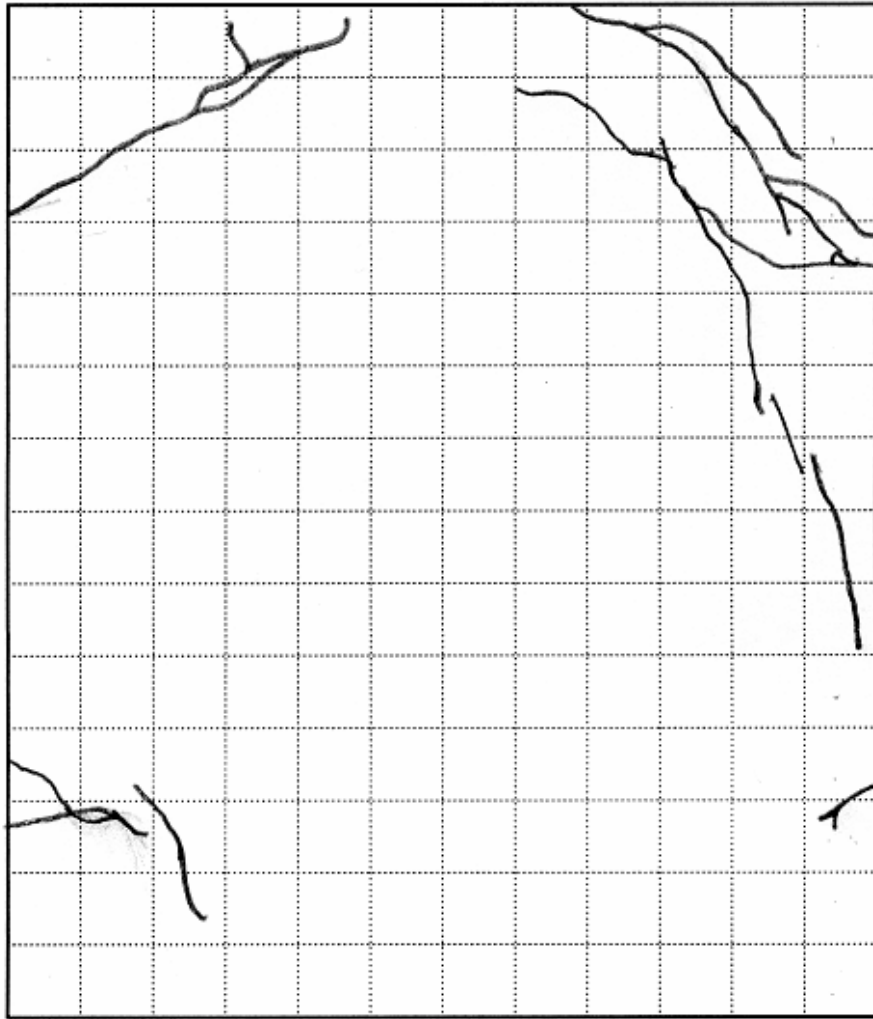


Figure 4.1 Crack Pattern for Specimen 1, north face

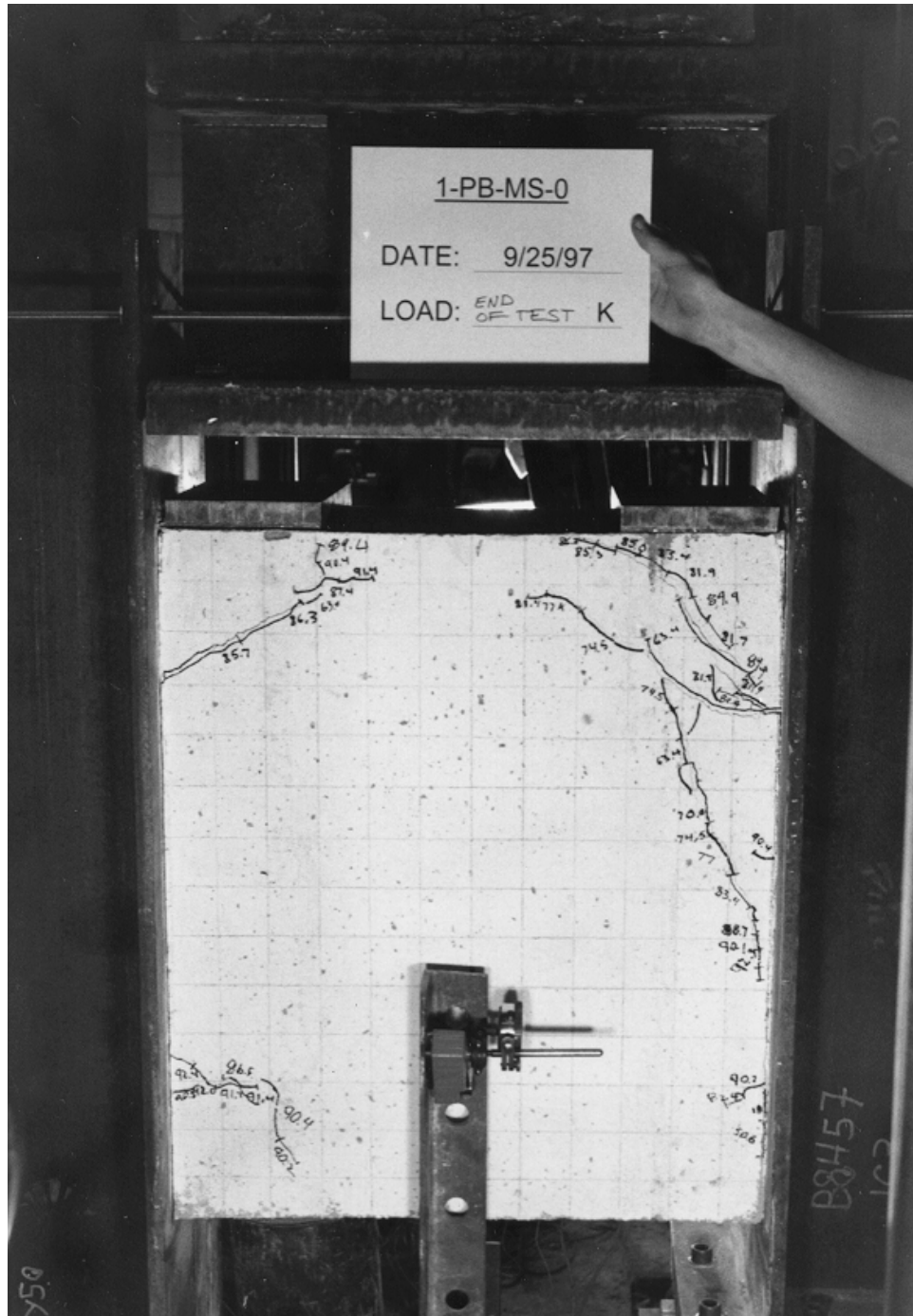


Figure 4.2 Photograph of Specimen 1, south face, after testing



Figure 4.3 Deformed stud for Specimen 1

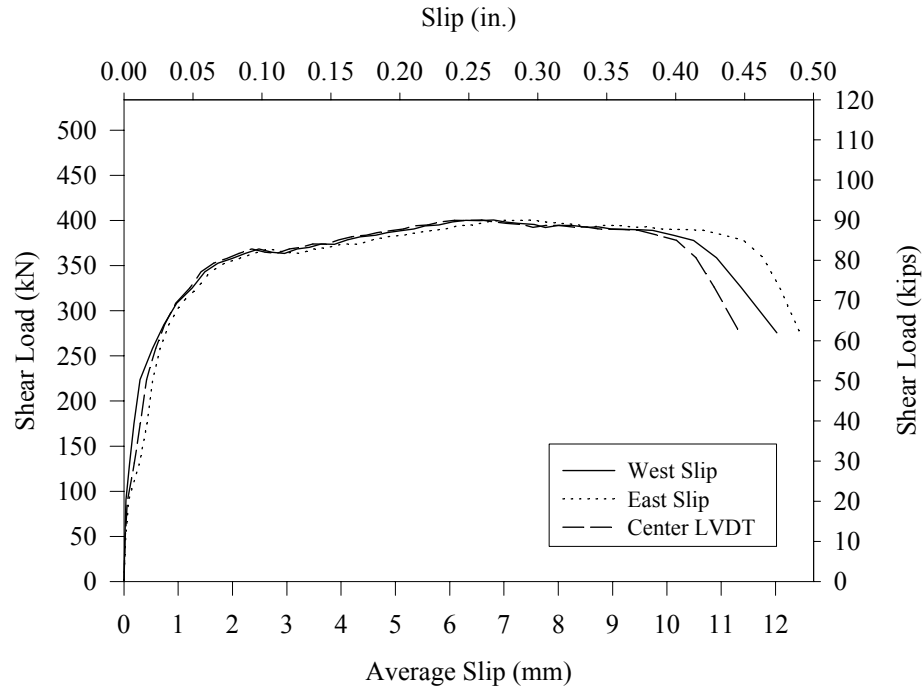


Figure 4.4 Load versus slip for Specimen 1

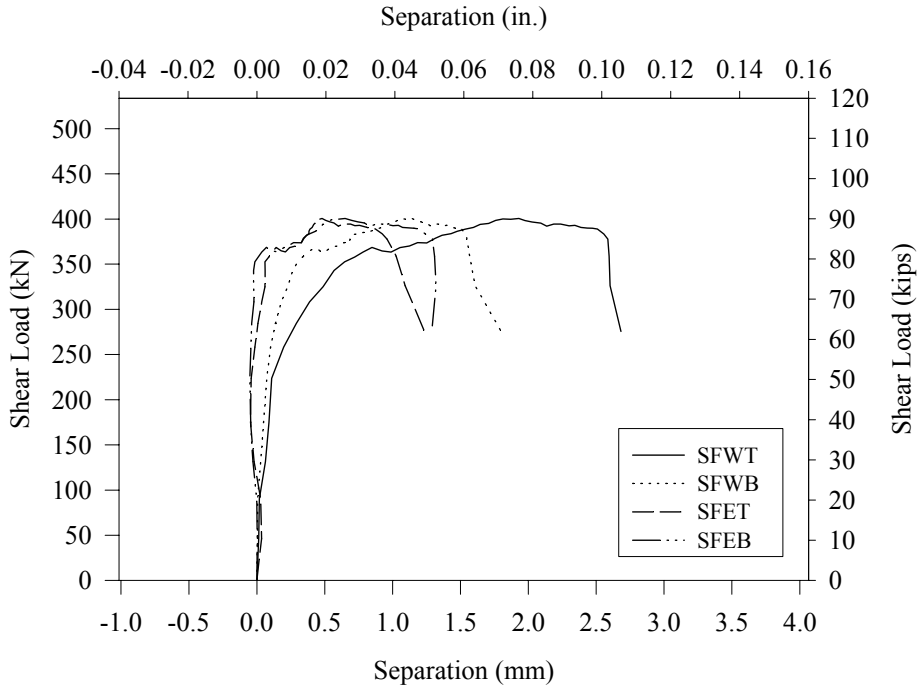


Figure 4.5 Load versus separation for Specimen 1

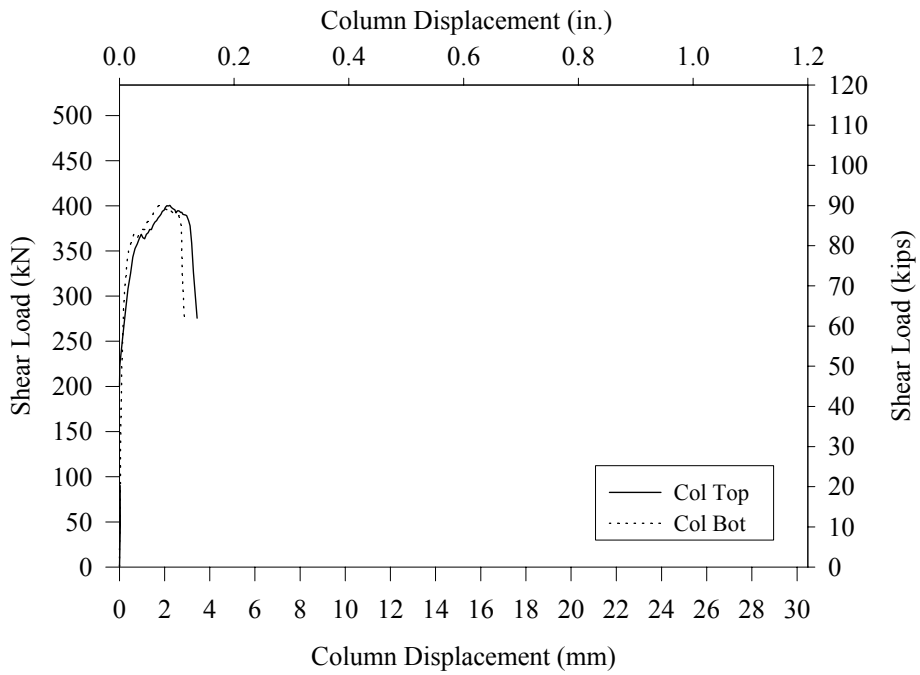


Figure 4.6 Load versus column displacement for Specimen 1

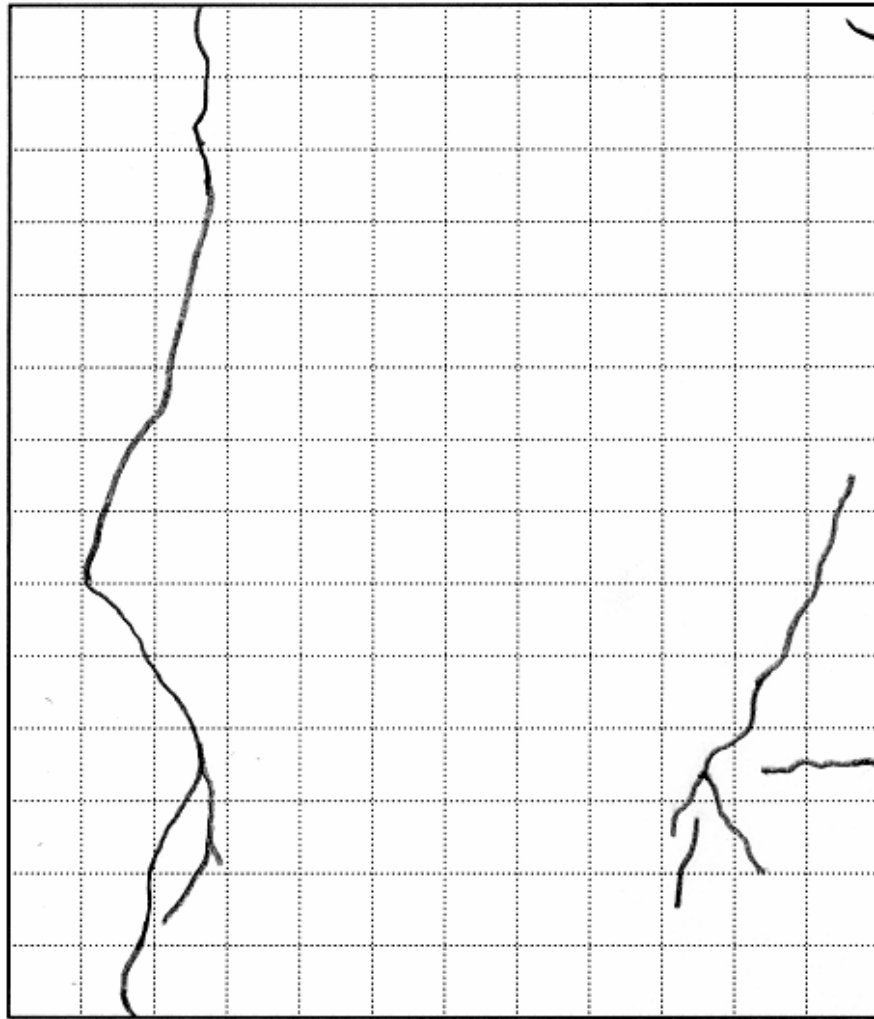


Figure 4.7 Crack pattern for Specimen 2, south face



Figure 4.8 Photo of Specimen 2, north face, after testing

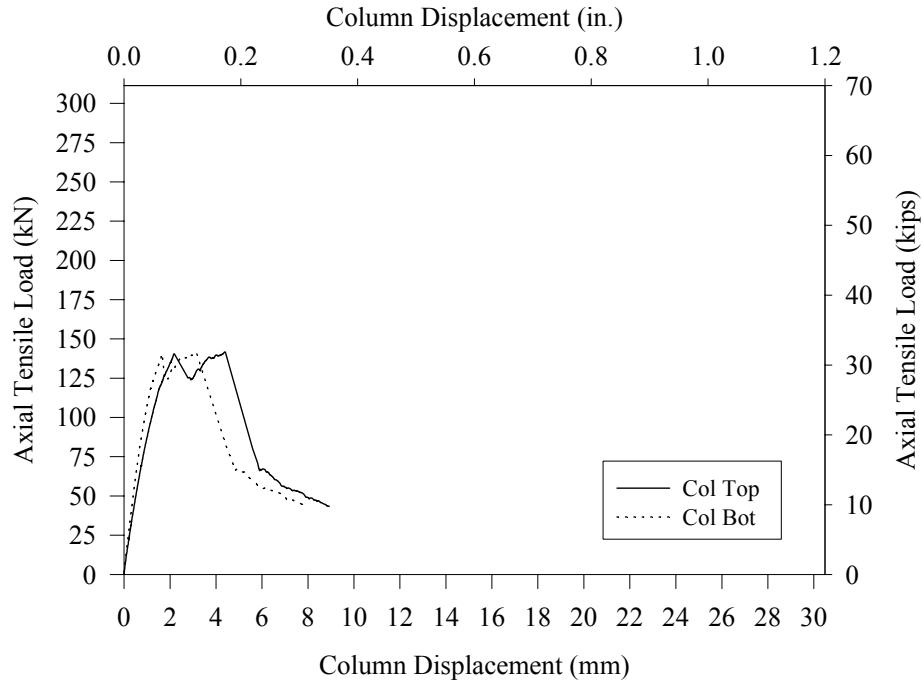


Figure 4.9 Load versus column displacement for Specimen 2

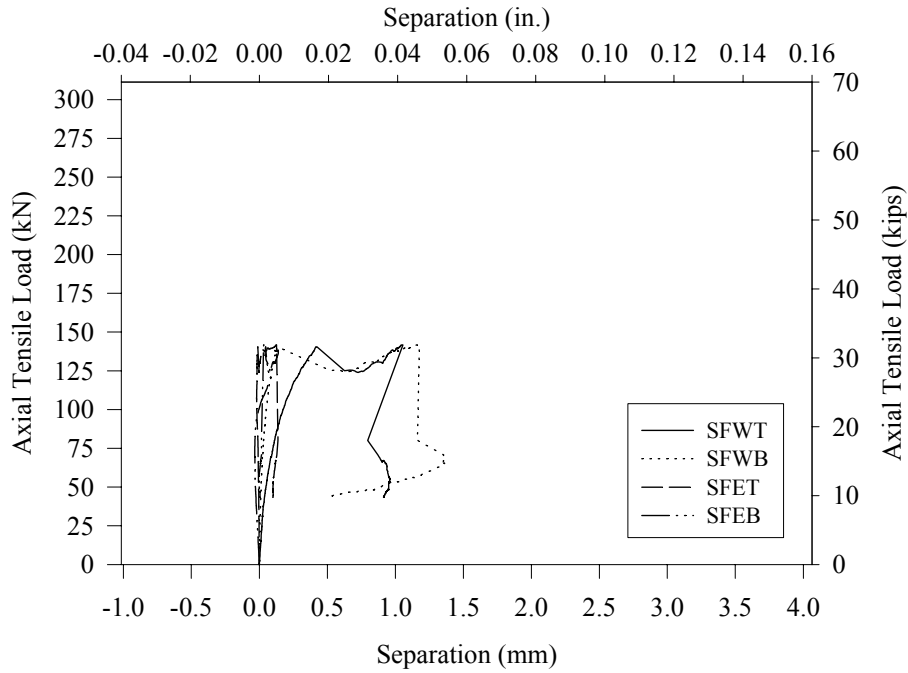


Figure 4.10 Load versus separation for south face LVDT's for Specimen 2

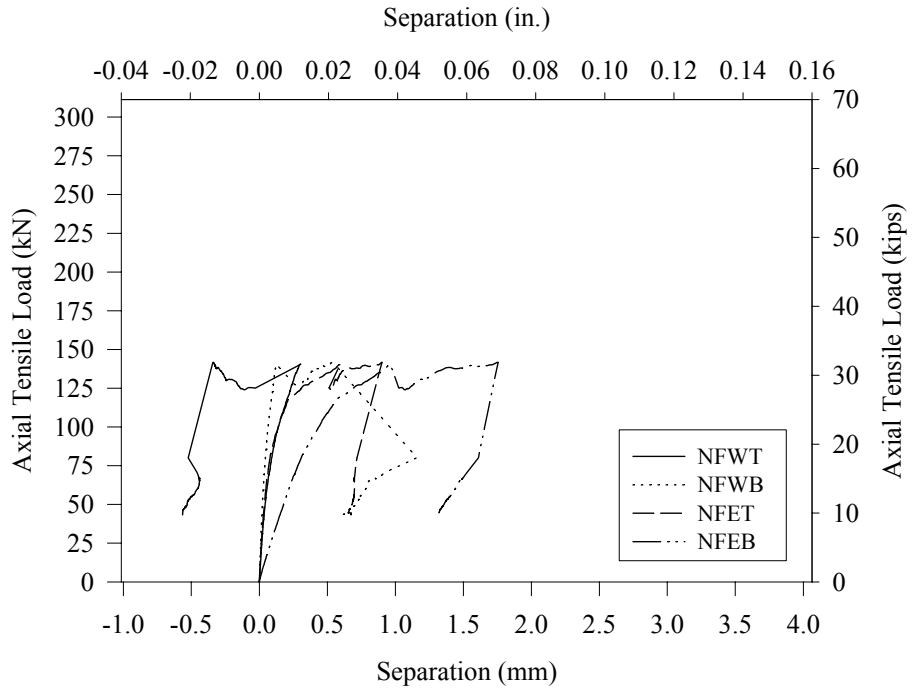


Figure 4.11 Load versus separation for north face LVDT's for Specimen 2

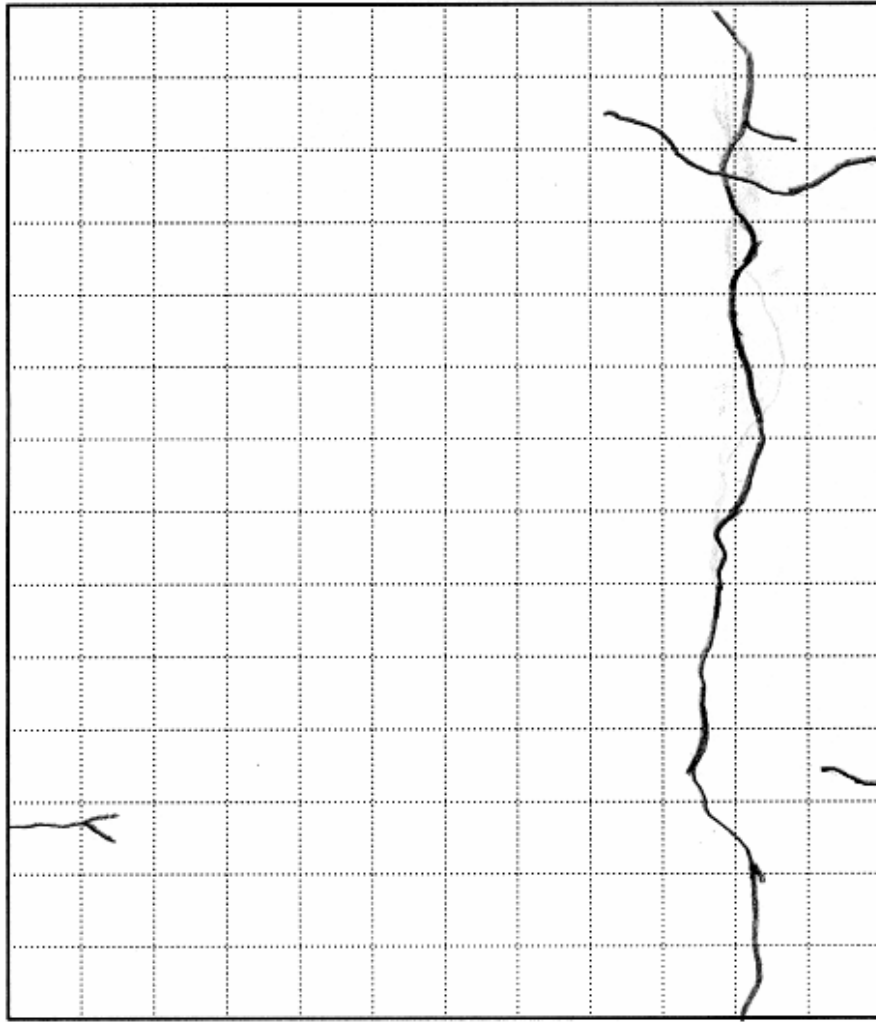


Figure 4.12 Crack pattern for Specimen 3, north face



Figure 4.13 Photograph of Specimen 3, north face, after testing

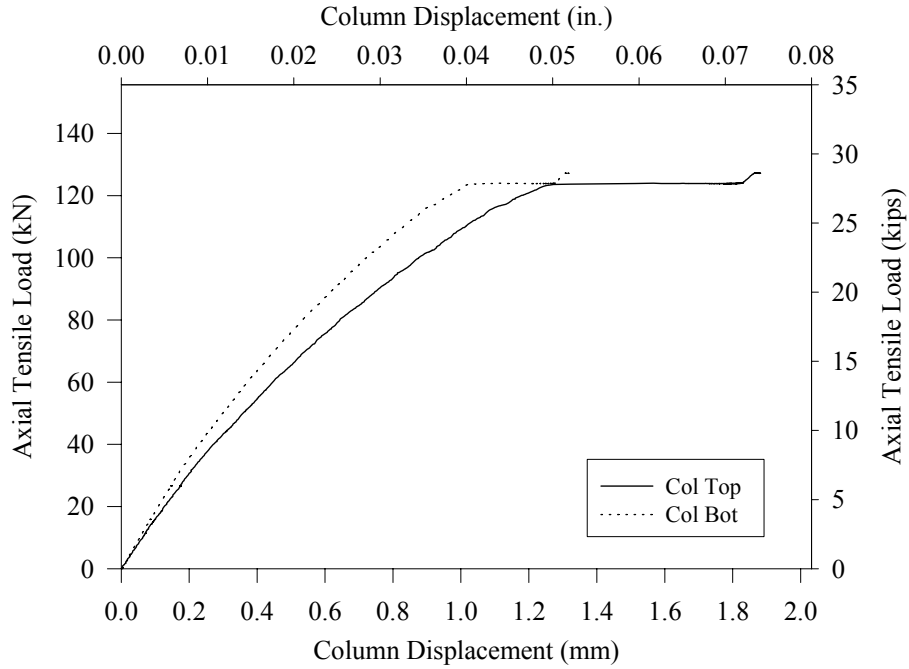


Figure 4.14 Load versus column displacement during tensile loading for Specimen 3

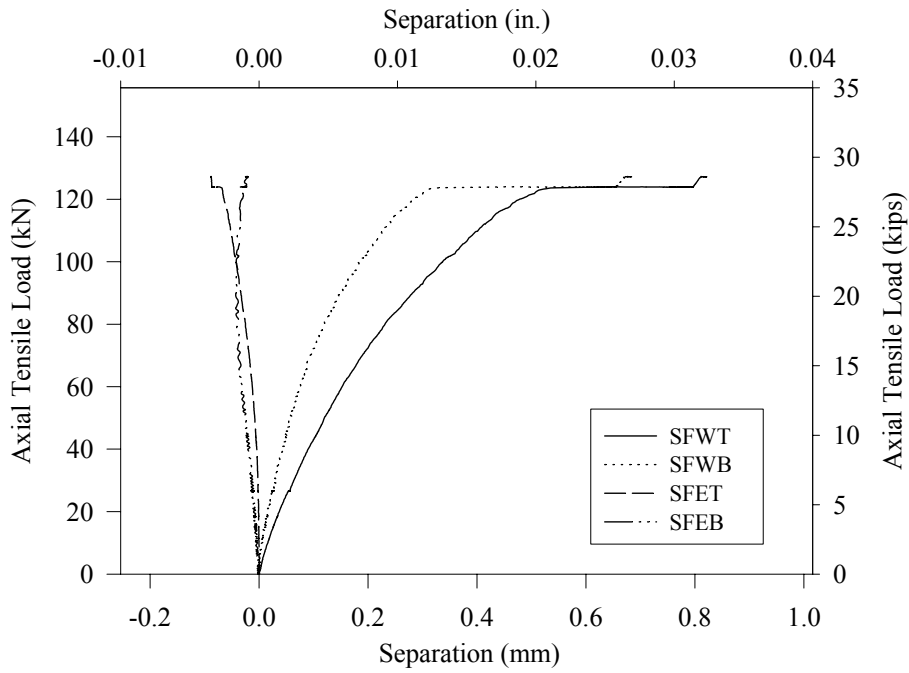


Figure 4.15 Load versus separation for south face LVDT's during tensile loading for Specimen 3

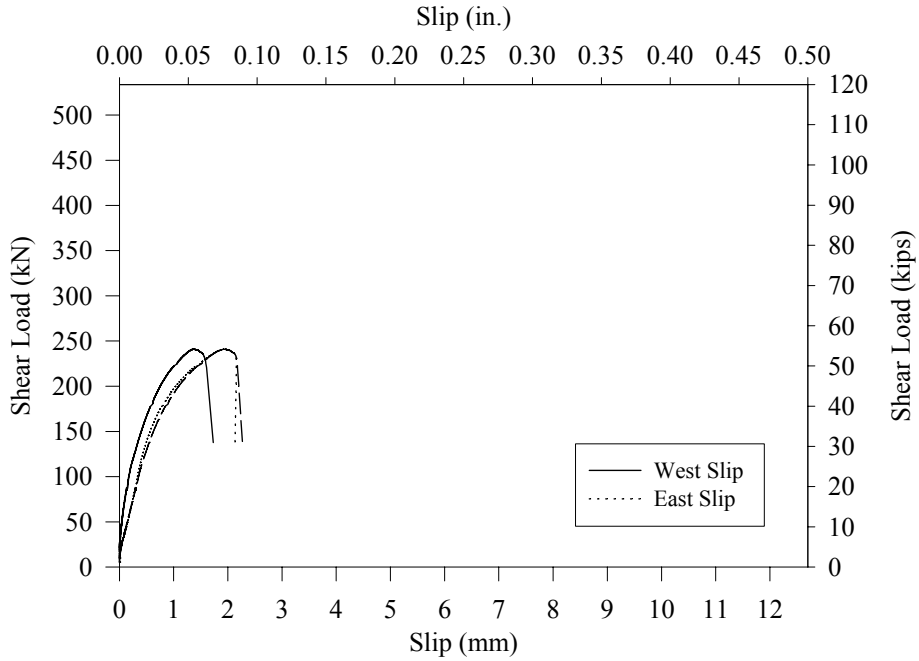


Figure 4.16 Load versus slip during shear loading for Specimen 3

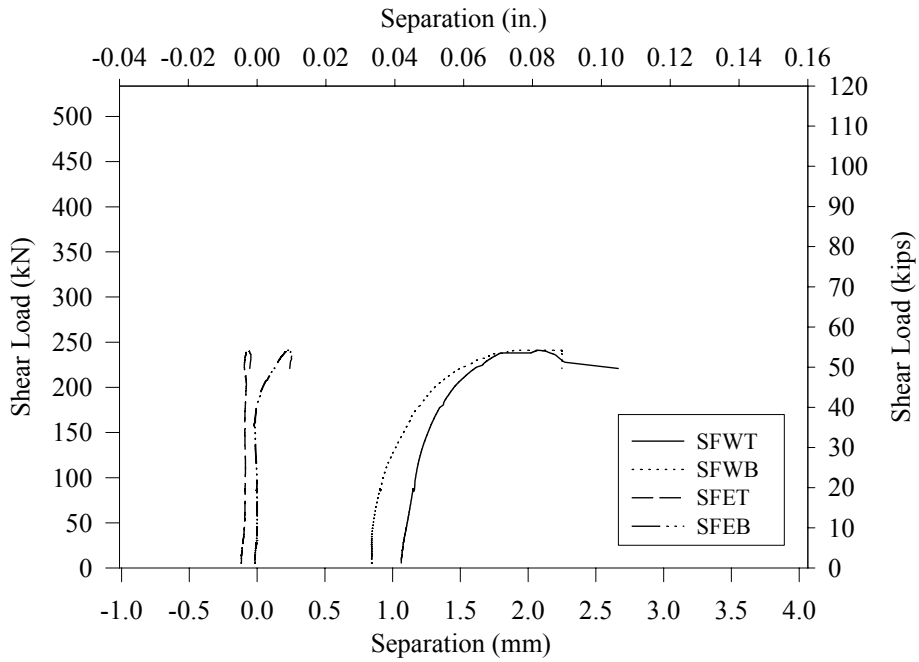


Figure 4.17 Load versus separation for south face LVDT's during shear loading for Specimen 3

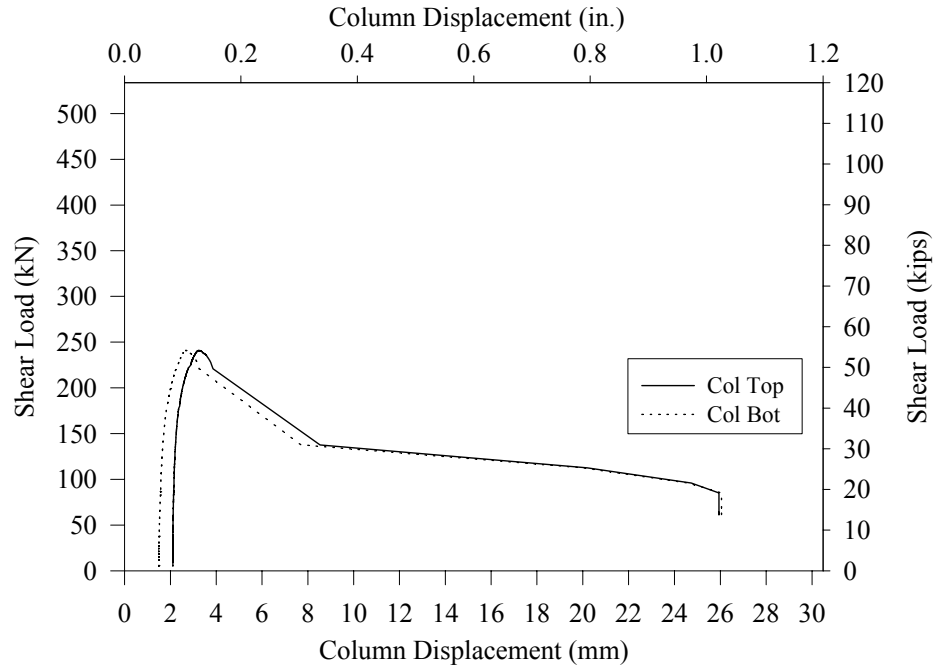


Figure 4.18 Load versus column displacement during shear loading for Specimen 3

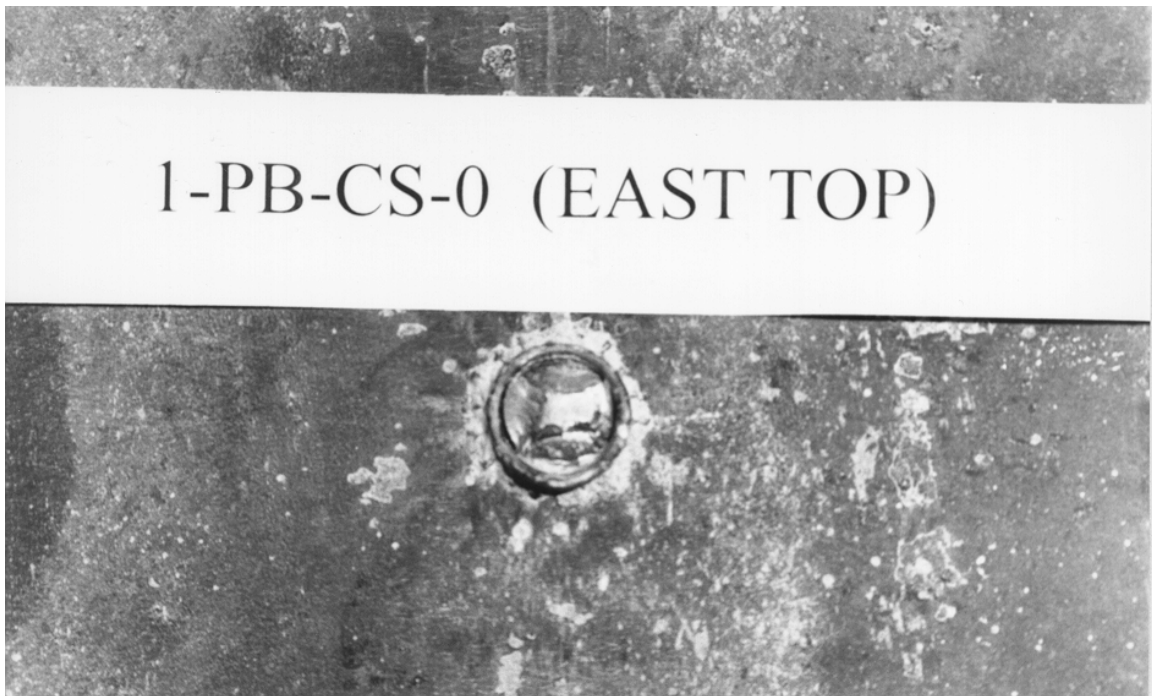


Figure 4.19 Photograph of stud failure surface for Specimen 4

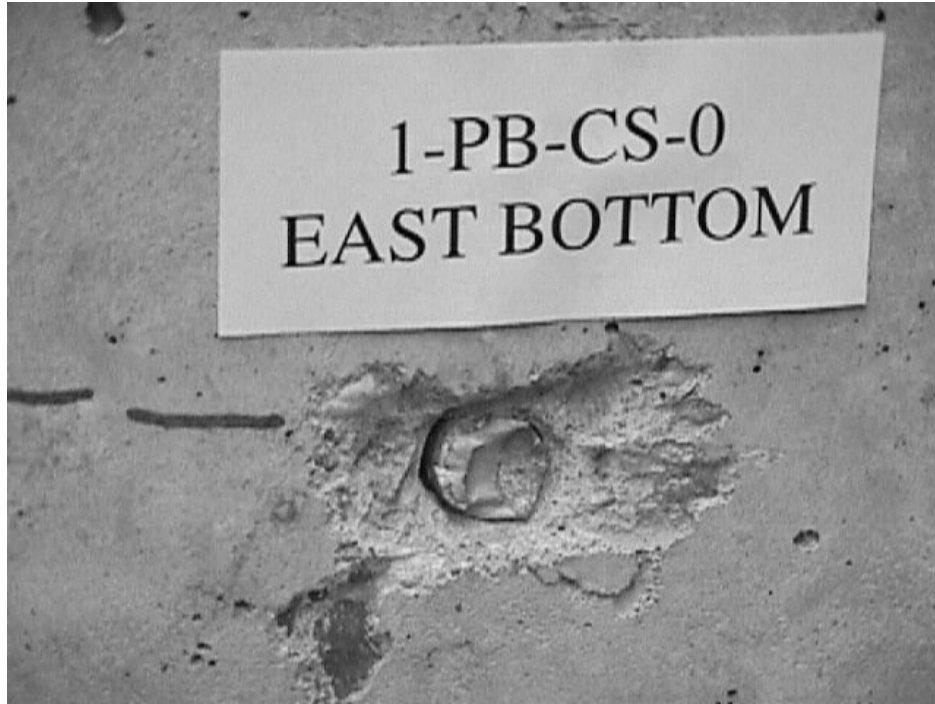


Figure 4.20 Concrete void created by crushing for Specimen 4

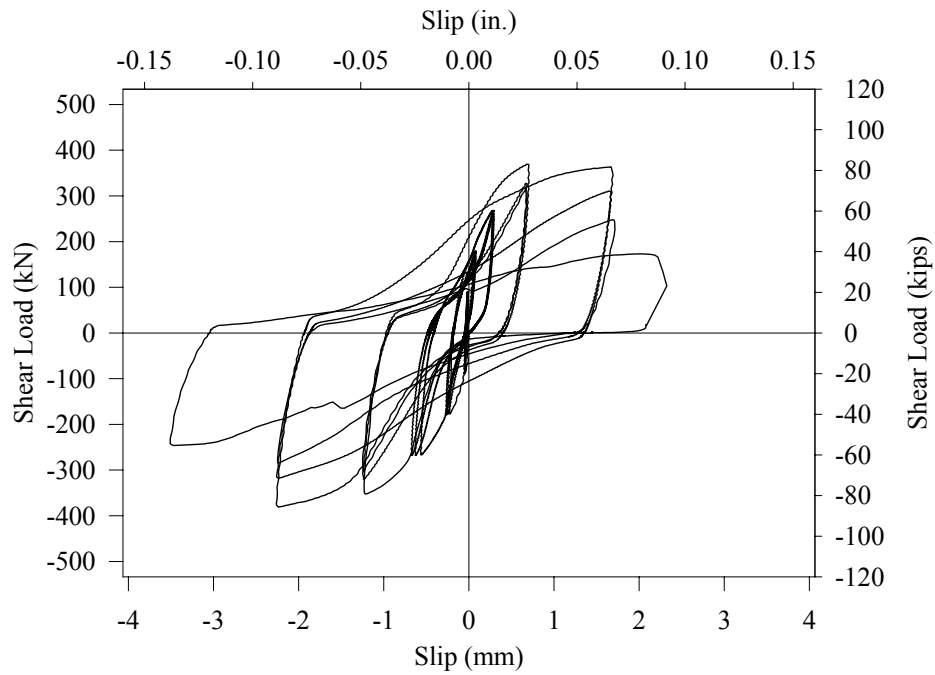


Figure 4.21 Load versus west slip for Specimen 4

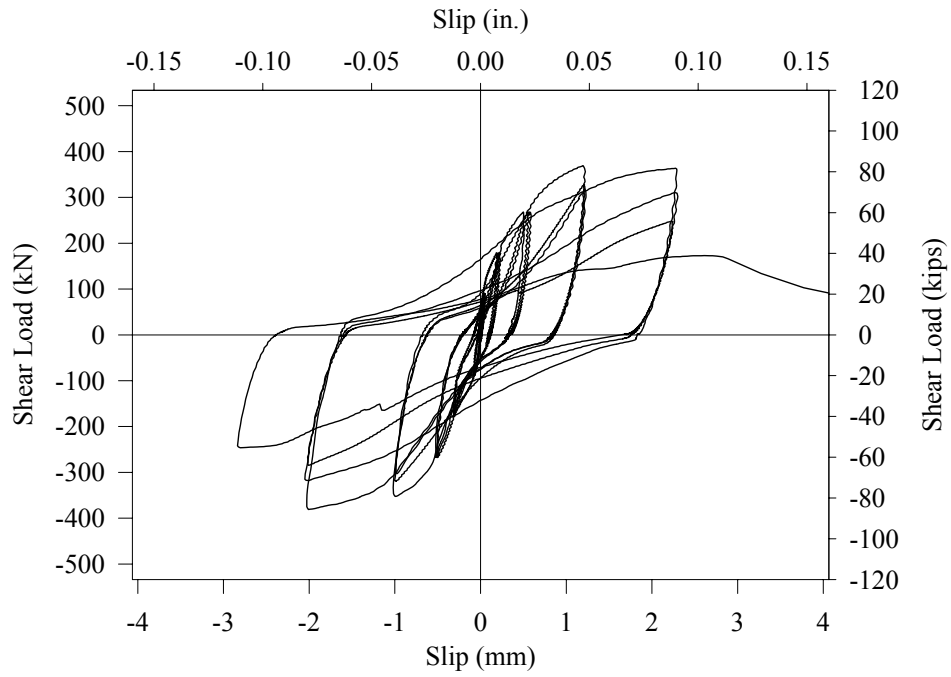


Figure 4.22 Load versus east slip for Specimen 4

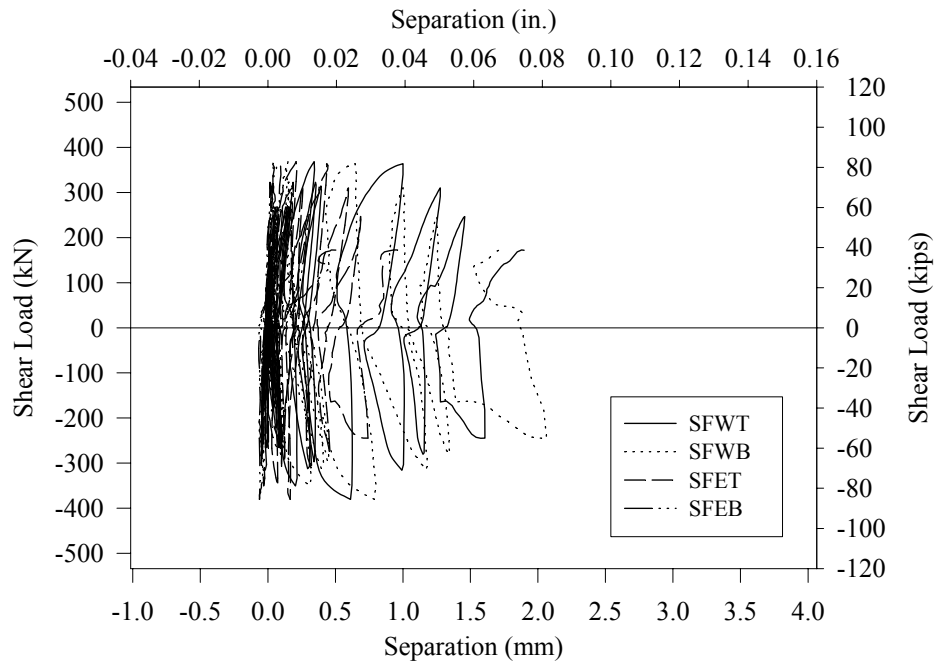


Figure 4.23 Load versus separation for south face LVDT's for Specimen 4

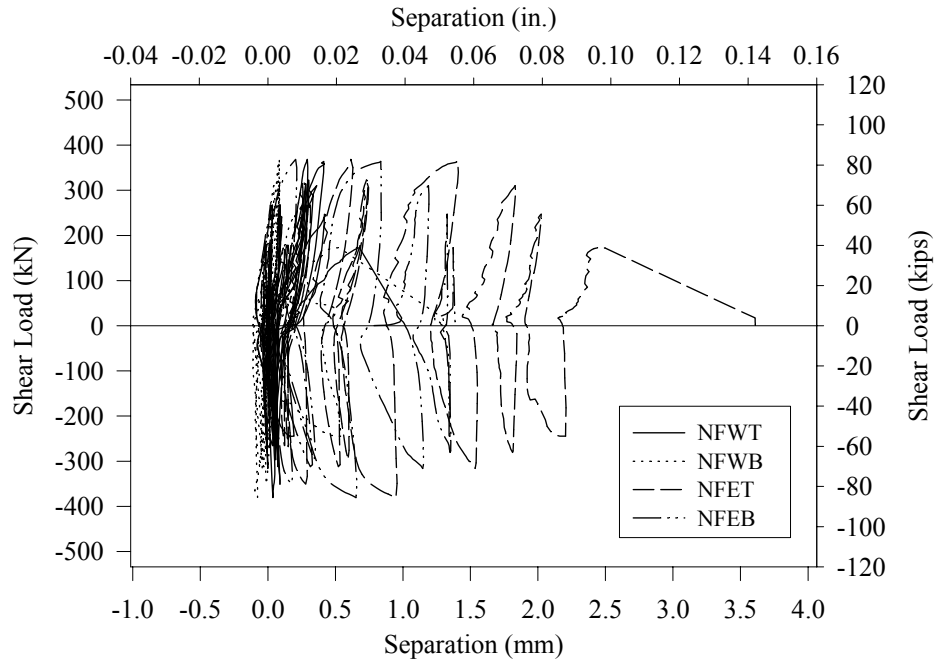


Figure 4.24 Load versus separation for north face LVDT's for Specimen 4

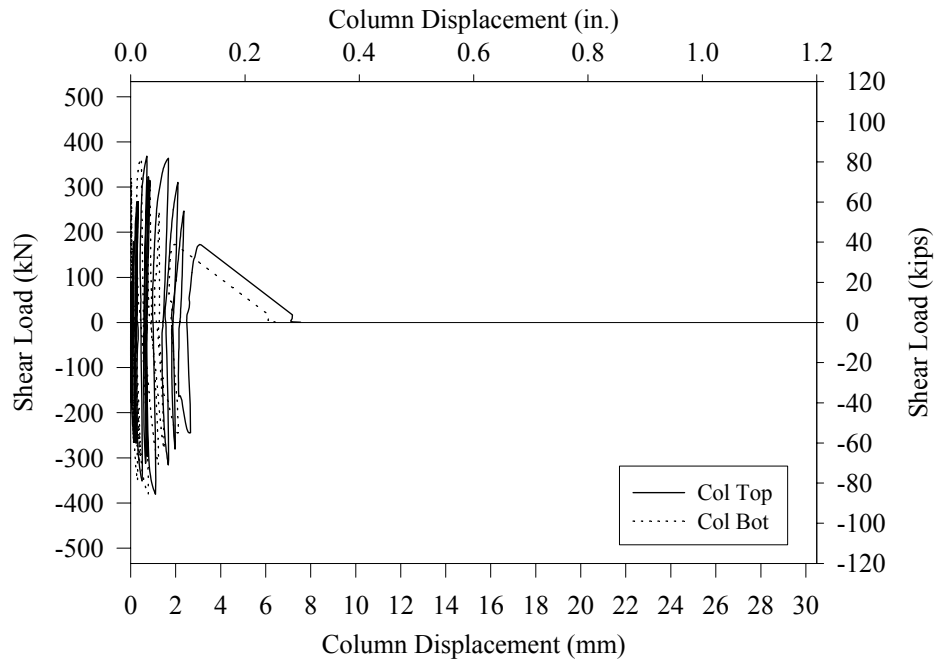


Figure 4.25 Load versus column displacement for Specimen 4

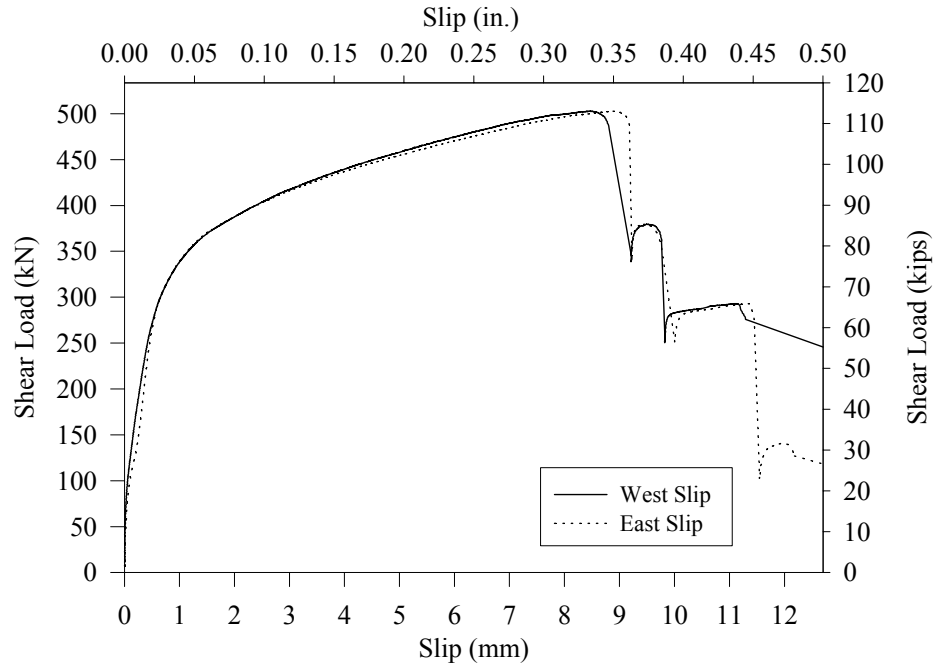


Figure 4.26 Load versus slip for Specimen 5

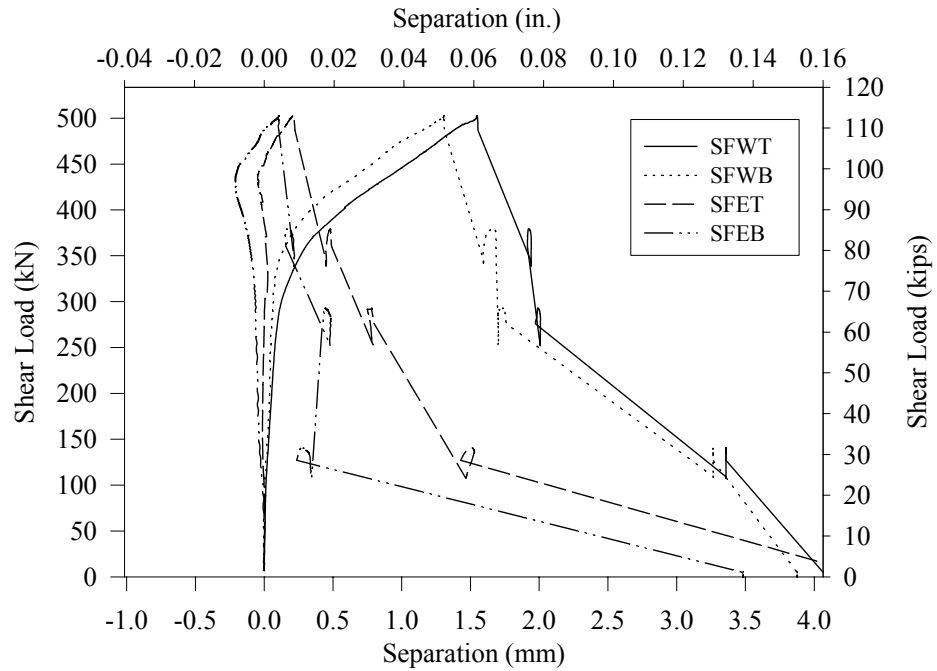


Figure 4.27 Load versus separation for SF LVDT's for Specimen 5

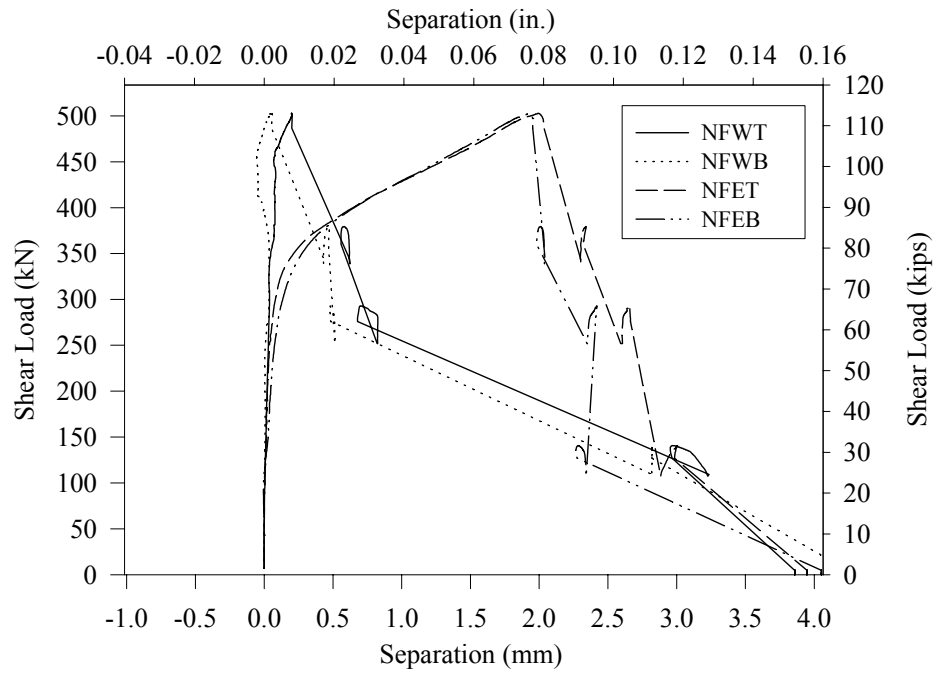


Figure 4.28 Load versus separation for NF LVDT's for Specimen 5

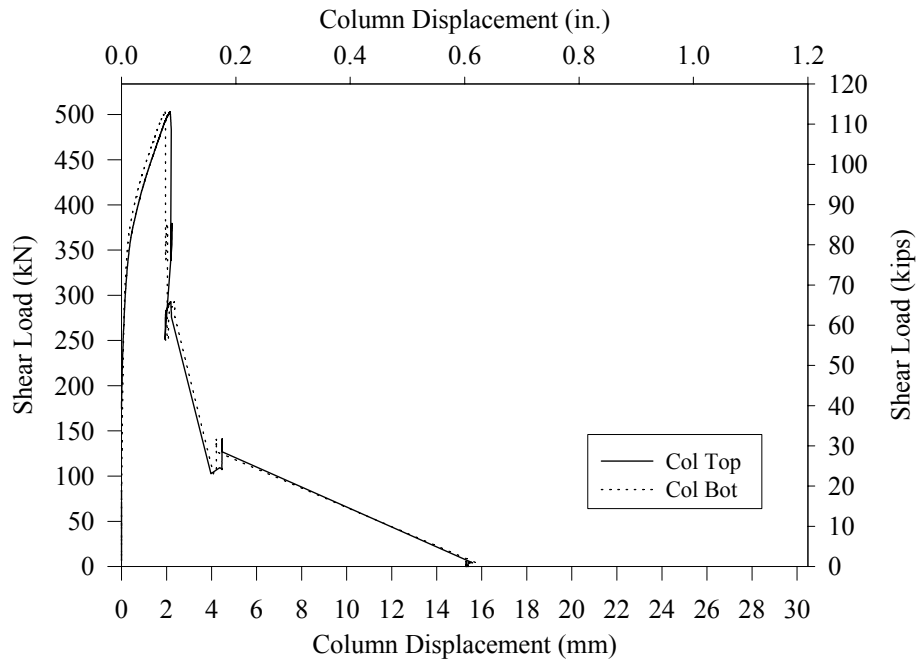


Figure 4.29 Load versus column displacement for Specimen 5

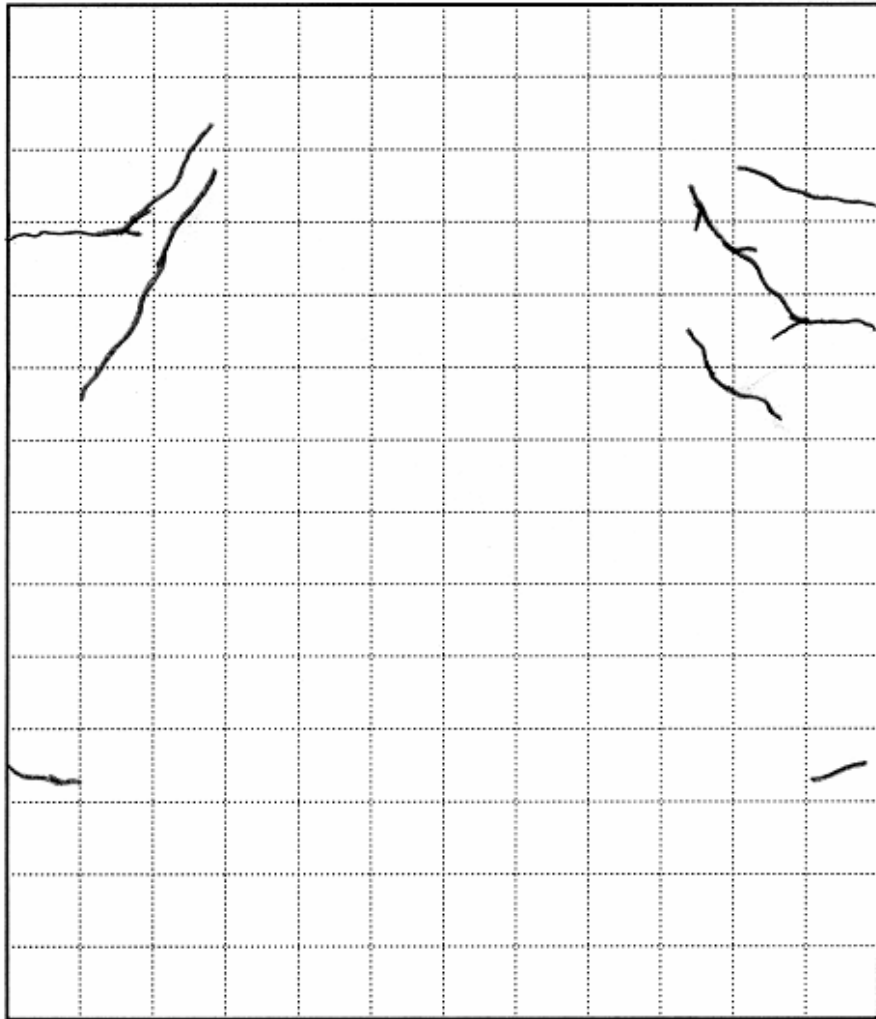


Figure 4.30 Crack Pattern for Specimen 6, north face



Figure 4.31 Photograph of stud failure surface for Specimen 6

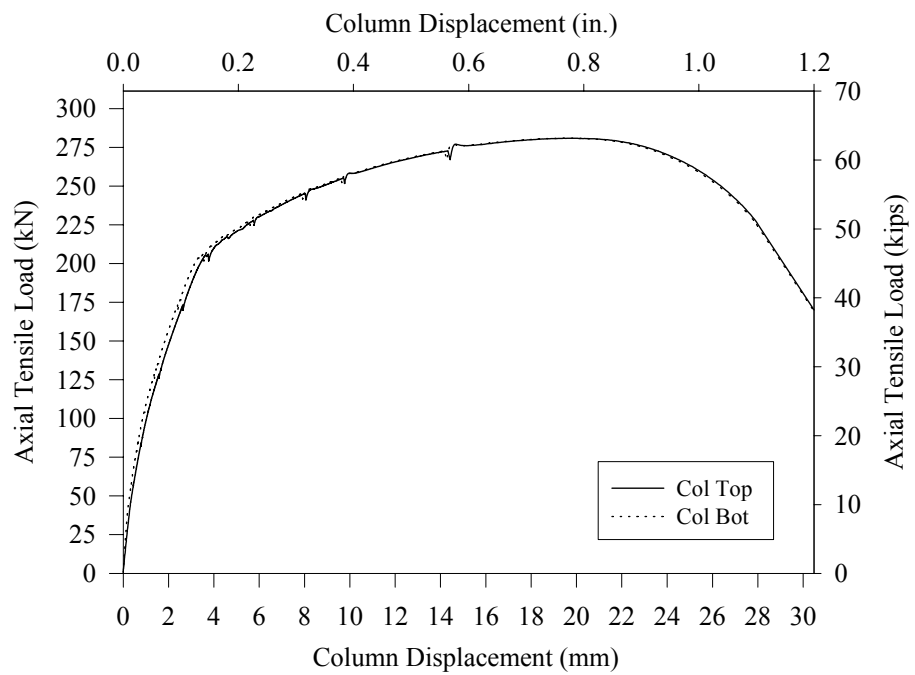


Figure 4.32 Load versus column displacement for Specimen 6

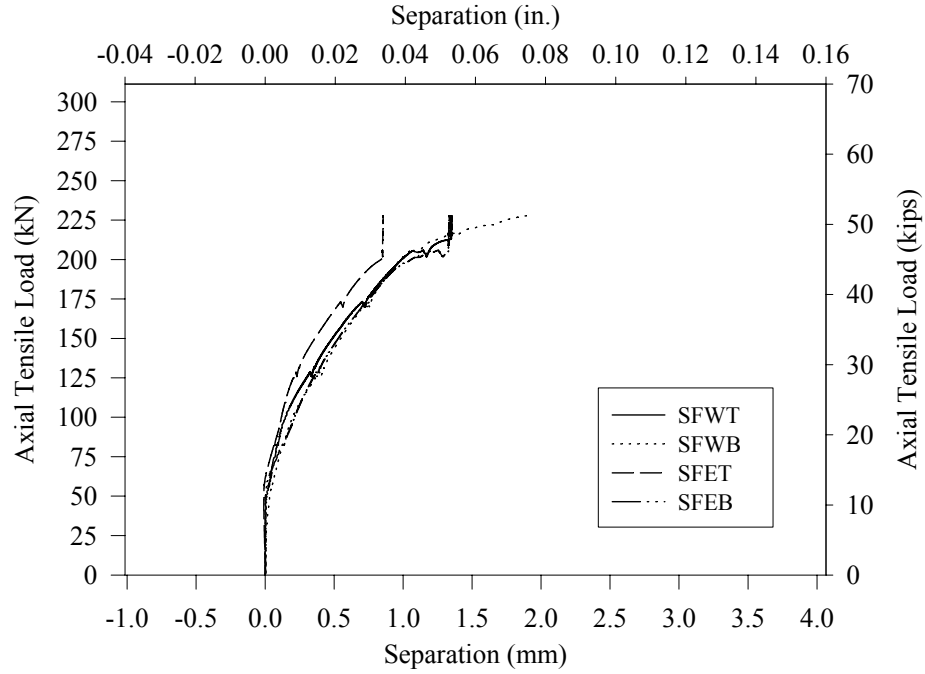


Figure 4.33 Load versus separation for south face LVDT's for Specimen 6

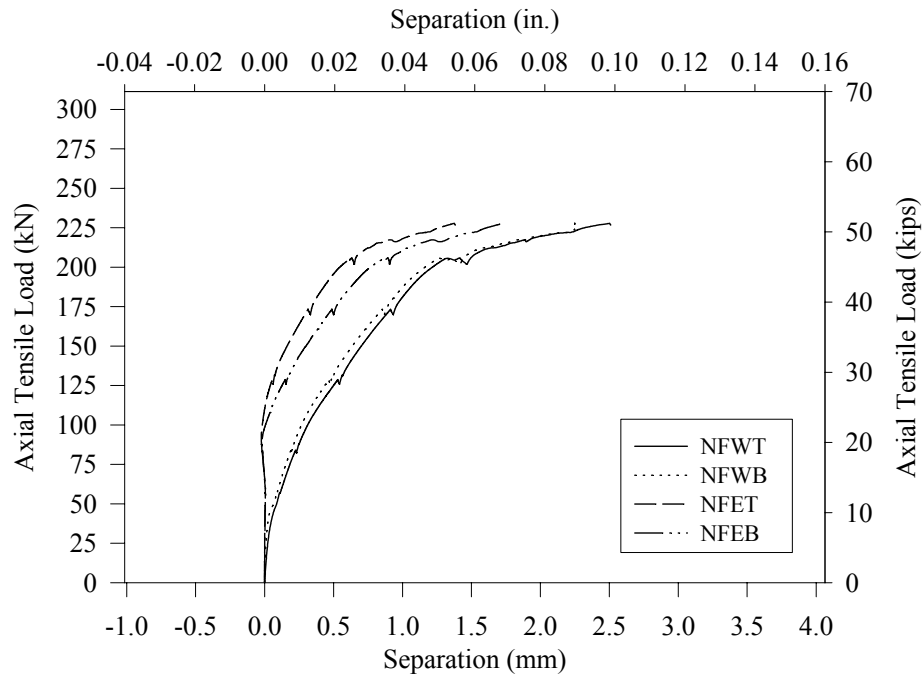


Figure 4.34 Load versus separation for north face LVDT's for Specimen 6

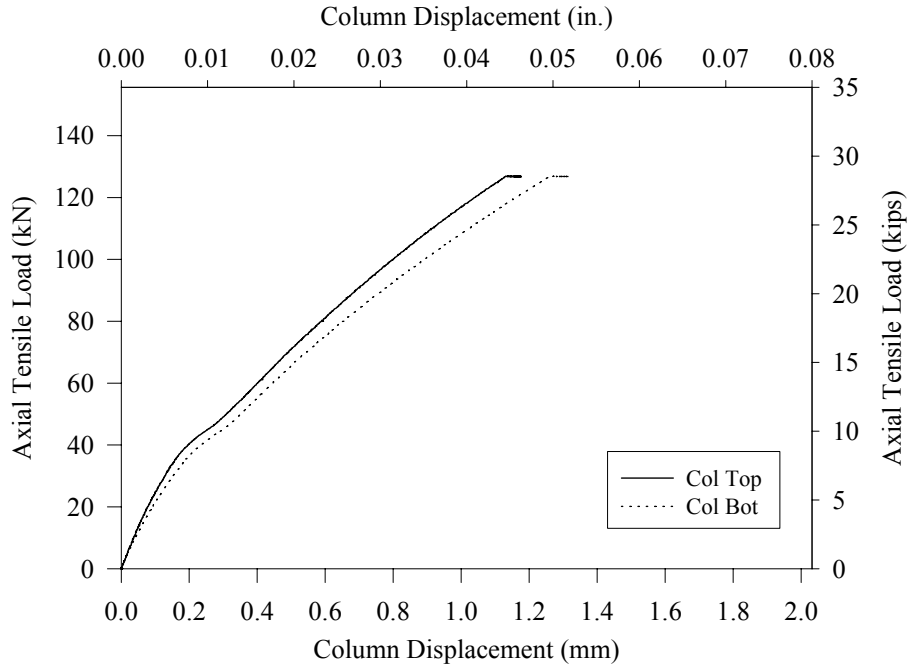


Figure 4.35 Load versus column displacement during tensile loading for Specimen 7

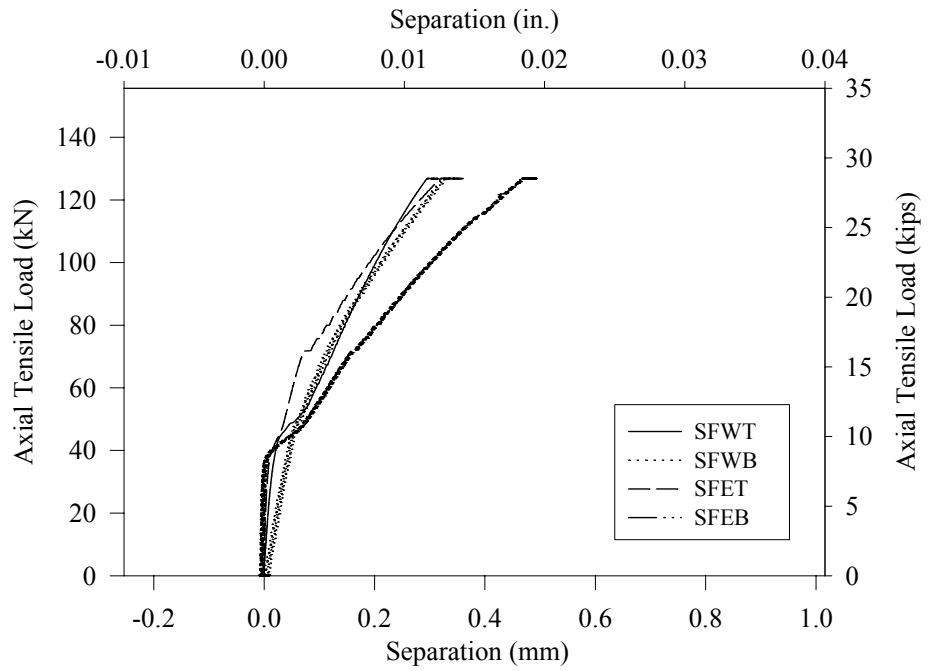


Figure 4.36 Load versus separation for south face LVDT's during tensile loading for Specimen 7

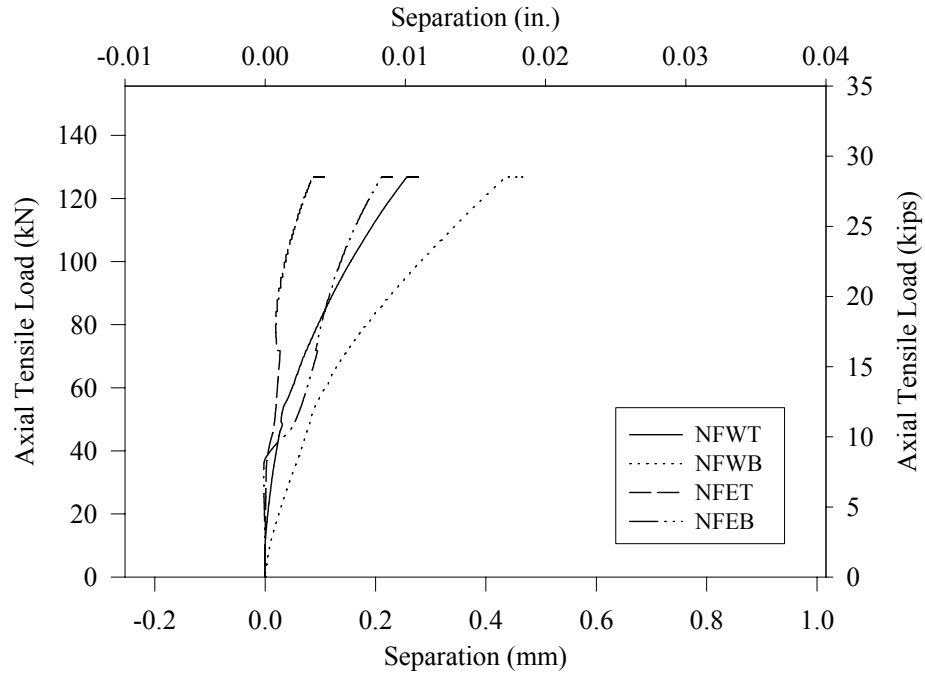


Figure 4.37 Load versus separation for north face LVDT's during tensile loading for Specimen 7

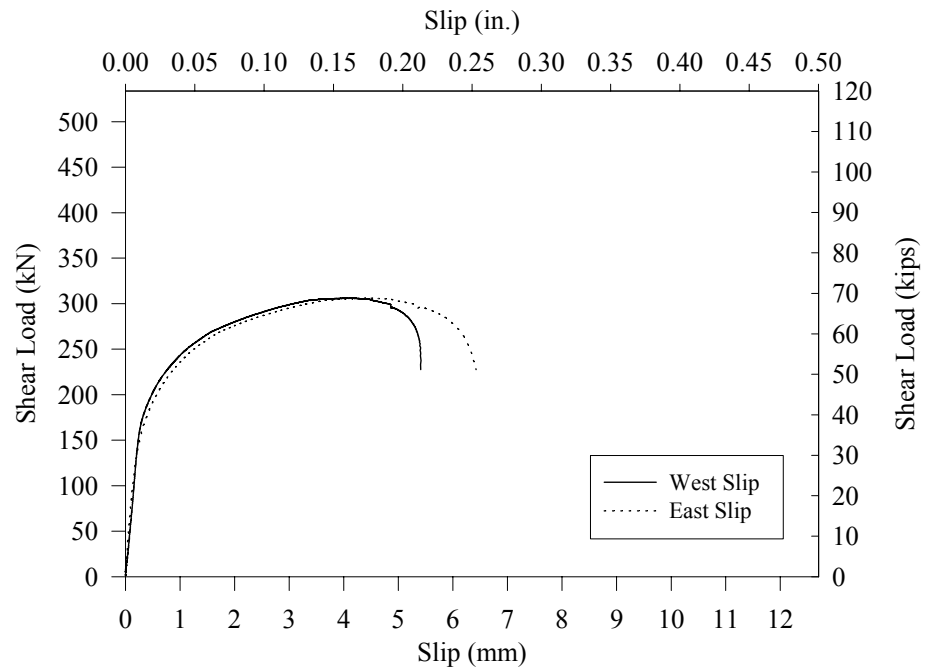


Figure 4.38 Load versus slip during shear loading for Specimen 7

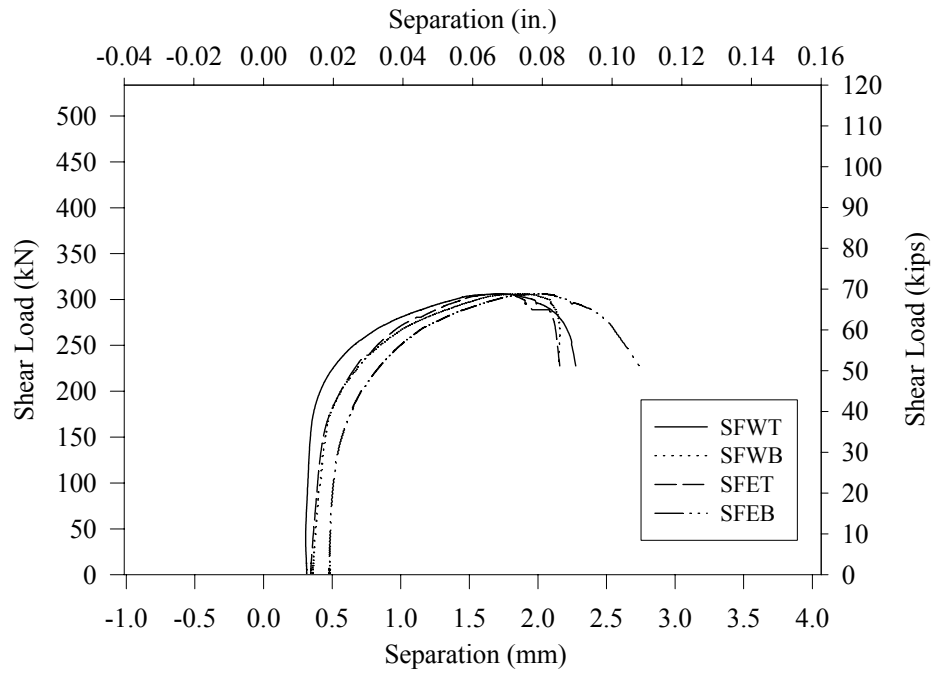


Figure 4.39 Load versus separation for south face LVDT's during shear loading for Specimen 7

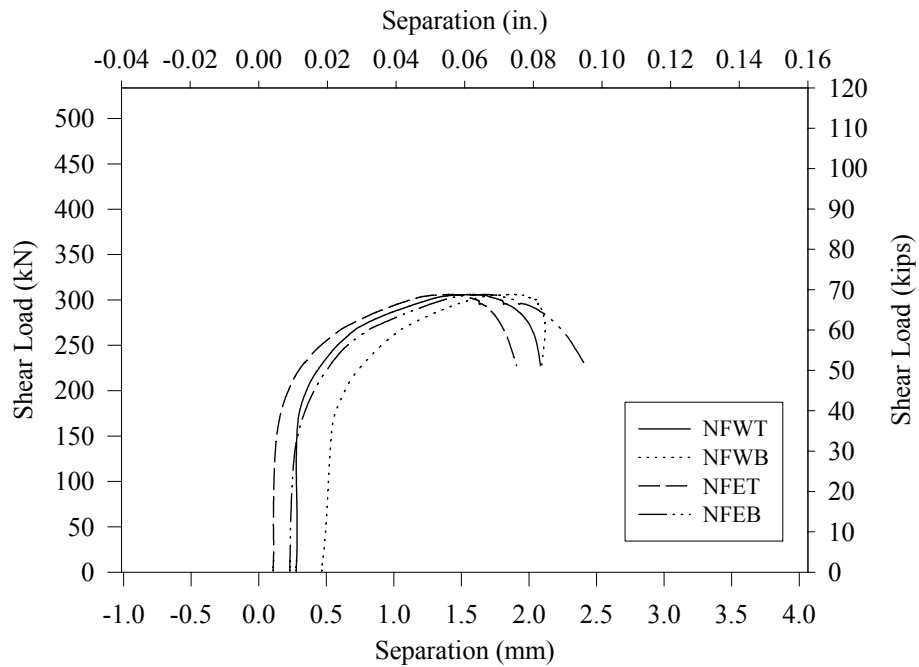


Figure 4.40 Load versus separation for north face LVDT's during shear loading for Specimen 7

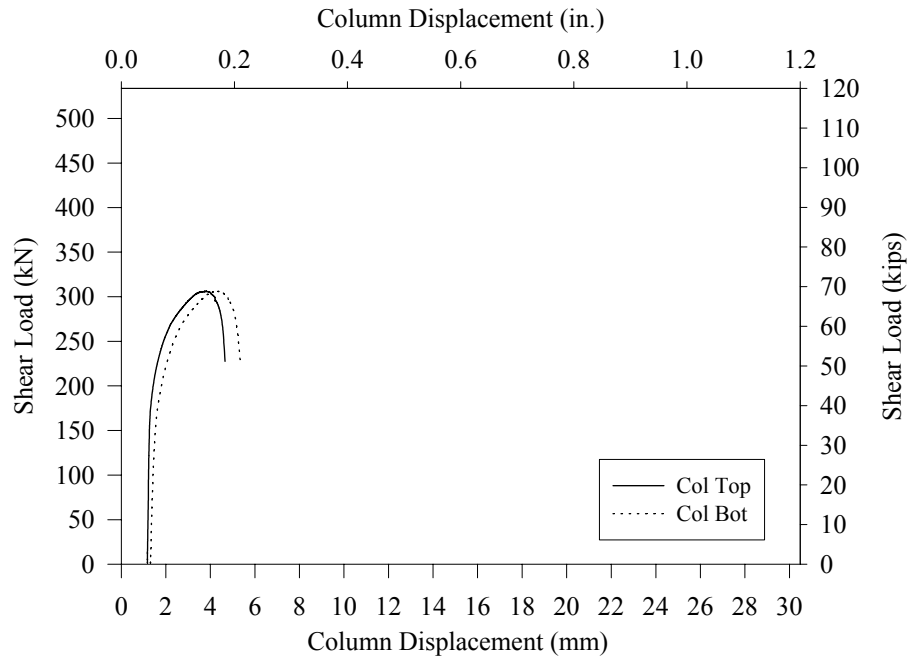


Figure 4.41 Load versus column displacement during shear loading for Specimen 7



Figure 4.42 Photograph of stud failure surface for Specimen 8

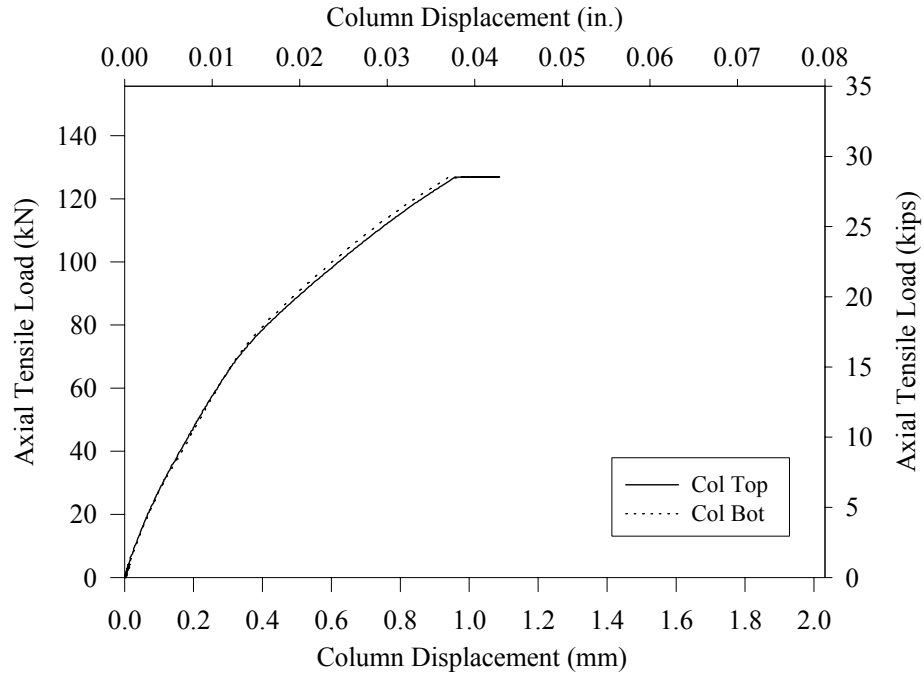


Figure 4.43 Load versus column displacement during tensile loading for Specimen 8

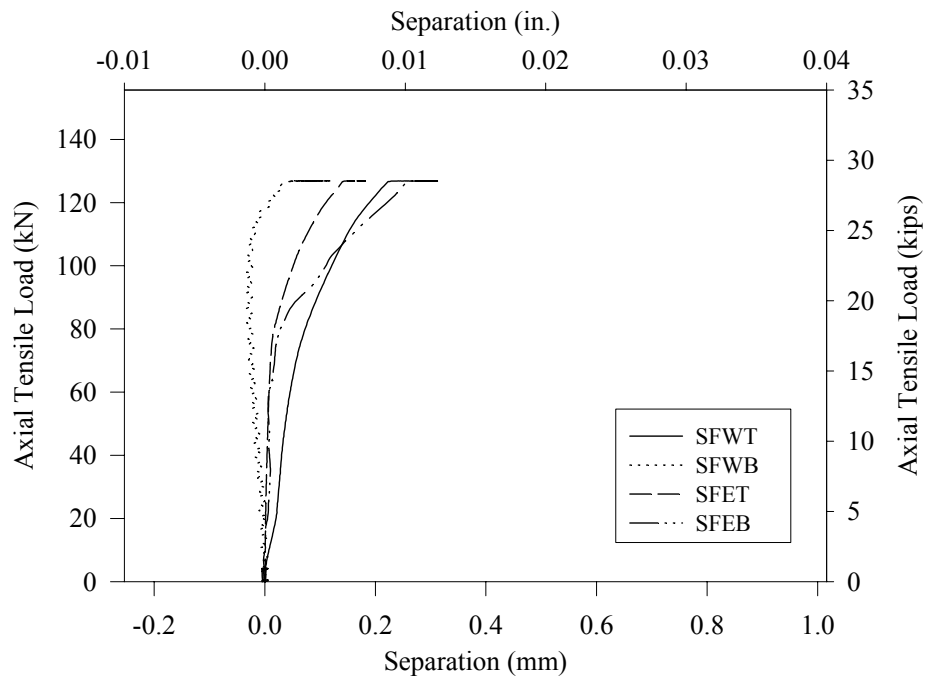


Figure 4.44 Load versus separation for south face LVDT's during tensile loading for Specimen 8

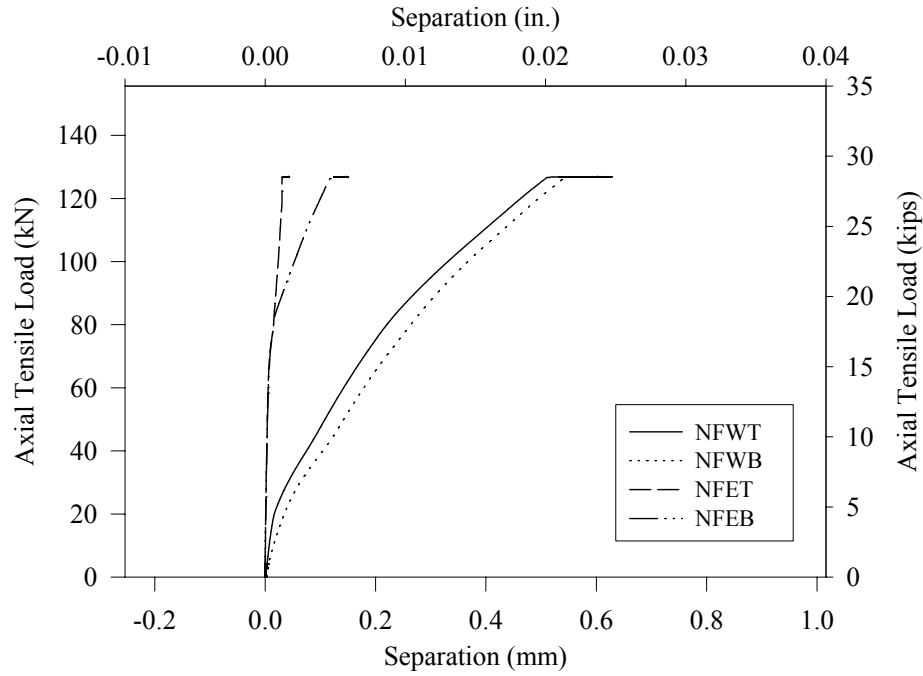


Figure 4.45 Load versus separation for north face LVDT's during tensile loading for Specimen 8

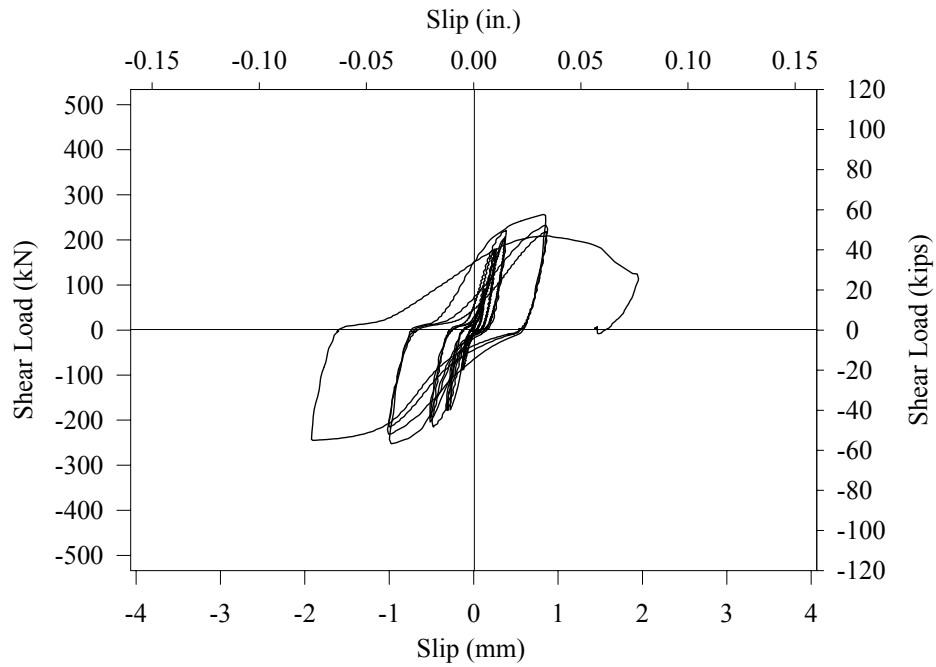


Figure 4.46 Load versus west slip during shear loading for Specimen 8

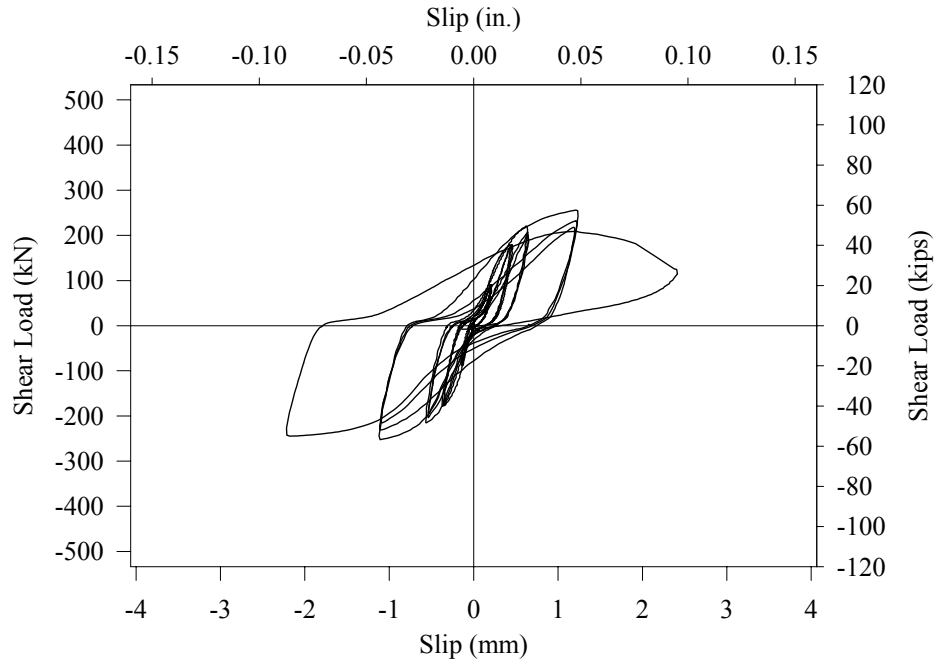


Figure 4.47 Load versus east slip during shear loading for Specimen 8

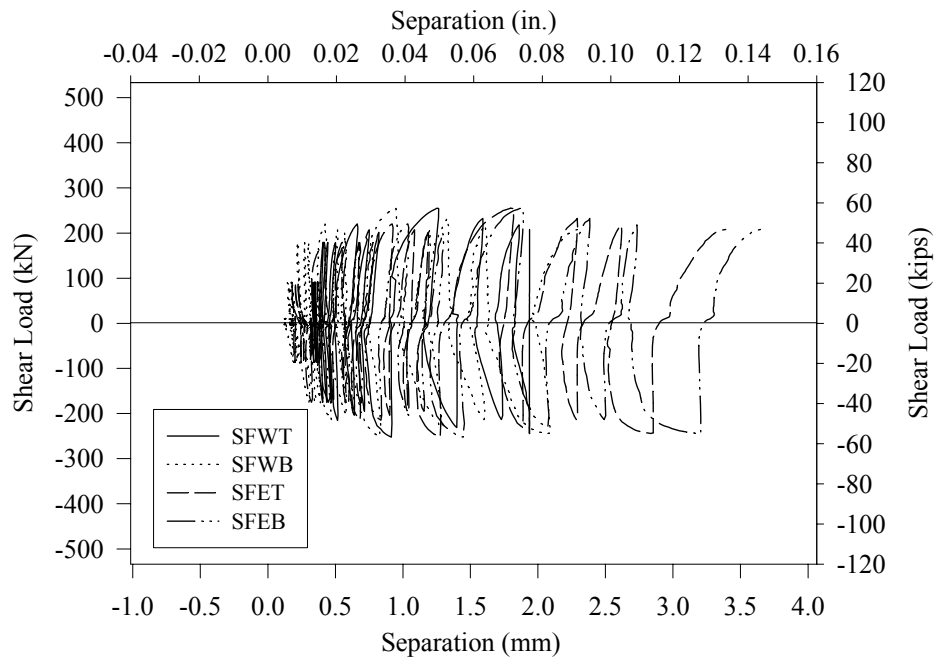


Figure 4.48 Load versus separation for south face LVDT's during shear loading for Specimen 8

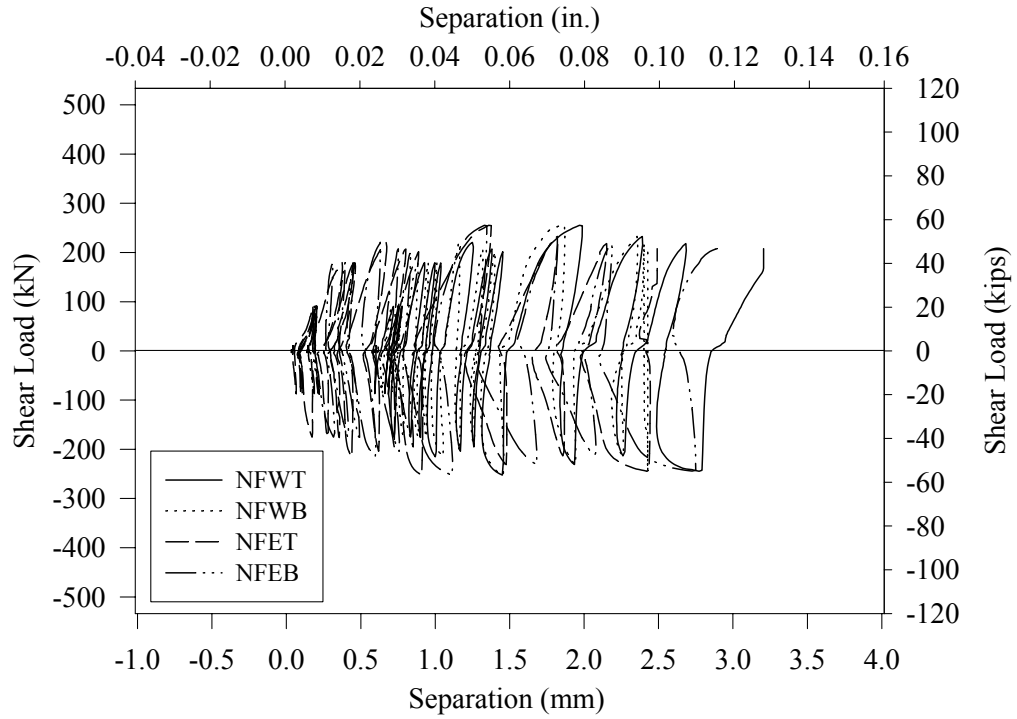


Figure 4.49 Load versus separation for north face LVDT's during shear loading for Specimen 8

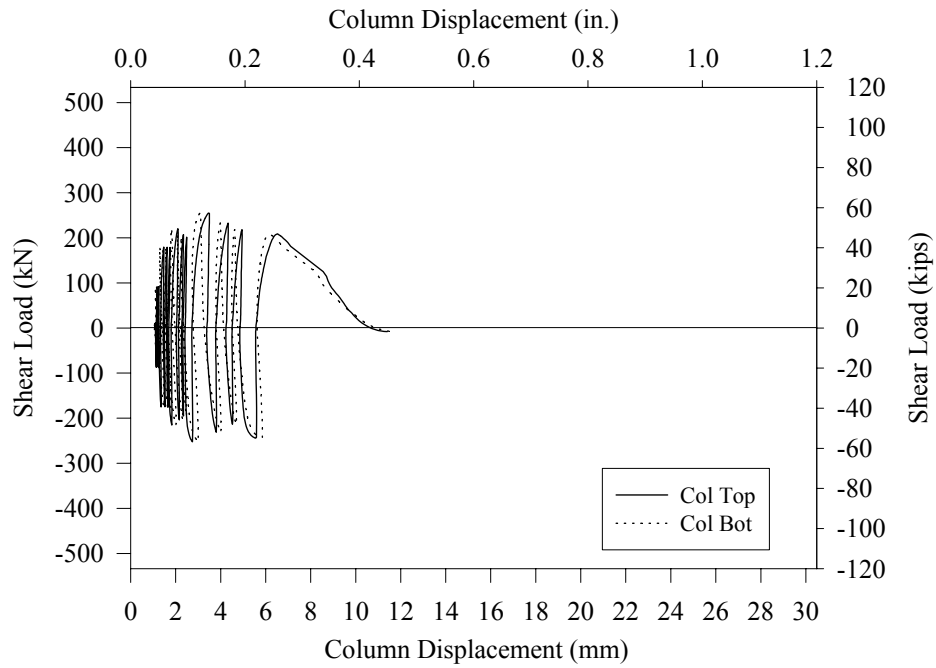


Figure 4.50 Load versus column displacement during shear loading for Specimen 8

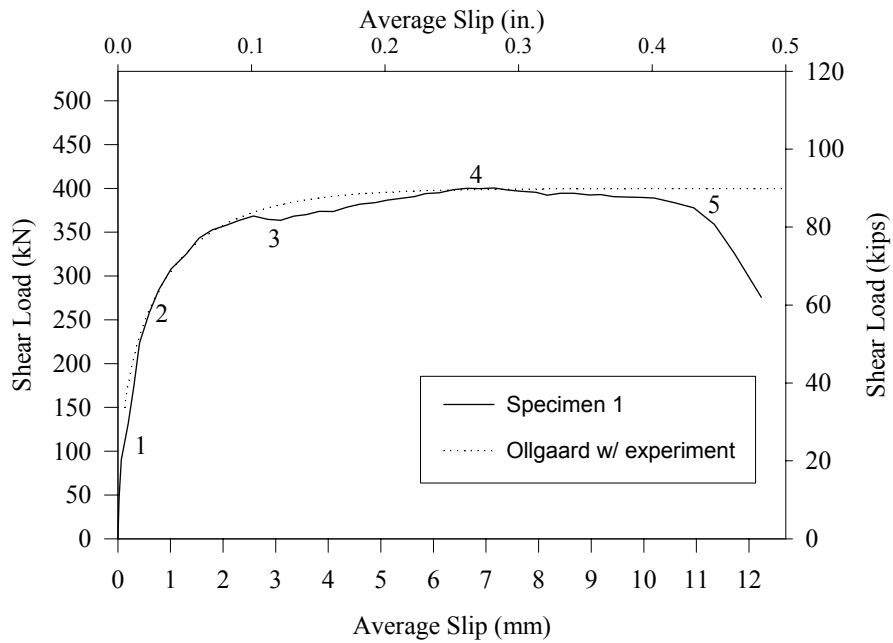


Figure 5.1 Load versus average slip for Specimen 1

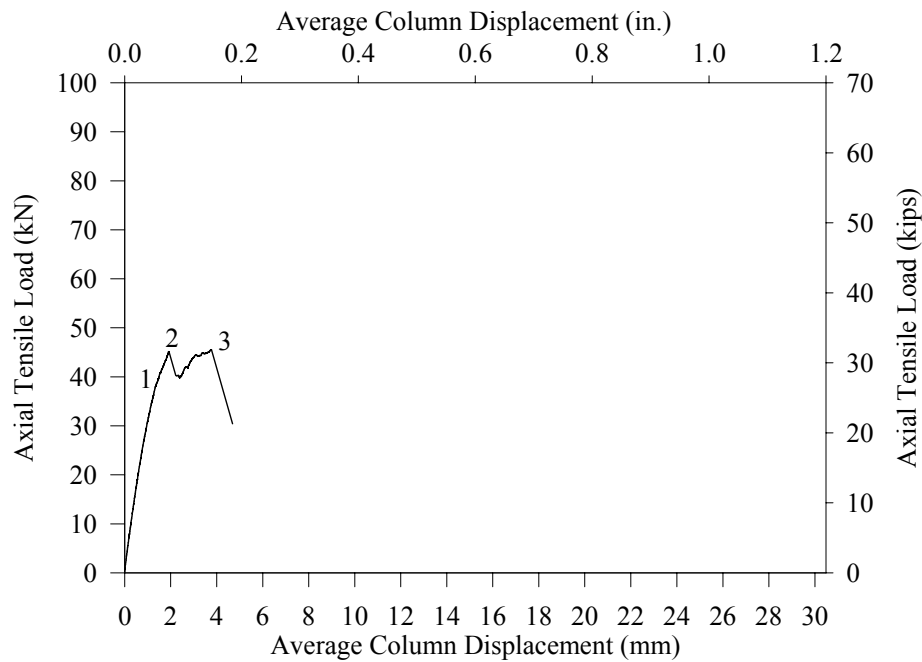


Figure 5.2 Load versus average column displacement for Specimen 2

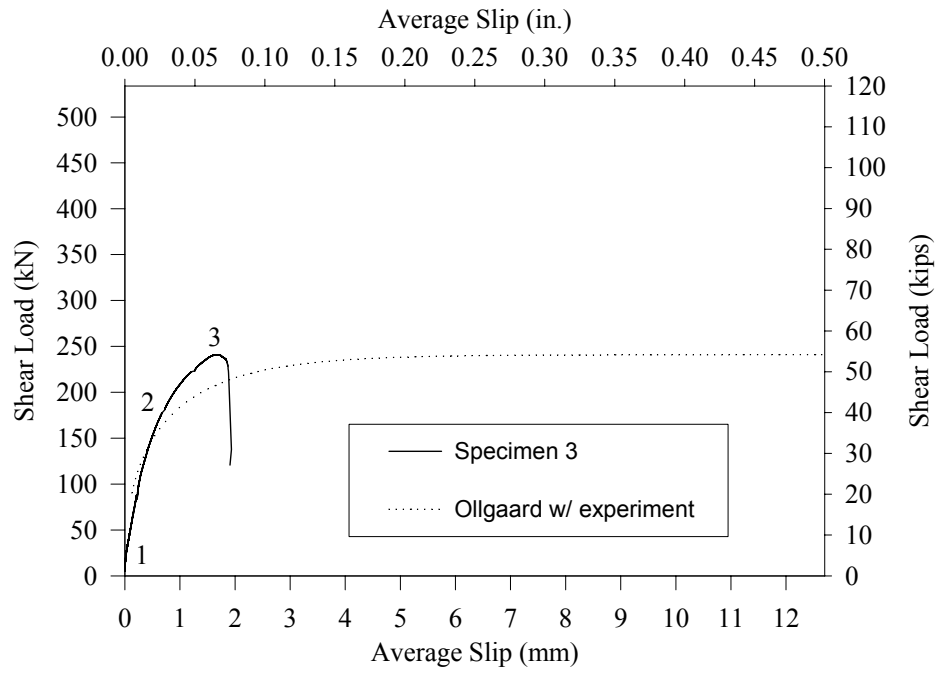


Figure 5.3 Load versus average slip for Specimen 3

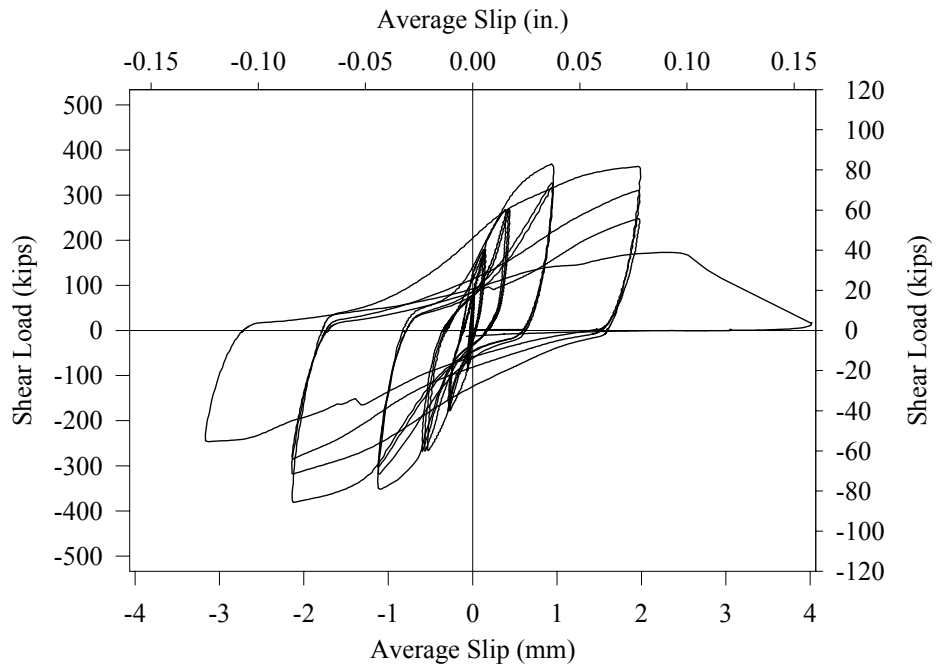


Figure 5.4 Load versus average slip for Specimen 4

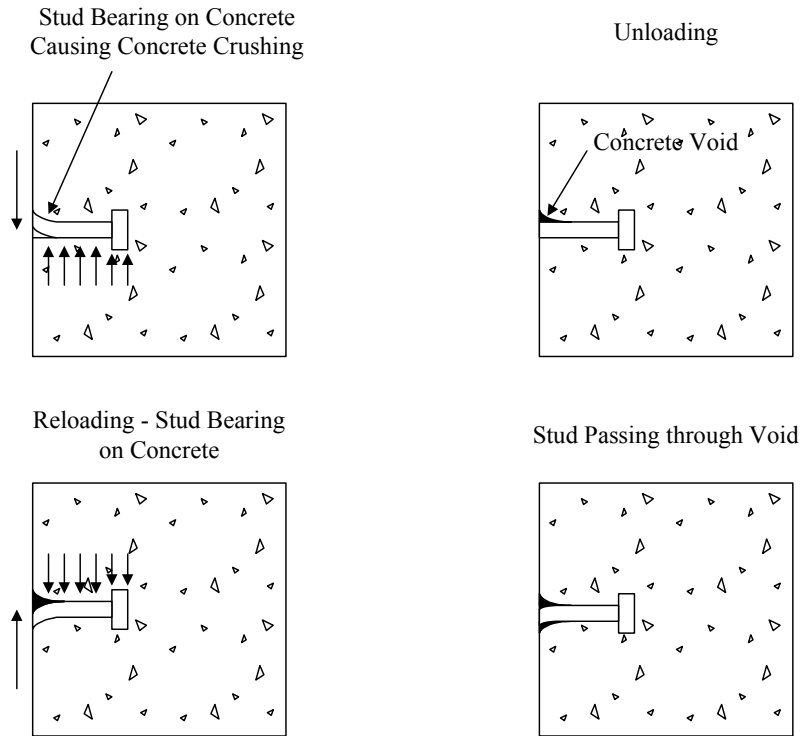


Figure 5.5 Progression of damage mechanisms for Cyclic Tests

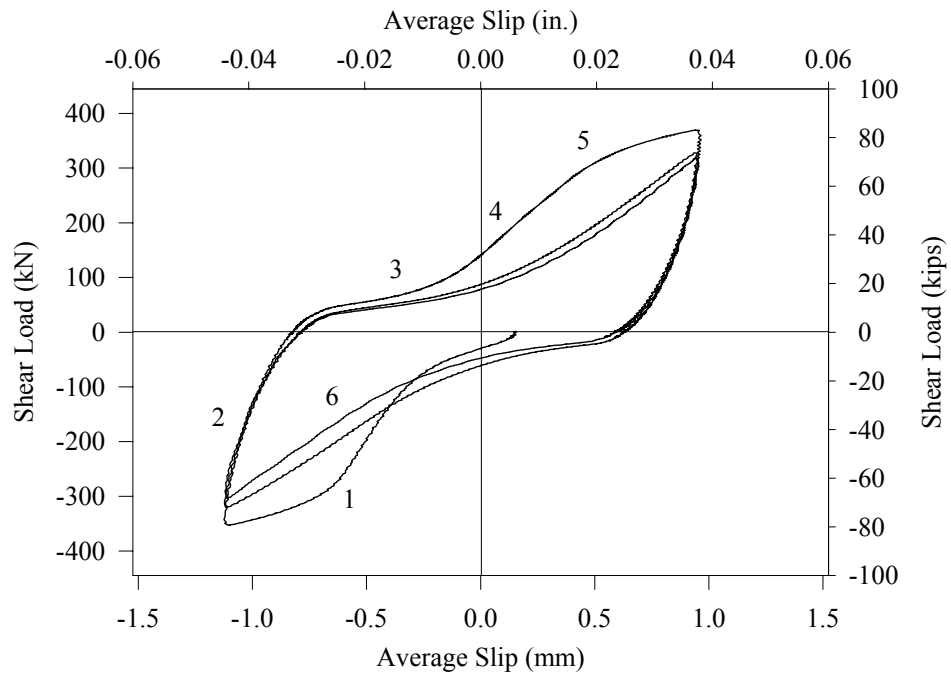


Figure 5.6 Typical cycle for Specimen 4

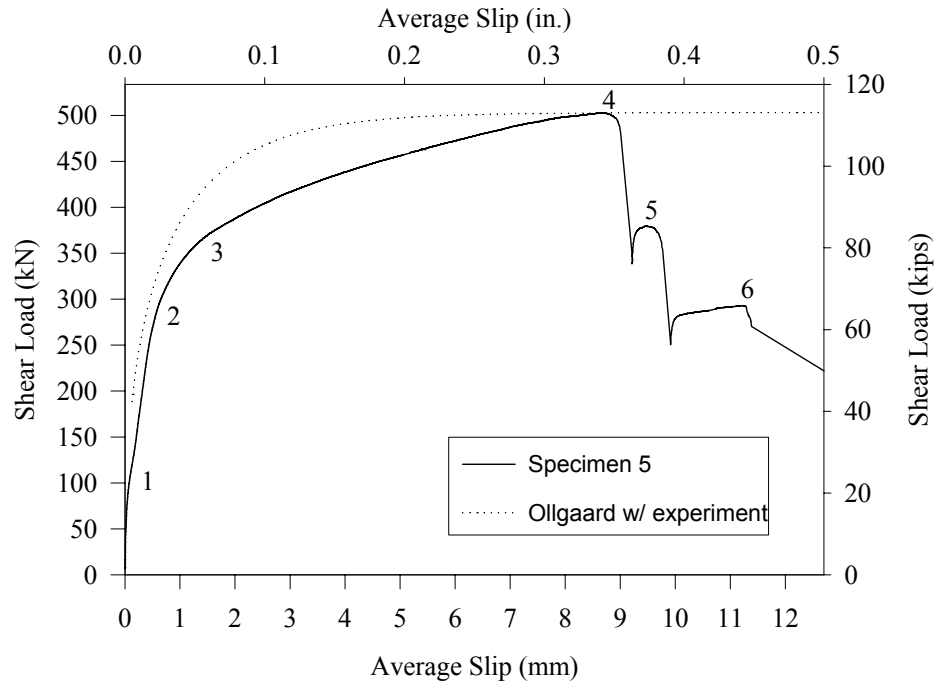


Figure 5.7 Load versus average slip for Specimen 5

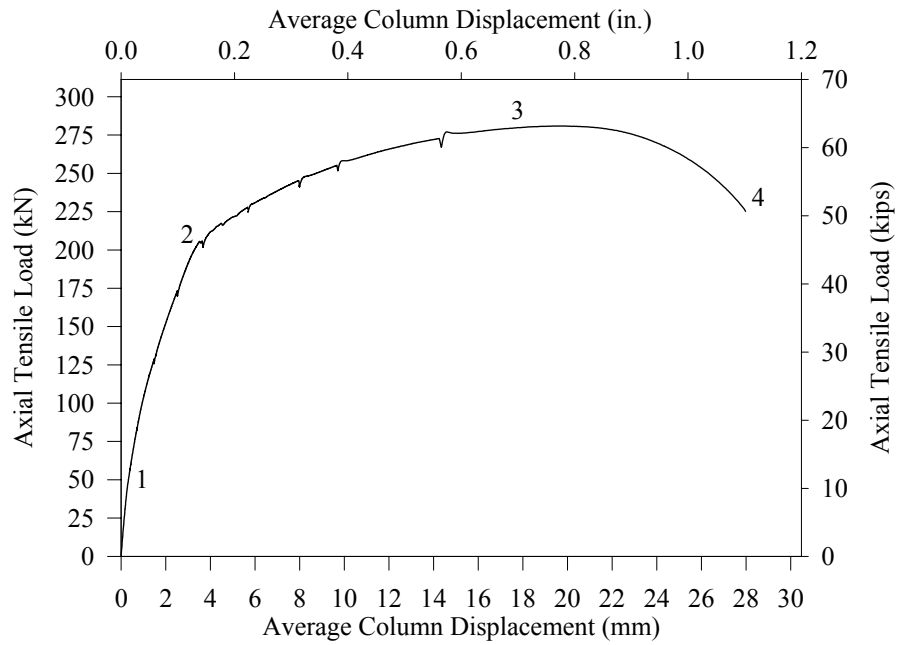


Figure 5.8 Load versus average column displacement for Specimen 6

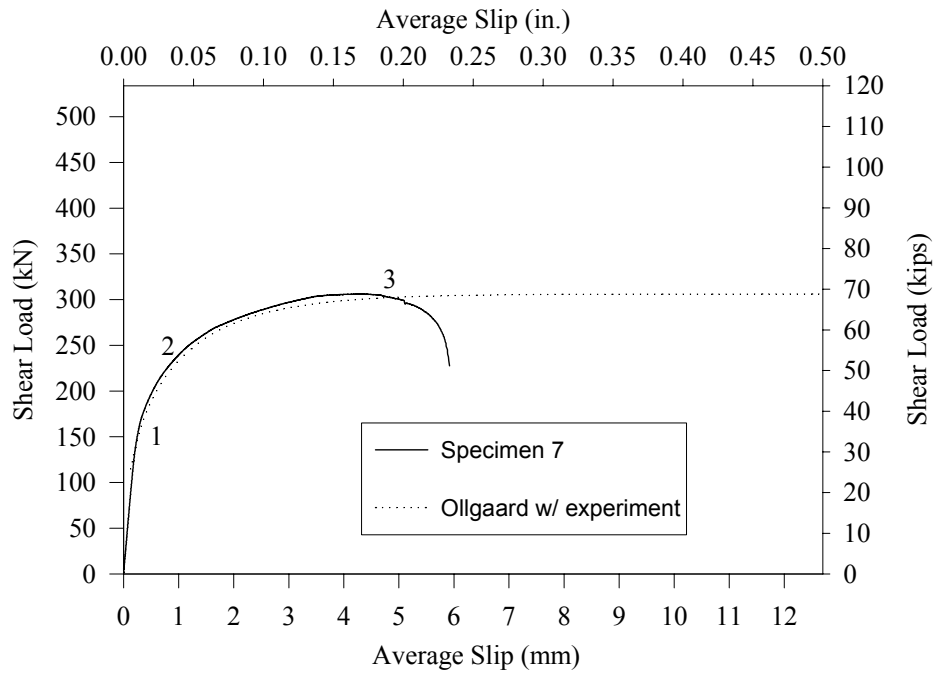


Figure 5.9 Load versus average slip for Specimen 7

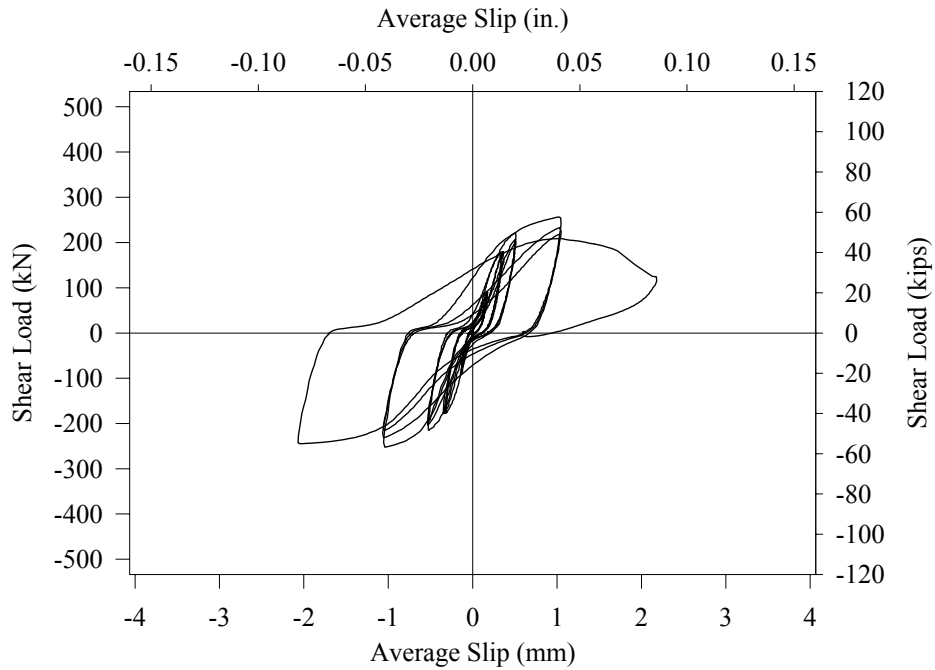


Figure 5.10 Load versus average slip for specimen 8

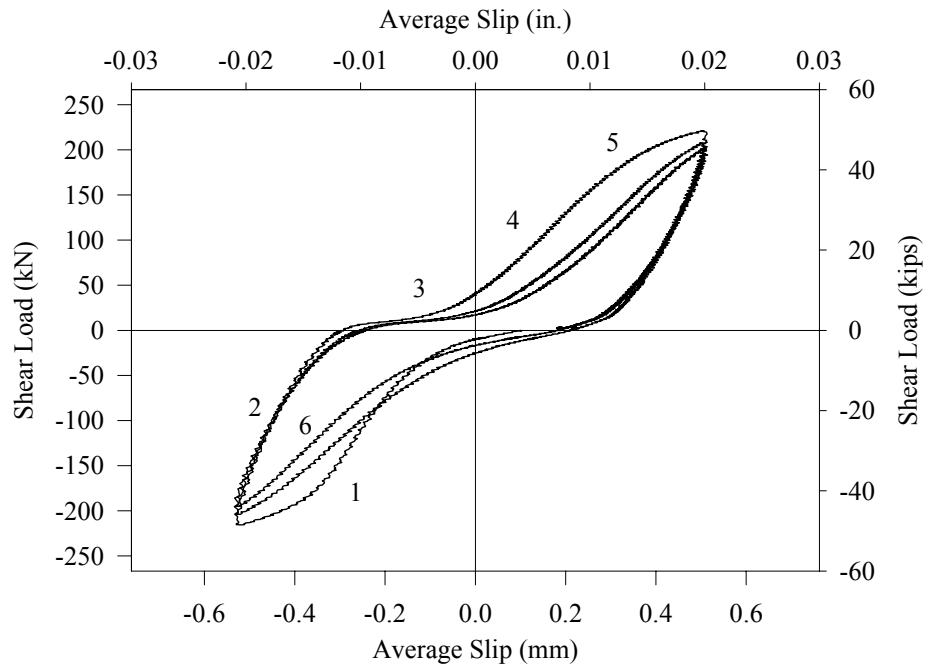


Figure 5.11 Typical cycle for Specimen 8

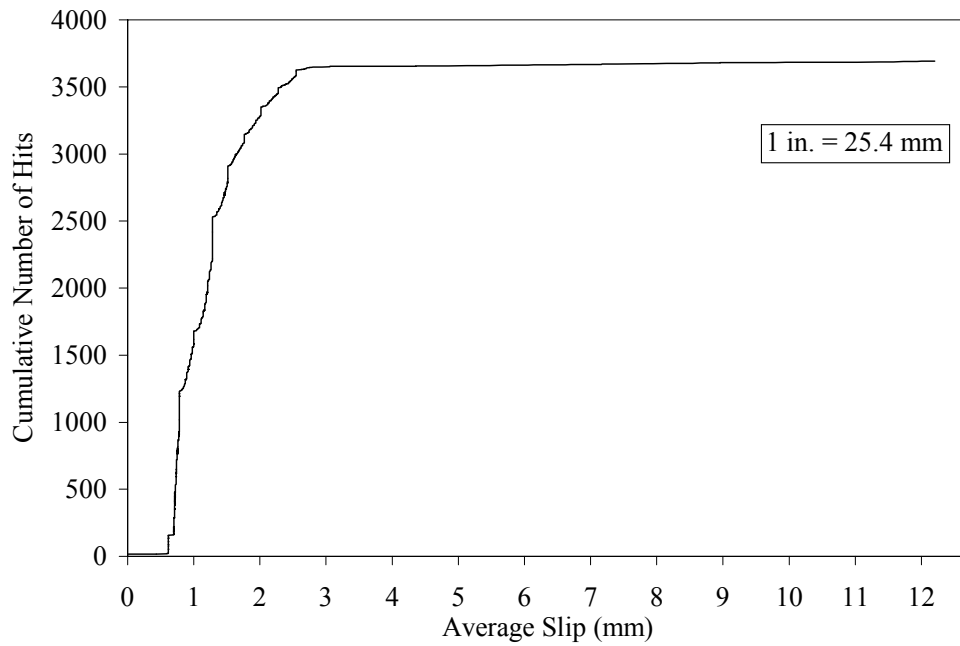


Figure 5.12 Acoustic emission activity for Specimen 1 at Sensor 1

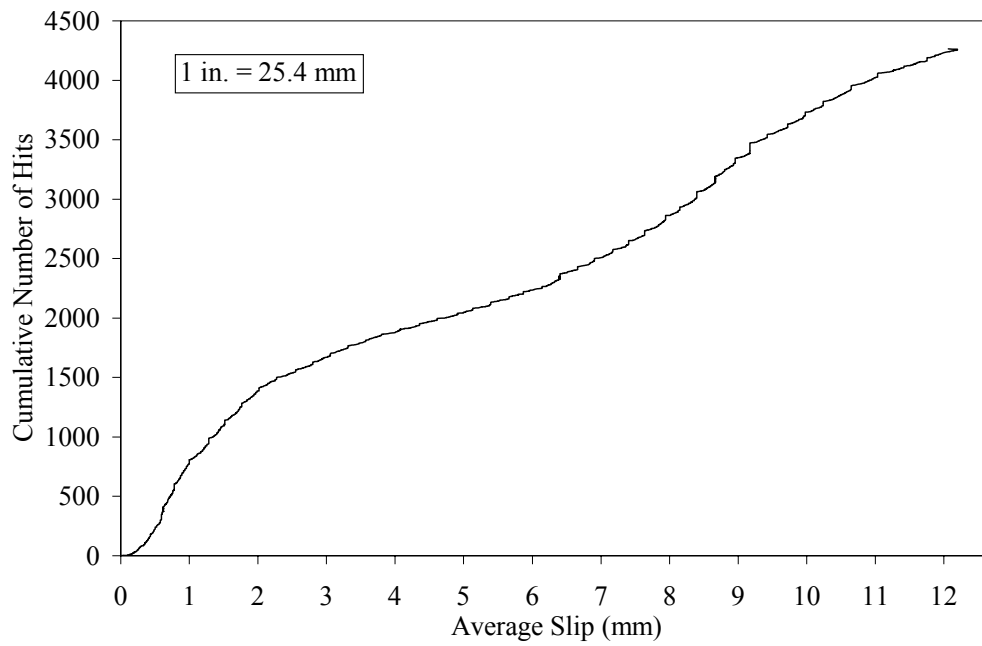


Figure 5.13 Acoustic emission activity for Specimen 1 at Sensor 3

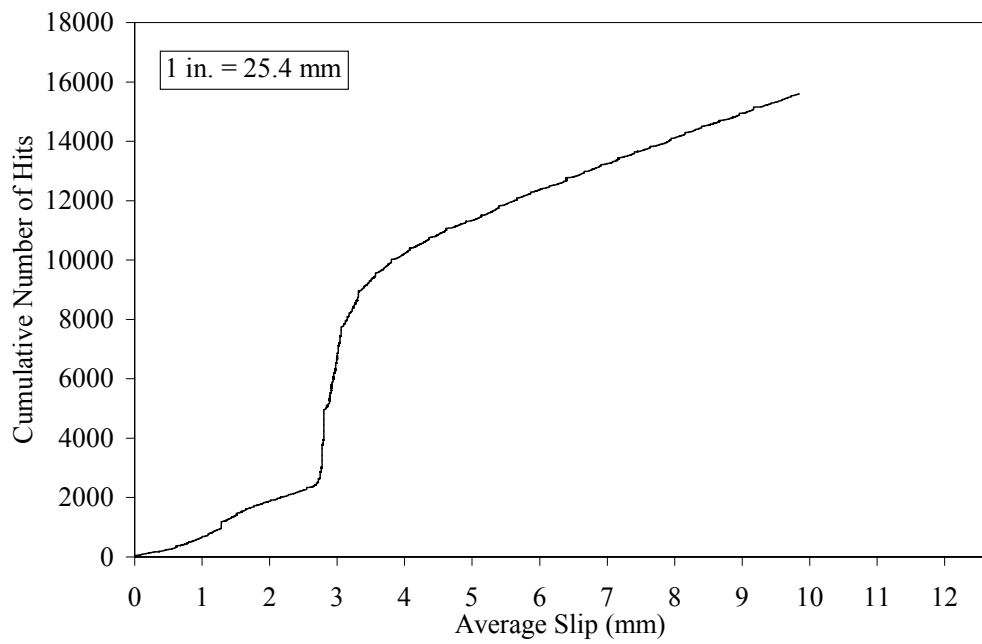


Figure 5.14 Acoustic emission activity for Specimen 1 at Sensor 4

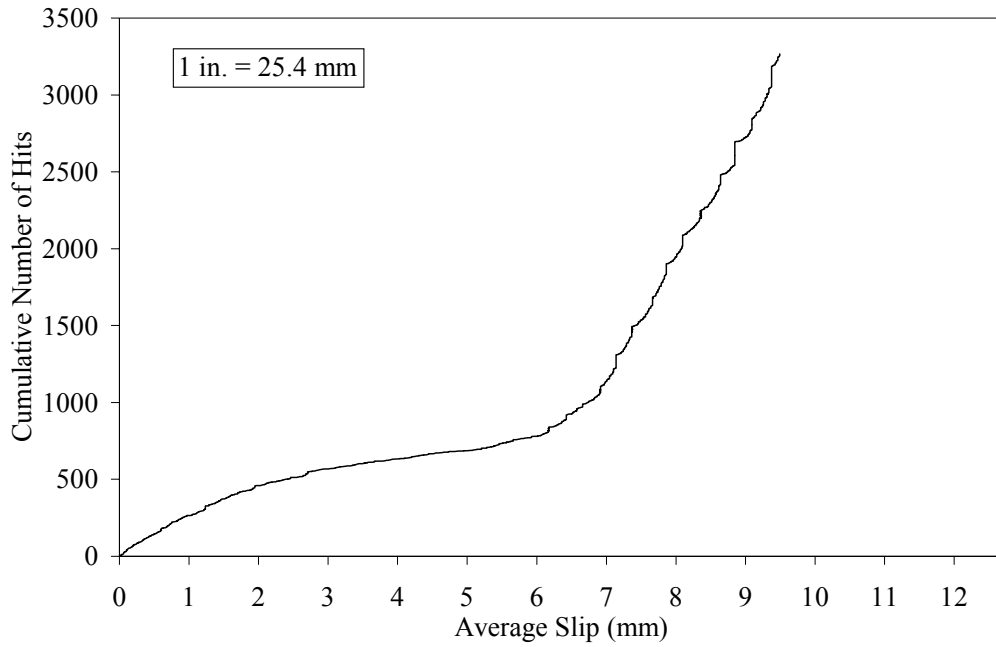


Figure 5.15 Acoustic emission activity for Specimen 1 at Sensor 6

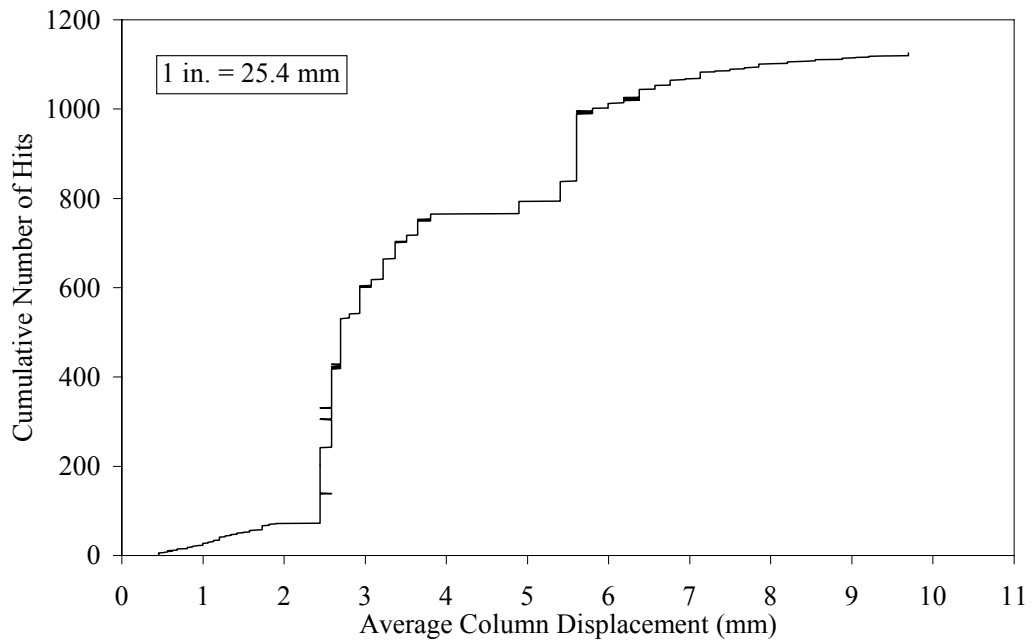


Figure 5.16 Acoustic emission activity for Specimen 2 at Sensor 1

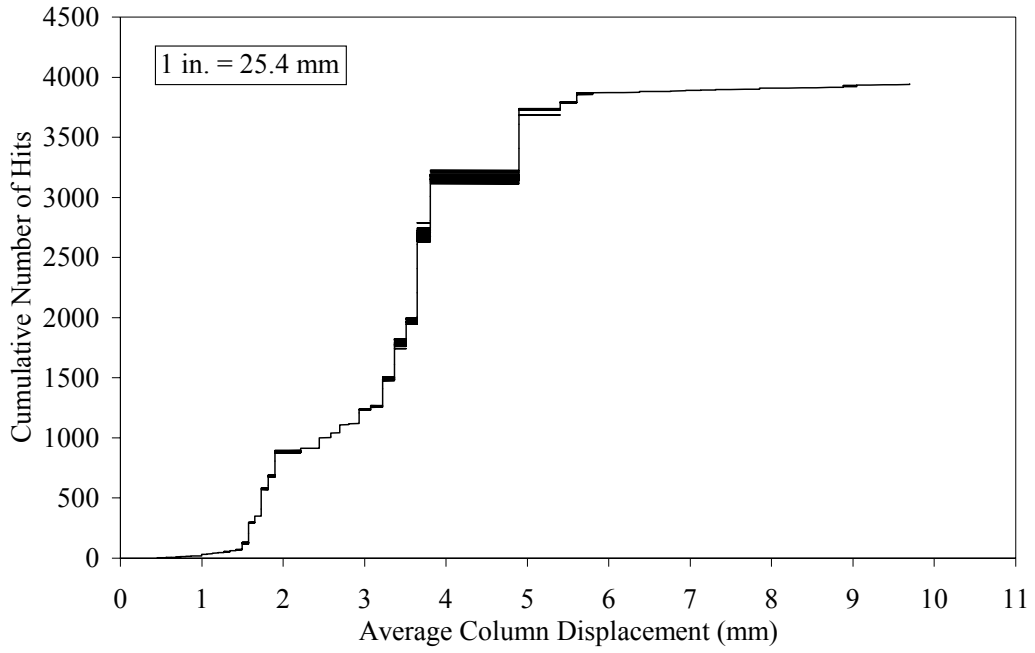


Figure 5.17 Acoustic emission activity for Specimen 2 at Sensor 6

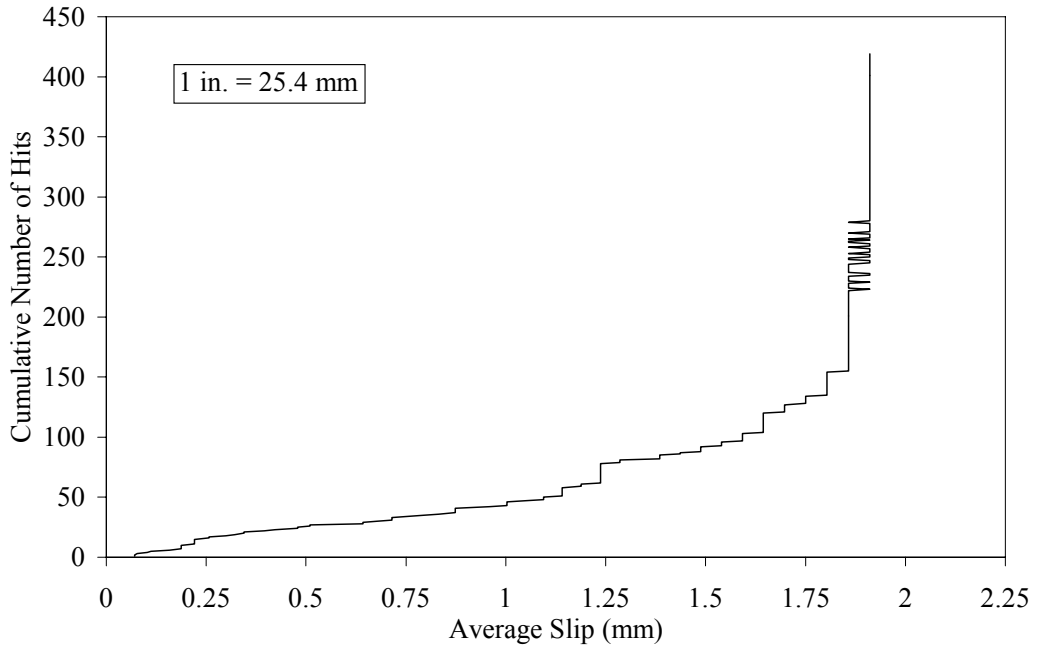


Figure 5.18 Acoustic emission activity for Specimen 3 at Sensor 1

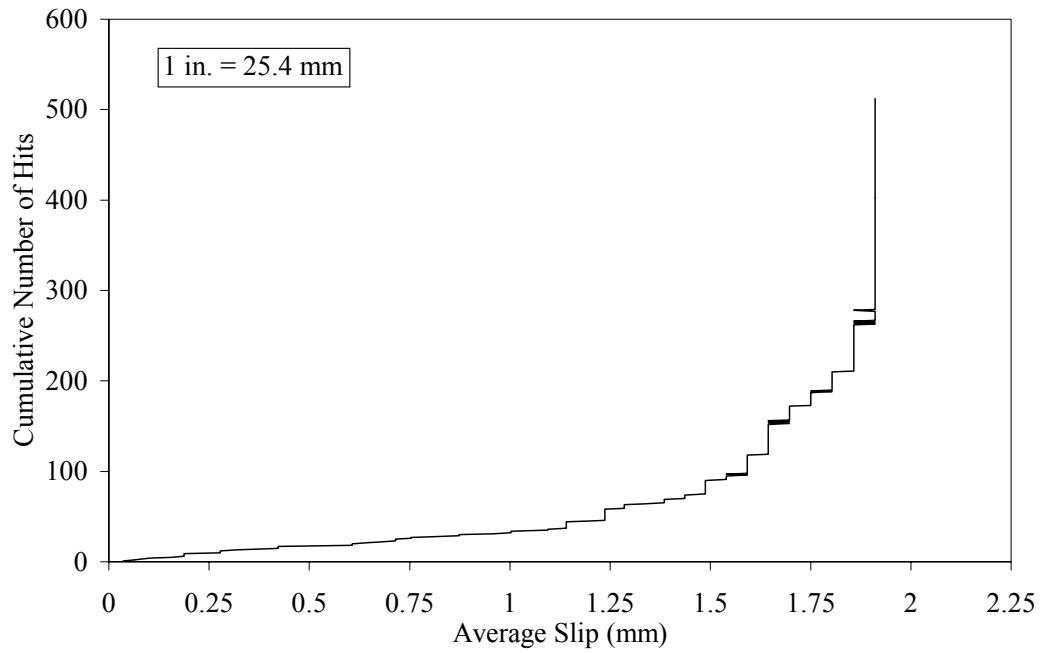


Figure 5.19 Acoustic emission activity for Specimen 3 at Sensor 6

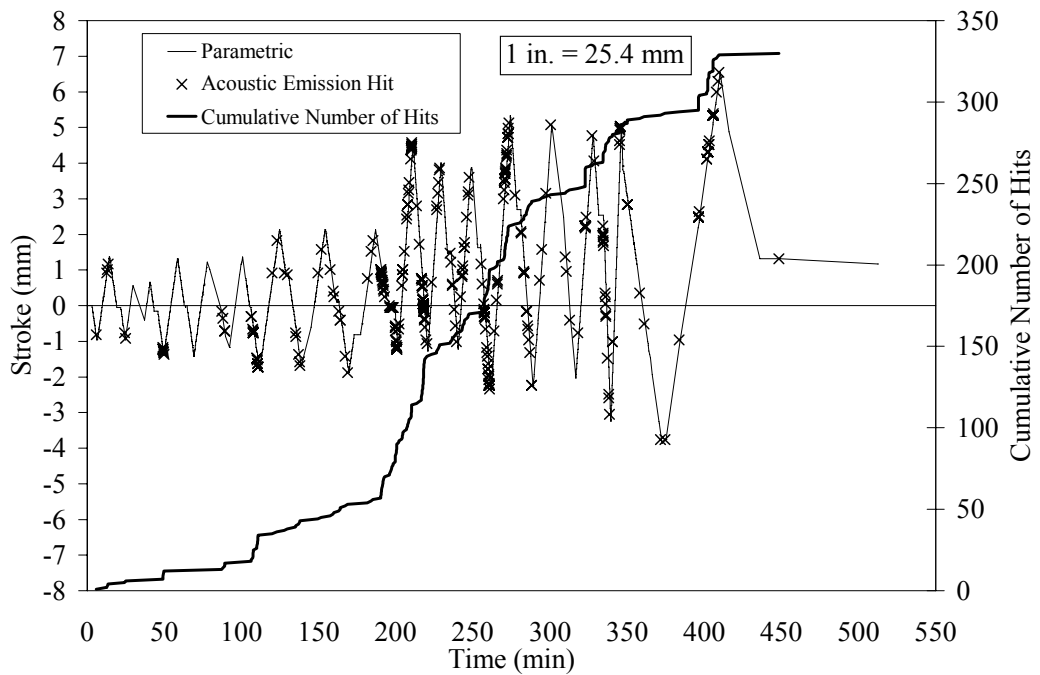


Figure 5.20 Acoustic emission activity for Specimen 4 at Sensor 2

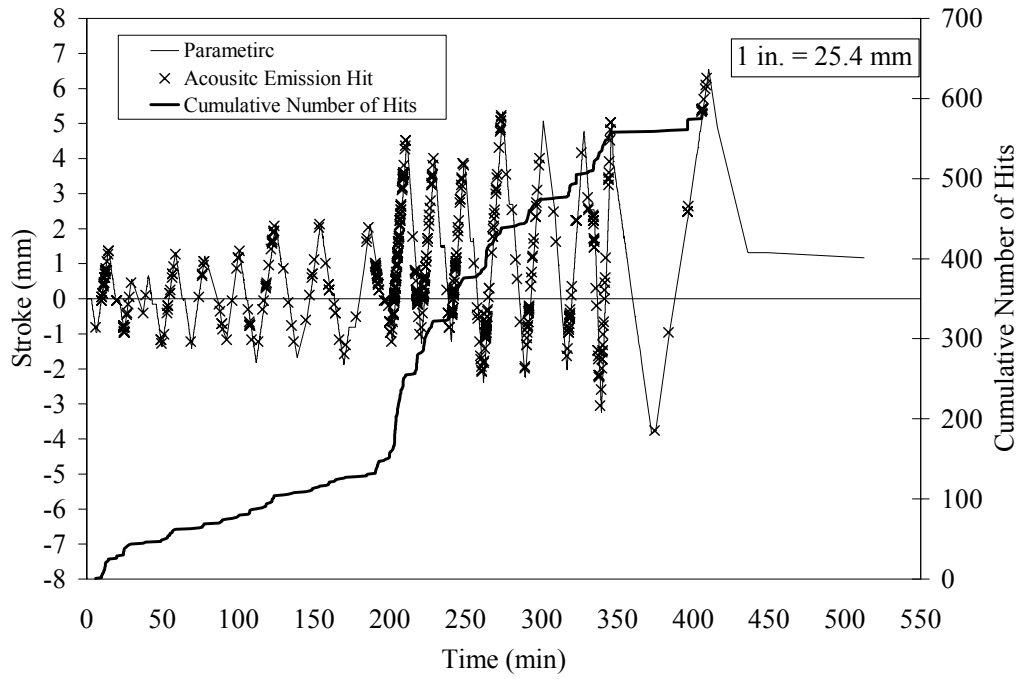


Figure 5.21 Acoustic emission activity for Specimen 4 at Sensor 6

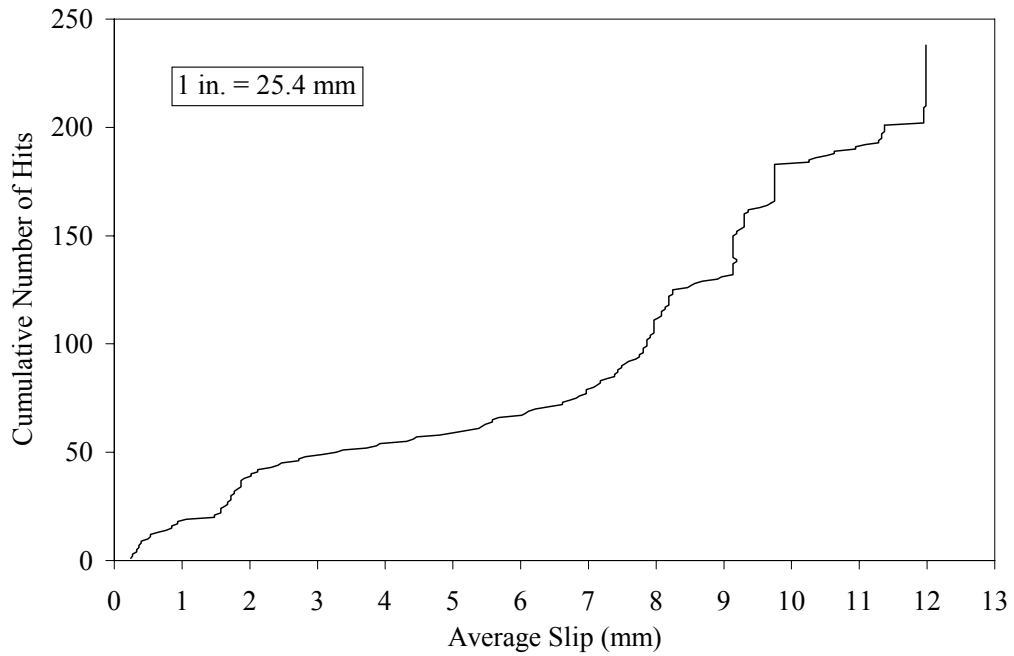


Figure 5.22 Acoustic emission activity for Specimen 5 at Sensor 1

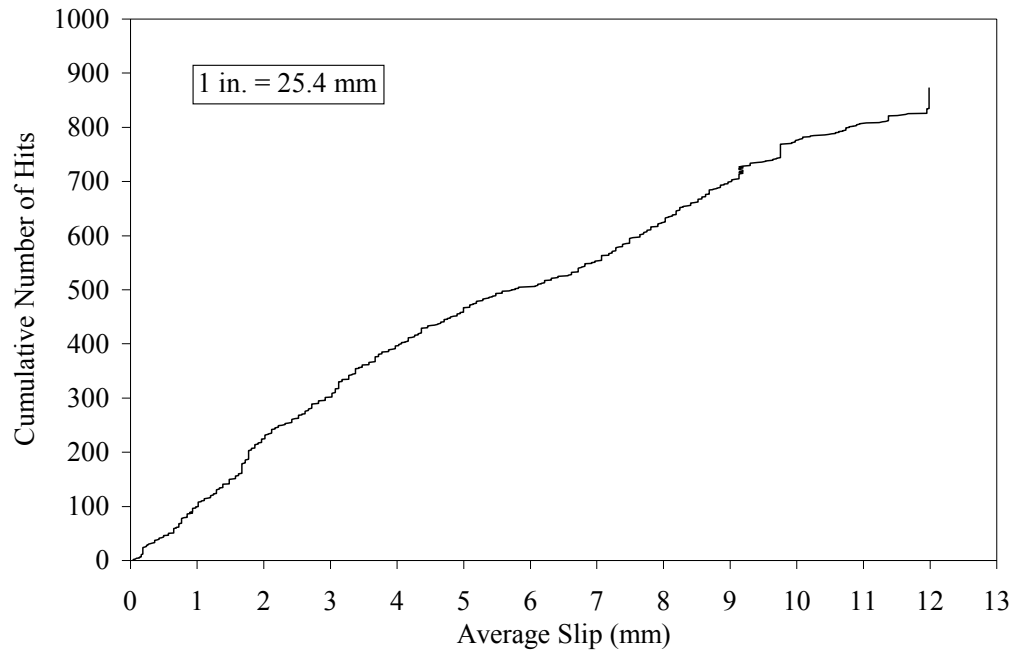


Figure 5.23 Acoustic emission activity for Specimen 5 at Sensor 4

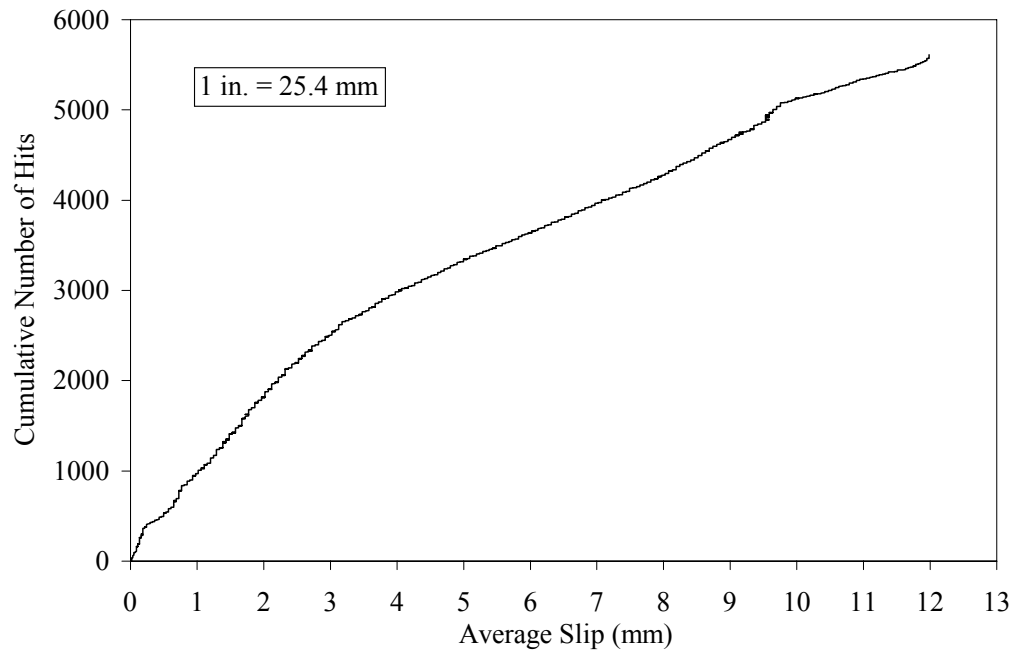


Figure 5.24 Acoustic emission activity for Specimen 5 at Sensor 9

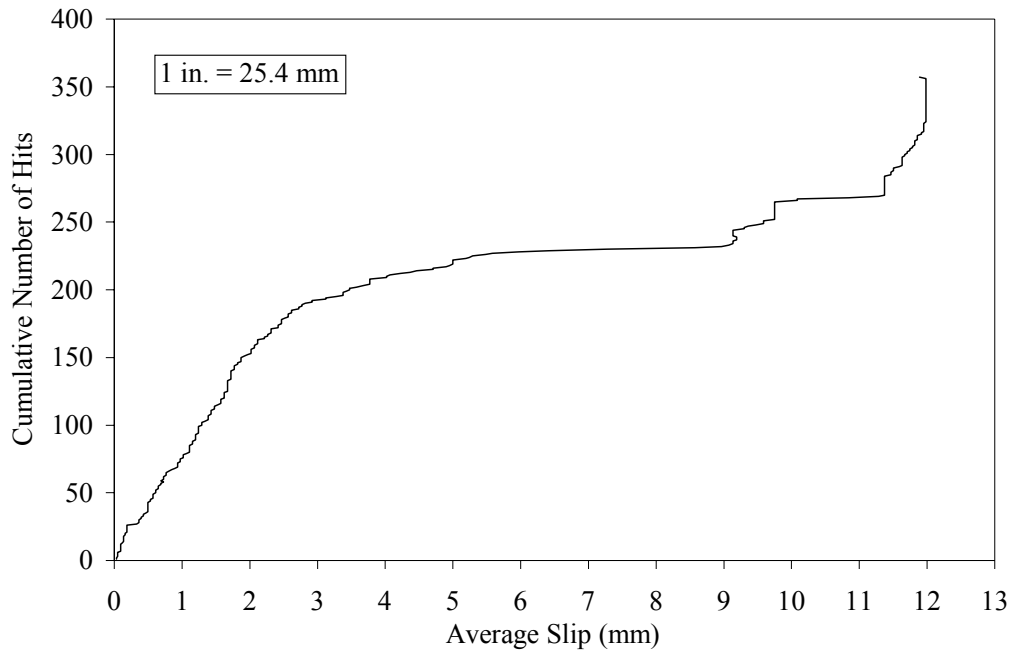


Figure 5.25 Acoustic emission activity for Specimen 5 at Sensor 6

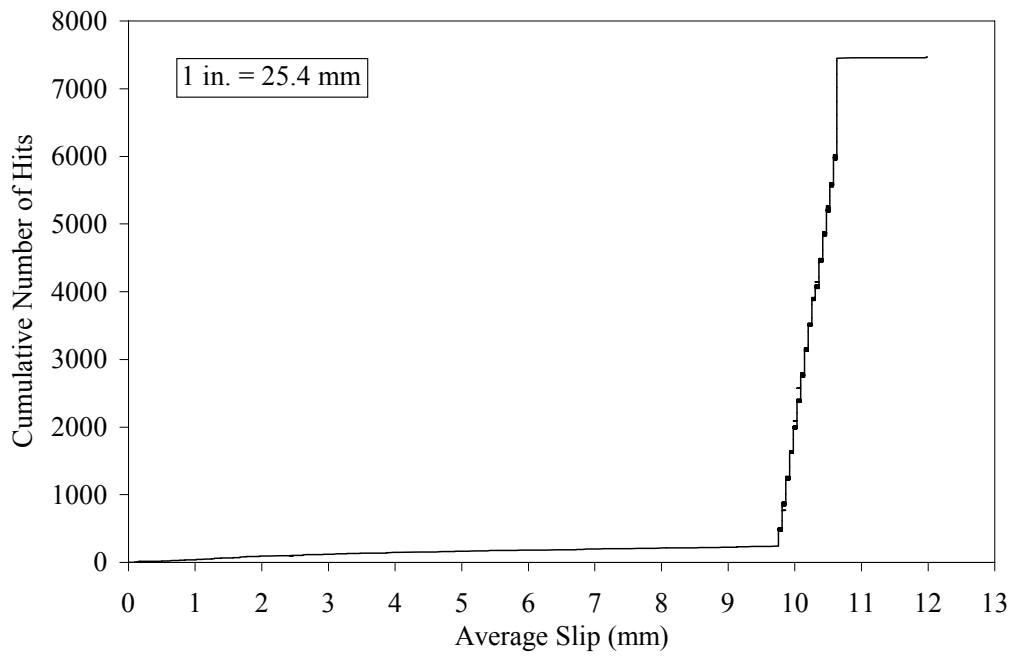


Figure 5.26 Acoustic emission activity for Specimen 5 at Sensor 10

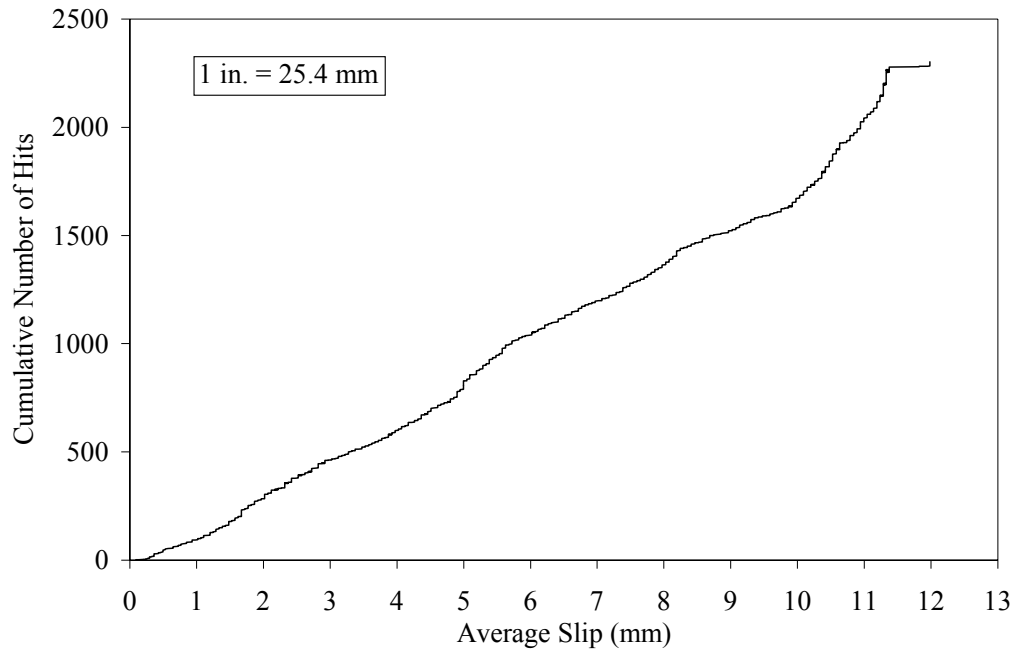


Figure 5.27 Acoustic emission activity for Specimen 5 at Sensor 7

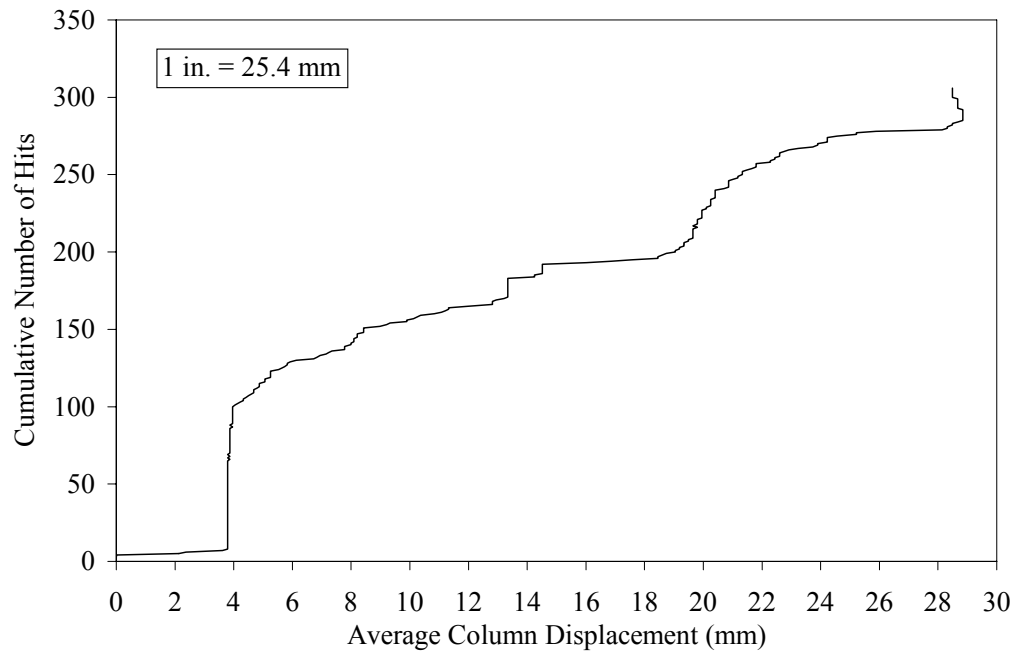


Figure 5.28 Acoustic emission activity for Specimen 6 at Sensor 1

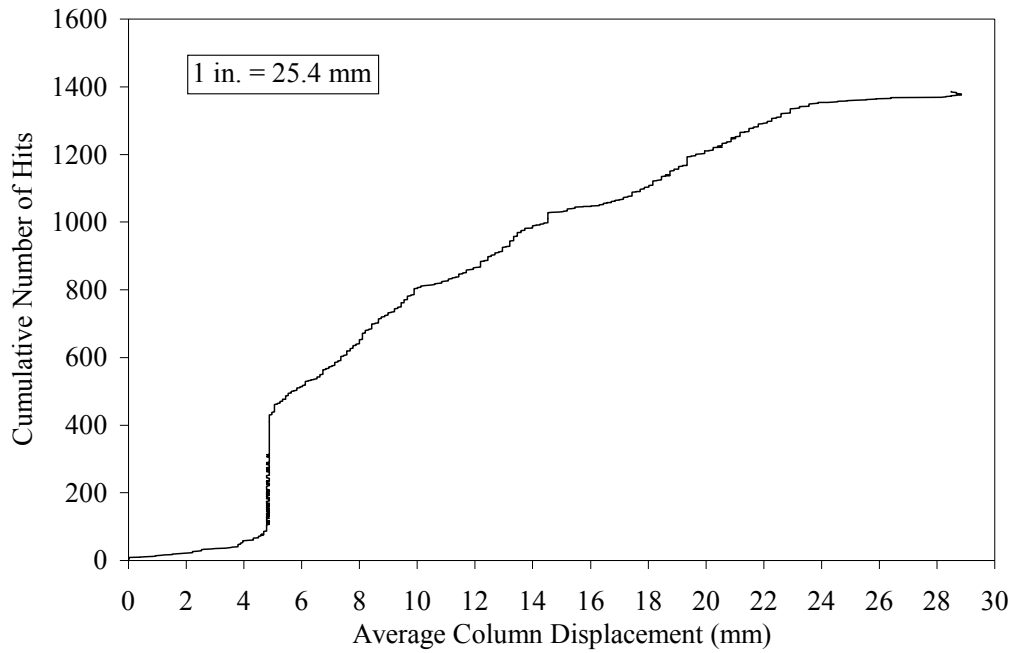


Figure 5.29 Acoustic emission activity for Specimen 6 at Sensor 4

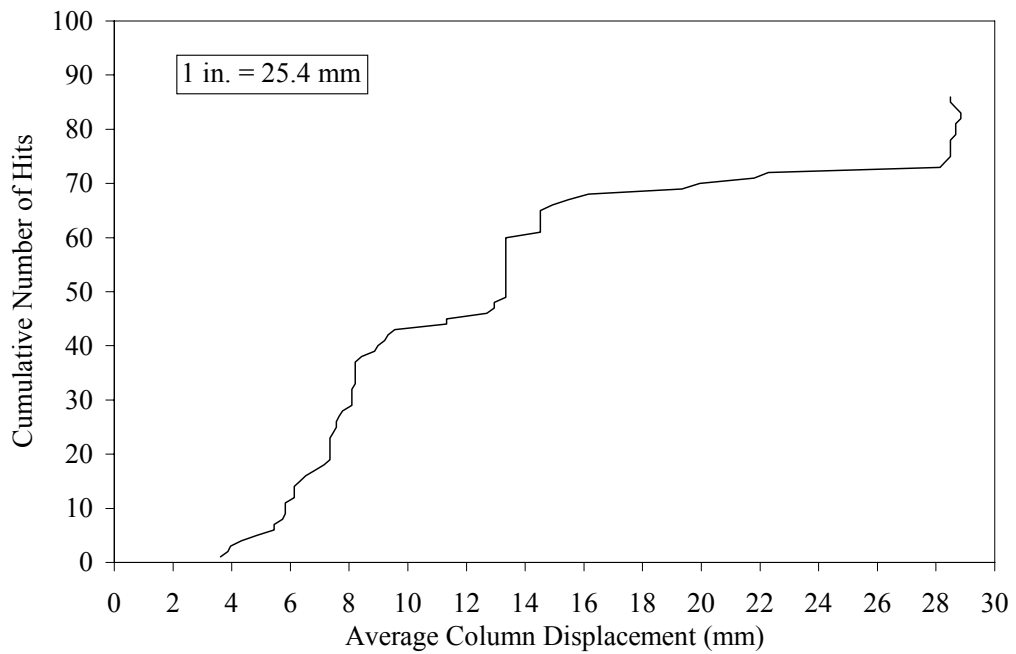


Figure 5.30 Acoustic emission activity for Specimen 6 at Sensor 6

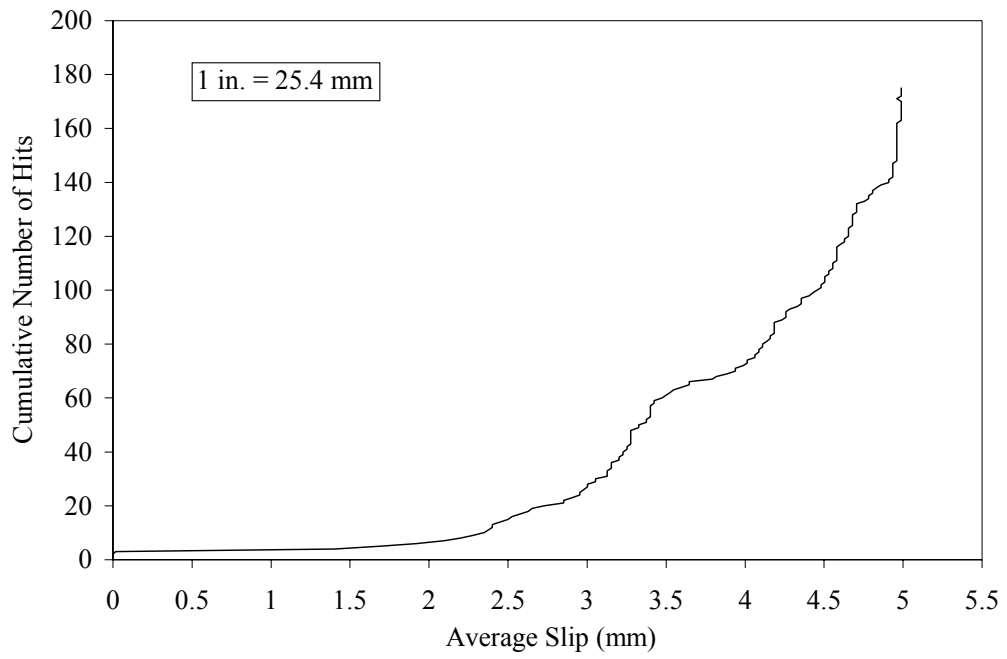


Figure 5.31 Acoustic emission activity for Specimen 7 at Sensor 4

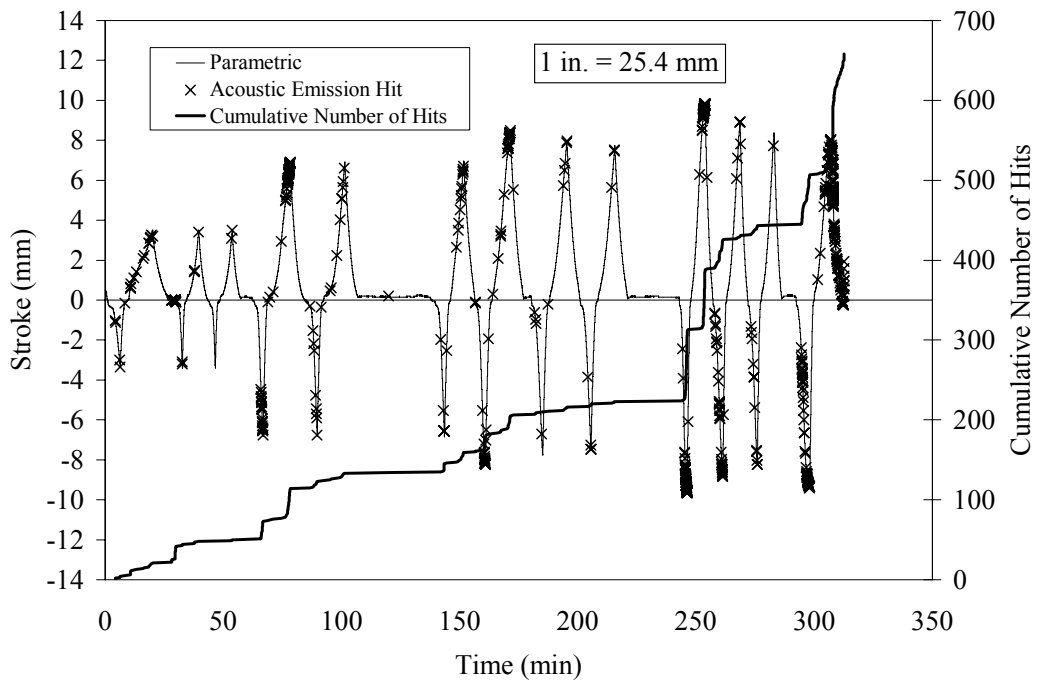


Figure 5.32 Acoustic emission activity for Specimen 8 at Sensor 10

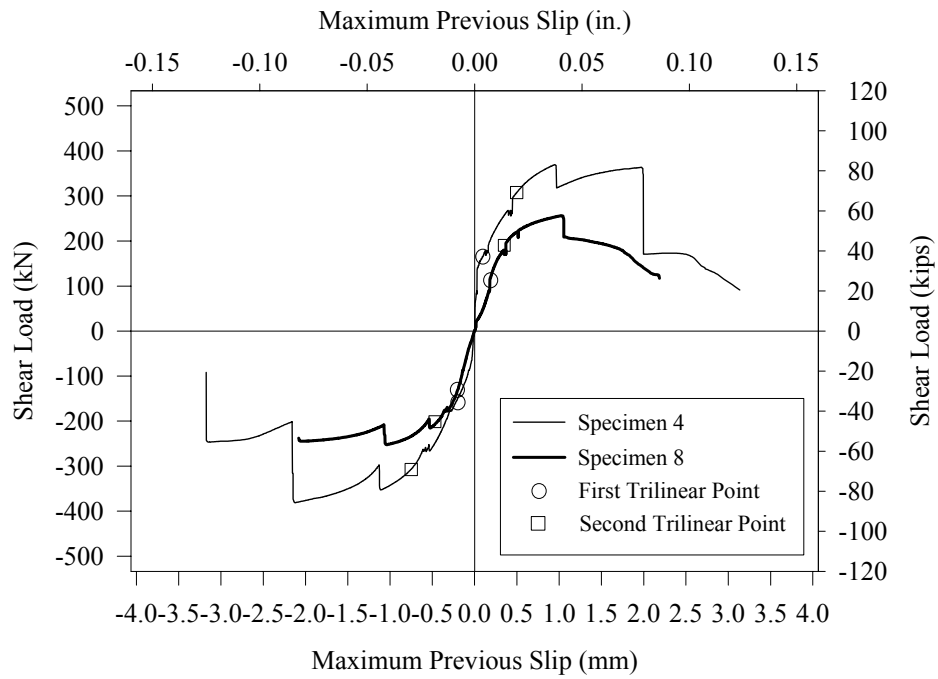


Figure 6.1 Envelope curves for Specimens 4 and 8

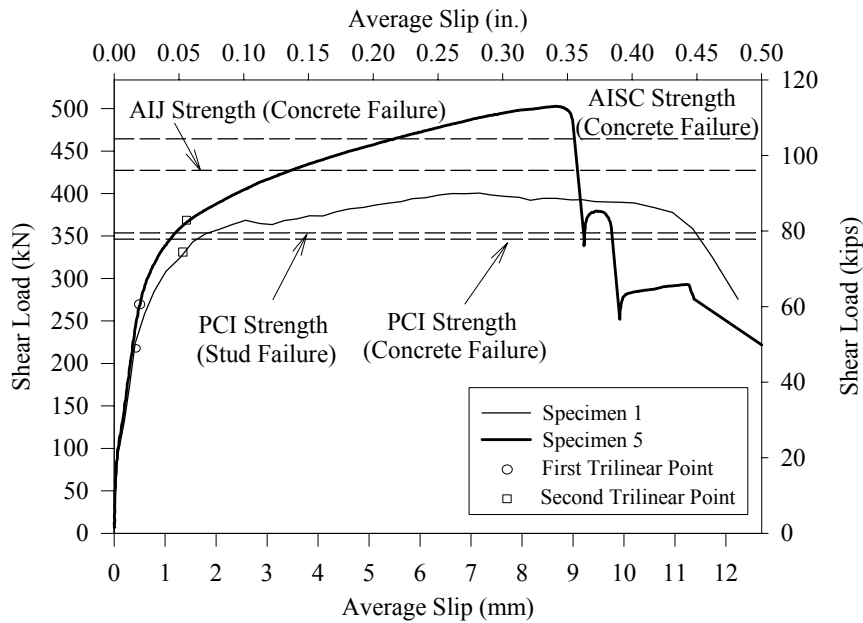


Figure 6.2 Comparison to design formulas for Specimens 1 and 5

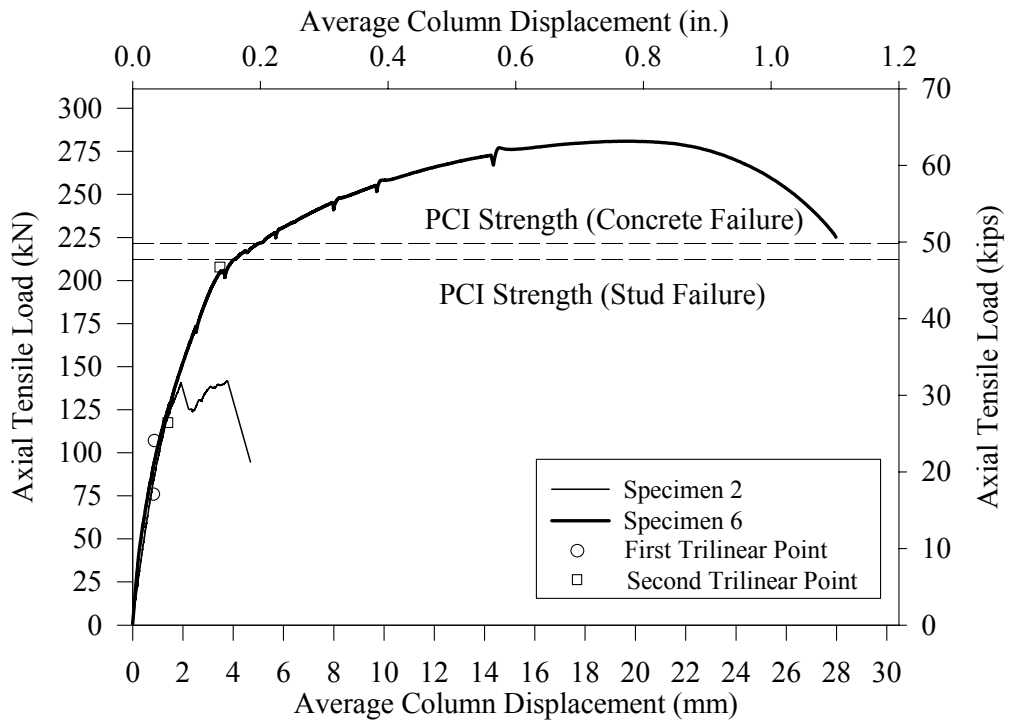


Figure 6.3 Comparison to design formulas for Specimens 2 and 6

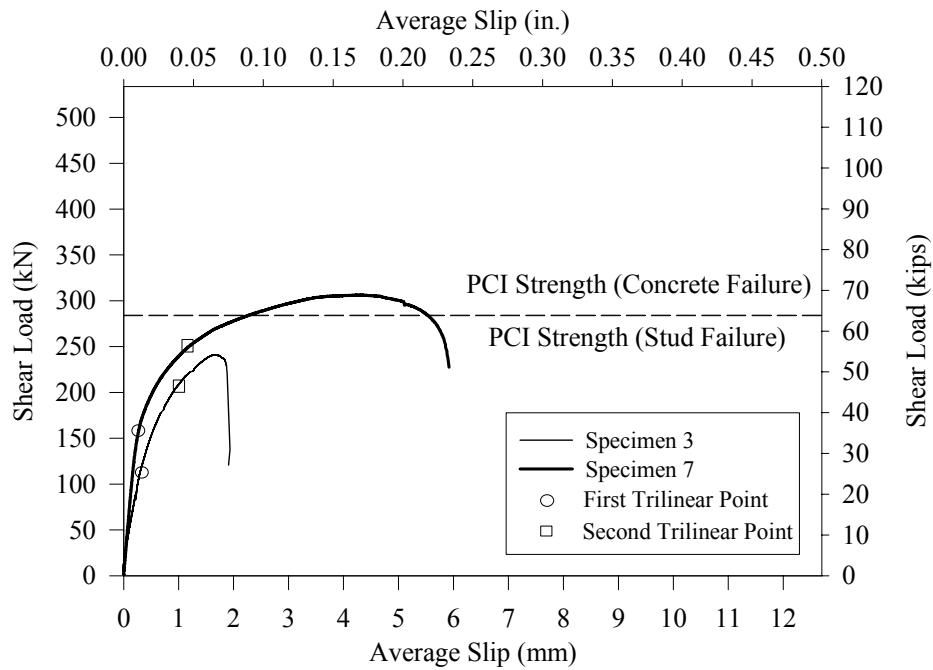


Figure 6.4 Comparison to design formulas for Specimens 3 and 7

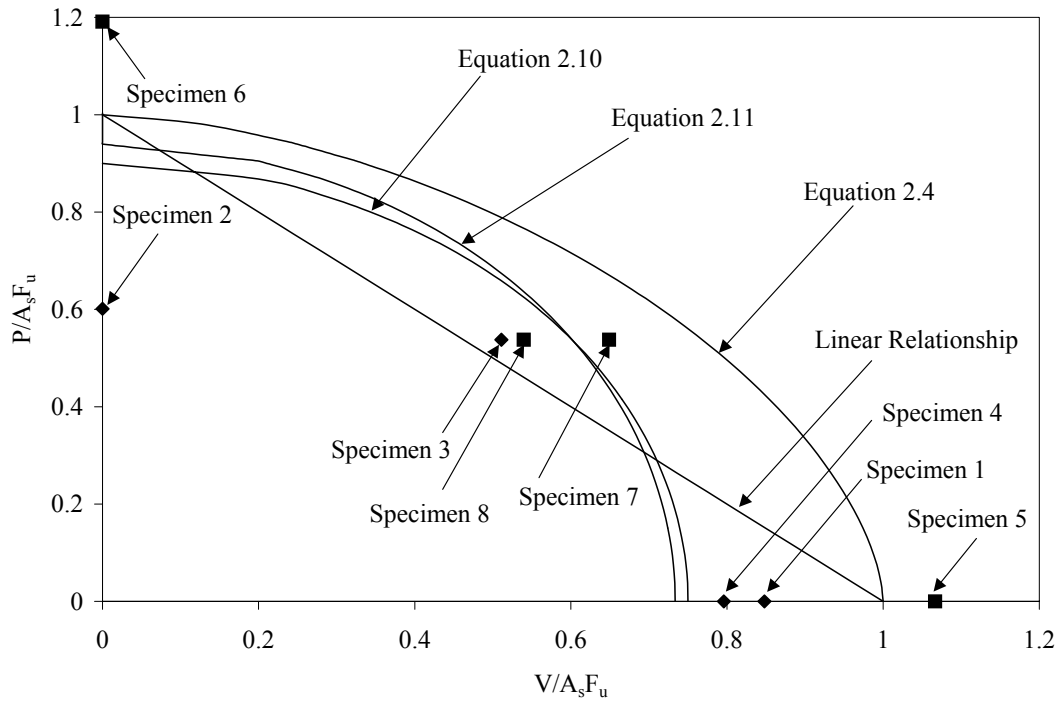


Figure 6.5 Comparison to interaction curves

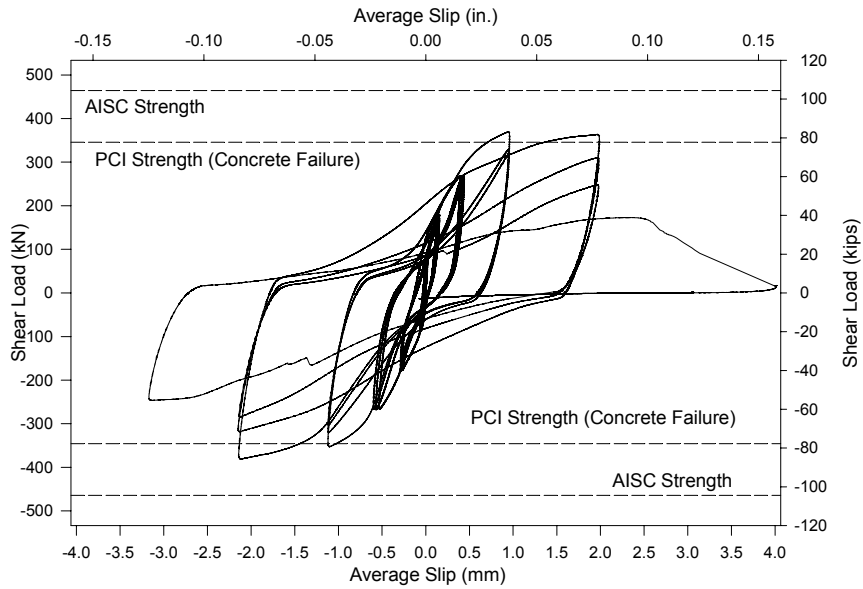


Figure 6.6 Comparison to design formulas for Specimen 4

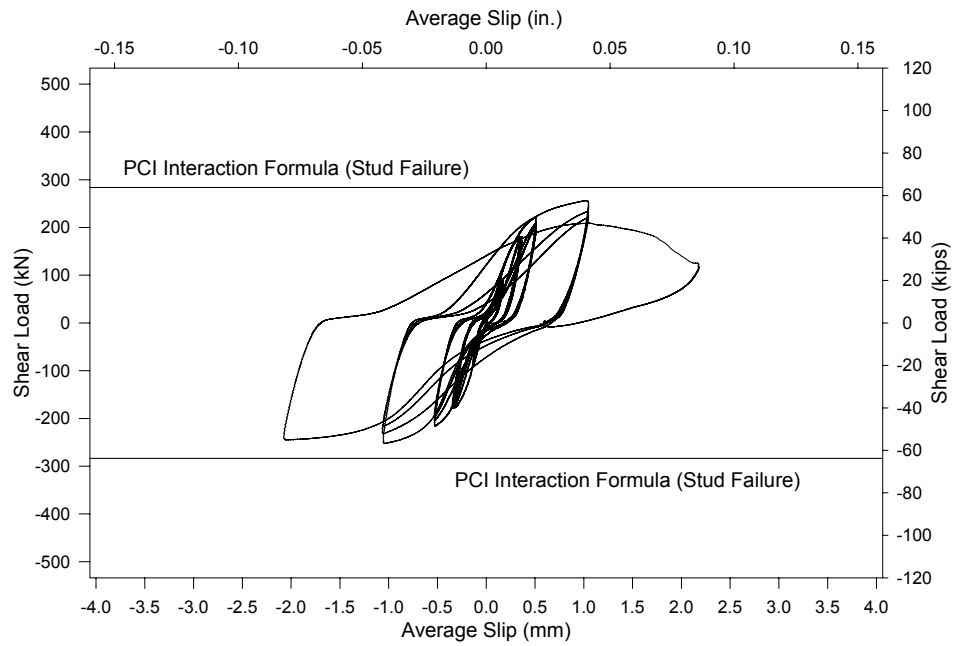


Figure 6.7 Comparison to design formulas for Specimen 8

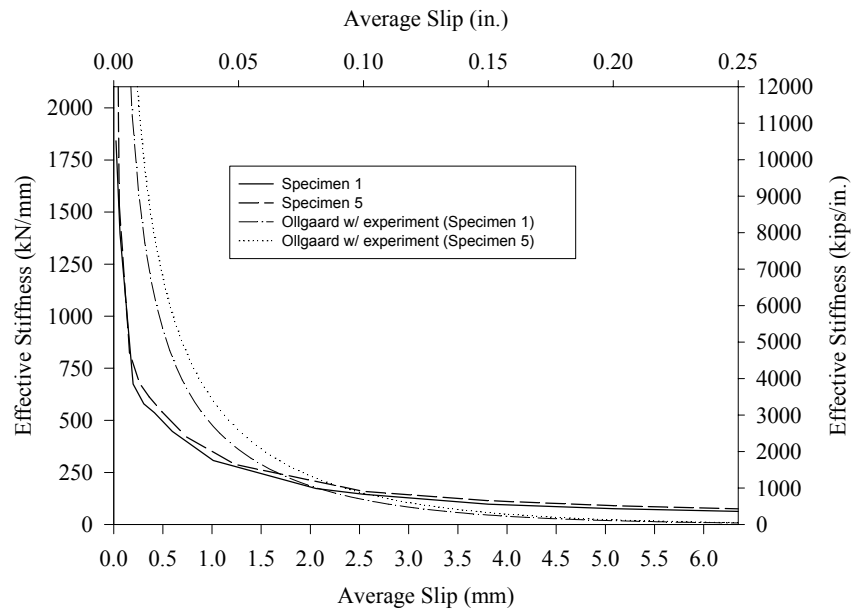


Figure 6.8 Effective secant stiffness versus average slip for Specimens 1 and 5

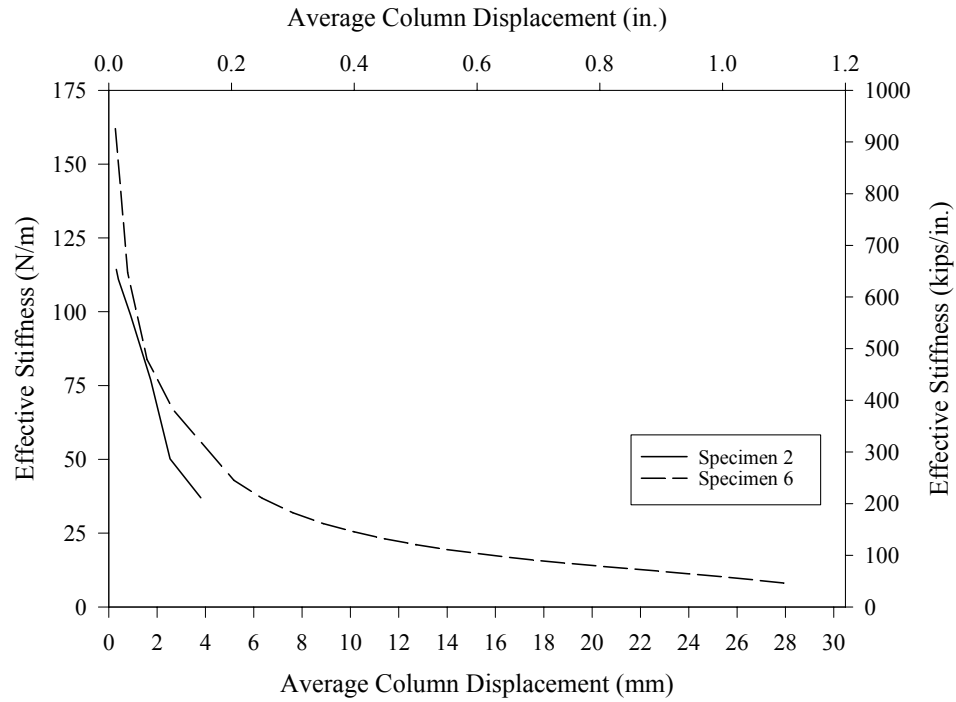


Figure 6.9 Effective secant stiffness versus average column displacement for Specimens 2 and 6

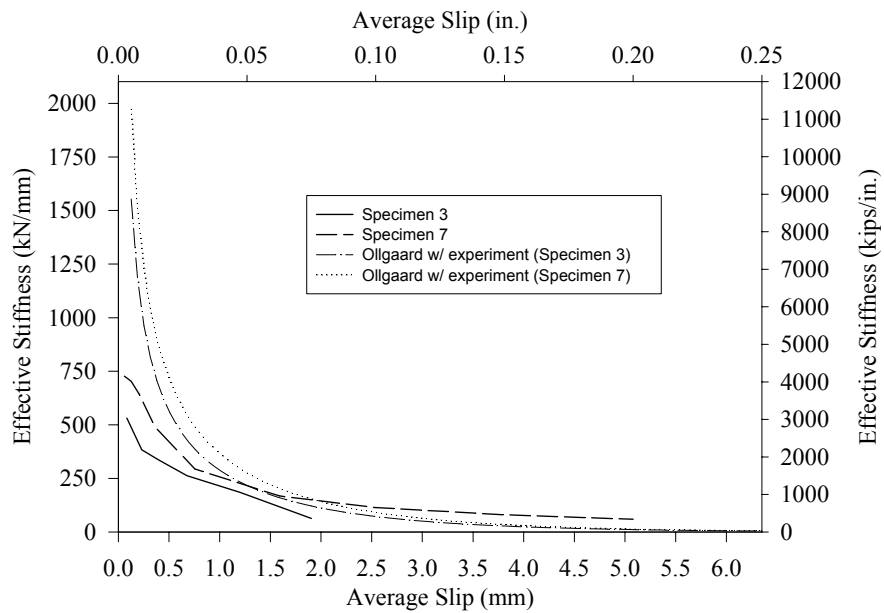


Figure 6.10 Effective secant stiffness versus average slip for Specimens 3 and 7

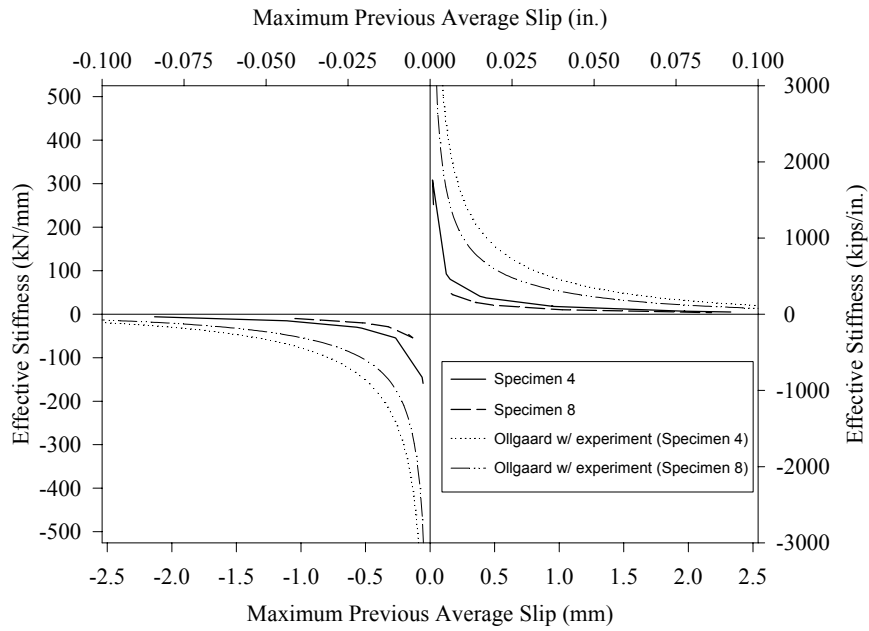


Figure 6.11 Effective stiffness versus average slip for Specimens 4 and 8

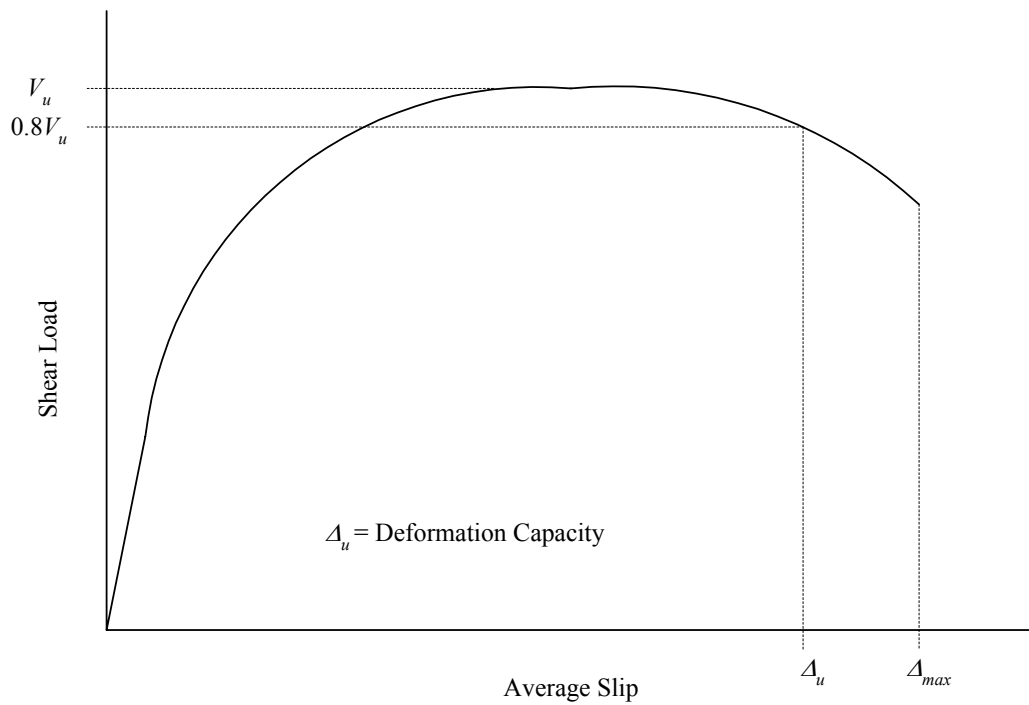


Figure 6.12 Deformation Capacity

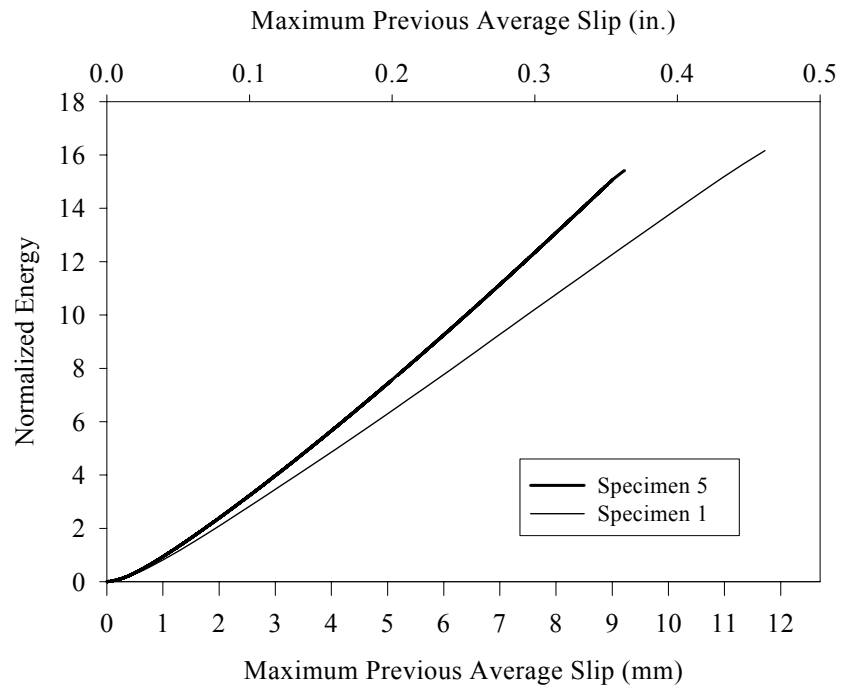


Figure 6.13 Normalized energy versus average slip for Specimens 1 and 5

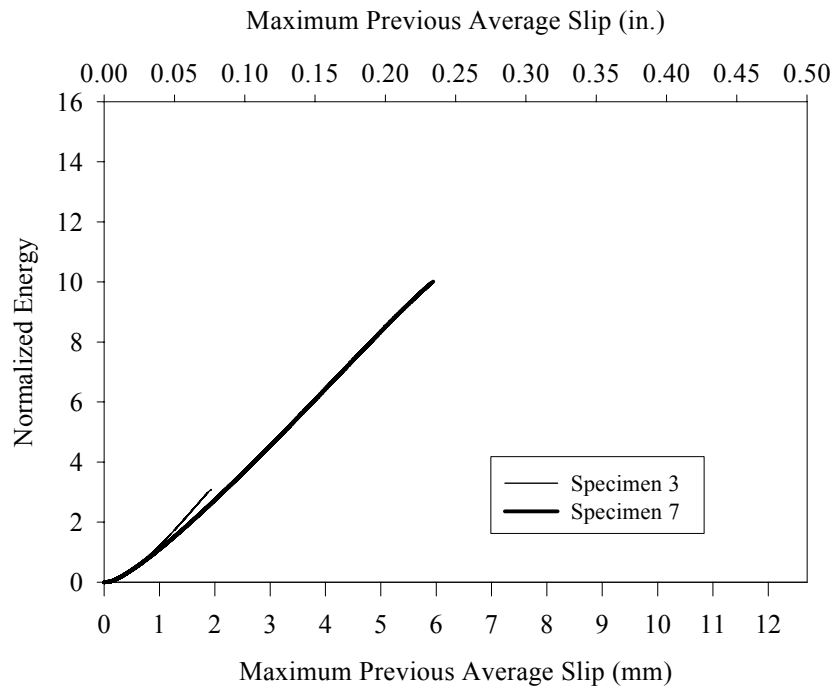


Figure 6.14 Normalized energy versus average slip for Specimens 3 and 7

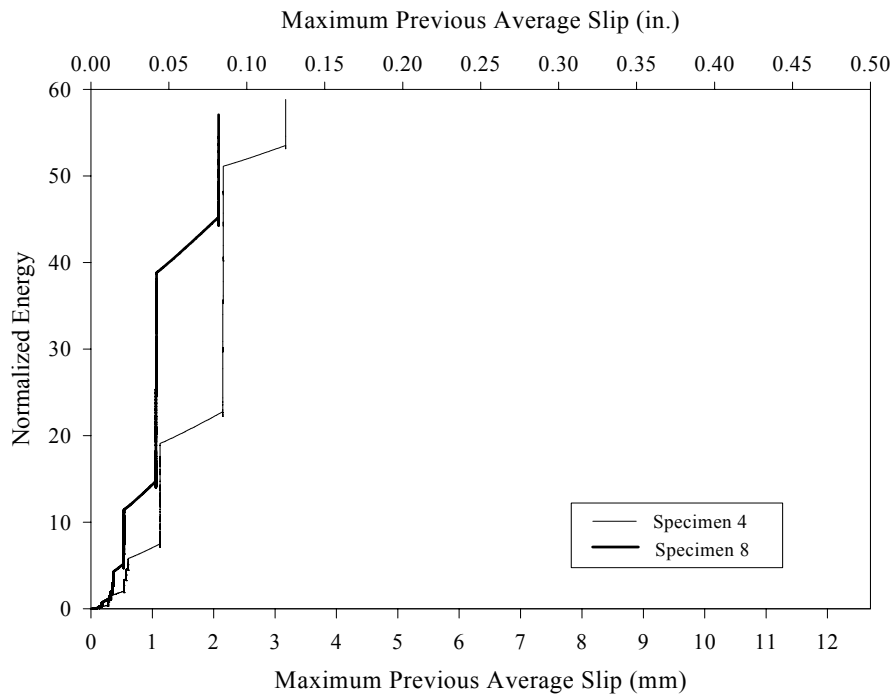


Figure 6.15 Cumulative normalized energy versus average slip for Specimens 4 and 8

A. Test Verification

The following appendix provides verification of the test setup used in the experimental program. The test data collected during the experiments was analyzed by defining the kinematics of the panel during the tests. Figure A.1 shows the degrees of freedom present for the concrete panel and the labeling system used to represent these degrees of freedom. A total of six degrees of freedom were present, including translation and rotation in the x, y, and z directions.

A.1 Translation in the Y Direction (Δ_y)

Translation in the y direction was found by subtracting the east slip from the west slip (Figure 3.9). Figures A.2 through A.9 show the graphs of this translation versus the average slip. From these graphs, the magnitude of this difference is seen to be small, especially at early stages in the load histories. The difference between slip displacements does increase at higher loads, and this is most likely due to damage present in the concrete panel or the shear studs, leading to a variance between the slips at each interface. When looking at the ratio of the difference in slip to the average slip, this ratio can be quite large early in the load history where small slips were measured, with the difference in slip is actually larger than the average slip. The worst case for monotonic shear and cyclic shear are shown in Figures A.10 and A.11 for Specimens 1 and 4, respectively. At small slips, the noise of the LVDT's can have an impact on the difference in slips, and could be a larger contributing factor to large slip differentials than the test setup. For larger slips, the ratio between the slip differential and the average slip

reduces, down to 10 percent for Specimen 1. There is a region between early in the load history (less than 1mm or 0.04 in.) where there is an increase in the slip differential for the two monotonic shear tests (Specimens 1 and 5), as shown in Figures A.2 and A.6. This could be a result of the loss of adhesion between the steel and concrete occurring at different loads. However, once the adhesion is lost at both interfaces, the slip differential reduces.

A.2 Rotation about the Z-Axis (θ_z)

The rotation about the z-axis was determined by taking the previously described difference in the east and west slips and dividing by the width of the panel, as shown in Figure A.12. Figures A.13 through A.20 show the relationship between load and rotation about the z-axis. Some rotation in the plane of the panel was present, but the magnitudes were small, with the largest rotation being approximately 0.0014 radians (0.08 degrees) for Specimen 4 (Figure A.16).

A.3 Translation in the X Direction (Δ_x)

Translation in the x-direction was found by taking the displacement measured from the top column LVDT, and subtracting the average of the displacements from the top four separation LVDT's (Figures 3.9 and 3.10). The same procedure was used for the bottom column and separation LVDT's.

The load versus translation in the x direction is provided in Figures A.21 through A.26. No graphs are provided for the Specimens 1 and 3, since separation LVDT's were present on the south face of the panel only. With the exception of the two pullout tests, the difference between the total separation measured and the column displacement is small. For the two pullout tests, this difference is more substantial, as expected. One possible explanation could be that the A-Frame column was translating. However, a dial gage was placed near the base of the A-Frame column for each test (Figure 3.12), and

showed no translation of the column. A more likely possibility lies in other sources of displacement included in the column displacement that are not measured by the separation LVDT's, namely concrete cracking. There was considerable cracking present in the monotonic tension tests, and the additional displacements being measured by the column LVDT's represent the opening of cracks in the panel.

For Specimen 2 in Figure A.21, it is noticed that the top displacement differential is larger than for the bottom. For this test, the largest cracks with respect to the panel thickness were in the top of the panel, leading to a larger difference between the column and separation LVDT's for the top of the panel. For the other monotonic tension test (Specimen 6) in Figure A.24, the maximum difference in displacement is less than was the case for Specimen 2. Even though there was cracking present in the panel for Specimen 6, the cracks did not open to the extent of Specimen 2 due to the confinement cage used in Specimen 6. This explains the smaller magnitudes in the difference between the column LVDT's and the separation LVDT's.

A.4 Rotation about the Y-Axis (θ_y)

Figure A.27 shows the rotation about the y-axis. Rotation about the y-axis was calculated by taking the difference in the displacements between the north and south face separation LVDT's, and dividing by the thickness of the panel. This was performed for each pair of north and south face separation LVDT's. Figures A.28 through A.33 show the load versus θ_y plots. As discussed in the previous section, there are no graphs for Specimens 1 and 3, since separation LVDT's were not placed on the north face.

There was minimal rotation present about the y-axis. In addition, several specimens (2, 4, 5, and 6) indicate that the rotation at the east panel-column interface is in the opposite direction than that at the west panel-column interface. The worst case was noted for Specimen 5 (Figure A.30) with a maximum rotation equal to 0.007 radians (0.4 degrees). However, the cosine of that angle was equal to approximately 0.99998,

which is beyond the accuracy of the measuring instrument (i.e. the LVDT) itself, indicating that no correction of the separation displacements is necessary.

A.5 Translation in the Z-Direction (Δ_z)

One dial gage was used to measure the out-of-plane translation of the panel. Monitoring of this gage during testing showed that the out-of-plane translation did not exceed 0.01 in. with respect to the foundation beam.

A.6 Rotation about the X-Axis (θ_x)

As was the case with the out-of-plane translation, there was no instrumentation continuously collecting data during testing which could be used to determine the out-of-plane rotation. However, the small magnitudes of out-of-plane translation would seem to indicate that any out-of-plane rotation of the panel were small.

A.7 Verification of Slip Measurements

Based on the rotation of the panel about the y-axis, further investigation was required to determine the impact this rotation on the measurement of slip. As the panel rotates, the studs are deformed horizontal in addition to vertically, indicating that the measured vertical slip is a component of the true slip, as shown in Figure A.34. To assess the difference between the true slip and its vertical component, the angle between the true slip and its vertical component was calculated. This angle was determined by first taking the average θ_y of the separation LVDT's for each panel- column interface, and then multiplying by the corresponding average separation displacements at each interface. An additional contribution exists from the rotation of the panel relative to the steel columns. This component is equal to one-half of the width of the panel multiplied

by the average of θ_y . With the width of the panel being large with respect to the measured slips, this contribution may potentially affect the results. However, with no out-of-plane bracing present for the steel columns, it is likely that there is also out-of-plane movement of the steel columns. Furthermore, θ_y was determined using separation displacements, a highly localized quantity, and to relate this to a global displacement as suggested may not be reasonable. As a result, this second contribution to the horizontal displacement was neglected.

As a result of the preceding arguments, taking the inverse tangent of the quantity previously defined divided by the measured slip at the interface gives the angle between the true slip and the measured vertical component. The true slip is then the measured vertical slip divided by the cosine of this angle (β). The cosine of the angle between the true slip and the measured vertical component (β) was calculated over the entire slip history for each test. The smallest cosine would give the largest discrepancy between the measured and true slips. The worst case calculated was for Specimen 5, but the cosine was equal to approximately 0.999999, which is well beyond the accuracy of the slip LVDT's, indicating that no correction of the measured slips was necessary.

Based on the preceding analysis, the test setup and measurements appear to be sufficiently accurate. Thus, the measured and computed displacements are the same and need no correction.

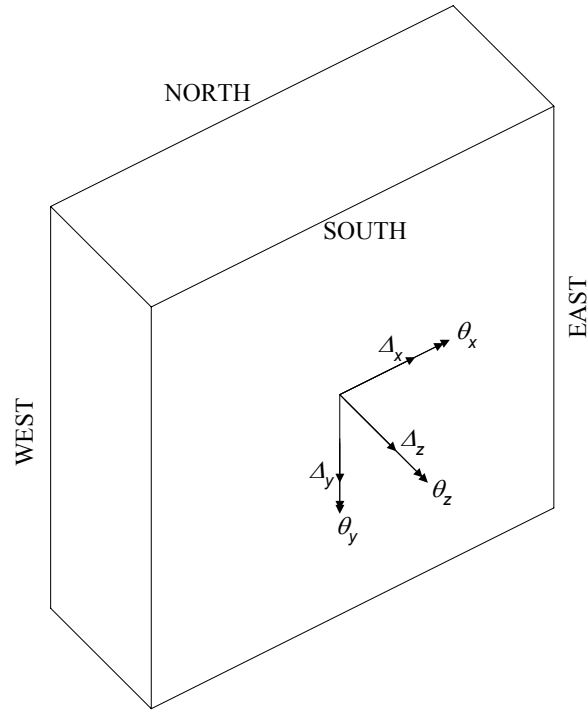


Figure A.1 Degrees of freedom for panel translation and rotation

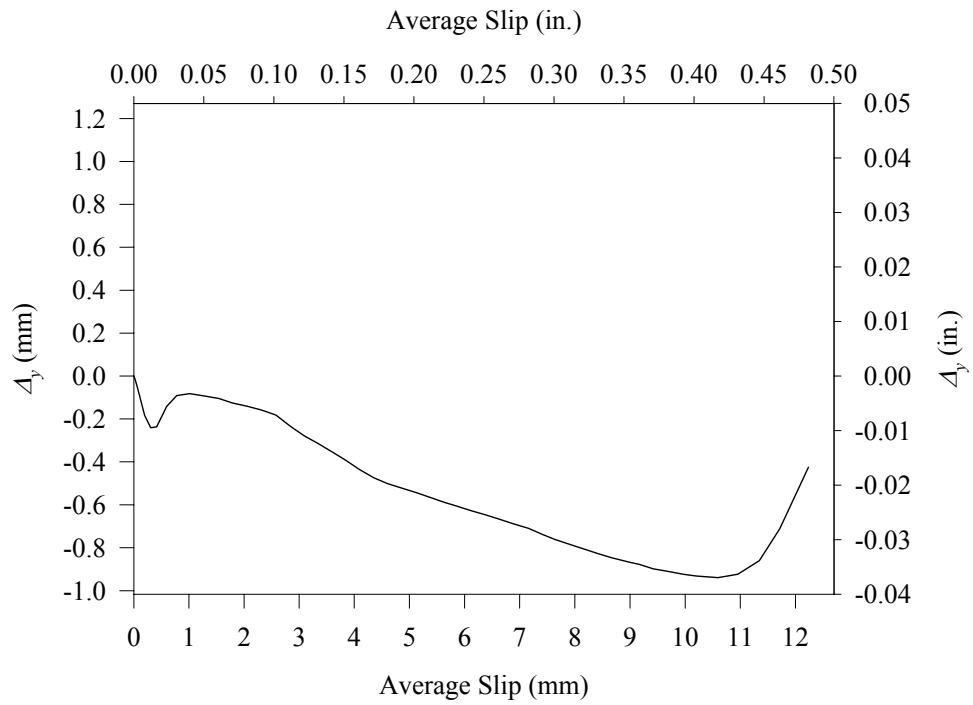


Figure A.2 Translation in the y-direction, Δ_y , for Specimen 1

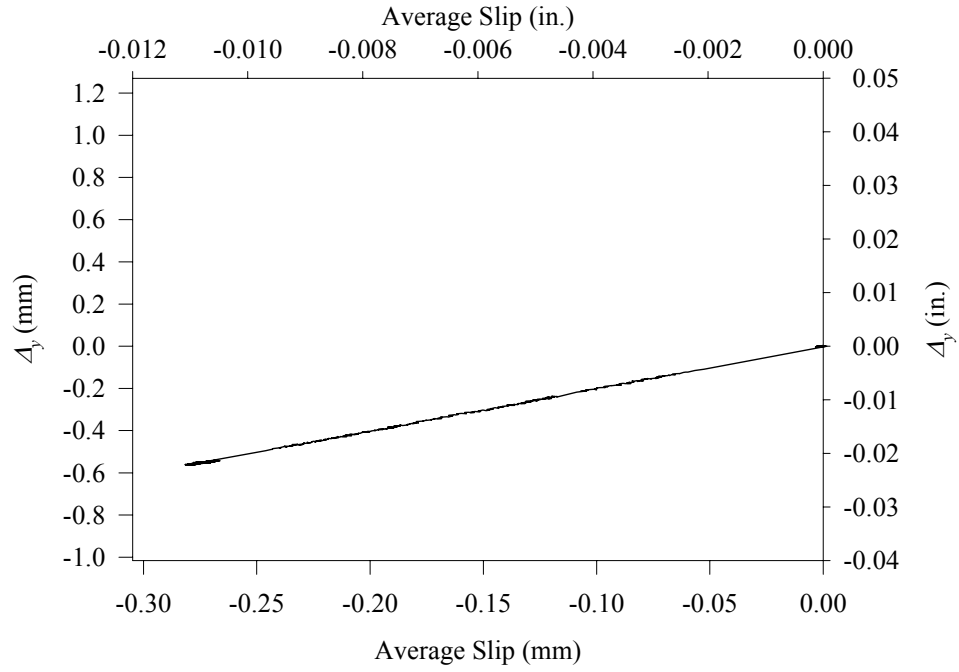


Figure A.3 Translation in the y-direction, Δ_y , for Specimen 2

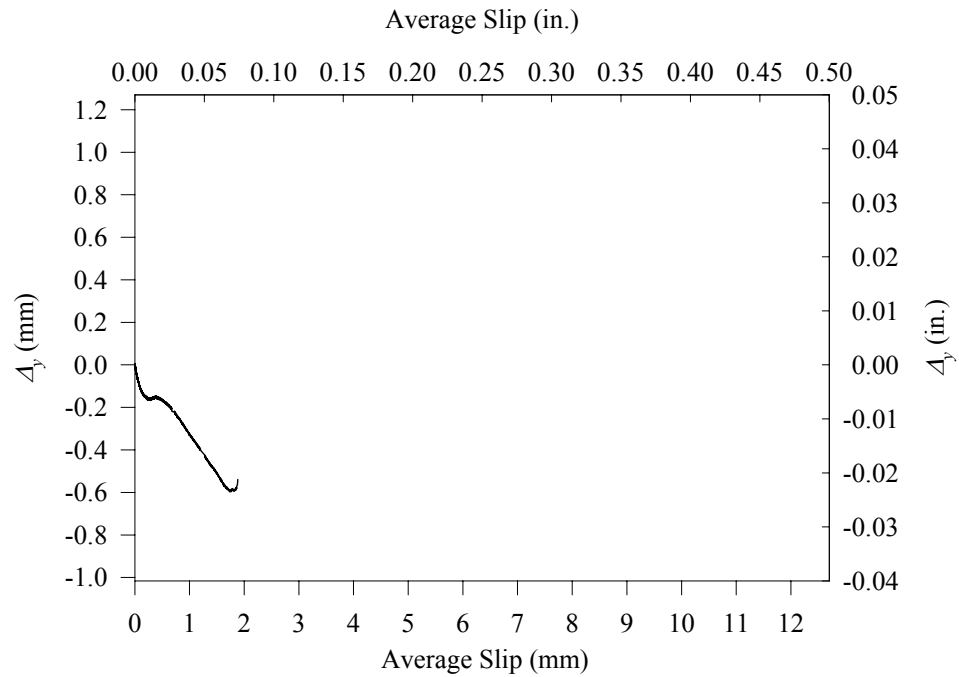


Figure A.4 Translation in the y-direction, Δ_y , for Specimen 3

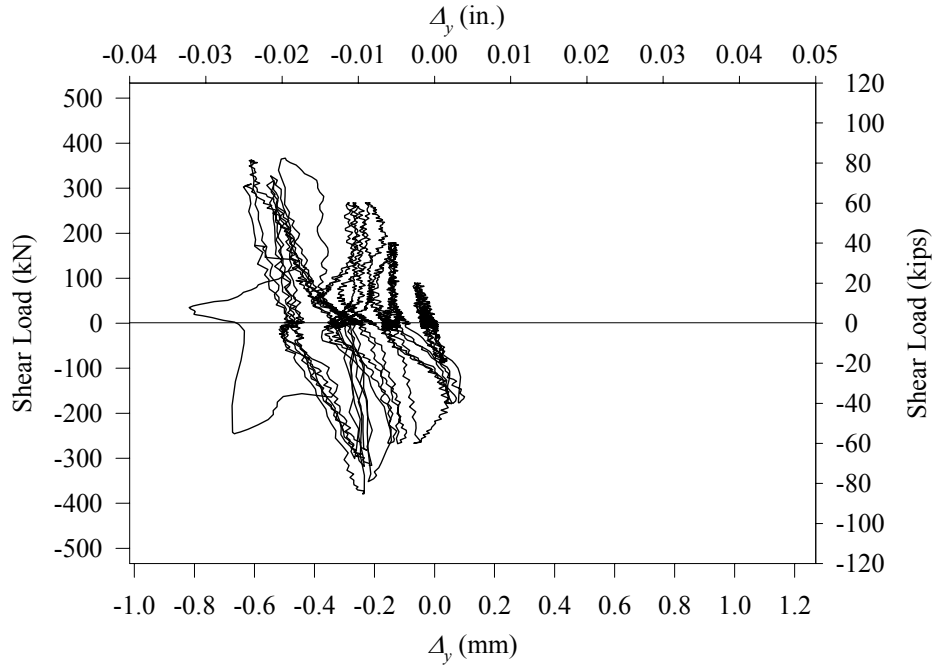


Figure A.5 Translation in the y-direction, Δ_y , for Specimen 4

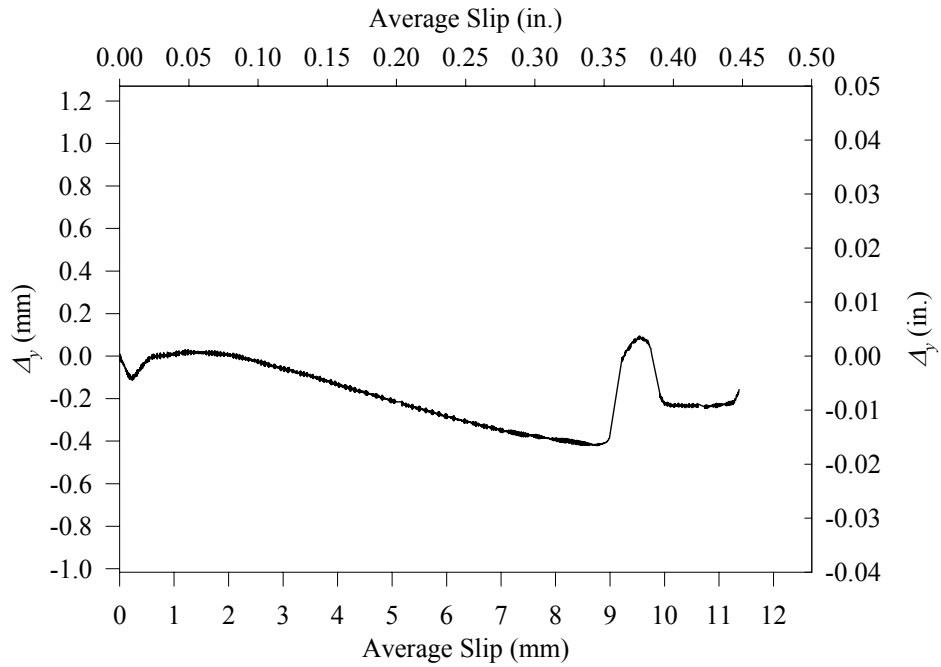


Figure A.6 Translation in the y-direction, Δ_y , for Specimen 5

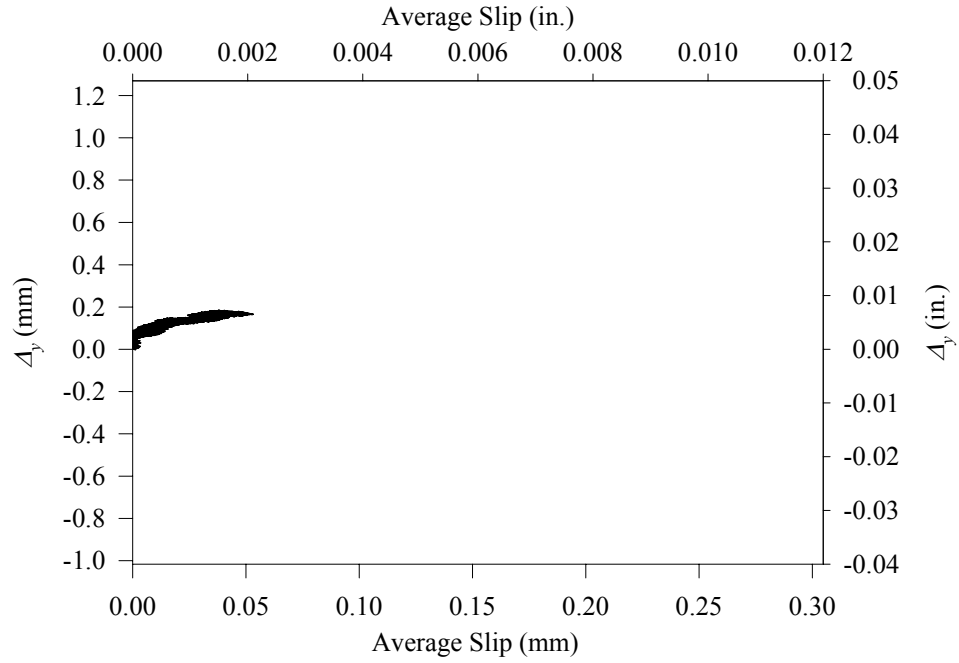


Figure A.7 Translation in the y-direction, Δ_y , for Specimen 6

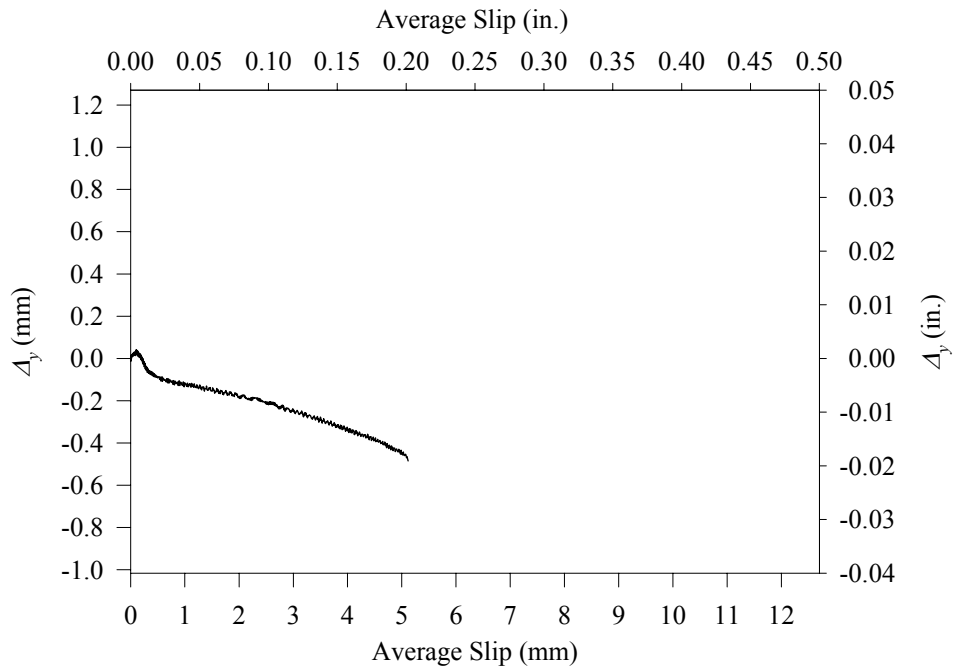


Figure A.8 Translation in the y-direction, Δ_y , for Specimen 7

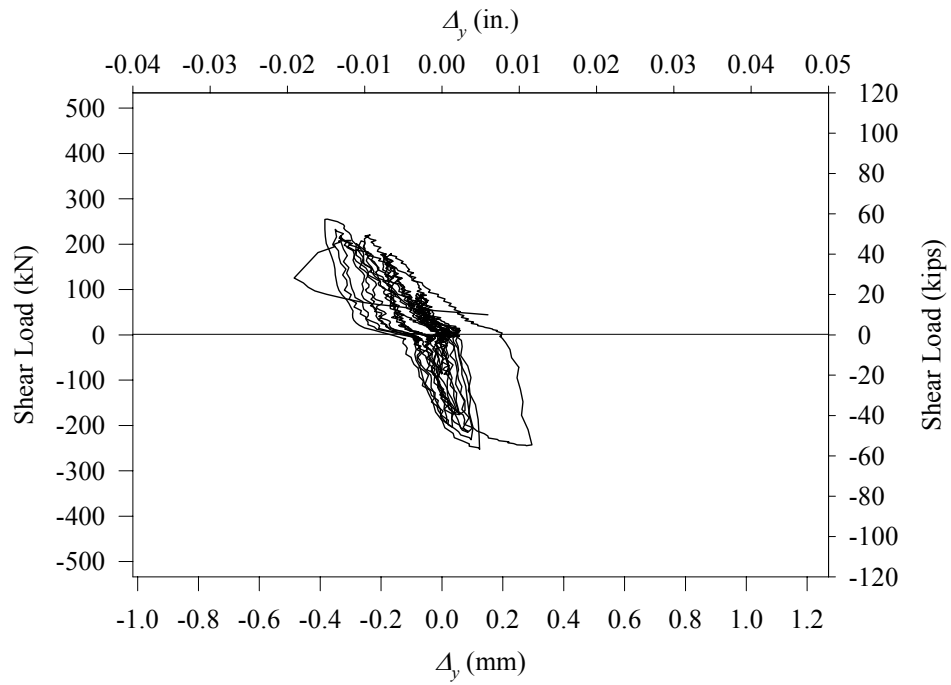


Figure A.9 Translation in the y-direction, Δ_y , for Specimen 8

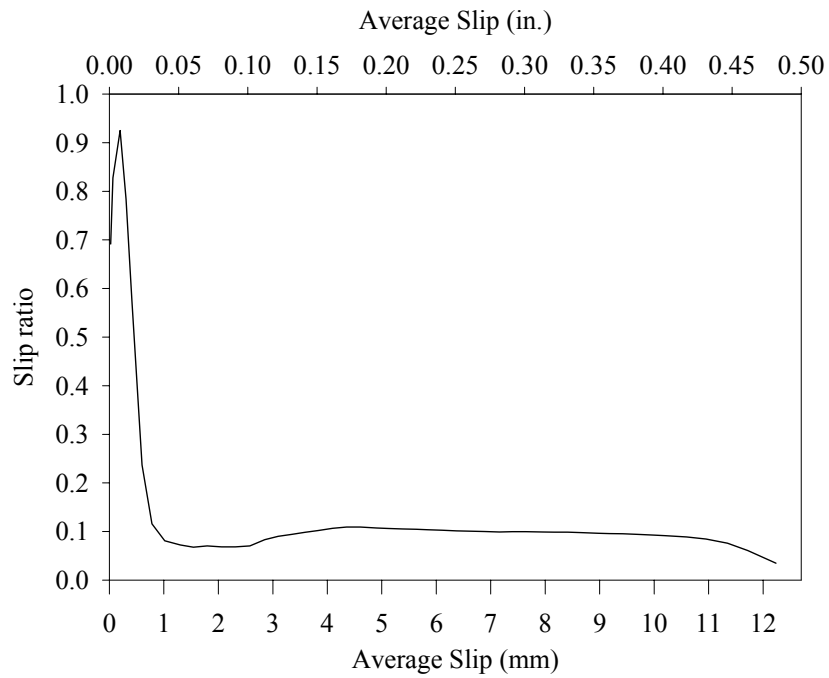


Figure A.10 Slip ratio versus average slip for Specimen 1

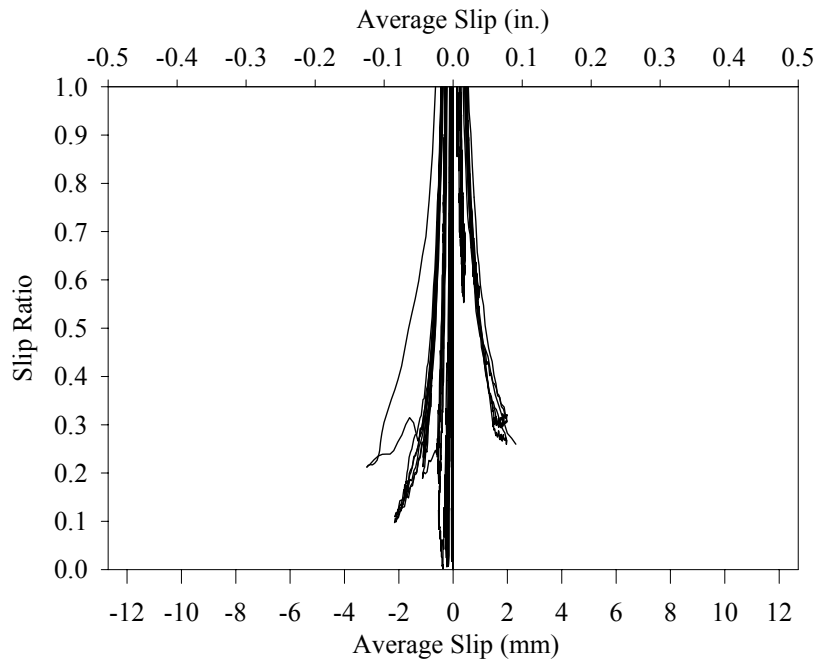


Figure A.11 Slip ratio versus average slip for Specimen 4

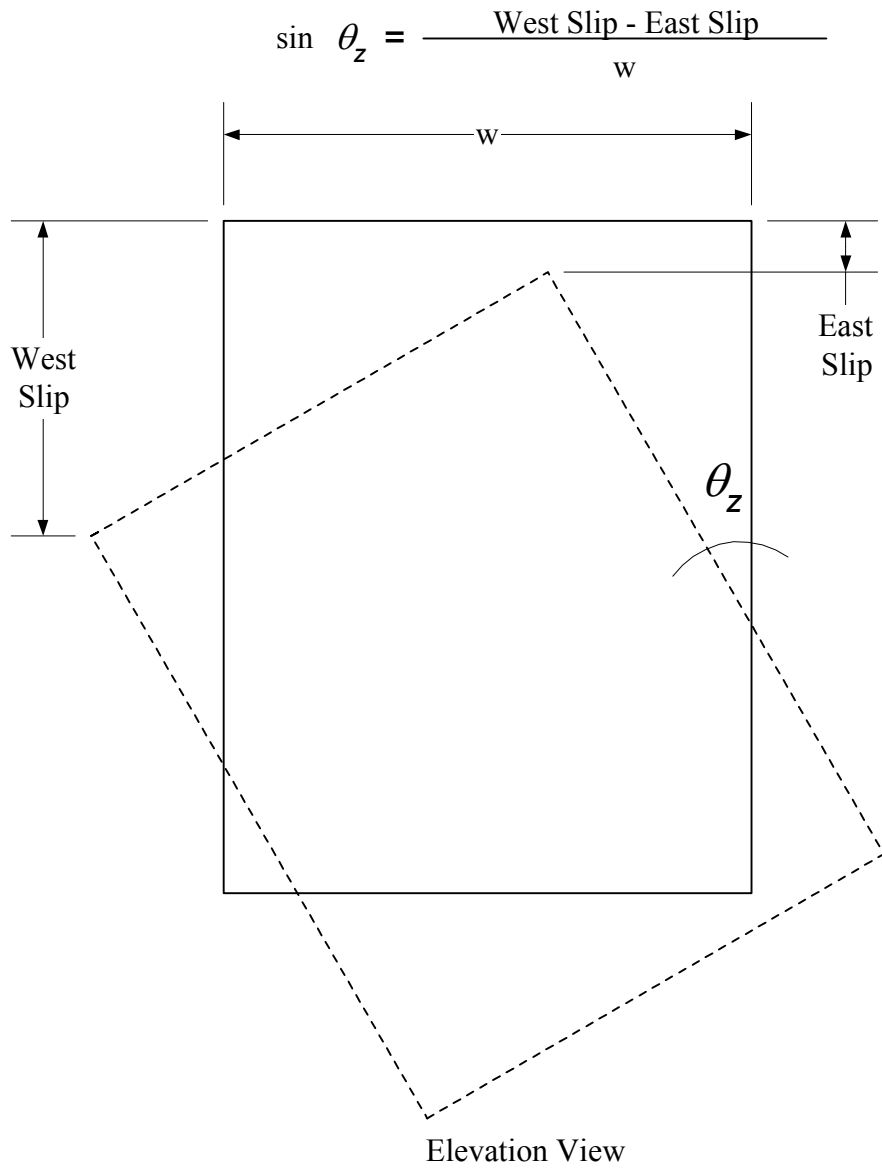


Figure A.12 Rotation about the z-axis, θ_z

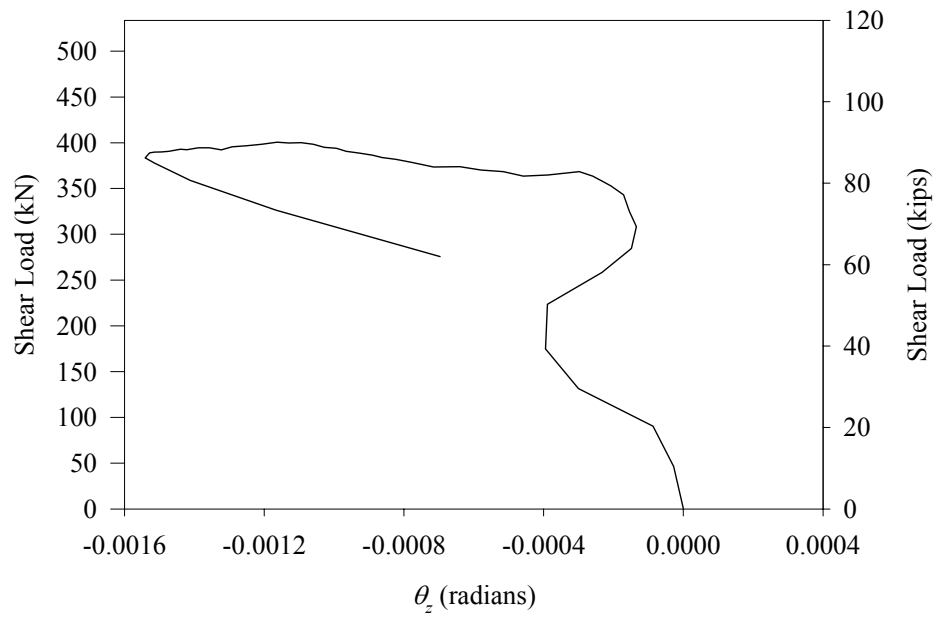


Figure A.13 Rotation about the z-axis, θ_z , for Specimen 1

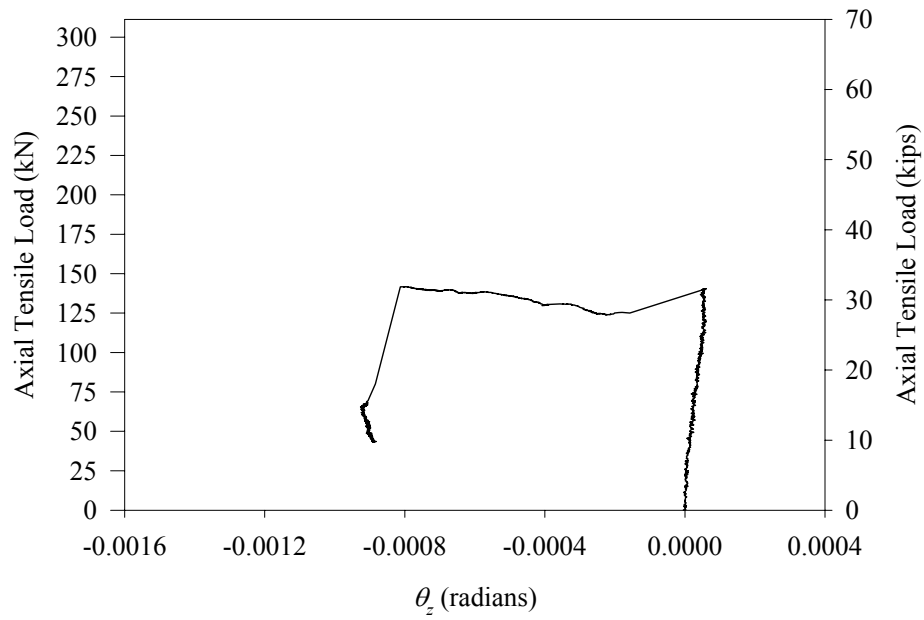


Figure A.14 Rotation about the z-axis, θ_z , for Specimen 2

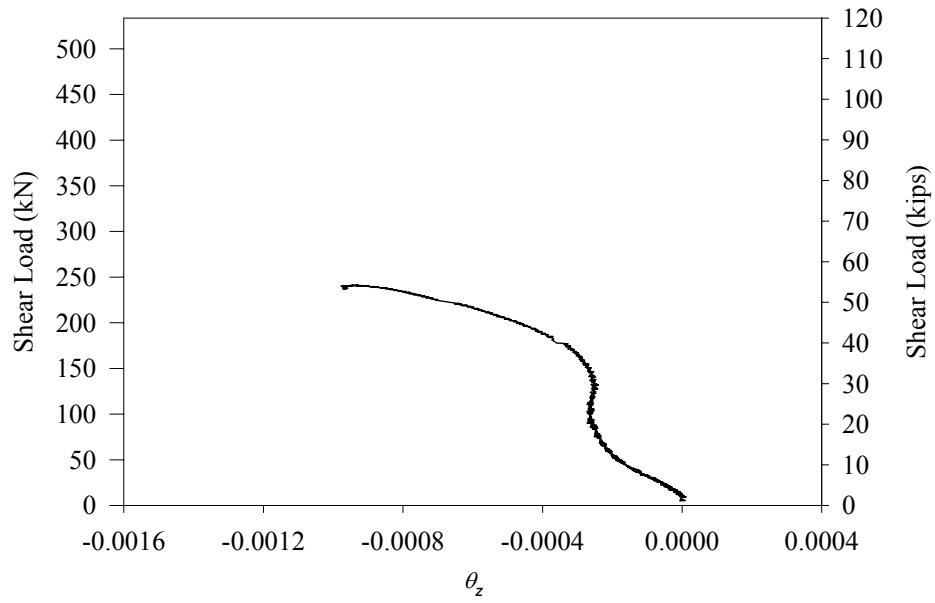


Figure A.15 Rotation about the z-axis, θ_z , for Specimen 3

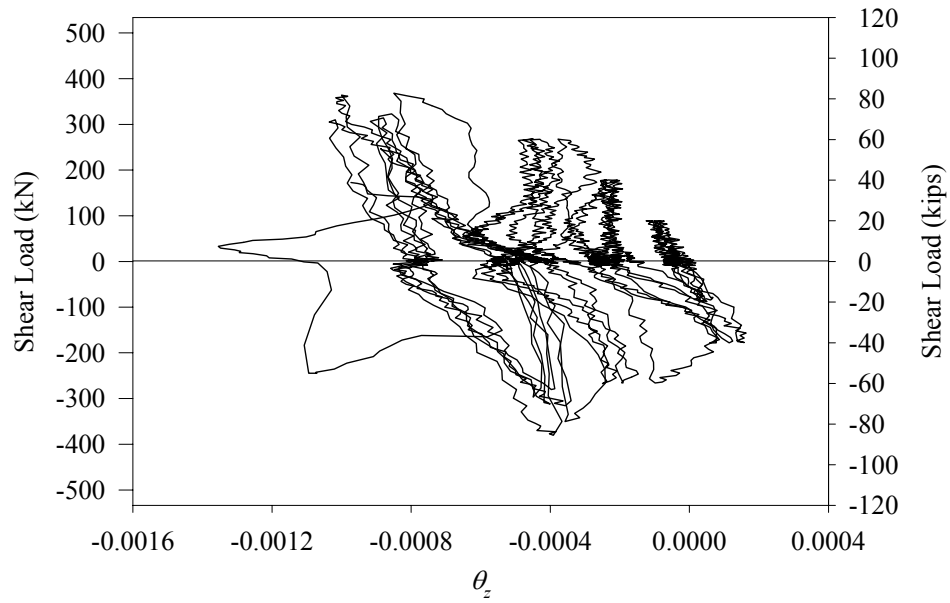


Figure A.16 Rotation about the z-axis, θ_z , for Specimen 4

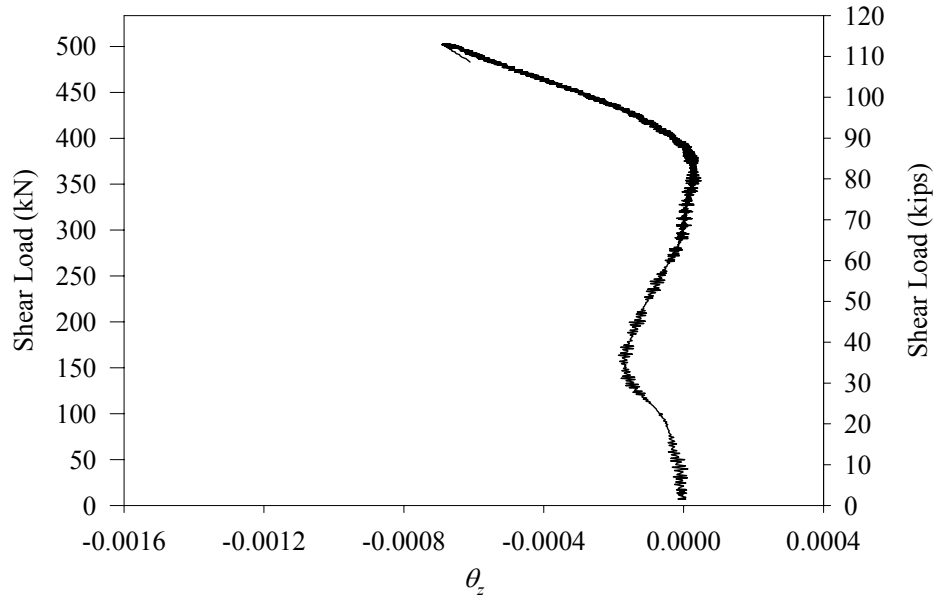


Figure A.17 Rotation about the z-axis, θ_z , for Specimen 5

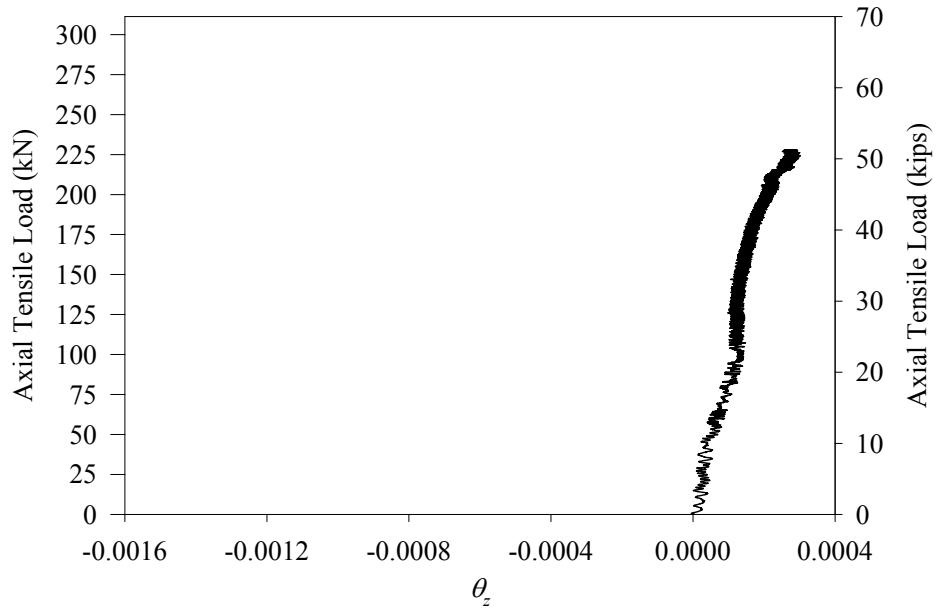


Figure A.18 Rotation about the z-axis, θ_z , for Specimen 6

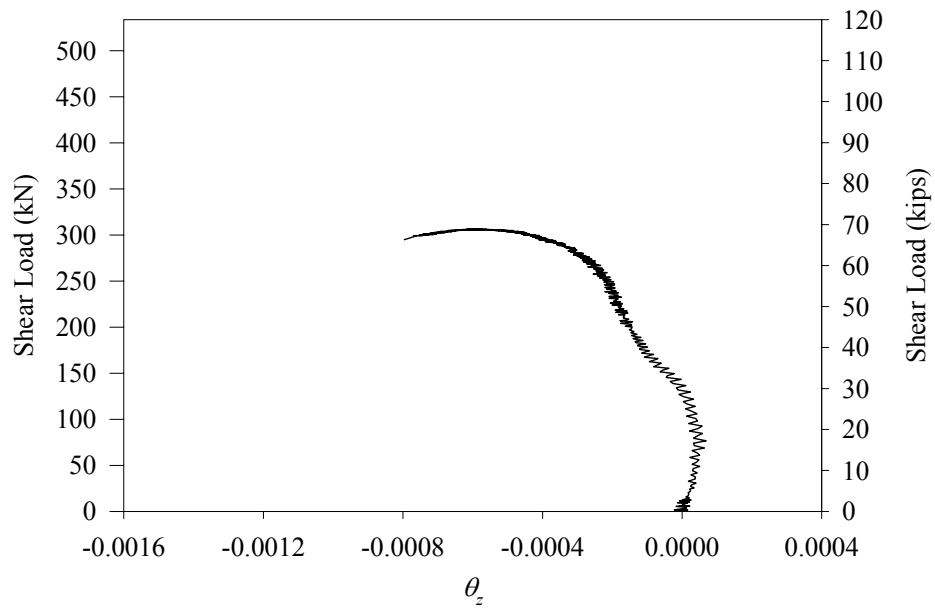


Figure A.19 Rotation about the z-axis, θ_z , for Specimen 7

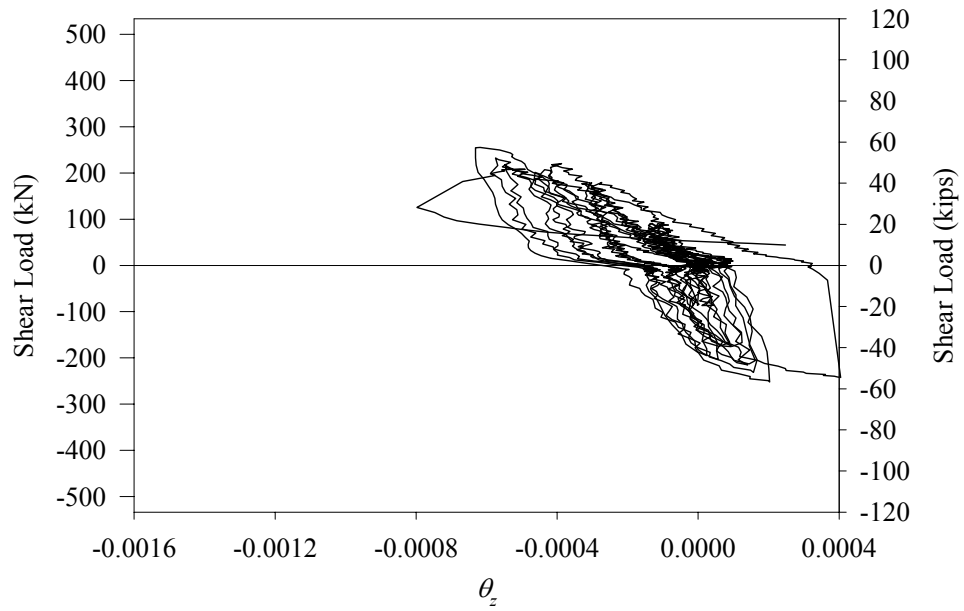


Figure A.20 Rotation about the z-axis, θ_z , for Specimen 8

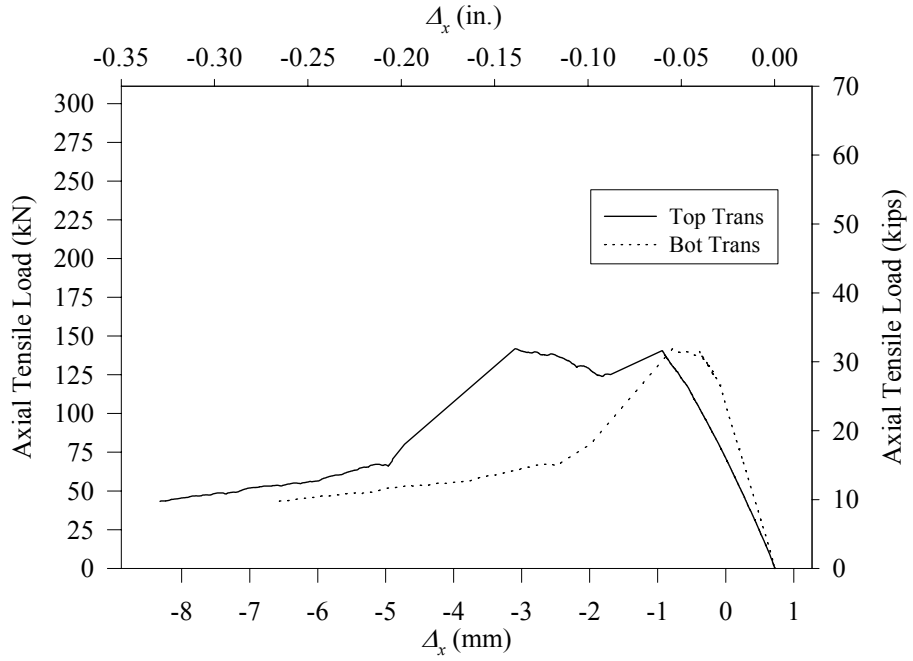


Figure A.21 Translation in the x-direction, Δ_x , for Specimen 2

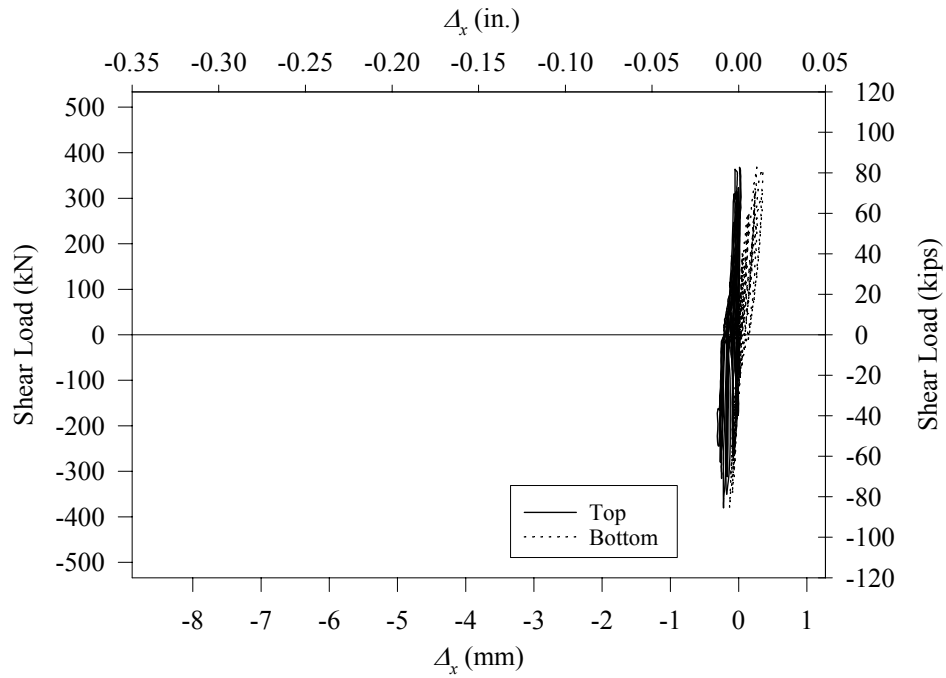


Figure A.22 Translation in the x-direction, Δ_x , for Specimen 4

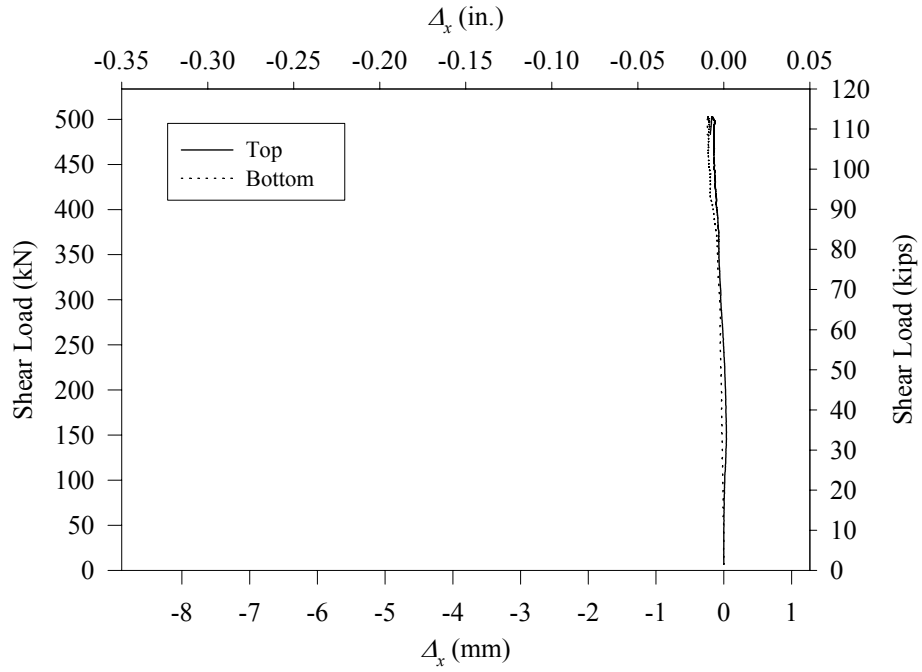


Figure A.23 Translation in the x-direction, Δ_x , for Specimen 5

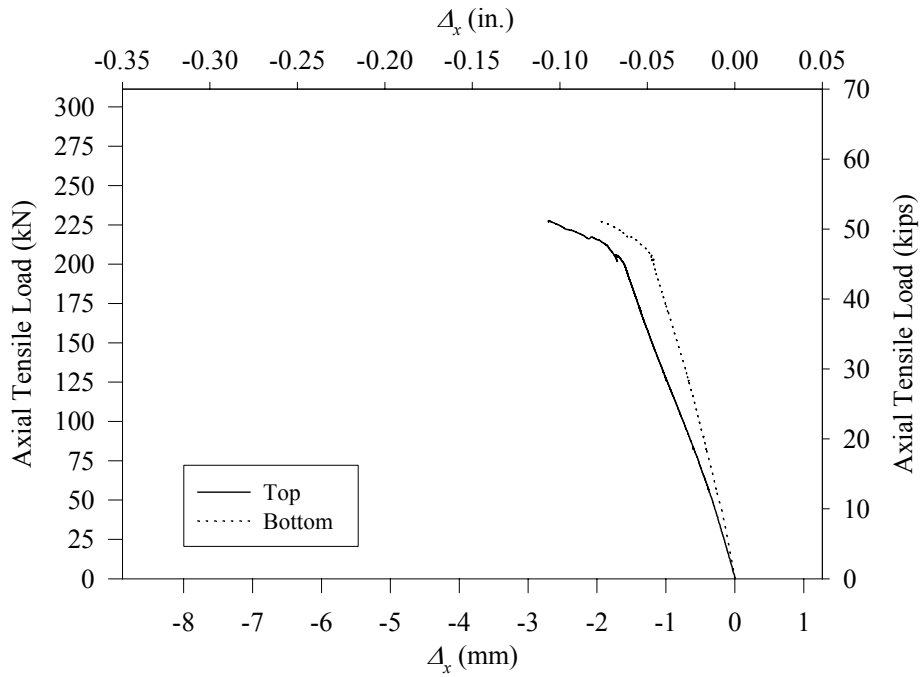


Figure A.24 Translation in the x-direction, Δ_x , for Specimen 6

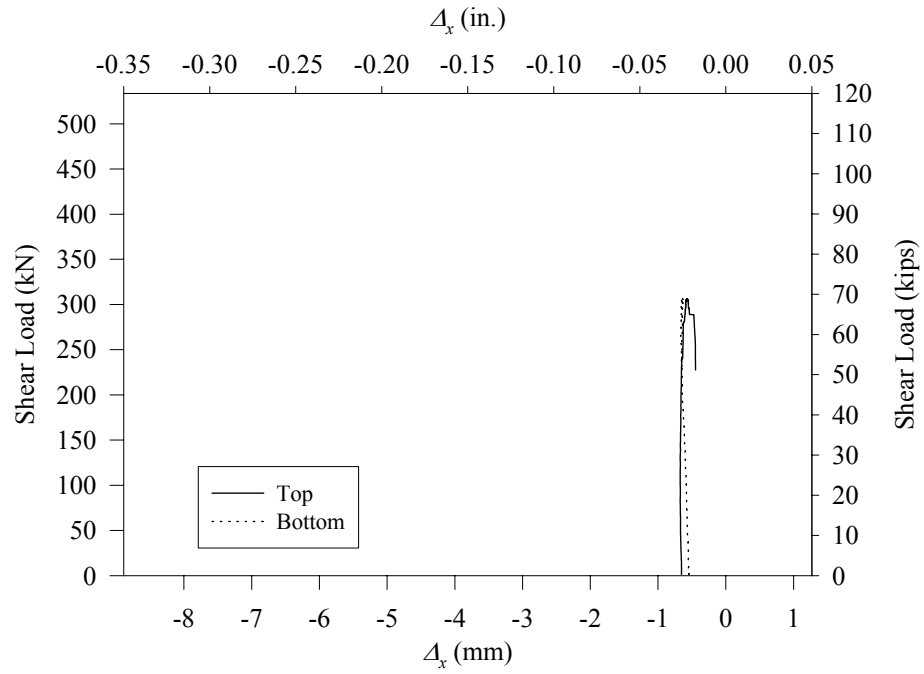


Figure A.25 Translation in the x-direction, Δ_x , for Specimen 7

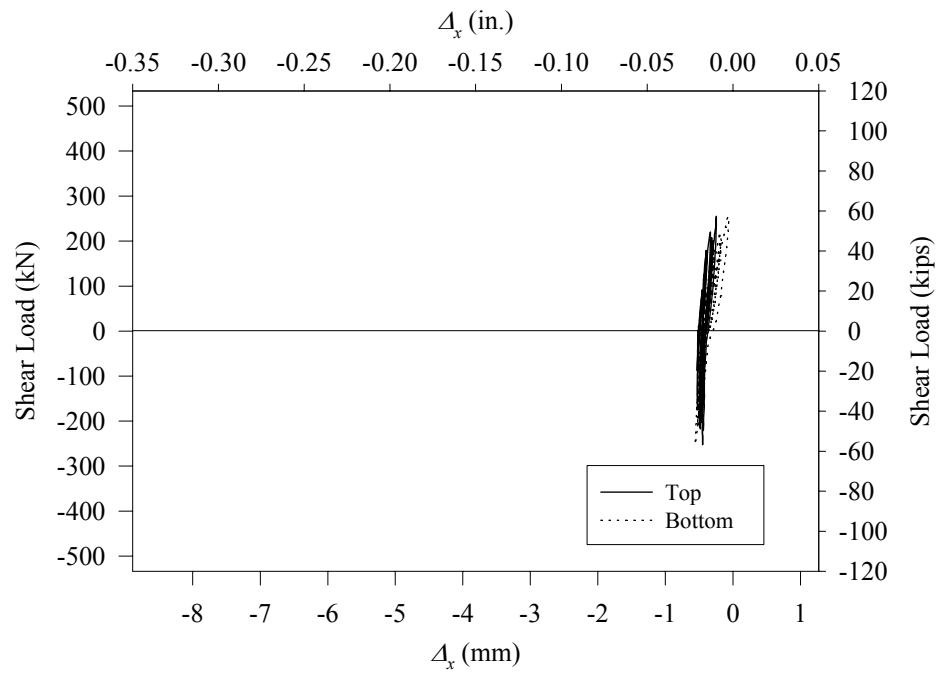


Figure A.26 Translation in the x-direction, Δ_x , for Specimen 8

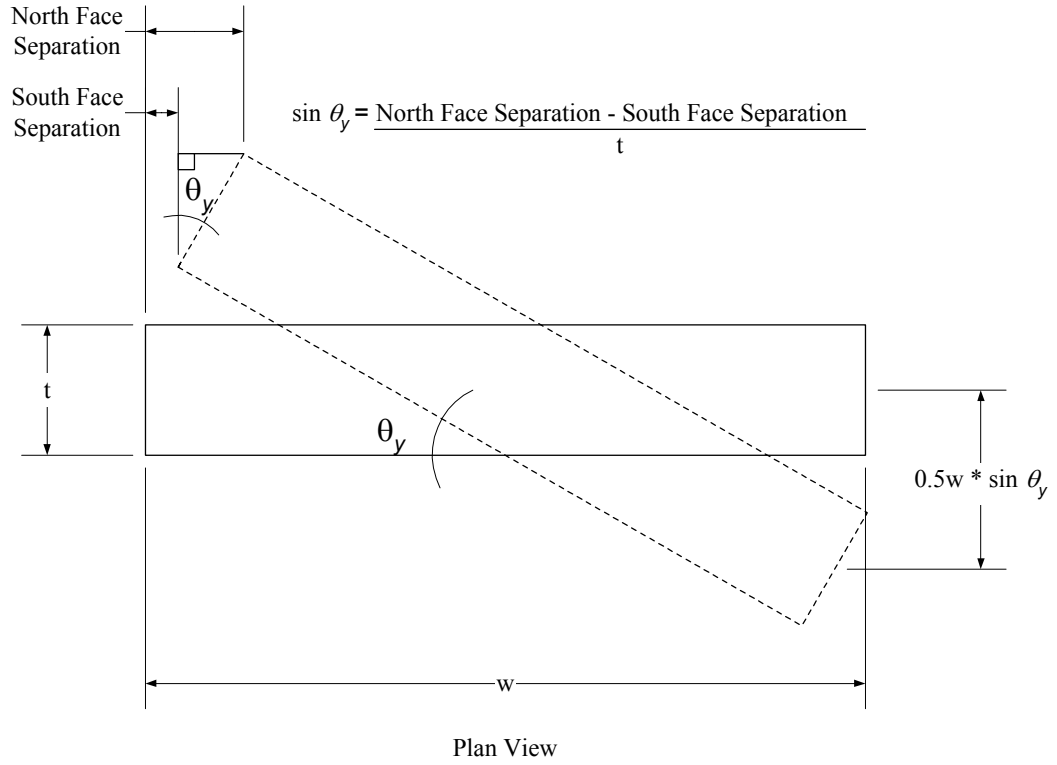


Figure A.27 Rotation about the y-axis, θ_y

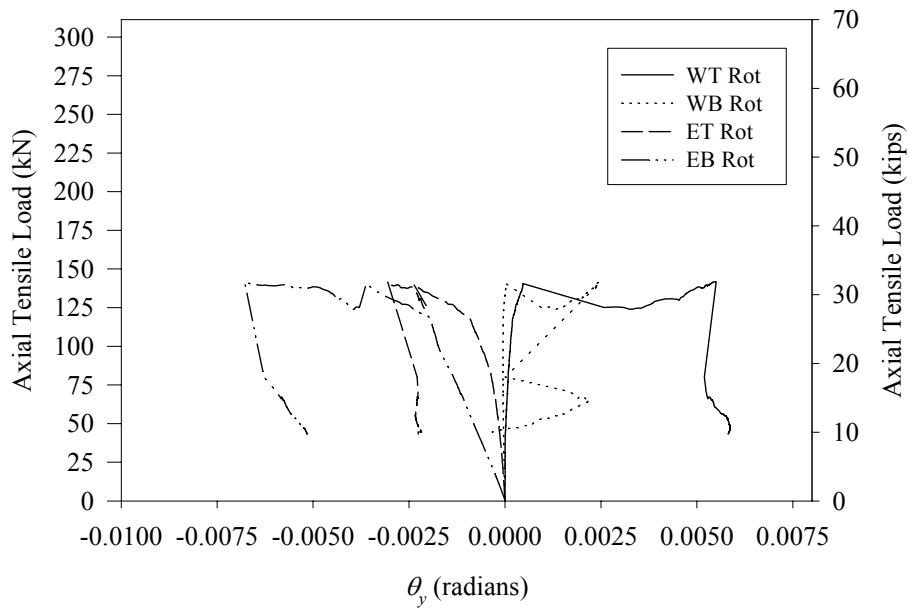


Figure A.28 Rotation about the y-axis, θ_y , for Specimen 2

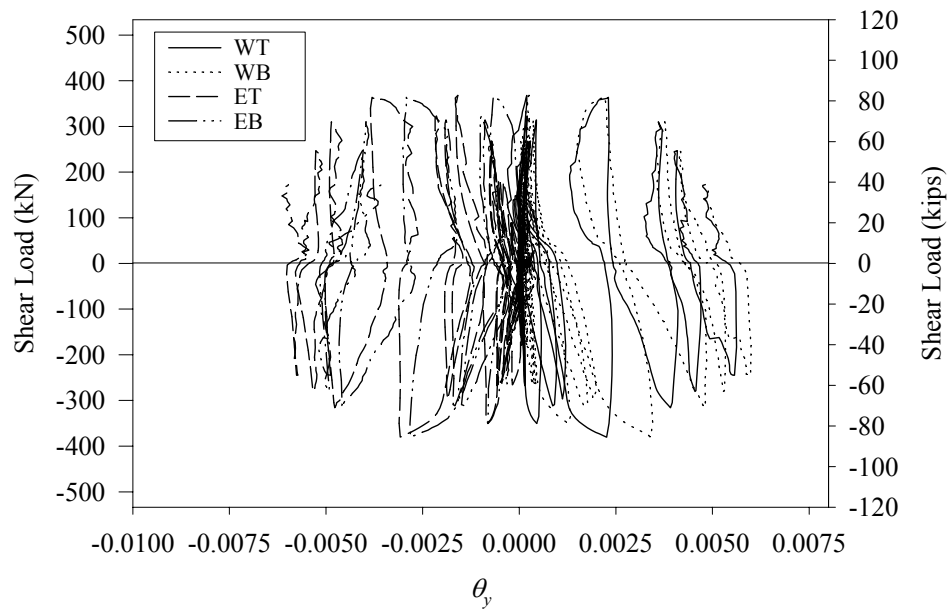


Figure A.29 Rotation about the y-axis, θ_y , for Specimen 4

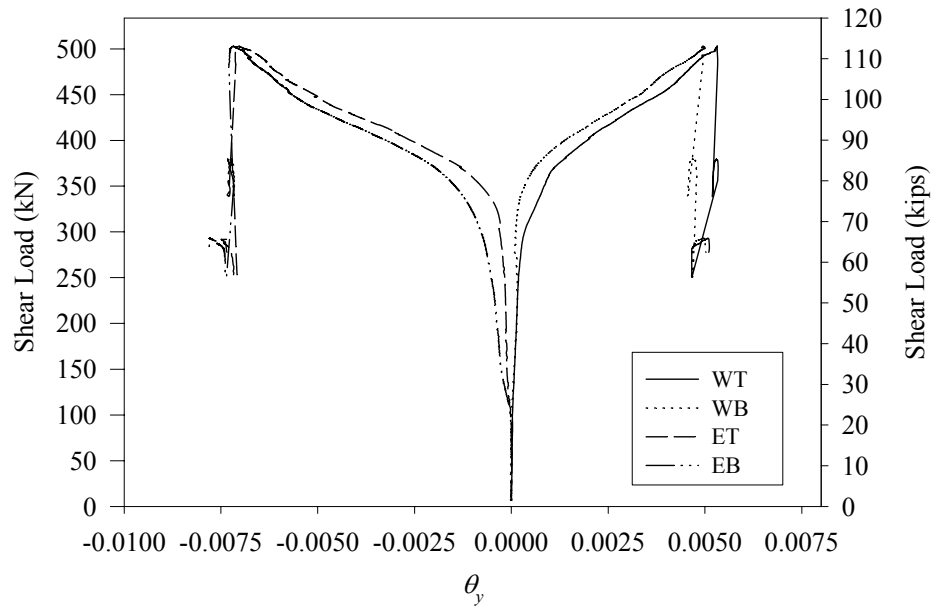


Figure A.30 Rotation about the y-axis, θ_y , for Specimen 5

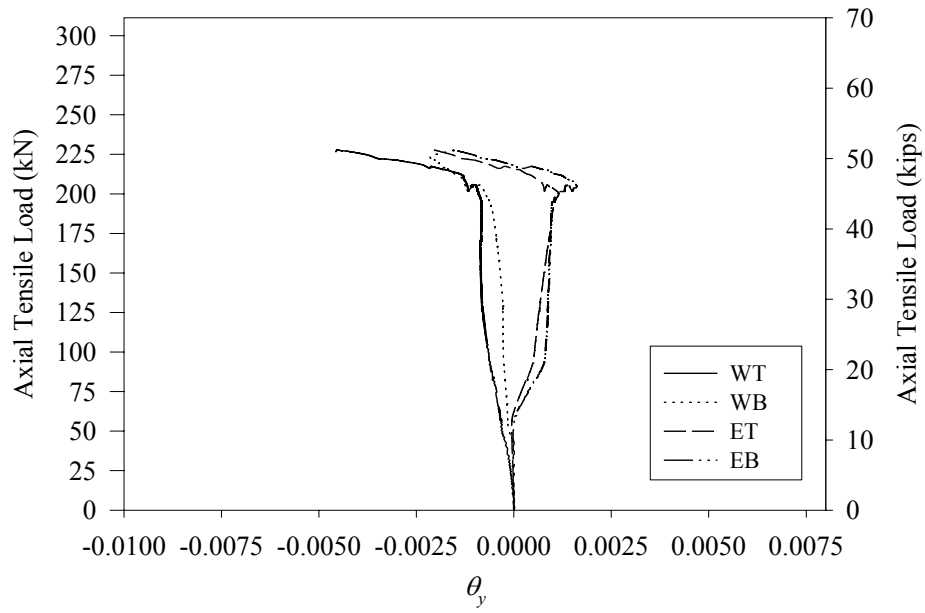


Figure A.31 Rotation about the y-axis, θ_y , for Specimen 6

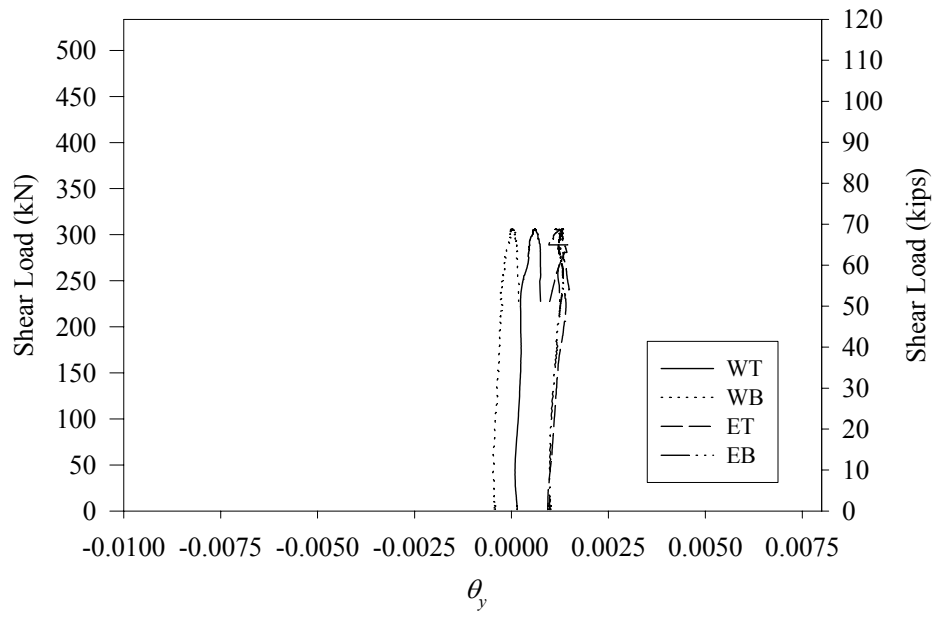


Figure A.32 Rotation about the y-axis, θ_y , for Specimen 7

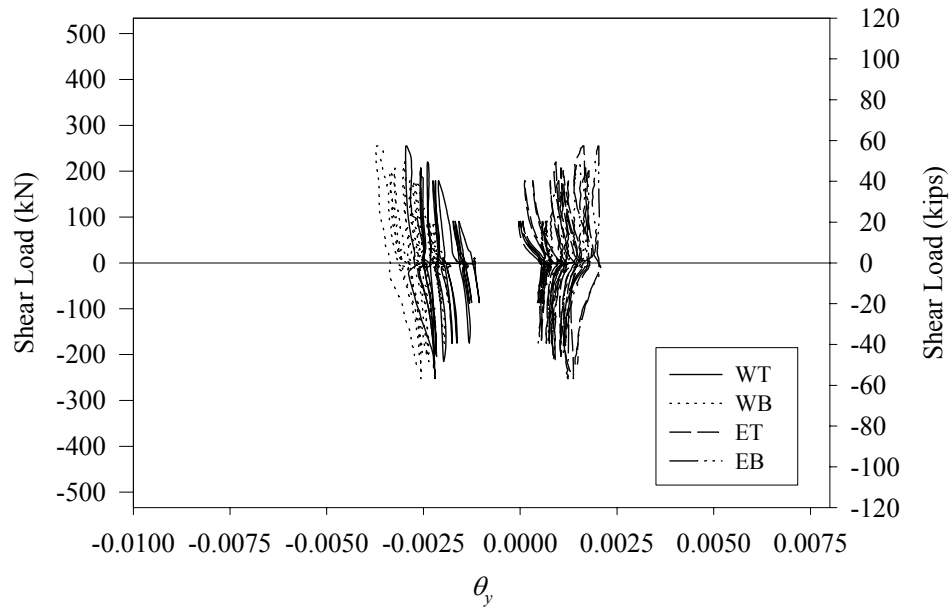


Figure A.33 Rotation about the y-axis, θ_y , for Specimen 8

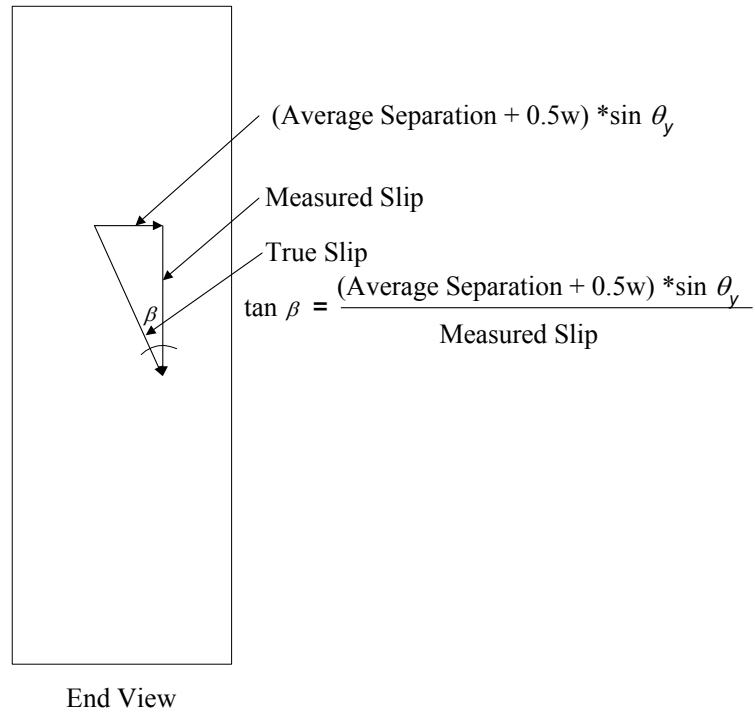


Figure A.34 True versus measured slip